

## **Cross-Flow Instability**

### **Flow diagnostics and control of swept wing boundary layers**

Serpieri, Jacopo

**DOI**

[10.4233/uuid:3dac1e78-fcc3-437f-9579-048b74439f55](https://doi.org/10.4233/uuid:3dac1e78-fcc3-437f-9579-048b74439f55)

**Publication date**

2018

**Document Version**

Final published version

**Citation (APA)**

Serpieri, J. (2018). *Cross-Flow Instability: Flow diagnostics and control of swept wing boundary layers*. [Dissertation (TU Delft), Delft University of Technology]. <https://doi.org/10.4233/uuid:3dac1e78-fcc3-437f-9579-048b74439f55>

**Important note**

To cite this publication, please use the final published version (if applicable). Please check the document version above.

**Copyright**

Other than for strictly personal use, it is not permitted to download, forward or distribute the text or part of it, without the consent of the author(s) and/or copyright holder(s), unless the work is under an open content license such as Creative Commons.

**Takedown policy**

Please contact us and provide details if you believe this document breaches copyrights. We will remove access to the work immediately and investigate your claim.

# **CROSS-FLOW INSTABILITY**

FLOW DIAGNOSTICS AND CONTROL OF  
SWEPT WING BOUNDARY LAYERS



# **CROSS-FLOW INSTABILITY**

FLOW DIAGNOSTICS AND CONTROL OF  
SWEPT WING BOUNDARY LAYERS

## **Dissertation**

for the purpose of obtaining the degree of doctor  
at Delft University of Technology  
by the authority of the Rector Magnificus prof. dr. ir. T.H.J.J. van der Hagen  
Chair of the Board for Doctorates  
to be defended publicly on  
Thursday 15 March 2018 at 12:30 o'clock

by

**Jacopo SERPIERI**

Master of Science in Aerospace Engineering,  
University of Naples "Federico II", Naples, Italy,  
born in Naples, Italy.

This dissertation has been approved by the

promotor: Prof. dr. F. Scarano

copromotor: Dr. M. Kotsonis

Composition of the doctoral committee:

Rector Magnificus,	chairman
Prof. dr. F. Scarano,	Delft University of Technology
Dr. M. Kotsonis,	Delft University of Technology

*Independent members:*

Prof. dr. ir. L. L. M. Veldhuis,	Delft University of Technology
Prof. dr. K. S. Choi,	University of Nottingham, Nottingham, United Kingdom
Prof. dr. E. White,	Texas A&M University, College Station, United States of America
Dr. A. Antunes,	Embraer S. A., San José dos Campos, Brazil
Dr.-Ing. M. J. Kloker,	IAG, Universität Stuttgart, Germany
Prof. dr. S. Hickel,	Delft University of Technology, reserve member



*Keywords:* Swept wings, boundary layer transition, cross-flow instability

*Printed by:* Rijnja Repro Delft

*Front & Back:* Author's cartoon of the cross-flow instability flow structures and of the flow streamlines around a swept wing

Copyright © 2018 by J. Serpieri

ISBN 978-94-6186-879-4

An electronic version of this dissertation is available at

<http://repository.tudelft.nl/>.

*to Giulio Regeni,*  
(PhD Researcher,  
tortured and assassinated in Egypt)



# PREFACE

## ABOUT MY PHD

This booklet contains part of the research work done during my PhD at Delft University of Technology, *Aerodynamics*, in the period from November 2013 to November 2017. This research focused on the instability mechanisms of laminar swept wing boundary layers. It started from an idea (that got funded by a *NWO Veni* grant) from my PhD supervisor, Marios, of investigating this flow phenomenon with state-of-art technology present in the laboratory of *Aerodynamics* (and at *Aero- and Hydro- Dynamics*). Moreover, advanced flow control devices (plasma actuators) were planned to be used during this research as a natural consequence of Marios' amusement with these shivering toys...

It was a rather open and challenging adventure as it started from nothing but some intriguing ideas. Nevertheless, despite some little frustrations mainly related to the rather limited share of the wind-tunnel schedule dedicated to research, we (Marios and I) dived into this research with enthusiasm and dedication.

This adventure has been a long life-changing trip into science, around the world and into myself. I met many colleagues and inspiring persons (for merits or, in a few cases, demerits), I learnt to run experiments, analyse and synthesise data, communicate results, defend them or instead conjecture them, to supervise students and handle their and mine emotions.

I am a very different person from the one that entered the high-speed-lab for the first time. This was my goal for my PhD and I am happy and proud to call it accomplished!

## ACKNOWLEDGEMENTS

My PhD could not have been so enjoyable without the support from many colleagues, friends and relatives. Here my acknowledgements.

## PHD

I will never be thankful enough to Marios. The day I started my PhD, he addressed me saying: "Welcome on board! The next four years will be the happiest of your life...". I had to realize that from science to life, Marios is a person from which there is much to learn. Indeed, he was right: these last years, have been a very happy period. What he didn't say then is that he would have been a main cause of it... Marios in fact has been not only my PhD supervisor, but a friend and a companion of many discussions (often accompanied by sophisticated drinks) from Fluid Dynamics to Politics, Economics and Art. He always embraced my ideas with enthusiasm and dedication. The lack of formality that Marios establishes with his students never compromises the working (hierarchical) relationship. The latter doesn't hold on authority but on the example he gives. I always felt that all what he asked me to do was not only feasible but he either did it already or could do it. He was

always the first one to push and support me but also the first one to stand in front of or next to me during some lab issues/frictions. Marios is just a leader and one of the most brilliant persons I ever met. What a luck to have him as my PhD supervisor!

Another inspiring guy I worked with during these years is Fulvio (my PhD promotor). In these years, with Fulvio we had many intriguing conversations from Fluid Dynamics to emotions or lab issues often accompanied with a nice Italian meal in the center of Delft. He was always available for some advices on experiments or publications "strategies", always happy to share his expertise. Fulvio's usual challenging (and sometimes provoking) attitude is a constant stimulus to excellence.

I wish to thank my PhD-defense committee members. In a special way, I am thankful to Drs. Markus Kloker and Edward White who followed the steps of this research and addressed it with precious advices through the years. From College Station to Stuttgart passing from Delft, I enjoyed the time spent together chatting about cross-flow instability and non-related cross-topics. Also Embraer S. A., in the persons of Dr. Alexandre Antunes and Renato Cosin, has been an enthusiastic work companion. I enjoyed all the moments when the work done together crossed with my PhD research.

In the last four years, I met so many other persons that filled my stay in the Netherlands with friendship and joy. Starting from my colleagues, I wish to thank all those that passed from the PhD-room in these years and, especially, Andrea, Mustafa, Shuanghou, Rogier and Kyle (the "older" experts), Shaafi, Haohua, Rakesh, Wouter & Wouter, Zeno, Martin, Varun, Weibo, Liesbeth, Tiago, Paul, Henri, Mirja, Yi and, lastly, Alberto. To Alberto, the youngest colleague, go my good luck wishes. The idea that, if with this research we started something, it will be (in part) continued by such a nice, prepared and enthusiastic person makes me leave happier.

With some of the PhD-room colleagues it happened to build a closer friendship. These deserve a special acknowledgement as they had to withstand me as a colleague and as a friend (I am fully aware of how hard it is to deal with a constantly provoking person like me!). Thus, a big "thanks" goes to Valeria and Qingqing for all the laughters and serious talks had together. With Jan (or Gianni, another one that doesn't go shallow with provocations), Theo, Koen and Beppe with their unique (yet so diverse among them) humour, personality and intelligence we had countless moments of amusement as well as more serious ones dedicated to Fluid Dynamics and related experiments or to PhD life emotions and situations. To Koen and Jan goes one more "thank you" for translating to Dutch propositions and summary, respectively. A special mention goes also to Peppe, "il Maestro": the dictionary definition of "determination" and "motivation" and yet such a fun person.

Besides my closer office mates, I wish to thank all the colleagues working at *Aerodynamics/Wind Energy/Flight Performance and Propulsion* as well as those in the lab of *Aero- and Hydro- Dynamics* for all the interesting discussions we had during some department events or simply waiting for a cup of coffee behind a vending machine.

Moving out from our group and from the high-speed-lab, the first two persons that I need to thank for all the time spent together, for being always available, for helping me from setting up an experiment to data processing as well as in my personal life, for all the beers, jokes, laughters, trips, dinners, beers again, bike tours etc. had together, are Dani and Francesco. Quite a pair of diverse personalities yet making together an exceptional

research group and an amusing company. Good luck, boys.

Another couple of persons that need to be especially acknowledged are Andrea and Stefan who were invited to the defence ceremony as my *paranymphs*. Two exceptional scientists and persons with whom to discuss about everything and, from whom, I always received extremely interesting ideas and points of view (often so different from mine) when not open critics. Real friends are those that tell you everything... Somehow, in different moments and places and without knowing each other, Andrea and Stefan believed in me becoming a scientist. The esteem I have for them made me think I could accept a challenge that was often felt by me as too big. If you are now reading these lines, it means they were foreseeing right.

I need to thank all the technical and administrative personnel of *Aerodynamics* for helping and facilitating my work and stay. In particular, I wish to thank Nando, for being always available and for sharing with me the LTT-planning frustrations, to Henk-Jan for guaranteeing and improving the safety of the lab and to Ruud for arranging the finances and administrations of the projects I have been involved in. "Thanks" to Nico, Pieter and Fritz for the assistance received. To Denis, who recently joined the group, I wish to enjoy the new job. To Stefan and Leo goes my deepest gratitude for all the work done for and with me to run my experiments in the LTT. Leo is such a good work companion and a wonderful person: the low-speed-lab will not be the same after his retirement and I am happy that this will happen only after the completion of my activities there. I will also miss the enjoyable chats with Stefan who has been another fantastic work and leisure companion.

Another special person, without whom *Aerodynamics* would not be the same, is Colette. More than a secretary, Colette has been my bureaucratic assistant and friend helping me out in many situations rendering my stay abroad much easier! A "thanks" goes also to all the Graduate School -related persons I met or worked behind the screens (which often ended up being again Colette!).

Finally, I need to acknowledge Edwin (from the lab of *Aero- and Hydro- Dynamics*) for lending me lab equipment and arranging it for me.

I want to thank and wish success to all the students I have co-supervised in these years at *Aerodynamics*: Mudit, Srikar, Filippo, Marc and Paolo as well as all the MSc and BSc students of *Flow Measurement Techniques* and of the *High and Low Speed Aerodynamics lab practicals*. Working with you has been a main feeding source of new energies in these years. I hope to have transmitted you some knowledge and passion with clarity and emotion. Nevertheless, despite my efforts, I have often failed. This became very obvious that day in the low-speed-lab when I looked back at the whiteboard at the end of my lecture and, next to my name, somebody wrote with the red marker: "SUCKS"...

## PRIVATE LIFE

Finally, I need to thank all the friends I made in the Netherlands: Sara, Massimo, Daniele, Matteo, Silvia, Greta and Sere who have been my second family together with all the fantastic people I shared home with: Tia, Annie, Chiara, Fabri, Elena, Lucià and (again) Dani & Sere (Dani, this the second time I am thanking you, don't say that I don't love you!). Having your friendship has been crucial to spend and yet enjoy so many years far away from (what used to be) home, always knowing of being not alone. Also my sweet feline

flatmates Tigre and Fatima need to be mentioned for their charming company.

An acknowledgement also goes to some other friends who further contributed to make my stay in the Netherlands so pleasant: Fisca, Fabio, Cuono, Matteo, Pablo, Vincenzo & Judit, Antonio & Antonio, Manu, Jan V., Anke, Egle, Giuseppe T., Cristina, Nalini, Jeff, Robin, Ramona and the little Aya... Too many, too nice persons. My Neapolitan friends are my emotional backbone. Among them especially Giulia, Micol, Federica, Giuggi, Totò, Renato, Peppe and Edo. Lately, a piece of my heart got stolen by the nephews/nieces that came along in these years: Noah, Gio', Caterina and Carolina; a constant reminder of how life is a wonderful and yet un-understandable adventure. A "thank you" goes also to my former university study-mates who contributed to my Aerospace adventure and with whom we built, through the years, a close friendship.

My gratitude goes to my family: my mother, my father and my sister for always being supportive, patient, helpful and full of love. Carolina, having such a brilliant person as younger sister has been such a strong source of inspiration. Am very proud of you! Mamma, sometimes we crash against each other but I know that many of my qualities are a shade of your love. Papà, your love and support, in these years, (re-)became a constant upon which rely. I am deeply thankful to my parents for many things but above all, for having never (willingly) conditioned my decisions, always encouraging me to find my way, whatever that was.

My other relatives also shared with me countless important moments throughout my life. "Thank you" for all the love received. Among them, a special mention needs to be done for my grandmothers Maria and Rosanna and for nonno Carlo that aren't here celebrating this moment with me but whose love I will always feel. Nonno Franco, I dedicate this achievement to you because I know you will be one of the happiest persons about it and because you are my main role model. Making proud of me the person I am the most proud of has been and will be my main drive.

Lastly, there is the person with whom I shared (in the exact same period, even) an adventure way bigger, for emotional intensity, than the PhD. The person that in these years had the strongest impact on me and on the way I think and see the world: Claudia.

If I found thousands words to describe my research in this booklet, I almost never had words to you. But your heart never needed words and neither did mine. Claudia, you are special. Please remain the pure person you are because this world needs more persons like you. Or, at least, I do. For all the love and joy we shared and for all the patience you dedicated to me, "grazie"!

**Jacopo Serpieri**  
*Casa, Massa Lubrense,  
September 2017*

*Fatti non foste a viver come bruti*

...



# CONTENTS

<b>Preface</b>	<b>vii</b>
<b>Summary</b>	<b>xvii</b>
<b>Samenvatting</b>	<b>xix</b>
<b>I Prologue</b>	<b>1</b>
<b>1 Cross-flow instability and this research</b>	<b>3</b>
1.1 Introduction . . . . .	4
1.2 Boundary layer and boundary-layer transition . . . . .	4
1.2.1 2D and 3D boundary-layer transition . . . . .	7
1.3 Cross-flow instability . . . . .	9
1.3.1 Primary instability . . . . .	11
1.3.2 Secondary instability. . . . .	13
1.4 Control of cross-flow instability. . . . .	16
1.4.1 DRE/UFD . . . . .	16
1.4.2 Base-flow manipulation . . . . .	18
1.5 Motivation of this research . . . . .	20
1.6 Layout of this booklet . . . . .	21
<b>2 Techniques and data analysis</b>	<b>23</b>
2.1 Flow diagnostics . . . . .	24
2.1.1 Oil-flow visualization . . . . .	24
2.1.2 Infrared thermography. . . . .	24
2.1.3 Hot-wire anemometry . . . . .	25
2.1.4 Particle image velocimetry. . . . .	25
2.1.5 Tomographic particle image velocimetry . . . . .	27
2.2 Wind tunnel model and facility . . . . .	28
2.3 Reference systems . . . . .	29
2.4 Flow control devices . . . . .	31
2.4.1 Considered passive and active devices . . . . .	31
2.4.2 Passive devices for stationary CFI control . . . . .	32
2.4.3 AC-DBD plasma actuators for stationary CFI control . . . . .	33
2.4.4 AC-DBD plasma actuators for base-flow manipulation . . . . .	34
2.4.5 AC-DBD plasma actuators for unsteady/secondary CFI control . . . . .	35
2.5 Laminar-boundary-layer numerical solution . . . . .	35
2.5.1 Semi-infinite swept wing. . . . .	35
2.5.2 Semi-infinite swept wing with 2D plasma actuators . . . . .	36

2.6	Linear stability theory . . . . .	37
2.7	Data analysis . . . . .	38
2.7.1	Welch's modified periodogram . . . . .	38
2.7.2	Proper orthogonal decomposition . . . . .	39
2.7.3	Butterworth filters . . . . .	40
2.7.4	Parseval's theorem normalization . . . . .	40
2.7.5	Flow metrics . . . . .	40
2.8	Non-dimensionalization . . . . .	41
<b>3</b>	<b>Wind tunnel model</b>	<b>43</b>
3.1	Introduction . . . . .	44
3.2	Model design . . . . .	44
3.2.1	Airfoil . . . . .	44
3.2.2	Wall liners . . . . .	45
3.3	Wind tunnel preliminary experiments . . . . .	46
3.3.1	Flow spanwise-uniformity . . . . .	46
3.3.2	Laminar-to-turbulent transition . . . . .	48
3.3.3	Cross-flow instability . . . . .	50
3.3.4	Effects of free-stream turbulence and surface roughness on CFI . . . . .	52
3.4	Stability of the laminar boundary layer . . . . .	53
3.5	Conclusions. . . . .	55
<b>II</b>	<b>Flow diagnostics</b>	<b>57</b>
<b>4</b>	<b>Primary cross-flow instability</b>	<b>59</b>
4.1	Introduction . . . . .	60
4.2	Experimental setup . . . . .	60
4.2.1	Flow conditions . . . . .	60
4.2.2	Flow visualisation . . . . .	60
4.2.3	Hot-wire anemometry . . . . .	61
4.2.4	Tomographic PIV. . . . .	62
4.3	Results and discussion . . . . .	64
4.3.1	Laminar-to-turbulent transition . . . . .	64
4.3.2	Streamwise evolution . . . . .	65
4.3.3	Comparison between computed and measured boundary layers . . . . .	70
4.3.4	Spatial organisation . . . . .	71
4.4	Conclusions. . . . .	75
<b>5</b>	<b>Secondary cross-flow instability</b>	<b>77</b>
5.1	Introduction . . . . .	78
5.2	Experimental setup . . . . .	78
5.2.1	Time-resolved PIV . . . . .	78
5.3	Results and discussion . . . . .	79
5.3.1	Spectral characteristics . . . . .	80
5.3.2	Streamwise evolution . . . . .	82
5.3.3	Spatial organisation . . . . .	84
5.3.4	Time-resolved analysis. . . . .	93

5.4	Conclusions. . . . .	97
<b>III</b>	<b>Flow control</b>	<b>99</b>
<b>6</b>	<b>Primary cross-flow instability</b>	<b>101</b>
6.1	Introduction . . . . .	102
6.2	Experimental setup . . . . .	102
6.2.1	Infrared thermography. . . . .	103
6.2.2	Particle image velocimetry . . . . .	104
6.2.3	AC-DBD plasma actuator . . . . .	106
6.3	Test cases . . . . .	109
6.4	Results and discussion . . . . .	110
6.4.1	Infrared flow visualisation . . . . .	110
6.4.2	Velocity field . . . . .	113
6.4.3	Effects of plasma forcing on flow stability: a simplified model . . . . .	125
6.5	Conclusions. . . . .	128
<b>7</b>	<b>Secondary cross-flow instability</b>	<b>133</b>
7.1	Introduction . . . . .	134
7.2	Experimental setup . . . . .	134
7.2.1	Hot-wire anemometry . . . . .	134
7.2.2	AC-DBD plasma actuator . . . . .	135
7.3	Test cases . . . . .	139
7.4	Results and discussion . . . . .	139
7.4.1	Statistical analysis . . . . .	139
7.4.2	Spectral analysis . . . . .	141
7.4.3	Spatial evolution . . . . .	143
7.4.4	Spatio-temporal organisation . . . . .	144
7.4.5	Effect of stationary CFVs amplitude . . . . .	147
7.4.6	Effect of actuator location . . . . .	149
7.5	Conclusions. . . . .	151
<b>IV</b>	<b>Epilogue</b>	<b>153</b>
<b>8</b>	<b>Conclusions and outlook</b>	<b>155</b>
8.1	Flow diagnostics . . . . .	156
8.2	Flow control. . . . .	157
8.3	Outlook: a proof-of-concept experiment . . . . .	158
<b>9</b>	<b>Nomenclature</b>	<b>161</b>
	<b>References</b>	<b>165</b>
	<b>Scientific contributions</b>	<b>a</b>
	<b>Biographical note</b>	<b>c</b>



# SUMMARY

The dramatic increase of air traffic together with the augmented attention towards the related pollution and costs require the scientific community to dedicate research effort towards more efficient concepts for commercial aviation. Specifically, from a fluid mechanics perspective, boundary layer transition is a main topic of research attracting interest from the major research groups around the world. The transition of the boundary layer flow from a laminar to a turbulent state is related to increased skin drag and heat exchange between the flowing fluid and the aerodynamic body.

Modern jet airliners feature swept wing geometries allowing them to reduce the flow compressibility effects during cruise flight. The boundary layer transition, in swept wing flows, is mainly influenced by the cross-flow instability. This instability is caused by a secondary flow, the cross-flow, developing within the boundary layer in flows where three-dimensionally curved streamlines take place. In flight conditions, this instability manifests in co-rotating stationary vortices roughly aligned with the flow. These vortices strongly modulate the velocity field within the boundary layer. Moreover, the strong shears caused by the cross-flow vortices undergo secondary instability. Different secondary instability modes, featuring different characteristics in terms of topology and evolution, can develop and lead to the laminar boundary layer breakdown.

The research presented in this booklet focusses on the cross-flow instability. Applying traditional and advanced flow diagnostics, the boundary layer evolution is studied in detail. The topology and evolution of both primary and secondary instability mechanisms is revealed with unprecedented detail for experimental research paving the way for new advanced-diagnostics investigations. Important confirmations of the outcomes of past experimental, numerical and theoretical studies are achieved together with the description of a newly-reported flow phenomenon. The latter consists of a low frequency motion of the "stationary" primary vortices. While this phenomenon is considered not relevant for the transition evolution, it is deemed important for experimental investigations as it encompasses very high levels of turbulent kinetic energy.

Advanced flow control experiments based on alternating current dielectric barrier discharge plasma actuators are also performed following different instability control approaches. The primary instability is conditioned by the external forcing either in the wavenumber spectrum (by inducing selected spanwise modes) or in intensity (by weakening or enhancing the cross-flow velocity). The secondary instability modes are conditioned in the frequency spectrum and phase. These efforts achieved the intended scopes. Although, when selected stationary modes were forced, the boundary layer fluctuations were enhanced. These fluctuations can directly cause the turbulent breakdown vanishing the beneficial effect of the performed instability control. The cross-flow forcing, making use of newer actuators reaching higher frequencies, resulted successful yielding transition promotion or delay depending on the forcing direction.



# SAMENVATTING

De dramatische toename van luchtvaart, in combinatie met de vergrootte belangstelling voor de geassocieerde vervuiling en kosten, vereisen de wetenschappelijke gemeenschap aandacht te schenken aan onderzoek naar meer efficiënte concepten voor commerciële luchtvaart. Om precies te zijn, vanuit het perspectief van de stromingsleer is grenslaag transitie een hoofdonderwerp voor onderzoek, dat veel aandacht krijgt van belangrijke onderzoeksgroepen wereldwijd. Grenslaag transitie van laminair naar turbulent is gerelateerd aan vergrootte oppervlakteweerstand en warmtewisseling tussen de stroming en het aerodynamische object. Moderne luchtvaartmaatschappijen gebruiken geveegde vleugel geometrieën, wat ze toestaat de effecten van compressibiliteit te verminderen tijdens de kruisvlucht. Grenslaag transitie wordt bij geveegde vleugelstromingen vooral beïnvloed door de dwarsstromingsinstabiliteit. Deze instabiliteit wordt veroorzaakt door een secundaire stroming, de dwarsstroming, die ontwikkelt binnen de grenslaag in stromingen waarin driedimensionale gebogen stroomlijnen te vinden zijn. Tijdens vliegomstandigheden manifesteert deze instabiliteit zich in co-roterende stationaire wervelingen die ongeveer uitgelijnd zijn met de stroming. Deze wervelingen moduleren het snelheidsveld binnen de grenslaag sterk. Daarbovenop ondergaan de sterke schuifstromen, veroorzaakt door de dwarsstroom wervelingen, een secundaire instabiliteit. Verschillende secundaire instabiliteitsmodi, met verschillende karakteristieken in termen van topologie en evolutie, kunnen zich ontwikkelen en vervolgens leiden tot verschillende laminaire grenslaagafbraak. Het onderzoek dat in dit boek gepresenteerd wordt focust zich op de dwarsstromingsinstabiliteit. Met behulp van traditionele en geavanceerde methoden voor stromingsdiagnostiek wordt de grenslaag in detail onderzocht. De topologie en evolutie van zowel de primaire als secundaire instabiliteitsmechanismen wordt onthuld met voor experimenteel onderzoek ongehoord detail, wat de weg vrij maakt voor nieuw geavanceerd diagnostisch onderzoek. Belangrijke resultaten van eerder experimenteel, numeriek en theoretisch onderzoek worden bevestigd, in combinatie met de beschrijving van een nieuw stromingsfenomeen. Dit stromingsfenomeen bestaat uit een laagfrequente beweging van de 'stationaire' primaire wervelingen. Hoewel dit fenomeen niet als relevant beschouwd wordt voor transitie evolutie, wordt het belangrijk geacht voor experimenteel onderzoek omdat het zeer hoge niveaus van turbulente kinetische energie bevat. Geavanceerde stromingscontrole experimenten gebaseerd op alternerende stroming dielectric barrier discharge plasma actuatoren zijn ook uitgevoerd volgens verschillende aanpakken voor instabiliteitscontrole. De primaire instabiliteit wordt geconditioneerd door de externe versterking in het golfgetal spectrum (door geselecteerde spanwijze modi te induceren), ofwel in intensiteit (door de dwarsstroom snelheid te verzwakken of versterken). De secundaire instabiliteitsmodi worden in het frequentiespectrum en in fase geconditioneerd. Deze inspanningen hebben de beoogde resultaten bereikt. Hoewel, wanneer geselecteerde stationaire modi geforceerd werden, werden grenslaag fluctuaties verstrekt. Deze fluctuaties kunnen direct grenslaagafbraak veroorzaken, wat het beoogde

gunstige effect van de uitgevoerde instabiliteitscontrole teniet doet. De dwarsstroom versterking, gebruik makend van nieuwere actuatoren die hogere frequenties bereiken, geeft een positief resultaat: transitie promotie of vertraging, afhankelijk van de richting van de versterking.

# I

## PROLOGUE



# 1

## CROSS-FLOW INSTABILITY AND THIS RESEARCH

*This chapter provides the reader with an introduction to boundary-layer stability and laminar-to-turbulent transition with a focus on the cross-flow instability of swept wing boundary layers. The control strategies proposed to weaken this flow mechanism are also illustrated together with a description of the motivation for the present research and of the booklet arrangement.*

---

**J. Serpieri** & M. Kotsonis, *Three-dimensional organisation of primary and secondary cross-flow instability*, [Journal of Fluid Mechanics](#), **799**, 200–245 (2016)

**J. Serpieri**, S. Yadala Venkata & M. Kotsonis, *Conditioning of cross-flow instability modes using dielectric barrier discharge plasma actuators*, [Journal of Fluid Mechanics](#), **833**, 164–205 (2017)

## 1.1. INTRODUCTION

The introduction of jet engines after the second World War led to airplanes capable of flying at higher speeds. Swept wings have been a direct consequence of this need. When swept, the wing does not "see" the airspeed at which the airplane flies, but the component of it orthogonal to the leading edge. Therefore skewing the wing leading edge is an *escamotage* to increase the inferior critical Mach number (i.e. the minimum flight Mach number at which a first sonic point appears in the flow field) on the wing. The simplicity of the idea declared its success and today the majority of jet engine airplanes feature swept wings (although different sweep angles are used).

Despite the mentioned advantage, swept wings introduce complications from the structural, aerodynamic and flight dynamics points of view. Moreover swept wings are technologically more complex than the unswept counterparts thus featuring design, manufacturing and maintenance drawbacks.

Nevertheless, the advantage of having faster airplanes, overcomes all these complications and related costs. As such, huge effort has been put by research institutions and airplanes manufacturers in the last fifty years to solve or reduce the complications arisen in the mentioned fields. This thesis is a contribution to this effort. Specifically, the aim of this study is to investigate the main mechanism of laminar-turbulent transition of swept wing boundary layers and condition this mechanism in perspective of more efficient swept wings. In fact, a share close to 40% of the total drag of an airplane is caused by the turbulent flow over the lifting surfaces [11]. Therefore, understanding and developing technologies capable of postponing the flow transition can have crucial impact on the aviation industry as more efficient wings lead to fuel saving with the related beneficial reduction of costs and pollution.

To ensure a clear understanding of the described flow physics, the following sections of this chapter introduce the reader to the flow mechanisms under study and provide an overview of the related literature.

## 1.2. BOUNDARY LAYER AND BOUNDARY-LAYER TRANSITION

Prandtl focused his research on investigating the reasons behind the discrepancies between inviscid flow field theoretical solutions and experimental observations. Among these, the most emblematic case is known as the "d'Alembert paradox" and considers the incompressible, stationary flow field around a two-dimensional circular cylinder. The answer to the observed discrepancies was related to a small region of flow in the very proximity of the aerodynamic body where the inviscid assumption, upon which the theoretical solutions were derived, does not hold. Prandtl named this region "boundary (or frictional) layer" [107]. It is the flow region where, despite the low viscosity of the considered fluids, viscous effects play a non negligible role. The dynamics of the flow in this relatively small region has macroscopic effects on the overall flow field and thus on the aerodynamic performance of a considered body. This explains why, after Prandtl's first conclusions, many research groups around the world concentrated their attention to a variety of viscous (or frictional) layers, free (shear layers) or wall-bounded (boundary layers). As a simple description, the boundary layer is the region of flow field where the velocity field goes from the external inviscid values to relative rest at the body wall.

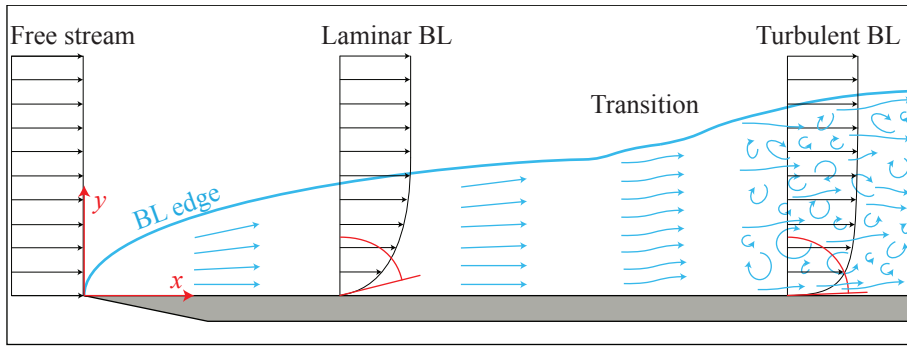


Figure 1.1: Schematic of boundary layer evolution over a flat plate and wall-normal velocity distributions ( $u(y)$ ) for laminar and turbulent BLs. The velocity profiles tangents at the wall and related angle are shown in red. The angle corresponds to  $\frac{\partial u}{\partial y} |_{wall}$ .

Given the lower velocity, the relative effect of the viscous forces with respect to (w.r.t.) the inertial forces is non-negligible. The boundary layer influences the external inviscid flow as it subtracts flowing mass (and momentum). Mechanisms like flow separation, which drastically modify the overall flow field, are also related to flow mechanisms within the boundary layer.

The expression "boundary-layer transition" refers to the process that brings an initially developing boundary layer from the laminar to the turbulent state (see the plume of the candle of figure 1.2a). In laminar boundary layers, fluid layers flow parallel to each other, exchanging momentum via diffusion (viscous shears) and no particles movement occurs in the direction perpendicular to the parallel flow layers. In turbulent boundary layers, instead, chaotic motion of particles enhances the kinetic energy mixing. A schematic of a laminar and a turbulent boundary layer over a flat plate is presented together with the respective wall-normal velocity distributions in figure 1.1. Consequently, laminar and turbulent boundary layers feature very different properties: the latter are much "fuller" meaning that a very strong velocity variation occurs in the proximity of the wall after which the velocity wall-normal distribution slowly approaches the external inviscid value. The wall skin friction ( $\tau$ ) is proportional to the slope of the velocity profile at the wall as expressed in equation 1.1, where  $\mu$  is the fluid viscosity,

$$\tau = \mu \frac{\partial u}{\partial y} |_{wall} \quad (1.1)$$

The wall-normal velocity slope (i.e.  $\frac{\partial u}{\partial y} |_{wall}$ ) of the laminar and turbulent velocity profiles is also shown in figure 1.1. It appears that fuller turbulent velocity profiles are related to higher levels of friction drag compared to laminar boundary layers. Moreover, as the non dimensional wall skin friction ( $c_f$ ) is proportional to the heat convection flux coefficient ( $h$ ), turbulent boundary layers feature stronger heat fluxes between the body and flow (the direction of the fluxes depending on the temperatures of body and fluid and on the flow regime). These two aspects are crucial as they relate the boundary layer transition to enhanced levels of drag and heat flux explaining the interest towards

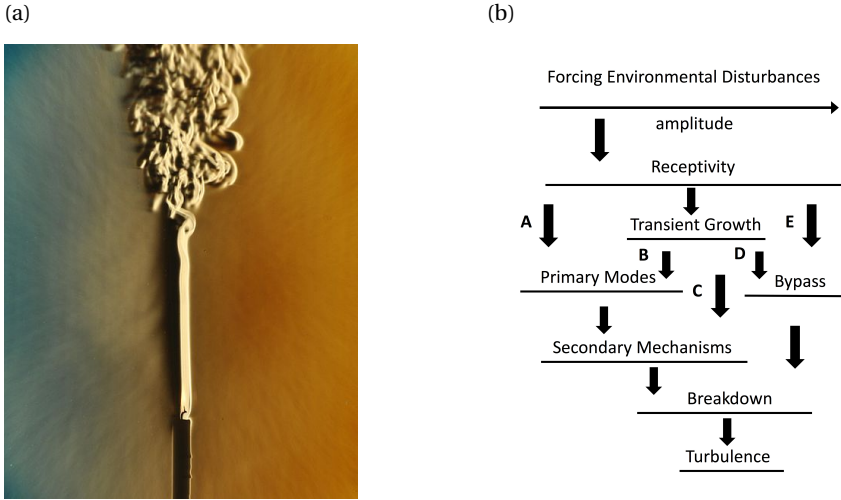


Figure 1.2: (a) Schlieren image of the convection plume from a candle in still air by Settles [117]. (b) Paths to turbulence. Re-adapted from Morkovin *et al.* [87].

the phenomenon. Understanding its mechanisms and possibly controlling them allows to optimize the design of aerodynamic bodies. Limiting the friction drag translates in increased flight endurance and reduced flight cost, while knowing the position of laminar-to-turbulent transition on high speed (e.g. atmospheric re-entry) vehicles leads to optimized thermal shielding.

A further aspect that distinguishes the two regimes is the resistance to separation. Boundary-layer separation occurs when the pressure ( $p$ ) distribution around the body is such to feature a pressure increase along the streamwise direction ( $x$ ) (i.e.  $\partial p / \partial x > 0$ ). Increasing levels of pressure, imposed to the boundary layer, cannot be overcome by the lower kinetic energy particles of the boundary layer and, consequently, the flow escapes from the wall (separation). Nonetheless, the mixing of particles with higher and lower momentum occurring within turbulent boundary layers leads to higher average levels of kinetic energy compared to the laminar counterpart. This signifies that turbulent boundary layers are considerably more resistant to separation and, as separation translates in increased wake drag and reduced lift, explains why, in many industrial applications, boundary layer transition is artificially promoted. This is the case of airplanes wings (see figure 1.3a) or high-lift devices for take-off and landing or bluff bodies (where wake drag is considerably larger than skin friction drag) like golf balls (see figure 1.3b). The dimples on the golf ball surface or the vortex generators on the *Harrier II* wing trip the laminar boundary layer and promote vortices enhancing the air mixing and reducing the separated region.

Laminar-to-turbulent transition has been and currently is the object of extended research. Many different mechanisms can take place leading to very diverse scenarios. Despite the underlying flow topology, five different paths to transition can be summarized



Figure 1.3: (a) Vortex generators on the wing suction side of a *Harrier II*. (b) Dimples on a golf ball.

with the schematic of figure 1.2b, presented by Morkovin *et al.* [87]. External disturbances such as free stream fluctuations (related to vortical structures or pressure waves) or surface roughness are assimilated by the boundary layer by the process of "Receptivity". If the amplitude of these perturbations is small enough, a modal description of the boundary layer unsteady flow field can be sought (i.e. the disturbance flow field can be described as a linear superposition of orthogonal modes). The flow structures described by the modal analysis "Primary Modes" can be very diverse depending on the considered flow case. Nonetheless, while undergoing amplitude (temporal or spatial) growth, they strongly modify the boundary layer to an extent that the distorted flow undergoes a "Secondary" instability. Usually the flow structures related to these secondary mechanisms are very different from the primary type modes. They usually amplify at a much higher rate and they cause the "Breakdown" of the laminar boundary layer that leads to the fully turbulent state ("Turbulence"). This research focuses on flow mechanisms as those described by the path "A" in the schematic of figure 1.2b.

When the amplitude of the external disturbances increases, non-modal growth of boundary-layer fluctuations takes place ("Transient Growth") leading either to secondary instability ("C") or direct breakdown ("D"). The path "E" is followed when the boundary fluctuations are so large that non-linear interactions or unknown mechanisms take place [87].

### 1.2.1. 2D AND 3D BOUNDARY-LAYER TRANSITION

While considering only "A" type paths, boundary layer transition can be caused by a variety of different mechanisms depending on the considered flow case and external disturbances. A comprehensive description of these phenomena can be found in classic books as Schlichting & Gersten [107] or White & Corfield [136]. In this section, a short overview of the transition instability mechanisms of two- and three-dimensional subsonic boundary layers is provided.

In two-dimensional flows, the unsteady flow field is often characterized by two-dimensional vortices aligned with the spanwise direction that are advected by the boundary-layer flow towards the trailing edge. These vortices are named Tollmien-Schlichting (TS)

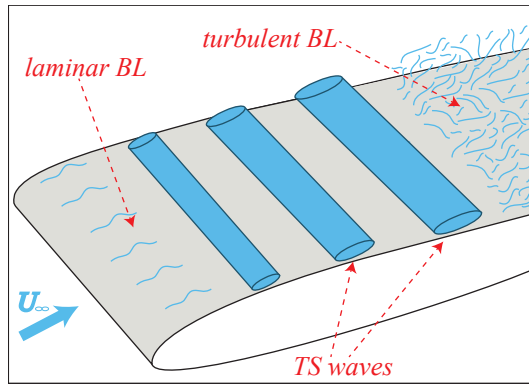


Figure 1.4: Schematic of two-dimensional-boundary-layer transition characterized by TS instability.

waves and are strongly amplified when the pressure gradient in the streamwise direction is positive. TS waves are very receptive to acoustic and vortical free-stream disturbance. Figure 1.4 schematically shows the transition evolution for two-dimensional boundary layers characterized by TS instability.

Moving downstream the vortices grow in amplitude. Moreover, more downstream the advection velocity decreases as a consequence of the boundary layer thickening. Consequently, neighbouring vortices may collapse on each other merging together and generating larger waves at double wavelength (thus a fixed flow probe sees fluctuations at half the initial frequency). This phenomenon is referred to as "vortex pairing". Finally, secondary instability mechanisms, in the form of a spanwise modulation of the two-dimensional rollers, cause the flow breakdown [79, 78, 84]. The transition front follows this three-dimensional modulation. Nonetheless, the spanwise modulation and transition onset vary in time. In a time-averaged perspective, the transition front appears rather uniform in the spanwise direction as shown in the schematic of figure 1.4.

Three-dimensional boundary layers feature a different main transition scenario (described in the schematic of figure 1.5) characterised by the cross-flow instability (CFI). A deeper description of the phenomenon is presented in the following sections. Nonetheless, for comparison with 2D boundary layers transition, the main features of CFI transition are introduced. A characteristic of this phenomenon are co-rotating vortices aligned with the flow direction called cross-flow vortices (CFVs). These vortices are amplified in accelerating flows. They are stationary when the free-stream turbulence is low whereas they travel along the spanwise and streamwise direction when the latter is higher. Despite the stationary or travelling nature, the CFVs amplitude increases towards the trailing edge. Also in this case, vortices interactions can take place as well as secondary instability mechanisms. Both primary and secondary CFI mechanisms are not receptive to free stream acoustic perturbations [19, 27]. In cases where stationary CFI waves occur, a spanwise modulation of the transition front (in the time-averaged perspective) is observed. The spanwise position of the turbulent wedge apex corresponds to vortices that underwent stronger amplification (see the schematic of figure 1.5). This usually happens when some localised surface roughness or imperfections are present on the surface as CFI boundary

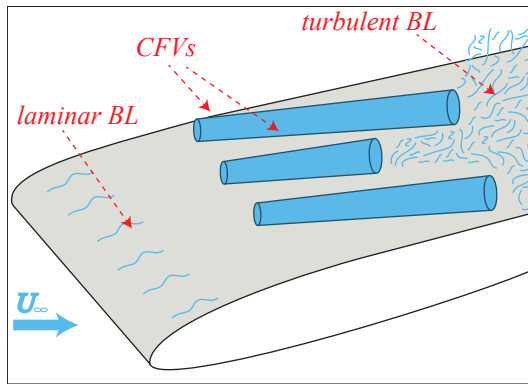


Figure 1.5: Schematic of three-dimensional boundary layer transition characterized by CF instability.

layers are much receptive to this type of perturbations [97, 94, 32, 121, 62] (i.e. CFVs packets [129]).

While TS modes often dominate the transition scenario in decelerating 2D boundary layers and CFV in accelerating 3D flows, other transition mechanisms can take place depending on the considered flow. A brief overview of the main mechanisms occurring in subsonic boundary layers is provided. If the aerodynamic body features concave surfaces, Görtler vortices with related secondary instability might cause the boundary layer transition [38, 69, 109]. When the laminar boundary layer flows over large roughness elements direct (immediately downstream) or indirect (related to the element wake) transition to turbulence occurs for both 2D [52, 92, 140] and 3D boundary layers [63, 10]. Finally, in swept bodies with small leading edge curvature like e.g. swept cylinders, a boundary layer develops along the attachment line. This flow can undergo instability thus contaminating the overall boundary layer [93, 37, 122].

### 1.3. CROSS-FLOW INSTABILITY

The flow over swept wings is subject to laminar-turbulent transition due to the growth and breakdown of the so-called cross-flow instability modes. This inviscid instability mechanism can be traced back to the flow topology of the boundary layer developing over the wing (e.g. [75, 104]). This flow, as well as the one around axisymmetric bodies at incidence or spinning about the symmetry axis (e.g. [70, 111, 43, 44, 88, 65]), follows three-dimensional trajectories. Considering a particle of air moving along a streamline near the aerodynamic body, the force equilibrium in the direction orthogonal to the streamline itself and parallel to the model surface is dictated by the pressure forces (which cause centripetal acceleration) balanced by the centrifugal forces (which, instead, tear the particle outwards of the streamline). While the equilibrium holds in the inviscid flow field, it does not hold within the boundary layer where, given the lack of momentum, the air particle will move perpendicularly to the inviscid streamlines. This secondary flow is called cross-flow (CF). In practice, the boundary-layer velocity profile along the direction orthogonal to the inviscid streamlines will have null values at the wall and at the outer

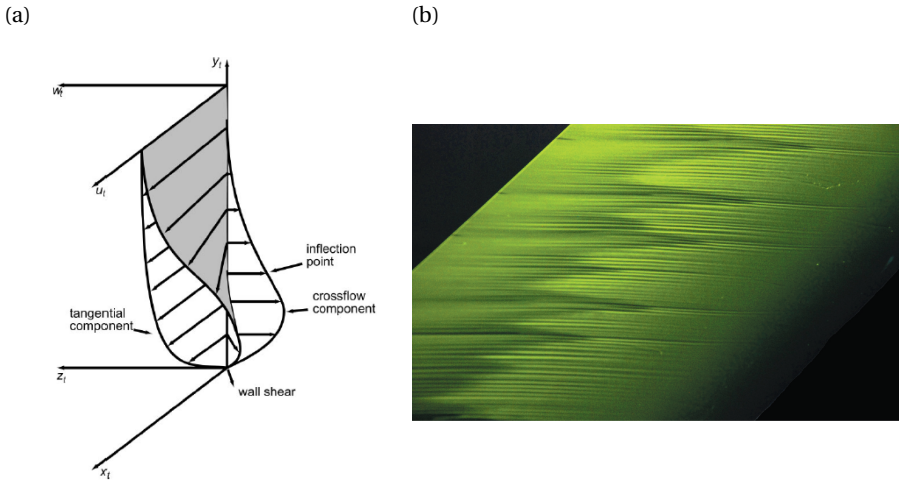


Figure 1.6: (a) Boundary layer velocity profiles in the inviscid streamline reference system. Reproduced from [104]. (b) Fluorescent oil visualization on a 45 degrees swept wing at  $Re = 1.3 \cdot 10^6$  in TU Delft LTT facility. Flow from right. The darker areas show the turbulent region of the boundary layer. The CFVs' horizontal streaks are also captured.

edge but a finite local maximum at a given wall-normal position as shown in figure 1.6a.

The velocity profiles feature a point of inflection and this gives rise to inviscid instability modes [104]. These can be of a travelling or stationary nature depending on the boundary-layer receptivity to free-stream turbulence and surface roughness [6].

Surface flow visualisation and infrared thermography experiments in low-turbulence wind tunnels (e.g. [18, 6, 104, 103]) have shown a distinctive transition scenario for this type of boundary layer, characterised by sequences of streaks aligned, within a few degrees, with the flow direction. These streaks are the footprint of stationary boundary layer vortices causing a velocity modulation along the wing span and therefore of the wall skin friction and of the convective heat flux (quantities usually captured in these experiments). The picture of figure 1.6b shows the CFI transition pattern on a 45 degrees swept wing at  $Re = 1.3 \cdot 10^6$  installed in the TU Delft LTT facility. The stationary vortices' streaks and the jagged transition front are evidenced by the visualization.

The cross-flow vortices, although relatively weak, modify the mean flow and, consequently, the stability of the boundary layer. They tear low-momentum flow from the lower regions of the boundary layer and displace it upwards in high-momentum regions, and *vice versa*. This results in a modified boundary layer featuring a momentum modulation of the flow in the spanwise direction and in the development of strong velocity shears in the spanwise and wall-normal directions, which are highly unstable to secondary instability mechanisms.

Experimental investigations on three-dimensional boundary layers were mainly carried out in Germany (Deutsches Zentrum für Luft- und Raumfahrt (DLR) Göttingen) by Bippes and coworkers [6, 19] and in United States by William Saric and his group (Arizona

State University (ASU) first and Texas A&M University (TAMU) later) [104, 135]. These campaigns made use of very quiet wind tunnels, exhibiting a free-stream turbulence level typically lower than 0.1% of the free-stream velocity. Surface flow visualisation was performed by means of infrared thermography [103], hydrogen bubbles tracing [6], naphthalene sublimation techniques [18, 100, 134] and fluorescent mineral oil [112, 113]. Hot-wire-anemometry (HWA) boundary-layer measurements were performed using precision sensor traversing systems (e.g. [97, 19, 51, 135]). Glauser *et al.* [34] reported the use of hot-film surface sensors. Along with these experimental efforts, several studies based on stability theories (e.g. [30, 77, 39, 45, 54, 53, 8, 67, 88]) and on numerical investigations (e.g. [47, 40, 42, 129, 130, 8]) have been performed.

A short review of the main studies on the cross-flow instability is presented in the next section. For more complete reviews the reader is instead referred to Bippes [6], Arnal & Casalis [2], Saric *et al.* [104] and to some more recent studies such as [129, 130, 135, 8, 27].

### 1.3.1. PRIMARY INSTABILITY

In his review article, Bippes [6] reported several experiments, conducted over a period of years at DLR (e.g. [19]), making use of different models and placed in several facilities in order to see the effect of model geometry and free-stream turbulence on the instability development. It was found that the model-leading edge radius influences the attachment line instability while the curvature of the surface has a stabilising effect if convex and a destabilising effect when concave due to the generation of Görtler vortices. The free-stream turbulence level instead changes the type of the amplified cross-flow instability modes: in lower turbulence wind tunnels (with a free stream turbulence intensity related to the free stream velocity of  $\frac{TU}{U_\infty} < 0.15\%$ ) stationary cross-flow waves are observed while, in higher turbulence facilities, travelling modes take place and dominate the transition scenario.

Similar results were recently shown through the extensive measurements performed by Downs & White [27], by carefully modifying and measuring the turbulence intensity of the KSWT facility at TAMU by means of turbulence screens. Their results confirm the effectiveness of surface roughness in forcing the primary stationary modes and the capability of free-stream turbulence to enhance primary travelling modes adding that the latter are also highly sensitive to the surface roughness.

The studies carried out at ASU concentrated mainly on the effect of surface roughness on the stability of the boundary layer and led to significant conclusions: Reibert *et al.* [97] measured several stationary waves in the boundary layer developing on a 45° swept wing featuring a laminar airfoil at chord Reynolds number of  $2.4 \cdot 10^6$ . Towards simplifying the flow arrangement and to facilitate comparison with numerical results, they made use of small roughness elements (cylindrical rub-on transfers with a diameter of 3.7 mm and height of 6  $\mu\text{m}$ ) placed at the model leading-edge region. The roughness elements were spaced along the spanwise direction at distances matching the wavelength predicted by Linear Stability Theory (LST) for the most amplified stationary mode. The discrete roughness elements fixed the wavelength of the amplified mode leading to a more uniform transition pattern compared to the unforced case. The amplitude of the stationary vortices features a monotonic growth till a given saturation amplitude prior to the onset of transition. In the same study, the flow configuration was forced by placing the roughness



Figure 1.7: Streamwise evolution (from left to right) of primary CFVs. Contours of streamwise velocity (re-adapted from Tempelmann *et al.* [121]).

elements at three times the wavelength of the naturally dominant mode. This case showed again the naturally most amplified mode to dominate the transition process but showed also that all the higher harmonics of the forced mode (i.e. shorter wavelength modes) were amplified. In contrast, no lower harmonics were observed in both the performed tests. Moreover, they showed that, if stationary modes undergo amplitude saturation, then the forcing amplitude does not modify the transition process.

These observations were at the base of the study done by Saric *et al.* [100], centred on the idea of forcing a sub-critical mode (which is a mode with a wavelength smaller than that of the most amplified mode) to achieve transition delay. The following efforts in controlling CFI transition are summarized in the next sections.

Radeztsky *et al.* [94] demonstrated the effect of discrete surface roughness on transition location. They performed a careful study on the geometrical parameters (width and height) of the roughness elements showing promotion of transition for taller roughness elements of diameter up to 0.08 times the mode wavelength. For larger diameters, increasing the height of the roughness elements did not have an effect on the transition onset. Additionally, they showed relative insensitivity of the transition process to strong and broadband acoustic forcing in agreement with the work of Deyhle & Bippes [19].

Haynes & Reed [39] used linear and non-linear PSEs as well as LST to investigate the boundary layer experimentally measured by Reibert *et al.* [97]. Their results are in very good agreement with the experimental data. Furthermore, the study highlighted the importance of including non-linear terms and surface curvature. Convex surfaces have a stabilising effect on the primary vortices and, as such, promote their saturation and the occurrence of secondary modes and transition.

Tempelmann *et al.* [121] studied the boundary-layer receptivity to surface roughness by means of Parabolised Stability Equations (PSE) and adjoint PSE together with Direct Numerical Simulation (DNS) (see figure 1.7). They commented on the discrepancies with the experimental results of Reibert *et al.* [97] pointing at possible small imperfections in the application of roughness elements on the model (which is very likely in laboratory conditions given the micrometric size of these elements). The problem of receptivity to surface roughness was further investigated by e.g. Kachanov [50], Gaponenko *et al.* [32], Schrader *et al.* [108], Meneghello *et al.* [80], Mistry *et al.* [85] and Kurz & Kloker [62]. Kurz & Kloker [62] found that the amplitude of the fundamental stationary mode scales linearly with the roughness height only when the roughness array features null spanwise-averaged shape and flow blockage.

### 1.3.2. SECONDARY INSTABILITY

In a study on the stability of a swept cylinder boundary layer, Poll [93] measured high-frequency boundary-layer fluctuations superimposed on the primary cross-flow instability mode. These were reported also in the swept wing experiments by Kohama *et al.* [55] and identified as a secondary instability mechanism acting on the boundary layer modified by the primary stationary cross-flow modes. Since these early works, efforts in revealing the nature and the evolution of the cross-flow secondary instability have intensified.

Malik *et al.* [77], following previous work on Hiemenz flow [76], exploited linear and non-linear parabolised stability equations (PSE and NPSE) to assess the evolution of the primary instabilities as well as a temporal two-dimensional eigenvalue problem to study the secondary instability for the flow case of the ASU experiments [97]. Under the assumption that the secondary modes are of a convective nature (see also the theoretical efforts on the nature of the secondary instability e.g. Fischer & Dallmann [30], Lingwood [71], Janke & Balakumar [45], Koch *et al.* [54] and Koch [53]), they used Gaster's transformation [33] to track the modes' spatial evolution finding good agreement with the experimental results. Another key contribution of Malik *et al.* [77] is the classification of the secondary instability into two main modes. The first is the *type-I* mode, related to the streamwise flow velocity gradient along the spanwise direction (usually  $z$ , from which this mode was referred to as the *z-mode*) located at the outer side of the upwelling region of the primary cross-flow vortex and characterised by higher energy and lower frequencies. The second is the *type-II* mode or *y-mode* that is located on the top of the primary vortices where the streamwise velocity wall-normal ( $y$ ) gradients are larger. This mode usually features lower energy but higher frequencies w.r.t. the *type-I* mode. As last outcome of this study, a transition estimation criterion based on secondary instability amplification was presented showing good correlation with the transition locations measured by Reibert *et al.* [97].

Floquet analysis was used by Fischer & Dallmann [30] and Janke & Balakumar [45] to inspect the secondary stability of the CF vortices of the DLR experiment [19] (in the second study, the secondary instability of a Hiemenz flow boundary layer was also considered). One of the main outcomes from these studies is the investigation of the low-frequency *type-III* mode. This mode refers to the interactions between primary stationary and primary travelling modes and, therefore, its relevance in the transition pattern depends on the free stream turbulence level (see also [40, 27]).

White & Saric [135] dedicated a detailed experimental investigation to the secondary instability mechanisms and sensitivity to different base-flow cases. Hot-wire measurements of velocity fluctuations corresponding to the secondary instability were extracted for a chord Reynolds number flow of  $Re = 2.4 \cdot 10^6$  under stationary critical-mode forcing. Following previous works, micron-sized roughness elements were placed at the leading edge region spaced at the wavelength of the most amplified mode. The different secondary instability modes were detected and their appearance and sudden growth identified as the cause of turbulent breakdown. The conditions under which the *type-II* mode arises and reaches higher energies were those of super-critical forcing (same roughness spacing as the  $Re = 2.4 \cdot 10^6$  case but Reynolds number increased to  $Re = 2.8 \cdot 10^6$ ) where the spanwise shear and hence *type-I* modes are mitigated (see also Hosseini *et al.* [41]).

Furthermore, the influence of increased free-stream turbulence and of acoustic forcing on the transition scenario were also investigated although required further dedicated efforts which came later with the already mentioned study by Downs & White [27].

The first spatial DNS study on the development of secondary instability modes over the primary stationary vortices was performed by Högberg & Henningson [40]. They studied the evolution of a Falkner-Skan-Cooke boundary layer subject to fixed steady primary forcing and random unsteady excitation of the secondary instability via the use of volume body forces. The location of the unsteady volume forces changed the nature of the amplified modes: a more upstream forcing gave rise to lower-frequency *type-III* modes, while a more downstream forcing, close to the location of primary saturation, led to the triggering of the aforementioned high-frequency *type-I* modes. The latter mode showed much larger growth rates than the low-frequency *type-III* mode.

Two later DNS investigations by Wassermann & Kloker [129, 130] further described the topology and the nature of the secondary instability modes developing around stationary and travelling CF vortices, respectively. In these works, the *type-I* secondary instability vortices are visualised and described as a sequence of corotating helicoidal structures superimposed on the upwelling region of the primary vortices and convecting downstream. The axes of these structures form a considerable angle with the one of the primary waves and the spinning direction of the two modes is opposite. An interesting outcome of the simulations of Wassermann & Kloker [129, 130] is that, when the unsteady disturbance that triggers the secondary modes is switched off, the associated structures are advected downstream, thus confirming the findings of e.g. Kawakami *et al.* [51] and Koch [53] regarding the convective nature of these instability modes (see figure 1.8). The evolution of travelling CFI modes with related secondary instability mechanisms was also studied by Li *et al.* [68, 66]. Wassermann & Kloker [131] studied also the transition evolution in presence of pressure gradient changeover with consequent amplification of instability modes of different type.

Another relevant investigation on the secondary instability of stationary and travelling primary CF vortices was reported by Bonfigli & Kloker [8]. The authors used spatial DNS and secondary linear stability theory (SLST), the latter previously applied by Fischer & Dallmann [30], Malik *et al.* [76, 77], Janke & Balakumar [45] and Koch [53]. The two techniques showed good agreement in terms of eigenfunctions and growth rates when the DNS analysis is tuned to the simplified base-flow of the SLST. The two techniques captured the structures related to the *type-I* and *type-III* instabilities, whereas DNS did not show amplification of the *type-II* instability still predicted by SLST. For the analysis of the travelling primary CF instability, with no stationary modes considered, destabilisation of the *type-III* mode is not reported. This is expected given that this mode is generated by the spanwise modulation of the primary travelling waves caused by the stationary CF vortices (see also [30, 40, 45]). One more important outcome of Bonfigli & Kloker [8] relates to the nature of *type-I* and *type-II* modes. The behaviour and location of these modes associates them to instabilities of the Kelvin-Helmholtz (KH) type.

The possibility of experimentally confirming the outcomes of these theoretical and numerical investigations on the spatio-temporal development of the secondary instability has been so far limited. This is attributed to the inherent features of the technique mainly used in wind tunnel tests: single- or double-wire hot-wire probes. Hot-wires, although

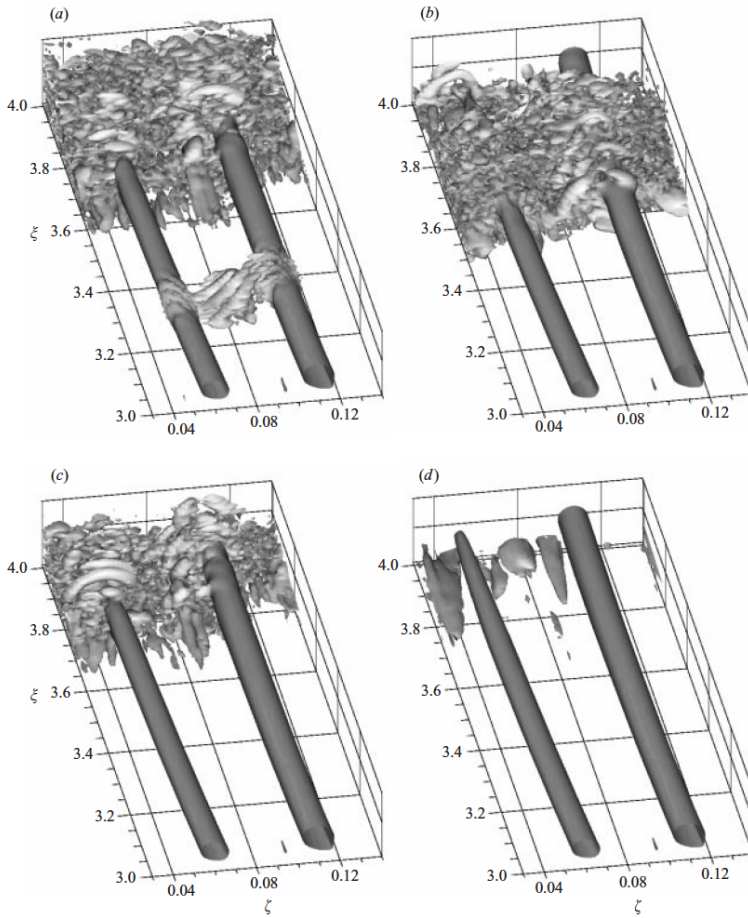


Figure 1.8: Time sequence (after the unsteady forcing is stopped) of  $\lambda_2$  visualizations of primary and secondary CFI modes showing the convective nature of the latter (reproduced from Wassermann & Kloker [129]).

being very accurate for this type of experiment, are a point measurement technique and, as such, cannot infer any information regarding the spatio-temporal evolution of the unsteady structures described in the mentioned numerical/theoretical studies [40, 76, 77, 129, 130, 8].

A successful attempt to overcome this limitation was performed by Kawakami *et al.* [51] who inferred the spatio-temporal evolution of the secondary instabilities in an experimental framework. Although the technique they used was still based on hot-wire measurements, they forced the secondary modes at their respective frequencies by applying unsteady blowing and suction in the boundary layer undergoing primary instability saturation. By correlating the wire signal at the several phases of the actuation, they were able to reconstruct the shape, the direction and the velocity by which the secondary *type-I* waves and the lower-frequency *type-III* modes are evolving in the boundary layer.

Similarly to Kawakami *et al.* [51], Chernoray *et al.* [13] performed phase-locked hot-wire measurements on the secondary instability of streamwise vortices in a swept wing boundary layer. These vortices were not generated by cross-flow instability mechanisms, but rather directly caused by large roughness elements or localised continuous suction and were subsequently subject to the boundary-layer crossflow. Despite these differences, their measurements encompassed full volumes and hence led to the description of the three-dimensional organisation and streamwise evolution of the streamwise vortices and their instability. van Bokhorst & Atkin [7] also followed the same approach and focussed their research on the effect of changing the forcing amplitude on the development of the secondary modes.

Simultaneous multipoint measurements have also been performed using surface-mounted hot-film sensors by Glauser *et al.* [34]. However, the sensors were located at the wall and the region of flow field that was investigated was quite small and not in the zone of the boundary layer directly influenced by the secondary instability. Despite this, the simultaneous use of multiple sensors allowed the study of the spatial coherence of the vortical structures by means of proper orthogonal decomposition (POD). A correlation between the first and second POD mode with the primary travelling cross-flow mode and the secondary instability, respectively, was proposed for a transition prediction criterion.

## 1.4. CONTROL OF CROSS-FLOW INSTABILITY

The term Laminar Flow Control (LFC) generally describes the deployment of passive and active techniques to maintain laminar flow over aerodynamic bodies by delaying laminar-turbulent transition. A review of the techniques developed for this purpose was compiled by Joslin [46]. As discussed in the previous sections, regarding the specific case of swept wing flows, the main driver of the transition process is the cross-flow instability [104]. The main contributions towards control of cross-flow instability are summarised in the following sections.

### 1.4.1. DRE/UFD

As mentioned in the previous section, Saric *et al.* [100] introduced the idea of inducing sub-critical stationary modes, featuring smaller wavelength compared to the naturally dominant mode, to delay transition in three-dimensional boundary layers, based on the observations of Reibert *et al.* [97]. Further investigations [77, 129, 64, 41] in theoretical and numerical studies confirmed the reported positive effects, towards delaying transition. This approach, named sub-critical discrete roughness elements (DREs) [100], leads to enhanced amplitude levels of shorter-wavelength modes by means of roughness-elements forcing. The term upstream flow deformation (UFD) is more generally used when making use of any device capable of inducing selected stationary modes [129]. The inception of the sub-critical modes leads to a mean flow deformation which delays the destabilisation of the critical mode thus postponing the amplification of secondary modes and, therefore, the eventual flow breakdown [129]. Following the DRE/UFD concept, several studies have been carried out encompassing wind tunnel and free flight experiments as well as numerical simulations. White & Saric [134] performed wind tunnel campaigns with pneumatically actuated surface roughness elements. The idea behind this study was

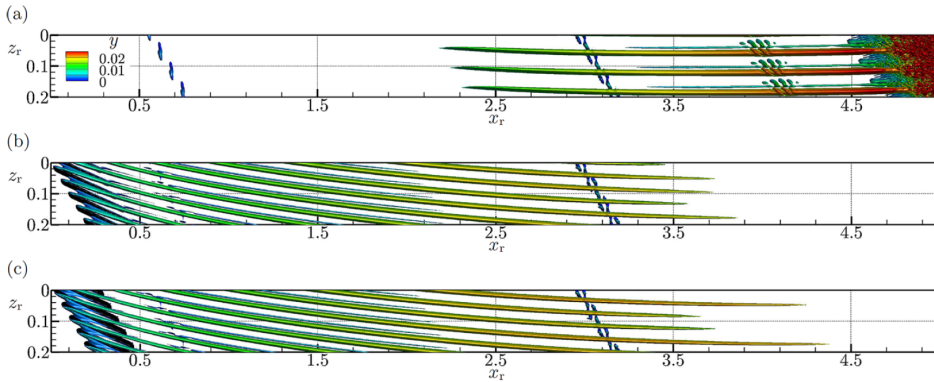


Figure 1.9:  $\lambda_2$  visualizations of primary CFI modes without (a) and with (b and c) active flow control (reproduced from Dörr & Kloker [24]).

to develop an active flow control device that could perform sub-critical leading edge forcing for a wide range of Reynolds numbers and pressure distributions (i.e. angle of attack). Potentially, this can allow variations of both wavelength and height of the DREs. Unfortunately, the device did not perform as wished because of technological issues but enhanced the interest towards active LFC based on the DRE/UFD approach. The flow case of the experiment of Saric *et al.* [100] was later investigated by Hosseini *et al.* [41] with direct numerical simulations. Similar outcomes in terms of transition delay were obtained. The extension of the sub-critical DRE/UFD strategy to supersonic flows was demonstrated with the works of Saric & Reed [101] and Schuele *et al.* [111] for swept wings and circular cones at incidence, respectively. Flight experiments are reported by Tucker *et al.* [124] and Saric *et al.* [102] for subsonic and supersonic regimes, respectively.

The sub-critical DRE/UFD concepts hold on the same physical mechanism. However, the UFD strategy considers not only surface roughness for the sub-critical forcing of the primary stationary mode. As a fact, a wide range of devices has been used to force monochromatic stationary cross-flow instability modes. While not primarily intended for flow control, Deyhle & Bippes [19] made use of localised surface heated spots. Schuele *et al.* [111] employed leading edge surface indentations placed at critical and sub-critical (azimuthal) wavelengths. Transition was enhanced by critical forcing and delayed for the sub-critical case with respect to the smooth cone tip (see [111], figure 27). An array of alternating current dielectric barrier discharge (AC-DBD) plasma actuators was also tested, towards the same goal. This was mounted such that the jets induced by the individual localised discharges, would create a boundary layer perturbation similar to that caused by the three-dimensional dimples. Indeed the flow arranged similarly in both experiments for the critical forcing case. Unfortunately, the sub-critical case with plasma actuation, and eventual transition postponement, is not reported. In a recent experimental investigation, Lohse *et al.* [72] applied localised blowing and suction to condition the cross-flow primary instability. They showed effective conditioning of the primary modes by blowing and suction, with the latter being more robust.

It is evident that the global working mechanisms at the basis of the DRE/UFD strate-

gies are sufficiently assessed through the previous extensive experimental, numerical and theoretical investigations. However, eventual transition delay, with respect to the unforced flow, has not always been demonstrated effectively (e.g. Downs & White [27]). The inherent challenges towards successful demonstration of transition delay using DRE/UFD methods suggest a high sensitivity of the approach to a number of factors. Among others, these factors include background surface roughness and free-stream turbulence effects (boundary layer receptivity) and Reynolds-number and pressure-distribution effects (boundary layer-stability). The latter parameters are crucial as the DRE/UFD strategy has been shown effective only in case the sub-critical control mode is considerably more amplified, closer to the leading edge, than the dominant mode. These considerations deserve further dedicated investigation towards successful and robust implementations of the DRE/UFD technique for effective and efficient LFC.

Recently, Dörr & Kloker [24] and Dörr *et al.* [26] used plasma actuators as UFD devices similarly to the work of Schuele *et al.* [111] (see figure 1.9). The latter work focused on the effects of free-stream modes impinging on the forced boundary layer. The actuators effectively induced the shorter-wavelength control mode with consequent beneficial effects on the flow stability. In all these studies, the forcing direction that maximizes the flow stabilization is against the local crossflow. However, even forcing along the CF causes beneficial mean-flow distortions. Shahriari [118] also followed this approach and presented successful delay of the transition front when the sub-critical control mode was introduced by ring-like plasma actuators. In these studies, the AC-DBD plasma actuators were modelled as steady body force sources.

#### 1.4.2. BASE-FLOW MANIPULATION

Relevant contributions to LFC of three-dimensional boundary layers came in the last decade from the group of Kloker at IAG (Institut für Aerodynamik und Gasdynamik), Univesität Stuttgart. Several studies were carried out by means of direct numerical simulations investigating different control devices and strategies. Suction is known to have beneficial effects, with respect to transition, in two dimensional boundary layers [107, 46]. In an application to three-dimensional flows, Messing & Kloker [81] showed that suction effectively enhances boundary layer-stability as it leads to fuller streamwise (along the inviscid streamline) velocity profiles at the wall and weaker crossflow velocities. They also reported that overwhelming suction can lead to undesired promotion of the laminar-to-turbulent breakdown. This occurs either by too high suction flow rates or by amplification of cross-flow vortices due to slight manufacturing imperfections of the suction orifices, which are likely to happen in real life applications. Messing & Kloker [81] also studied the combination of distributed suction and UFD in what they refer to as 'formative suction' approach. The further benefit of the combined technique is the eventual reduction of the required mass flow rate with positive consequences on the energy cost of the active control device.

Bonfigli & Kloker [8] showed that small induced velocities orthogonal to the local shears are highly effective in enhancing the flow stability. This observation originated many further efforts. Pinpoint suction aiming at directly weakening the cross-flow vortices was approached by Friederich & Kloker [31] and showed beneficial effects in delaying transition. A similar approach, albeit making use of modelled plasma actuators, was more

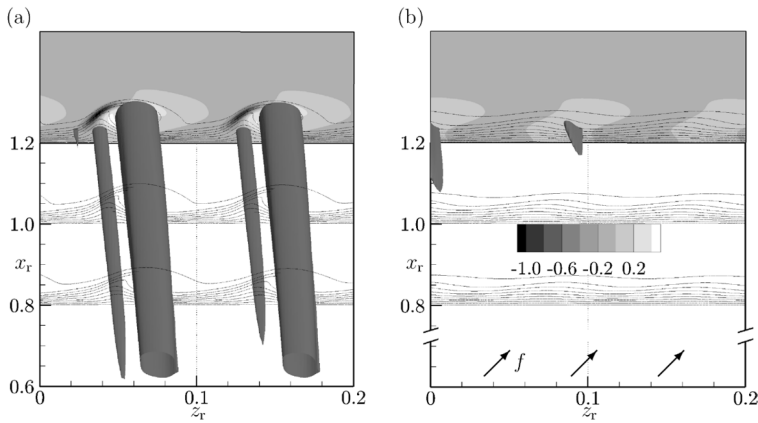


Figure 1.10:  $\lambda_2$  visualizations of primary CFI modes without (a) and with (b) active flow control (reproduced from Dörr & Kloker [22]).

recently published by Dörr & Kloker [23]. The effects of suction holes/plasma actuators positioning, geometry and operational parameters were carefully inspected in these DNS studies. It was shown that, when the forcing is against the cross-flow, the performance of control is highly sensitive to the relative spanwise position between the stationary CFVs and the suction holes/actuators. For both forcing techniques, the most effective position with respect to the stationary CFVs is such that the forced downwelling flow counteracts the CFVs upwelling motion. Weakened CFVs lead to hindered velocity shears thus dampening the secondary high-frequency instability and eventually postponing the laminar-to-turbulent breakdown.

Dörr & Kloker [22] studied the effect of sub-critical leading edge forcing by means of localised blowing, spots of moving walls (a simplified plasma actuator model) and plasma actuators. The first technique shows detrimental effects. Transition was promoted by the boundary-layer thickening with related momentum loss of the streamwise velocity component. These results were experimentally corroborated by Lohse *et al.* [72]. The other two devices have instead beneficial effects, with plasma actuators being more effective (see figure 1.10). In this case, as well as in [23], the plasma actuators are modelled as a local steady wall-parallel body force whose amplitude is retrieved from the induced velocity field. Nevertheless, it is well known that plasma discharges are characterised by strong oscillatory components, which are evident also in the production of the body force [17, 5].

Recognising the aforementioned effect, Dörr & Kloker [22, 23], studied the effect of unsteady forcing. They confirmed the enhancement of only the unsteady travelling mode corresponding to the specific forced frequency. However, the actuated frequencies were well beyond the frequency band of the secondary instability modes. Therefore, the authors acknowledge that, for higher Reynolds number flows compared to their simulations, forcing at such high frequencies could be technologically unfeasible and introduction of undesired flow fluctuations from the actuator might occur.

Finally, Rizzetta & Visbal [98] used leading-edge plasma actuators to stabilize the flow

after roughness elements causing bypass transition on different sweep-angle wings.

## 1.5. MOTIVATION OF THIS RESEARCH

This research is aimed at deploying advanced flow diagnostics and control technologies to experimentally investigate and condition the flow mechanisms leading to boundary layer transition on swept wings. Traditional flow diagnostics and control technologies are used to "prepare the ground" for innovative experimental efforts. Thus, while the research poses on solid bases well embedded with previous literature, it aims at introducing several innovative aspects to a topic of main interest. As summarized in the previous sections, the flow diagnostics employed so far did not retrieve spatio-temporally correlated measurements (excluding the efforts of Kawakami *et al.* [51] and Chernoray *et al.* [13] through externally conditioning the unsteady flow field with periodic suction/blowing). Consequently, most of the recent outcomes on the topic came from numerical/theoretical studies. Another aspect where the measured data yielded limited access is the velocity-vector components and their derivatives. Again numerical simulations (LES/DNS) or (non-) linear PSEs overcame this limitation and allowed the deployment of secondary stability theory to investigate the instability of the boundary layer deformed by the cross-flow vortices (e.g. [77, 8]). With this research, we aim at filling this gap deploying spatially (and temporally) resolved flow diagnostics. Tomographic PIV is selected to investigate full volumes of a transitional swept-wing boundary layer. Planar, high-speed PIV is chosen to resolve instead the instantaneous evolution of the flow structures of interest. Powerful data analysis tools as Fourier analysis and proper orthogonal decomposition are employed to decipher the modal components of the unsteady velocity flow field. Moreover, these techniques allow to discern between the flow structures of interest and measurement noise. Thus, they can be used to increase the measurement quality.

The second area of this research investigates the possibility of conditioning the transition evolution by means of active flow control devices. Specifically, alternating current dielectric barrier discharge actuators are selected. These devices feature a broad spectrum frequency response and their authority can be easily tuned by adjusting the voltage amplitude. Novel manufacturing techniques are required to reduce as much as possible the passive (i.e. when non operated) flow disturbance. Extremely shallow and smooth actuators need to be developed, built and characterised. The possibility of using them to condition the spectrum of both the primary CFI (in the wavenumber domain and intensity) and the secondary instability of CFVs (in the frequency domain and phase) is the second main object of this research. The possibility of delaying transition is the final scope inspiring this effort.

Having estimations of the effects of the actuators on the flow stability would also contribute to improved design/usage of the actuators. Thus, a model of plasma actuators on CFI boundary layers is sought leveraging on the physical effect of AC-DBD plasma actuators. These devices introduce a body force in the flow in which they are operated. Therefore, a body-force term can be included in the Navier-Stokes (NS) or boundary layer equations. The exerted body force can be retrieved through dedicated experiments [21, 56].

## 1.6. LAYOUT OF THIS BOOKLET

The core of this booklet is divided in four parts divided themselves into chapters, sections and subsections. The four parts are:

- I **Prologue** opens the manuscript containing the current introductory chapter (1). The techniques and data analysis used in this research are presented in chapter 2. The wind tunnel model design and the first experimental validations are described in chapter 3 together with preliminary stability calculations performed on numerical solutions of the laminar boundary layer.
- II **Flow diagnostics** where the results of the investigations on the primary (chapter 4) and secondary (chapter 5) cross-flow instability are presented. Traditional and innovative flow diagnostics are employed in this part adding further knowledge on the flow structures related to CFI.
- III **Flow control** presents the outcomes of the flow control of the primary (chapter 6) and secondary (chapter 7) cross-flow instability. The active flow control research capitalizes on plasma actuators. Different applications, following the described control approaches, of these devices are performed and discussed.
- IV **Epilogue** discusses the research conclusions and presents the outlook of future work (chapter 8) where effective transition delay is achieved with active flow control. The nomenclature used throughout this booklet is presented in chapter 9.



# 2

## TECHNIQUES AND DATA ANALYSIS

*In this chapter, the employed investigation and data analysis techniques are introduced together with a description of the wind tunnel model and facility. The reference systems as well as the passive and active flow control devices are presented. Numerical solutions of the stationary boundary layer equations and linear stability theory which contributed to the content of this manuscript are also described.*

## 2.1. FLOW DIAGNOSTICS

In the following sections a brief introduction to the working principle of the employed flow diagnostics is presented. More detailed description on these techniques can be found in the specific literature as Tropea *et al.* [123] and Discetti & Ianiro [20].

### 2.1.1. OIL-FLOW VISUALIZATION

Oil-flow visualization is a simple and relatively fast technique to visualize the wall-shear distribution. It makes use of a mixture of viscous liquids (paraffin, petroleum) at the opportune (based on the application) viscosity and fluorescent pigments with which the model surface is carefully painted. When exposed to the flow, the luminescent mixture is displaced by the flow shears as the other forces acting on the oil film (namely: gravity, pressure forces and surface tension) are usually orders of magnitude weaker [120] (see figure 1.6b). In the current experiments, being the wing mounted vertically, gravity had an effect on the displacement of the oil film. To avoid having the oil film being displaced by the effect of gravity, the mixture viscosity was increased. The counter-side of this approach is the need of longer tunnel time to obtain evident displacements which is not a bigger problem for low speed experiments. The oil film was spread on the model with a roller brush leaving an extremely thin and uniform film that did not accumulate in droplets (subject to gravity and surface tension forces).

Finally, flow separation regions show accumulation of the mixture (thus emit more light) and turbulent-boundary-layers regions, characterized by stronger shears, appear darker than the laminar counterparts. The resulting pattern can be easily captured with a normal camera after exposing the painted surface to an ultra-violet light source. Quantitative information can also be retrieved in stationary CFI boundary layers from this visualization technique if an opportune model geometry mapping is performed. The chordwise position at which laminar-turbulent transition occurs as well as the chordwise width of the transition front (recall that CFI transition fronts show jagged patterns along the span; the width of the transition front indicates the relative strength of stationary vs. travelling CFI modes [27]), the wavelengths and the wave angles of the stationary vortices can be inferred with this technique.

### 2.1.2. INFRARED THERMOGRAPHY

Infrared (IR) thermography uses specific sensors to capture the IR radiation emitted by a body. In low speed applications, IR visualization is used in what is referred to as *active technique* i.e. the aerodynamic body is actively heated by an external device (printed electric circuits heated by Joule effect, halogen lamps radiation etc..) and cooled down by the flow through convection. Heat conduction through the model should be negligible. Moreover, for low speed applications, stationary (i.e. after the model surface reaches the equilibrium temperature) thermography experiments are performed. The advantage of this technique is the possibility of averaging together several independent observations of the same phenomenon such to lower the uncorrelated sensor noise.

Reynolds analogy ensures the correspondence between the convective heat flux (thus the emitted infrared radiation) and the flow shears. Therefore, this technique is used in this study in a similar way to oil-flow visualization to inspect the regions of laminar and turbulent boundary layer as well as the modulation of the transitional boundary layer

related to the primary stationary CFI. Consequently, no sensor calibration to match the IR camera thermal radiation levels to temperature was performed.

### 2.1.3. HOT-WIRE ANEMOMETRY

Hot-wire anemometry makes use of a flow probe (the hot-wire) and an opportune anemometer. In this study, a constant temperature anemometer (CTA) was used. This device operates the flow probe as one of the four resistances of a Wheatstone bridge whose voltage is kept balanced by a feedback mechanism. When the probe, through which a current is passed, is heated and exposed to the flow, its temperature would tend to change because of heat convection fluxes and so would do the wire resistance and the bridge voltage. The wire resistance is indeed directly related to its temperature by equation 2.1,

$$R_w = R_0(1 + \alpha_0(T_w - T_a)) \quad (2.1)$$

where  $R_0$  is the wire reference resistance,  $T_w$  its temperature,  $T_a$  the ambient temperature and  $\alpha_0$  the overheat coefficient.

The bridge feedback system reacts to the voltage imbalance by supplying a different voltage to the circuit. Therefore, the supplied voltage is an indirect measurement of the flow velocity. To retrieve velocity measurements, a calibration is sought by matching bridge voltages to known flow velocities (measured by a different device). The calibrated velocity points are then fitted by a fourth order polynomial (approximating King's law). Temperature and pressure corrections are applied to compensate the different conditions at which calibration and measurements are performed.

CTA hot-wires feature high amplitude response to very high frequencies rendering them (historically) the preferred flow diagnostics for transitional and turbulent flows. Furthermore, modern hot-wire probes are extremely small (diameter in the order of micrometres and length in the order of a millimetre) thus the spatial resolution of HWA measurements can be very high and depends on the traversing system used to perform the scans. The main limitations of HWA measurements are the impossibility, when using single-wire probes (which are often used for boundary layer applications), of discerning the different velocity components and the fact that it is a single-point diagnostics (i.e. it does not allow to infer the spatio/temporal correlation of the measured flow structures). Finally, hot-wires are sensible to the magnitude of the flow velocity and not to its direction (this can be problematic when flow reversal occurs).

### 2.1.4. PARTICLE IMAGE VELOCIMETRY

Particle image velocimetry (PIV) builds upon optical observations of the flow. The latter is seeded with opportune particles which do not interfere with and passively displace with the flowing fluid. These tracers need to be small enough and feature a density that approaches the density of the fluid in which they operate. In air, at low subsonic speeds, vaporized water glycol droplets (featuring, in average,  $1\mu\text{m}$  of diameter) is a common choice. Seeding particles operate in the Mie scattering regime (i.e. the particles average diameter is larger than light wavelength) where the scattered light intensity scales with the square power of the particles' diameter. Therefore, a trade-off between mechanic and optical properties of the tracers size needs to be found. Furthermore,

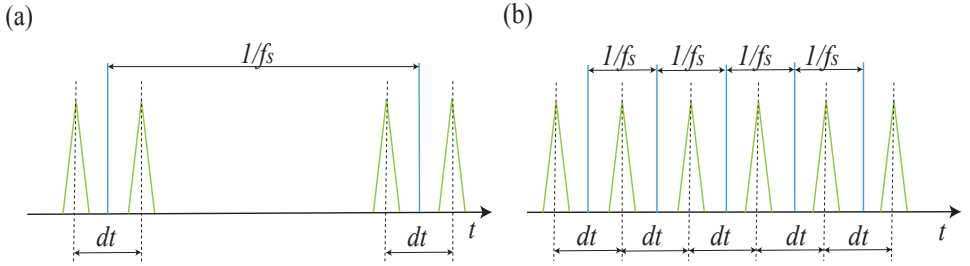


Figure 2.1: Schematic of the laser time signals (green lines) and of the velocity fields time series (cyan lines); (a) *double frame mode*, (b) *single-frame mode*.

some other properties of the seeding particles need to be considered depending on the application. An example is the dielectric strength when the seeded flow is exposed to strong electromagnetic fields as during PIV-based mechanical characterizations of plasma actuators.

In PIV applications, the imaged particles size mainly depends on its light diffraction diameter which follows from the optical setup. As such, despite being physically very small, the tracers result visible to the employed optics when opportunely illuminated. Light illumination is usually provided by laser light sources. Besides being very powerful light sources, lasers emit collimated light that can be shaped to different arrangements by using a combination of spherical and cylindrical lenses. Finally, laser pulses can be very short in time thus ensuring very limited (in time) light exposure. This is a crucial feature as, in the captured PIV images, the particles need to appear as neat as possible (long exposure pictures of moving particles would result in streaks).

In PIV experiments performed in what is referred to as *double-frame mode*, two subsequent pictures (frames, indicated by the subscript numbers 1 and 2), separated by a known time lag ( $dt$ ), are used to estimate the flow velocity distribution (within the captured images). The acquisition frequency ( $f_s$ ) corresponds to the inverse of time-lag between consecutive image pairs (see the schematic of figure 2.1a). Instead in *single-frame mode*, usually chosen for low speed flows measured at very high frequencies, subsequent images are correlated; in this case  $dt = 1/f_s$  (as shown in figure 2.1b).

Despite the chosen approach, the velocity vectors evaluation starts with dividing the captured images into small portions called interrogation windows. The same windows pertaining to the two observations are then compared by means of the normalised cross-correlation operator applied on the light intensity ( $I$ ) described by equation 2.2,

$$C(\delta_x, \delta_y) = \frac{\sum_j^J \sum_i^I I_1(i, j) \cdot I_2(i + \delta_x, j + \delta_y)}{\sqrt{\sum_j^J \sum_i^I I_1^2(i, j) \cdot \sum_j^J \sum_i^I I_2^2(i, j)}} \quad (2.2)$$

The cross-correlation is a mathematical operator that retrieves the similarity level between the two signals (the windows from the two frames) as a function of the sliding displacement of one of the two signals ( $\delta_x, \delta_y$ ). The displacement showing the largest level of  $C$  corresponds to the average displacement, within the window, of the seeding

particles and therefore, of the flow. As the time-lag  $dt$  (fixed by the operator) and the setup optical parameters (retrieved through the geometrical mapping of the imaged field) are known, one velocity vector for each interrogation window is computed.

The size of the interrogation windows follows from different considerations. While minimizing it, it allows to increase the spatial resolution of the measurement, it can lower the cross-correlation level. This happens because when the interrogation windows become too small, many particles of the first (in time) correlated frame will likely have left the second (in time) frame and, *vice versa*, many particles, not present in the first frame will enter in the second. In practise, the particles' average-displacement is too large compared to the windows size. To counteract this problem, the time lag between the correlated frames can be reduced. Nevertheless, too small  $dt$ , reducing the particle displacements, lower the signal (the displacement) to noise (spurious displacements) level. Multi-pass, multi-size cross-correlation has been proposed and implemented [105] to overcome this limit. These techniques make use of bigger windows to estimate the larger displacement and then perform the cross-correlation on smaller (and eventually deformed) windows shifted back w.r.t. the initially estimated displacement (usually a central shift is implemented where the first frame window is displaced of  $\delta_x/2$ ,  $\delta_y/2$  and the second frame window of  $-\delta_x/2$ ,  $-\delta_y/2$ ). This procedure, evaluating the residual displacement in smaller windows, enhances the measurement spatial resolution and reduces the smaller scales modulation deriving from the physical size of the interrogation windows [105].

The main advantages of PIV over HWA relate to the fact that, being a field measurement, it retrieves spatially correlated flow structures (and if the sampling rate is larger than the flow Nyquist frequency, also temporally correlated) and it measures the different velocity components (2 components for planar PIV, 3 components for stereo- and tomo- PIV). Nonetheless, PIV experiments at very high frequency need very expensive equipment and usually encounter lack of illumination problems.

### 2.1.1.5. TOMOGRAPHIC PARTICLE IMAGE VELOCIMETRY

In 2006 Elsinga *et al.* [29], extended the stereo-PIV to volumetric measurements thus leading to tomographic-PIV (or tomo-PIV). Finally, the full velocity vector and velocity-gradient tensor became experimentally accessible from instantaneous measurements. Scarano [106] offers a review on the more recent improvements. Tomo-PIV capitalizes on the volumetric reconstruction of light intensity (i.e. the particles) from different (at least three) observations from conventional PIV cameras by means of the Multiplicative Algebraic Reconstruction Technique (MART) or its newer versions (SMART or CSMART). These algorithms need a multi-plane (in the direction to be reconstructed) geometrical calibration of the cameras two-dimensional projections which is done with ad-hoc targets (e.g. *LaVision* calibration target *type-10*). Usually, this geometrical calibration is adjusted by successive iterations based on triangulation (among the camera views) of distributed light sources (e.g. light scattering particles) [137]. After calibration and reconstruction, the volumetric objects are divided in three-dimensional boxes and cross-correlated between the two frames of the pair (*double frame* mode) or between subsequent images (*single frame* mode) in a similar way to what described for PIV (although equation 2.2 needs to be modified to account for displacements also in the third direction).

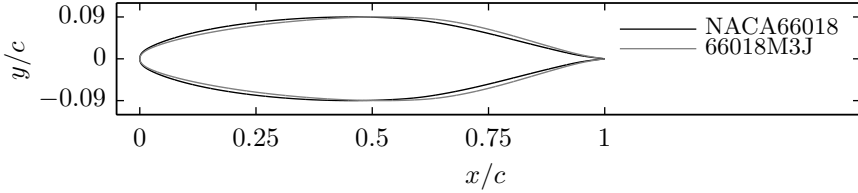


Figure 2.2: Comparison of the 66018M3J airfoil used in the present work with the NACA 66018 airfoil from which it was derived.

Tomo-PIV setups require some additional considerations and related hardware w.r.t. PIV experiments. First, different cameras, with different viewing angles, are needed thus requiring multiple optical access to the measurement region. Second, the imaged region needs to be in focus for all the cameras thus the need of optical adaptors to meet the Scheimpflug condition and extended depth of focus ( $\delta_z$ ). The latter consideration usually translates in reduced light exposure of the cameras sensors as the focal depth scales with the square of the numerical aperture ( $\delta_z \propto f_n^2$ ) and the latter is the ratio of the lenses focal length over the aperture ( $f_n = f/D$ ). This can be a limiting factor as already the laser beam is shaped such to illuminate the entire volume. Light constrains are particularly severe only for high-sampling rate measurements (as the energy per pulse of high speed lasers is typically an order of magnitude smaller than for low speed lasers) and large domains. Indeed, light illumination has been so far the main constrain for the size of tomo-PIV domains. Finally, regions outside of the measurement volume should be shadowed to increase the signal-to-noise of the reconstruction procedure and this usually implies the installation of light barriers on the setup.

## 2.2. WIND TUNNEL MODEL AND FACILITY

The model used in the current investigation is a swept wing of about 1.25 m of span ( $b$ ) and 1.27 m of chord in the free stream direction ( $c_X$ ). The sweep angle ( $\Lambda$ ) is  $45^\circ$ . The model is made of fibreglass with a very smooth polished surface featuring a measured value of surface roughness standard deviation of  $R_q = 0.20 \mu\text{m}$ . The airfoil used is an in-house modified version of the NACA 66018 shape that was named *66018M3J* and features a small leading edge radius of about 1% of the chord in order to avoid attachment line instability [93, 6]. Until about 70% of the chord, the airfoil shows accelerating flow, when at zero incidence, and no concave surfaces, to avoid the amplification of Tollmien-Schlichting (TS) waves and of Görtler vortices respectively. The airfoil used is shown in figure 2.2 together with the NACA 66018 on which it was based. It must be noticed that, for the considered swept wing application, the wing sections are presented along the normal to the leading edge direction.

The wind tunnel where the experiments were performed is the TU Delft Low Turbulence Tunnel (LTT) facility. This is a closed-loop low turbulence subsonic tunnel with a test section of  $1.25 \text{ m} \times 1.80 \text{ m}$  of height and width respectively and 2.6 m long. The tunnel is furnished with seven anti-turbulence screens and a contraction ratio of 17 : 1. Turbu-

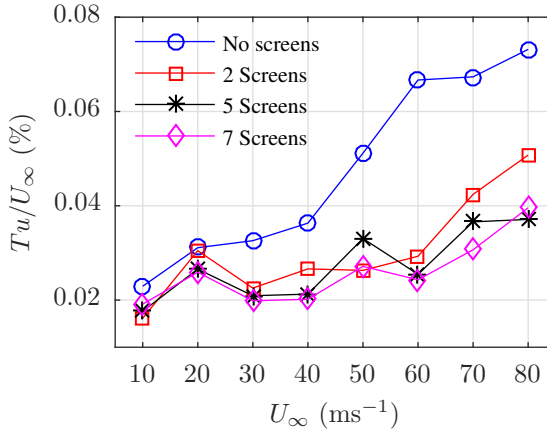


Figure 2.3: Free stream turbulence ( $Tu$ ) measured by a single hot-wire probe for different anti-turbulence screens configurations versus free stream velocity ( $U_\infty$ ). Hot-wire signal measured upstream of the 66018-M3J wing and band-pass filtered between 2 and 5000 Hz.

lence intensity was measured in the wind tunnel test section upstream of the 66018-M3J wing with a single hot-wire sensor at approximately the conditions of the experiment. The acquired signal was bandpass filtered between 2 Hz and 5000 Hz. The LTT allows to lift the screens in a opportune storage room thus removing them from the flow. The free stream turbulence was measured for different values of free stream velocity (between 10 and 80 m s<sup>-1</sup>) with all the seven screens installed and with only the five and two two more upstream screens installed in the tunnel. Finally, all the screens were lifted thus leaving only the upstream honeycomb mesh exposed to the flow. The results of these measurements are presented in figure 2.3.

At the free-stream velocity  $U_\infty = 24$  m s<sup>-1</sup>, with all the screens installed, the turbulence intensity was found to be  $Tu/U_\infty = 0.024\%$ . This value is low enough to observe stationary cross-flow waves [6, 27]. Overall even with all the screens removed, for the entire range of free stream velocities considered, the free stream turbulence is lower than 1% of the free stream velocity. The background acoustic emission of the tunnel, although considerable, is not relevant to the transition evolution for this type of flow [19, 94, 135].

Most of the experiments were performed at Mach number  $M = 0.075$  ( $U_\infty = 25.6$  m s<sup>-1</sup>) and Reynolds number  $Re = 2.17 \cdot 10^6$  (based on the free stream velocity and streamwise chord) and at incidence angle of  $\alpha = 3^\circ$ . The flow over the wing pressure side was investigated. The boundary layer over the wing suction side was forced to turbulent close to the leading edge using a tripping wire in order to avoid strong unsteady flow separation influencing the flow on the pressure side.

## 2.3. REFERENCE SYSTEMS

Due to the complexity of the swept wing geometry and the multitude of measurement techniques used in this study, a rigorous definition of the coordinate systems and of

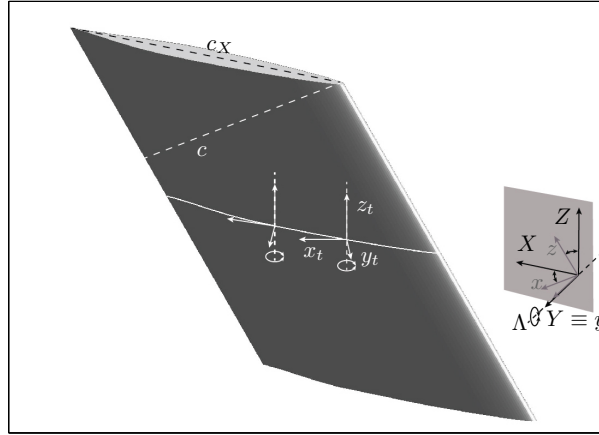


Figure 2.4: Schematic of the model and definition of the un-swept ( $XYZ$ ), the swept ( $xyz$ ) and the local tangential ( $x_t y_t z_t$ ) reference systems. The chord along  $X$  is defined with  $c_X$  and shown with a black dashed line while the chord along  $x$ , defined with  $c$ , is plotted with a white dashed line.

the velocity components is necessary towards correct interpretation of results. The used systems and respective notations are presented in figure 2.4. Firstly, the un-swept coordinate system is introduced and defined with the upper case letters  $XYZ$ . It is aligned with the wing chords plane and the velocity components along this coordinate system are indicated with upper case letters  $UVW$ .

When the swept wing model is placed at an incidence, the wind tunnel reference system does not coincide with the un-swept coordinates. The velocity components along the wind tunnel reference system are denoted with upper case letters and the subscript ( $\infty$ ), with  $U_\infty$  being the free stream velocity.

In figure 2.4 the swept reference system is plotted in grey and is such that its  $x$  axis is orthogonal to the wing leading edge direction,  $z$  parallel to it (both these axes lie in the chords plane) and  $y$  coincides with the un-swept  $Y$  direction. Rotation of  $\Lambda = 45^\circ$  about the  $Y$  axis transforms the  $XYZ$  system of coordinates to the swept  $xyz$  system. Note that in existing literature some ambiguity with the definition of *swept* and *un-swept* exists (e.g. [135, 121]). In this study the definition of White & Saric [135] is used. The velocity components in this system of coordinates are indicated with the lower case letters  $uvw$ . The origins of both the  $XYZ$  and  $xyz$  systems are at the wing leading edge at the mid-span location. In the schematic, the chords in the  $XYZ$  ( $c_X$ ) and  $xyz$  ( $c$ ) systems are indicated with black and white dashed lines respectively.  $X/c_X$  is used to define the streamwise measurement station as the HWA traverses were mainly along  $X$ . For the LST, the streamwise station is defined with  $x/c$  as the formulation of the problem is in the swept wing coordinate system. The two definitions of the chordwise locations are equivalent given the semi-infinite swept wing flow assumption.

One other coordinate system is the local tangential system where the definition of tangential is simplified as it implies only the surface curvature along the  $X$  direction. The system is such that the  $x_t$  axis is aligned with the local surface tangent, the  $y_t$  is the

wall-normal direction and  $z_t$  coincides with the  $Z$  axis (as shown in figure 2.4).

The reference system of the primary stationary CF vortices is referred to as  $X_W Y_W Z_W$ . It is locally aligned with the cross-flow vortices such to have the  $X_W$  direction along the vortices, the  $Z_W$  is along the model surface and is positive in the direction closer to the  $Z$  axis.

Finally, the reference system locally aligned with the flow inviscid streamline is indicated with the subscript  $_{ISL}$  and is such to have  $x_{ISL}$  along the inviscid flow and  $z_{ISL}$  orthogonal to it and positive in the direction closer to  $Z$ .

## 2.4. FLOW CONTROL DEVICES

Natural transition pertaining to swept wings manifests as a result of the amplification of a narrow band of primary cross-flow instability modes. Within the band, small variations in spanwise wavelength can compromise the measurement and interpretation of the developing flow field. Moreover, as discussed in section 1.4, laminar flow control approaches based on the artificial forcing of selected modes (DRE/UFD) have been developed. It becomes, thus, important to fix the dominant mode wavelength. Towards this goal, passive and active flow-forcing devices were used. These are described in the following sections. Active forcing of the cross-flow velocity and of the secondary CFI modes was also performed. The followed approaches and the used devices are also described.

### 2.4.1. CONSIDERED PASSIVE AND ACTIVE DEVICES

Micrometric roughness elements installed close to the leading edge have been employed to passively force single CFI modes. They cause a localized flow perturbation that locks the stationary mode to their spanwise spacing. Dedicated studies on the boundary layer receptivity to this type of forcing have been performed by many research groups (e.g. [97, 94, 32, 121, 62]).

Active forcing was achieved by means of AC-DBD plasma actuators. AC-DBD plasma actuators work on the principle of air ionisation (plasma) caused by an intense electric field. The latter is generated by a high-voltage electrode, exposed to the air, and a grounded electrode buried under a layer of dielectric material. A schematic of the hardware configuration of an AC-DBD plasma actuator is shown in figure 2.5. Through Coulombian interactions, the plasma formation transfers momentum to the surrounding neutral flow, thus leading to localised flow acceleration. Thorough reviews on the working mechanism of these actuators are reported by Moreau [86], Corke *et al.* [17] and Benard & Moreau [5]. A review of the application of AC-DBD plasma actuators for flow control was compiled by Wang *et al.* [128]. Flow control of two-dimensional boundary layers has been extensively studied (see e.g. [36, 59, 60, 28]). In contrast, usage of these devices in three-dimensional flows, dominated by CFI, is still rather limited (see [14, 111, 22, 23, 24, 118]).

These actuators offer several advantages over competing concepts for active flow control. Most of these stem from the pertinent electrical nature of their operation. They feature a broad dynamic range in forcing frequencies, enabled through the direct manipulation of the driving high voltage signal. Similarly, the induced forcing effect, and hence the actuators authority, can be adjusted by varying the amplitude of the supplied

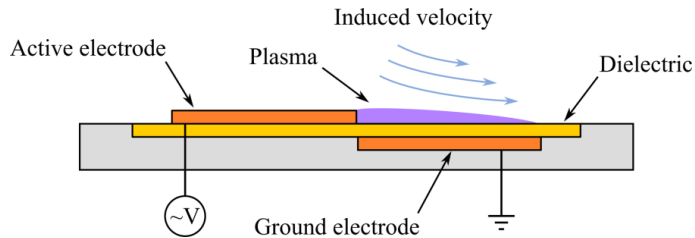


Figure 2.5: Schematic of an AC-DBD plasma actuator. Reproduced from Michelis & Kotsonis [82].

voltage. The peculiarity of exerting directional flow control is also an important feature for instability control applications [22, 23]. Furthermore, they do not require pneumatically or mechanically driven devices thus simplifying their operation and maintenance (recall the effort of White & Saric [134] in this direction). However, these actuators feature some drawbacks. They require high voltage amplifiers which are still, for many applications, expensive and cumbersome devices. They introduce considerable electromagnetic interference and their lifetime strongly depends on the chosen dielectric material and in specific on its dielectric, mechanical and thermal resistance. However, the main drawback of plasma actuators is their limited control authority at high Reynolds numbers [86, 17, 5]. As such, one must use plasma actuators for flow control applications in a 'smart' manner, where low energy forcing is applied to highly receptive flows thus producing a large impact downstream. In this regard, Dörr & Kloker [22] used plasma actuators to reduce the weak cross-flow velocity component; Jukes & Choi [48, 49] as vortex generators; Dörr & Kloker [23] to weaken the CFVs while Schuele *et al.* [111], Dörr & Kloker [24] and Dörr & Kloker [25] as localised flow disturbances to condition the CFI and TS modes, respectively.

Regarding the specific application to control CFI, an important consideration is the extreme sensitivity of this type of flows to the surface roughness at the leading edge (cf. [94, 6, 104, 62]). As such, notwithstanding the chosen flow control strategy, the used actuators should feature extremely low levels of roughness when installed on the model surface. AC-DBD can be manufactured accordingly [111], making them suitable for the control of these flows. The effect of using devices that are inherently unsteady on the boundary layer, deserves dissection given the stationary and travelling nature of CFI [23, 24]. The concerns of using fluctuating-forcing devices in a laminar boundary layer derive from the possibility of directly/indirectly triggering travelling waves thus promoting the flow breakdown. Furthermore, the secondary instability of the stationary vortices has an unsteady and convective nature [77, 129]. Therefore, also the secondary instability mechanisms can be directly influenced by the unsteady actuation.

#### 2.4.2. PASSIVE DEVICES FOR STATIONARY CFI CONTROL

Following the technique used by Reibert *et al.* [97], the primary stationary CFI was forced to a monochromatic (i.e. featuring a single mode) arrangement by means of micron-sized discrete roughness elements (DREs). A sequence of small cylindrical elements (rub-on transfers used for etch masking of printed circuit boards) was installed on the model surface close to the forced mode branch-I ( $x/c = 0.025$ , for  $Re = 2.17 \cdot 10^6$ ,  $\alpha = 3^\circ$  and  $\lambda_z = 9$  mm). The forcing elements used have a diameter of  $d_r = 2.8$  mm and an average

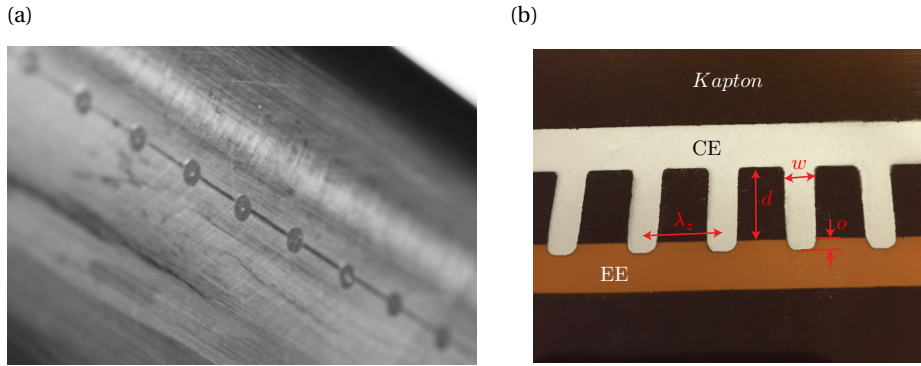


Figure 2.6: (a) Detail (picture) of the discrete roughness elements used to trigger monochromatic primary CFI modes mounted on the wing surface. (b) Detail (picture) of a DBD plasma actuator used for selective forcing of monochromatic primary cross-flow instability modes. The *Kapton* sheet, the covered electrode (CE), the exposed electrode (EE), the stems wavelength ( $\lambda_z$ ), the width ( $w$ ), the distance between the electrodes ( $d$ ) and the overlap ( $o$ ) are also shown. View of the underside of the actuator, CE on foreground, EE on background.

height of  $k_r = 10 \mu\text{m}$ . In figure 2.6a, a detail of the DREs used in [114] mounted close to wing leading edge is presented.

### 2.4.3. AC-DBD PLASMA ACTUATORS FOR STATIONARY CFI CONTROL

The chosen devices to actively force selected stationary CFI modes were spanwise modulated plasma actuators [116]. To this end, special actuators were designed, built and employed. The actuators were manufactured using a metal deposition technique developed in-house. The technique makes use of computer-controlled spraying of sub-micron conductive silver particles on the dielectric surface. The resulting electrode thickness is in the order of  $1 \mu\text{m}$ . For comparison, traditional hand-made actuators based on adhesive copper tape, typically have electrode thickness of  $60 \mu\text{m}$ . The plasma actuators were placed at  $x/c=0.025$ , close to the primary mode critical station (see the LST analysis of section 2.6). The plasma actuators were designed towards forcing a single monochromatic primary cross-flow mode. To force the desired mode, the employed actuators feature one straight electrode, which is exposed to the flow and is powered by the high-voltage supply. The grounded electrode is encapsulated below the dielectric barrier and is made of a series of stems spaced equally from each other and oriented along  $x$ . The spacing between the stems defines the spanwise wavelength of the plasma forcing and, as such, the spanwise wavelength of the forced CF modes.

A detail of the DBD plasma actuators used in this study is presented in the schematic of figure 2.7a and in the picture of figure 2.6b. The covered electrode stems are  $d=10 \text{ mm}$  long and  $w=3 \text{ mm}$  wide. They are projected towards the straight electrode overlapping with it by  $o=2 \text{ mm}$ , in order to ensure consistent plasma formation. A picture of the actuator mounted on the wing surface is presented in figure 2.8a. Given the relative large length of these stems, the flow ionisation region corresponds only to the electrode overlapping area thus ensuring the desired spanwise modulation of the forced jet. It is

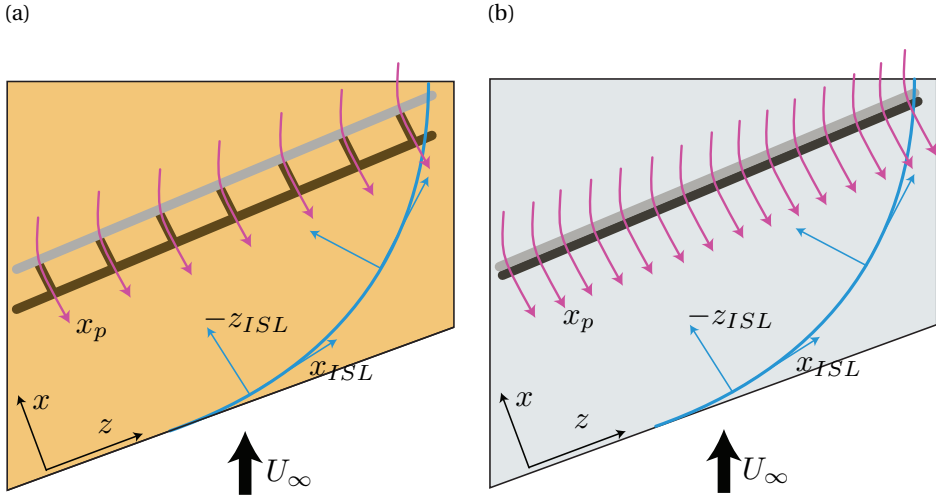


Figure 2.7: Schematic of the plasma actuator. The plasma jets (magenta), the inviscid streamline (cyan) and the related reference system (ISL) are shown together with the swept reference system ( $xz$ ). The schematics are not to scale. (a) Actuator for stationary CFI control with *Kapton* dielectric (orange); (b) Actuator for base-flow manipulation with *PET* dielectric (light grey).

important to note that the exposed electrode was placed downstream such to have the induced jet aligned with  $-x$ .

A *Kapton* polyimide film of  $50\ \mu\text{m}$  thickness was used as dielectric barrier. A second layer of *Kapton* was placed between the actuator and the model surface to better protect the latter in case of actuator failure (usually translating into spark discharges). The total thickness of the actuator resulted in  $125\ \mu\text{m}$ . In order to avoid exposure of the incoming flow to a step of such high thickness, the *Kapton* sheet was wrapped around the wing leading edge. This ensured that the only surface perturbation seen by the flow was a two-dimensional backward facing step of  $125\ \mu\text{m}$  at approximately 10% of the model chord. The actuator was powered using a *Trek 20/20C HS* high-speed high-voltage amplifier.

#### 2.4.4. AC-DBD PLASMA ACTUATORS FOR BASE-FLOW MANIPULATION

The actuators for base-flow manipulation, namely reduction of the boundary layer cross-flow velocity component, were designed to feature enhanced control authority thus to feed increased values of induced momentum [138]. Furthermore, it was chosen to operate them at higher frequencies ( $O(10\ \text{kHz})$ ) to avoid introduction of boundary layer fluctuations. For this purpose, the chosen dielectric material was  $500\ \mu\text{m}$  thick polyethylene terephthalate (PET). The dielectric foil was mounted flush on the wing surface wrapping around the leading edge and extending till  $x/c = 0.69$  which is far downstream of the transition region for the considered flow case. The electrodes were straight (spanwise-uniform forcing) silver sprayed strips  $5\ \text{mm}$  wide with no relative gap or overlap. These actuators were operated via a *GBS Elektronik Minipuls 4* high voltage amplifier. A schematic of the described actuator is shown in figure 2.7b.

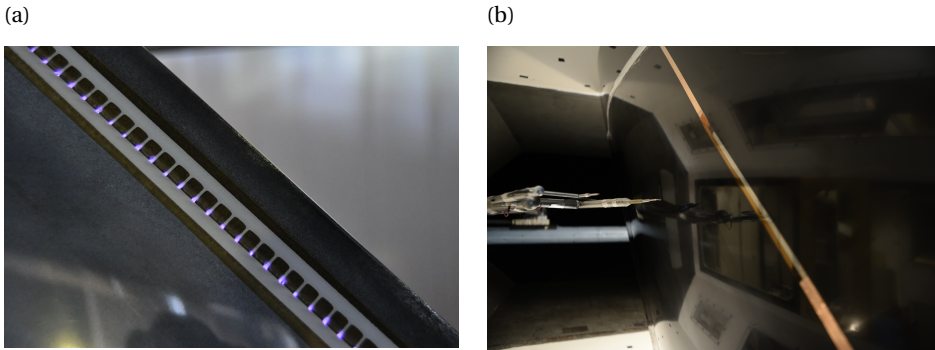


Figure 2.8: Details (pictures) of DBD plasma actuators used for (a) selective forcing of monochromatic primary cross-flow instability modes installed on the wing to condition the wavelength of the primary CFVs and (b) to condition the frequency and phase of the secondary CFI modes

#### 2.4.5. AC-DBD PLASMA ACTUATORS FOR UNSTEADY/SECONDARY CFI CONTROL

The actuators used to condition the unsteady/secondary CFI were manufactured using the same silver particles spraying technique. They were designed to yield spanwise-uniform forcing thus resulting in straight electrodes aligned with the leading edge-parallel direction ( $z$ ) [115]. They were installed such to induce an air flow along  $x$ . The streamwise length of both exposed ( $EE$ ) and covered electrode ( $CE$ ) was 7 mm while neither gap nor overlap between the electrodes were present.

A *Kapton* polyimide film of 50  $\mu\text{m}$  thickness was used as dielectric barrier. Also for this actuator, a second layer of *Kapton* was put between the actuator and the model surface to protect the wing surface in case of spark discharges. The total thickness of the actuator was measured to be 125  $\mu\text{m}$ . The wing mounted actuator is shown in the picture of figure 2.8b. The actuator was powered using a *Trek 20/20C HS* high-speed high-voltage amplifier.

## 2.5. LAMINAR-BOUNDARY-LAYER NUMERICAL SOLUTION

The velocity distributions within the laminar boundary layer developing on the wing at the experimental flow conditions were obtained by numerical solutions. These velocity distributions have been used for linear stability calculations as well as for comparison with the measured values. In the following two sections, the mathematical formulation and the solver details of the laminar-boundary-layer solutions are introduced for both the naturally developing flow and for the cases where a plasma actuator forcing was present.

### 2.5.1. SEMI-INFINITE SWEEP WING

The laminar boundary layer solutions are the result of numerical integration of the 2.5-D, steady, incompressible boundary layer equations with the opportune boundary conditions. The continuity equation is presented in equation 2.3 together with the streamwise and spanwise momentum equations 2.4 and 2.5 [107],

$$\frac{\partial u}{\partial x} + \frac{\partial v}{\partial y} = 0 \quad (2.3)$$

$$u \frac{\partial u}{\partial x} + v \frac{\partial u}{\partial y} = -\frac{1}{\rho} \frac{\partial p}{\partial x} + \nu \frac{\partial^2 u}{\partial y^2} \quad (2.4)$$

$$u \frac{\partial w}{\partial x} + v \frac{\partial w}{\partial y} = \nu \frac{\partial^2 w}{\partial y^2} \quad (2.5)$$

where  $\nu$  is the kinematic viscosity. To be noted that, based on flow-invariance along  $z$ , the  $z$ -momentum equation is decoupled from the others. This set of equations is solved on a Cartesian grid (wing curvature not accounted) stretched such to have  $x$  coinciding with the wing curvilinear abscissa. Besides the non-slip, non-penetration conditions at the wall, Dirichlet boundary conditions are prescribed at the inflow of the domain just after the stagnation point with an analytical Falkner-Skan-Cooke solution at equivalent pressure gradient [16]. At the top domain, the external velocity distributions specified in 2.6 are used,

$$u|_{y=\infty} = \sqrt{\vec{V}(x)^2 - w_{\infty}^2}; \quad w|_{y=\infty} = w_{\infty} = U_{\infty} \cdot \sin(\Lambda); \quad v|_{y=\infty} = 0; \quad (2.6)$$

where  $\vec{V}$  is the velocity vector. This quantity is retrieved from the first order linearisation of the pressure coefficient ( $C_p$ ) following equation 2.7,

$$|\vec{V}(x)| \approx U_{\infty} \sqrt{1 - C_p(x)} \quad (2.7)$$

where the vertical bars denote vector's magnitude. The measured pressure distribution of figure 3.3 is averaged between the two rows of pressure taps and is used in equation 2.7.  $C_p$  is based on the free-stream dynamic pressure.

The differential equations were discretised with second-order finite differences in  $x$  and with spectral elements (Chebyshev collocation method [132]), with 500 polynomials along  $y$ . The computed boundary layer was validated against Falkner-Skan-Cooke solutions [16] and compared to hot-wire measurements [114].

### 2.5.2. SEMI-INFINITE SWEEP WING WITH 2D PLASMA ACTUATORS

The effect on the time-invariant flow of a two-dimensional plasma actuator forcing the developing boundary layer was inspected by a simplified model. The suggested model is based on the addition of the actuator body force as a source term in the stationary, incompressible laminar boundary layer equations for the case of spanwise invariant flow (2.5D flow) presented in the previous section. Therefore, the analysis will focus on the generalised case of spanwise-uniform  $\pm x$ - forcing. The inclusion of the plasma effect can be conveniently modelled as a volume-distributed body force that can be extracted with numerical or experimental means [56]. It must be noted that certain assumptions are necessarily attached to such approach. It is assumed that the external flow does not affect the plasma actuator body force [22, 23, 91] and that thermal effects due to plasma are weak enough to assume incompressible conditions [56]. Additionally, the force is assumed to be time invariant and of negligible magnitude in the wall-normal direction

( $F_y \approx 0$ ). The latter is a common assumption [21] and is essential in the boundary layer formulation of the Navier–Stokes equations as wall-normal pressure invariance ( $\partial p / \partial y = 0$ ), upon which the system of equations 2.3, 2.4 and 2.5 is based, will otherwise not hold [107]. Finally,  $x$ -diffusion terms are also neglected. The stated set of assumptions allow the modification of only the  $x$ -momentum equation as shown in equation 2.8,

$$u \frac{\partial u}{\partial x} + v \frac{\partial u}{\partial y} = -\frac{1}{\rho} \frac{\partial p}{\partial x} + \nu \frac{\partial^2 u}{\partial y^2} + \frac{F_x}{\rho} \quad (2.8)$$

The boundary layer equations 2.3, 2.8, 2.5 with the boundary conditions described in the previous section are integrated with the same numerical solver described in the previous section. Body force distributions ( $F_x$ ), measured in dedicated experiments, were used for the proposed methodology. To this goal, the  $F_x$  fields were first smoothed and then interpolated on the solver grid at the actuator's chordwise position.

## 2.6. LINEAR STABILITY THEORY

Linear stability theory has been traditionally used in cross-flow instability studies (e.g. [97, 3, 77, 40, 39]) as a tool to predict the onset of the primary modes, the related wavelengths and directions, the frequencies and spatial growths. It is based upon the assumptions of parallel base flow (i.e. the flow does not vary in the direction of disturbances' amplification) and small disturbances (such to neglect non-linear effects of the disturbances on the base flow). In this research, the two-dimensional-disturbance problem was solved in the spatial formulation for the boundary layer computed as discussed in sections 2.5. A thorough description of LST for two-dimensional disturbances can be found in Mack [75] and in Högberg & Henningson [40]. Nonetheless, notwithstanding what is suggested by Mack, the stability equations are solved here in the swept coordinate system ( $xyz$ ). In this formulation, the invariance of the flow along the spanwise direction simplifies the solution of the problem allowing the assumption of null growth rates along the  $z$  direction.

Following Reynolds decomposition, the governing NS equations are first re-written for the unsteady quantities (denoted by apex):  $q' = q - \bar{q}$ , where the overbar denotes time-invariant terms and  $q = \{u, v, w, p\}^t$ ; and then linearised (i.e. only first-power-fluctuations terms are considered). The linearised NS equations, where the fluctuations are expressed in the form of waves with two-dimensional wavenumber vector as described in equation 2.9, are then reshaped in the Orr-Sommerfeld (OS) equation (equation 2.10) by means of the stream-function ( $\psi$ ),

$$\psi(x, y, z, t) = \Psi(y) e^{i(\alpha x + \beta z - \omega t)} \quad (2.9)$$

$$\left[ \left( \frac{\partial^2}{\partial y^2} - (\alpha^2 + \beta^2) \right)^2 - i Re(\alpha \bar{u} + \beta \bar{w} - \omega) \left( \frac{\partial^2}{\partial y^2} - (\alpha^2 + \beta^2) \right) - \left( \alpha \frac{\partial^2 \bar{u}}{\partial y^2} + \beta \frac{\partial^2 \bar{w}}{\partial y^2} \right) \right] \Psi = 0 \quad (2.10)$$

where  $\Psi(y)$  is the perturbation eigenfunction and  $Re$  is the Reynolds number. According to the spatial formulation, the streamwise and spanwise wavenumbers ( $\alpha$  and  $\beta$  respectively) are complex and the angular frequency ( $\omega$ ) is real. Nonetheless, the flow invariance along  $z$  ensures  $\beta_i = 0$ .

The OS equation, in the spatial formulation, is a fourth order non-linear homogeneous differential equation. In this study, it was solved, together with the boundary conditions,

$$\Psi|_{y=0} = \Psi|_{y=\infty} = \Psi'|_{y=0} = \Psi'|_{y=\infty} = 0 \quad (2.11)$$

with the Chebyshev collocation method using the *Matlab* differentiation suite of Weideman & Reddy [132], using 100 polynomials. The non-linearity to the eigenvalue is treated following the companion matrix technique of Bridges & Morris [9].

From spatial LST solutions, the amplification  $N$ -factor [125] of a mode with given frequency and  $z$ -wavelength ( $\lambda_z = \frac{2\pi}{\beta_r}$ ), is evaluated by computing the integral,

$$N(x, \lambda_z, \omega) = \int_{x_0(\lambda_z, \omega)}^x -\alpha_i(\zeta, \lambda_z, \omega) d\zeta \quad (2.12)$$

where  $x_0$  is the first unstable station for the considered mode. Envelope  $N$ -factors ( $N^{env}$ ) are the  $x$ -integral of the local maximum values, per chord station, among all the considered modes (i.e. wavenumbers) considered a given frequency [3, 114]. Equation 2.13 gives the mathematical formulation of this quantity,

$$N^{env}(x, \omega) = \max|_{\lambda_z}(N(x, \lambda_z, \omega)) \quad (2.13)$$

## 2.7. DATA ANALYSIS

Different data analysis techniques are used to decompose the measured velocity field in temporal or spatial modes. Moreover, the evolution of primary and secondary CFI modes and the possibility of comparing the actuators' authority require the definition of opportune metrics. This section introduces the used techniques and metrics.

### 2.7.1. WELCH'S MODIFIED PERIODOGRAM

Fourier decomposition is a commonly used tool to analyse stationary stochastic processes. In this booklet, the Welch modified periodogram [133] method is used to decompose spatial (temporal or spatio-temporal) signals in the wavenumber (frequency or wavenumber-frequency, respectively) components. This method is a modification of the Barlett averaged periodogram method [4]. The latter consists of dividing a signal of  $N$  realizations in  $M$  segments of  $N/M$  realizations. The power spectra of the  $M$  segments are estimated by elevating to the square power the magnitude of the discrete Fourier transform of the signal (see equation 2.14 for two-dimensional signals),

$$y_{p+1, q+1} = \sum_{i=0}^{I-1} \sum_{j=0}^{J-1} \omega_m^{ip} \omega_n^{jq} x_{i+1, j+1} \quad (2.14)$$

where  $\omega_m = e^{-\frac{2i\pi}{m}}$  and  $\omega_n = e^{-\frac{2j\pi}{n}}$ . The Fourier transform is usually evaluated with the Fast Fourier Transform algorithm. The  $M$  spectra are then averaged together to reduce the periodogram variation.

Welch [133] modified the Barlett periodogram method by overlapping consecutive segments and applying weighting functions to the segments in order to reduce spectral leakage. These approaches avoid to further reduce the spectra frequency resolution (already lowered by a factor  $M$  by the Barlett method).

### 2.7.2. PROPER ORTHOGONAL DECOMPOSITION

Proper orthogonal decomposition is a modal decomposition that considers the input-quantity variance as sorting criterion. When applied to velocity fields, the mode variance is a kinetic energy, thus a lower-order reconstruction from selected first POD modes ensures that most of the flow kinetic energy is correctly reproduced. The snapshot formulation, introduced by Sirovich [119], is here described as this is a common formulation used in fluid dynamics.

Starting from the Reynolds decomposition, the velocity components are rewritten considering the stationary and time-variant components  $q = \bar{q} + q'$ , where  $q = \{u, v, w\}^t$ . The fluctuating quantity vector is considered here. It is a function of the vector application point (i.e. the measurement position) and of time:  $q' = q'(\chi, t)$  (where, in general,  $\chi = [x, y, z]^t$ ). Considering  $M$  spatial points and  $N$  temporal observations, a  $M \times N$  snapshot matrix can be constructed as expressed in equation 2.15,

$$\mathbf{S} = \begin{pmatrix} q'(\chi_1, t_1) & q'(\chi_1, t_2) & \cdots & q'(\chi_1, t_N) \\ q'(\chi_2, t_1) & q'(\chi_2, t_2) & \cdots & q'(\chi_2, t_N) \\ \vdots & \vdots & \ddots & \vdots \\ q'(\chi_M, t_1) & q'(\chi_M, t_2) & \cdots & q'(\chi_M, t_N) \end{pmatrix} \quad (2.15)$$

The auto-covariance matrix is given by  $\mathbf{R} = \mathbf{S}^t \mathbf{S}$  and it is used to formulate an eigenvalue problem:

$$\mathbf{R} \vec{a} = \lambda \vec{a} \quad (2.16)$$

In equation 2.16, the vector  $\lambda$  is the eigenvalue vector while the vector  $\vec{a}$  contains the temporal eigenfunctions. The POD spatial modes derive from the projection of the velocity fluctuations fields on the temporal base  $\vec{a}$ :

$$\Phi^n(\chi) = \sum_{i=1}^N a^n(t_i) q'(\chi, t_i) \quad (2.17)$$

The  $\lambda$  vector, constituting of the eigenvalues of the velocity auto-covariance matrix, yields the kinetic energy level associated with each mode,

$$TKE^n = \frac{\lambda^n}{\sum_{i=1}^N \lambda^i} \quad (2.18)$$

Finally, the  $\Phi(\chi)$  spatial modes are sorted with decreasing  $\lambda$ . The velocity field can be reconstructed by a sub-ensemble of POD modes such that  $n < N$  by summing the time steady value ( $\bar{q}$ ) to a sum of POD modes as in equation 2.19,

$$q^{1-n}(\chi, t) = \bar{q}(\chi) + \sum_{i=1}^{n < N} a^i(t) \Phi^i(\chi) \quad (2.19)$$

### 2.7.3. BUTTERWORTH FILTERS

Butterworth filters are filters with maximal flatness in the passing band [12]. They feature a monotonic amplitude versus angular frequency function, thus ensuring absence of ripples. In the current study, Butterworth zero-phase distortions filters are used. The signal is thus filtered twice in the forward and reversed direction (to correct the phase distortion from the first pass). As a consequence, the amplitude transfer function has squared magnitude and the filter order results double w.r.t. the original (single pass) filter.

### 2.7.4. PARSEVAL'S THEOREM NORMALIZATION

In agreement with Parseval's theorem, when specified, the presented spectra are normalised as shown in equation 2.20,

$$\Phi_{\gamma}^* \cdot \delta_f = (\Phi_{\gamma} \cdot \delta_f) \frac{\sqrt{\frac{1}{ES-1} \sum_t (\gamma')^2}}{\sum_f (\Phi_{\gamma} \cdot \delta_f)} \quad (2.20)$$

where  $\Phi$  is the power spectral density (PSD),  $\delta_f$  is the spectra frequency resolution,  $\gamma$  is the spectra variable and  $ES$  the temporal ensemble size. The sums are performed w.r.t the subscript quantity (i.e. time ( $t$ ) at the numerator and frequency ( $f$ ) at the denominator). As such, the spectral energy pertaining to a given frequency band corresponds to the standard deviation of the velocity fluctuations within the specified band.

### 2.7.5. FLOW METRICS

In this section, the metrics used to describe CFI related amplitudes as well as to characterize the plasma actuator performance are introduced.

#### CROSS-FLOW INSTABILITY

There exist several options regarding the specific metric used for the estimation of stationary CFI modal growth. One option is to directly track the maxima of the mode-shape profiles (i.e. the spanwise standard deviation of the time-averaged velocity profiles) as described by equation 2.21 (e.g. [39]),

$$A_I^{max}(x) = \max|_{y_t} \left\{ \frac{|\bar{V}^{HWA}(x)|}{|\bar{V}_e^{HWA}(x)|} \right\}_z \quad (2.21)$$

where the brackets define the standard deviation operator w.r.t. the subscript quantity ( $z$ ). A second option is to track the wall-normal integral of the mode shape profiles using equation 2.22 (e.g. [27]),

$$A_I(x) = \frac{1}{y_t^m} \int_0^{y_t^m} \left\{ \frac{|\bar{V}^{HWA}(x)|}{|\bar{V}_e^{HWA}(x)|} \right\}_z dy_t \quad (2.22)$$

here  $y_t^m$  indicates the maximum  $y_t$  extent of the integral. With  $|\bar{V}^{HWA}|$  is intended the time-averaged (denoted by the overbar) velocity magnitude measured by the hot-wire ( $V^{HWA} = \sqrt{U^2 + V^2}$ , for the presented experiments) as this is the quantity used in this study. Nevertheless, the following metric could be used for different velocity components/magnitudes. Although the second formulation suffers less from measurement

errors and uncertainties both the approaches are followed in this study, when possible, for comparison with data from previous studies. It must be noted here that in order to arrive to non-dimensional amplitudes using the wall-normal integral metric ( $A_I^{int}$ ), the spanwise average boundary layer thickness ( $\delta_{99}^z$ ) is used for non-dimensionalising as shown in equation 2.22. This is done following the work of Downs & White [27].

$N$ -factors are also introduced for the primary CFI modes ( $N_I$ ). These are the natural logarithm of the local amplitudes normalised with the amplitude at the first instability point ( $x_0$ ) as defined by equation 2.23 and can be computed from both the expressions of the modal amplitudes  $A_I$ .

$$N_I(x) = \ln \frac{A_I(x)}{A_I(x_0)} \quad (2.23)$$

Similarly, the amplitude of the total and of band-pass filtered fluctuations fields is obtained by integrating, over the measured plane, the temporal standard deviation fields of the considered frequency band. The formulation of this quantity is reported in equation 2.24,

$$A_{II}(x) = \frac{1}{y_t^m} \frac{1}{z^m} \int_{f_1}^{f_2} \int_0^{y_t^m} \int_0^{z^m} \left\{ \frac{|V^{HWA'}(x)|}{|\bar{V}_e^{HWA}(x)|} \right\}_t dz dy_t df \quad (2.24)$$

where  $z^m$  indicates the maximum  $z$  extent of the integral and  $f_1$  and  $f_2$  the upper and lower cutoff frequencies of the considered band.

Using the computed amplitudes,  $N$ -factors of the unsteady modes can be estimated based on the reference amplitude at  $x_0$  ( $N_{II}$ ),

$$N_{II}(x) = \ln \frac{A_{II}(x)}{A_{II}(x_0)} \quad (2.25)$$

### AC-DBD PLASMA ACTUATORS

Following Corke *et al.* [17] and Kotsonis [56], the performance of plasma actuators is characterized by the momentum coefficient expressed in equation 2.26,

$$C_\mu = \frac{T}{\frac{1}{2} \rho u_e^2 \vartheta_u} \quad (2.26)$$

where  $\rho$  is the air density. For the considered applications, the velocity and length scales used are  $u_e$  and  $\vartheta_u$ . These are the local (at the position at which the actuator is installed) boundary layer edge velocity and momentum thickness along  $x$  for the considered flow-case. These quantities are extracted from numerical solution of the laminar, stationary, incompressible, 2.5-dimensional boundary layer equations described in section 2.5.

## 2.8. NON-DIMENSIONALIZATION

Several reference systems and different experimental and numerical techniques were used and described in the present study. Part of the results is therefore presented in non-dimensional units. The airfoil chords along the  $X$  and  $x$  directions as well as the CFVs wavelength are used as reference length scales for the related length-quantities. However, some results are presented in dimensional units to ease comparison with dimensional quantities and avoid introduction of elaborated nomenclature.

The plasma actuators performance can be described by non-dimensional quantities as e.g. the momentum coefficient. However, the main dimensional parameters, namely the frequency of the driving AC voltage and the wavelength of the electrodes, are crucial for the description and understanding of the presented analyses. Therefore, these parameters are often reported in metric units.

The velocity scale used in the remainder is the free stream velocity ( $U_\infty$ ) although, for boundary layers velocities, the values at the boundary layer edge (denoted with the subscript  $e$ ) are considered. Together with the chord in the free stream direction ( $c_X$ ),  $U_\infty$  is used for the definition of the Strouhal ( $St$ ) and Reynolds ( $Re$ ) numbers. In addition,  $U_\infty^2$  is used, when specified, to non-dimensionalise the velocity power spectra.

# 3

## WIND TUNNEL MODEL

*In this chapter, the design procedure of the wind tunnel model for cross-flow instability investigation is illustrated. The process involves the airfoil and the wall liners design. Wind tunnel tests encompassing oil-flow/infrared thermography visualization, surface pressure and boundary layer hot-wire measurements were performed validating the design procedure. The effectiveness of the wall liners to constrain the flow to a spanwise invariant arrangement is showed to be limited for the presented cases. Furthermore, linear stability theory is applied to numerically computed boundary layer solutions in order to evaluate the flow stability to stationary and travelling CFI modes.*

---

**J. Serpieri**, & M. Kotsonis, *Design of a swept wing wind tunnel model for study of cross-flow instability*, 33<sup>rd</sup> AIAA Applied Aerodynamics Conference, Dallas, USA, (2015)

**J. Serpieri**, S. Yadala Venkata & M. Kotsonis, *Conditioning of cross-flow instability modes using dielectric barrier discharge plasma actuators*, *Journal of Fluid Mechanics*, **833**, 164–205 (2017)

P. Rizzo, **J. Serpieri** & M. Kotsonis, *Effect of surface roughness and free stream turbulence on cross-flow instability transition*, (in preparation)

### 3.1. INTRODUCTION

To perform a research on cross-flow instability no matter whether the followed approach is experimental or numerical, it is preferred to respect the semi-infinite swept wing hypothesis. It allows to consider the flow invariant along the span which implies a series of simplifying consequences that will be highlighted in this chapter. Achieving this condition in experimental campaigns requires to use wall liners contoured as the streamlines thus complicating the design and installation of the model. Nonetheless, the design procedure is itself much simplified when this hypothesis is respected.

The cross-flow instability has a stationary and a travelling nature as described in chapter 1. Although stationary modes are expected to dominate in low free-stream turbulence flows, the presence of travelling waves in experimental campaigns cannot be avoided. Thus, CFI transitional boundary layers feature already a multitude of mechanisms interacting together, complicating the diagnostics and analyses. As a consequence, the wing geometry to adopt for CFI investigations should enhance CFI modes while possibly avoiding the amplification of different instabilities. These considerations are followed in the design procedure described in the following sections.

Previous wind tunnel campaigns made use of boundary-layer visualization techniques to assess the evolution of the developing instability (e.g. [18, 6, 104]). Quantitative measurements are usually performed using hot-wire probes mounted on opportune traverses (e.g. [19, 97, 135]). In order to investigate the evolution of the transitional boundary layer, these techniques have been employed in preliminary wind tunnel tests. The outcomes are presented in the following sections as a validation of the design procedure.

Solutions of the laminar steady boundary layer are straightforward when the semi-infinite swept wing assumption is respected (as shown in section 2.5). These solutions are used as input for linear stability theory calculations which retrieve useful prediction of the stability of the laminar boundary layer. These are presented in last section of this chapter.

### 3.2. MODEL DESIGN

#### 3.2.1. AIRFOIL

The airfoil served as a reference shape for this study is the one used in ASU/TAMU campaigns: the NLF(2)-0415 [97, 94]. This airfoil features some important characteristics needed to allow the experimental investigation of the CF instability: it has a small curvature radius at the leading edge which is meant to avoid the attachment line instability and it has the maximum-thickness point far downward from the leading edge which, for the given angle of attack, can ensure a favourable pressure gradient ( $\partial p/\partial x > 0$ ) for a good extent of the chord, this being a condition to avoid the growth of TS waves [6]. The inviscid pressure coefficient ( $-C_p$ ) on the NLF(2)-0415 set to an angle of attack ( $\alpha$ ) of -4 degrees and exposed to a free stream with Mach number of 0.1 is shown in figure 3.1. The  $C_p$  distribution is evaluated using *XFOil*. The ASU group chose this set for two reasons: first the  $C_p$  on the suction surface appears increasing up to the 71% of the chord thus ensuring that the disturbances observed in the boundary layer were due to CF modes and not to TS waves; the second reason is that the NLF(2)-0415 features zero lift at this angle of attack thus simplifying the overall design and operation of the model.

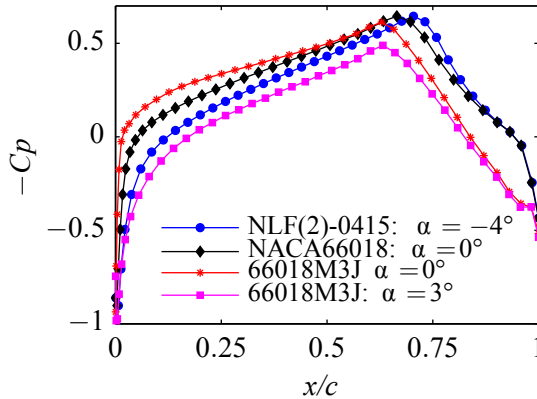


Figure 3.1: Inviscid pressure distributions for different configurations at  $M = 0.1$ , computed with *XFOil*.

Starting from these considerations a new airfoil was designed. The main difference with respect to the configuration adopted at Texas A&M is that, in this case, the preference was towards the use of a symmetrical airfoil swept wing this allowing a simplified design and construction procedure. The symmetrical airfoil that was then selected having similar features with respect to the NLF(2)-0415 at  $-4$  degrees, was the NACA 66018 at zero incidence. Some modifications to its original shape were then performed in order to obtain a more suitable  $C_p$  distribution. Figure 2.2 shows a comparison between the original NACA 66018 airfoil and the modified version called 66018M3J. The modified airfoil features the same maximum thickness (18% of the chord) of the NACA 66018 but the position of the maximum thickness point has been slightly moved downstream. Some small changes have been applied to the geometry of the leading edge as well.

The  $C_p$  distributions for the NACA 66018 at  $\alpha = 0^\circ$  and for the 66018M3J at  $\alpha = 0^\circ$  and at  $\alpha = 3^\circ$  are plotted in figure 3.1 for comparison with the one of the NLF(2)-0415 at  $-4$  degrees. The two last pressure distributions show a very similar slope. For all the presented curves, the maximum-velocity point is downstream of the  $x/c = 0.6$  station. The pressure distribution of the 66018M3J at the two incidences changes notably, thus influencing the transition scenario as it will be described later in this chapter.

### 3.2.2. WALL LINERS

To ensure the development of an infinite swept wing flow in experimental campaigns, the wind tunnel walls should be equipped with wall liners shaped as the three-dimensional streamlines around the corresponding infinite wing [19, 94, 97].

In this section, a way to estimate the shape of the contoured side plates is presented. The effectiveness of the streamlined liners is assessed by experimental tests presented in section 3.3.1. The steps needed for the design of such liners can be resumed in: two-dimensional potential flow estimation around the airfoil; evaluation of the three-

dimensional flow field and its transformation to the wind tunnel reference system ( $XYZ$ ); shape extrapolation and CAD design of the model. The flow around the airfoil is computed with *Ansys Fluent 14.5* while the structured mesh around the airfoil is built with *Gambit 2.2.3*. The parameters set for this computation are: steady laminar 2D flow, constant flow density, free stream velocity  $u_\infty = 30 \text{ m s}^{-1}$  and  $\alpha = 0^\circ$ .

Once the flow field is evaluated, two more operations are required to achieve the required flow: first the extrusion of the two-dimensional flow field in the normal-to-the-plane direction ( $z$ ), then the superposition of a free stream velocity component ( $w_\infty$ ) orthogonal to the 2-D field. The result of the first step is the flow field around an infinite rectangular wing. The latter step retrieves the flow field equivalent to the one around an infinite swept wing (with a sweep angle of  $\Lambda = \tan^{-1}(w_\infty/u_\infty)$ ). As the goal is to simulate the flow around a 45 degrees swept wing, the  $u_\infty$  and  $w_\infty$  free stream velocities have the same magnitude ( $30 \text{ m s}^{-1}$ ).

After these steps, it is possible to compute the three-dimensional streamlines. It should be noted that the streamlines computed in this manner will lay in a  $xyz$  reference. To have the streamlines' coordinates in the wind tunnel  $XYZ$  reference, a coordinates transformation is needed. This is done with the operation presented in equation 3.1,

$$\{XYZ\} = \{xyz\} \cdot \mathbf{A} \rightarrow \mathbf{A} = \begin{bmatrix} \cos(\Lambda) & 0 & \sin(\Lambda) \\ 0 & 1 & 0 \\ -\sin(\Lambda) & 0 & \cos(\Lambda) \end{bmatrix} \quad (3.1)$$

In figure 3.2a it is possible to see the streamlines' shape and to appreciate how much they curve as approaching the model surface. Due to the pressure difference along the vertical global direction  $z$ , the streamlines firstly curve upwards along  $Z$  in the leading edge region, then they bend and turn downwards until the maximum  $x$  velocity point. Downstream of this point, the streamlines bend again towards the  $z$ . Moving away from the model in the direction orthogonal to the chords' plane, the streamlines' shape goes from the wall inviscid streamlines to the undisturbed straight ones. From the streamlines of figure 3.2a, the wall liners surface can be designed. In figure 3.2b the CAD model of the wing, the wall liners (including opportune ramps from the wind tunnel walls) and the LTT wind tunnel section are presented.

Alternatively to the followed procedure full three-dimensional flow simulation can be performed. The results should be comparable with the ones presented although at a higher computational cost.

### 3.3. WIND TUNNEL PRELIMINARY EXPERIMENTS

To assess the validity of the design procedure described so far, preliminary wind tunnel tests have been performed encompassing surface pressure measurements, oil-flow and IR thermography visualization and hot-wire boundary layer measurements. The model was described in section 2.2. The tests were performed at a fixed free stream Reynolds number  $Re \approx 2.12 \cdot 10^6$  ( $U_\infty = 25 \text{ m s}^{-1}$ ) and at two angles of attack  $\alpha = 0^\circ, 3^\circ$ .

#### 3.3.1. FLOW SPANWISE-UNIFORMITY

The wing model is equipped with two series of 46 surface pressure taps along the free stream direction at two different spanwise stations, each of which is positioned at 300

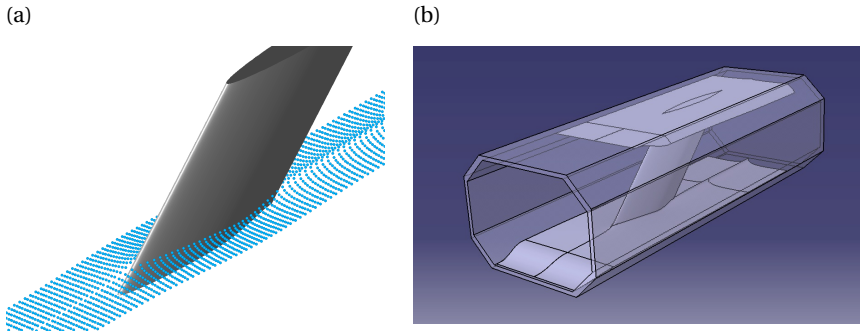


Figure 3.2: (a) 3D inviscid streamlines around the 66018M3J infinite  $45^\circ$  swept wing at  $\alpha = 0^\circ$ . (b) CAD of the model with the contoured wall liners installed in the LTT wind tunnel.

mm from the two wing tips. The series being close to the lower tip is referred to as  $AA'$ , while the one close to the top end is named  $BB'$ . By checking figure 3.2b, it can be seen that the bottom part of the wing is also the most upstream, given the way the wing is mounted in the LTT testing chamber. The pressure was measured with a multi-channel transducer. Two measurements have been performed with the streamlined wall liners installed and without. The angle of attack is  $\alpha = 0^\circ$  and the free stream is  $U_\infty = 25 \text{ m s}^{-1}$  ( $Re \approx 2.12 \cdot 10^6$ ). The results are plotted in figure 3.3. The largest discrepancy between the measurements with the liners and without has to be related to flow blockage caused by the wall liners in the test section thus changing the local flow velocity. When the liners are mounted, the flow has a higher velocity which results in a lower pressure. Besides this, what is here inspected is the pressure difference between the two spanwise locations for the two cases. Focusing on this aspect, it can be observed that, for both the cases, the more upstream stations do not show the same pressure values between the two sections. Moving more downstream, after the mid-chord station, it can be seen that the wall liners help constraining the flow thus achieving a more spanwise-uniform flow. The reason why the  $BB'$  stations show a lower pressure than the  $AA'$  ones can be explained again by wind tunnel blockage considerations: the  $BB'$  taps are placed more downstream. Because of this, they experience a flow that results accelerated by the blockage caused by the bottom part of the wing. This effect happens in both the configurations. To reduce it either the model cross-section should be reduced or the wind tunnel test section increased, both the options are considered not feasible. The blue lines of figure 3.3 refer to the flow case with  $\alpha = 3^\circ$  and the free stream is  $U_\infty = 25 \text{ m s}^{-1}$  ( $Re \approx 2.12 \cdot 10^6$ ) without liners mounted. For this case almost no difference between the two sections is noticeable.

In general, the pressure difference between the two sections does not seem so large for all the cases. Moreover the taps are placed at 30 cm from the tips on a 125 cm span model, this meaning that there is a region of 65 cm between the two sections, in a central position, where the wall effects are further mitigated.

The design procedure described in the section 3.2.2 is validated by the results plotted in figure 3.3. Besides these observations, the wall liners show a limited effectiveness: the change in flow uniformity does not appear drastic, being evident only after the mid-chord

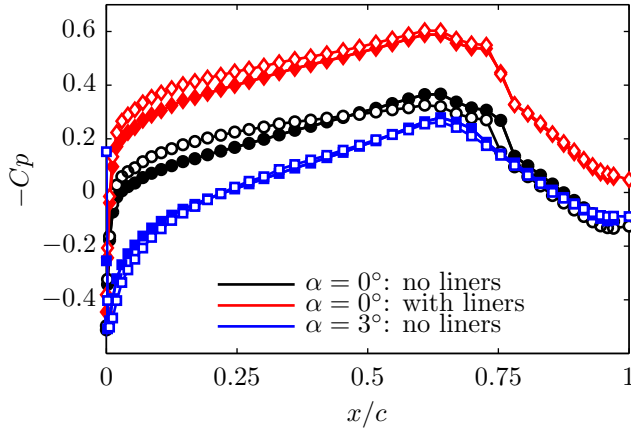


Figure 3.3: Pressure distributions around the 66018M3J swept wing for different configurations measured by two pressure taps arrays at different spanwise sections placed 300 mm (total wing span: 1.25 m) from the lower (section  $AA'$ : full markers) and upper (section  $BB'$ : empty markers) wing tips.  $Re \approx 2.12 \cdot 10^6$  and  $\alpha = 0^\circ$  and  $3^\circ$ .

station. Furthermore it should be noted that the flow blockage they cause in the test section leads to higher free stream velocities. For the remainder of the study, most of the experiments will be done at the incidence of 3 degrees to enhance the CFI as discussed in the following section. The spanwise coherence, at this incidence, is excellent even without the wall liners.

### 3.3.2. LAMINAR-TO-TURBULENT TRANSITION

Oil-flow visualization was performed to observe the boundary-layer evolution. The experiments were performed at  $Re = 2.12 \cdot 10^6$  and  $\alpha = 0^\circ$ . In figure 3.4, the flow is from right to left as indicated by the blue arrow and the model trailing edge is shown by the bright line at the bottom left. Three lines, with a  $45^\circ$  slope, are plotted on the figure: the dashed line located at the wing mid-chord ( $x/c = 0.50$ ) and the other two located at  $x/c = 0.25$  and  $x/c = 0.75$ . The central half span of the wing ( $30 \text{ cm} < Z < 90 \text{ cm}$  for a total span of 125 cm) is captured in all the following pictures. In the picture, no stationary waves are clearly observable if not very downstream (around station  $x/c = 0.65$ ). The laminar boundary layer region extends till  $x/c \approx 0.70$  where laminar separation occurs (the bright sharp line followed by a darker region). At the most downstream stations, turbulent reattachment occurs wiping away most of the oil. At these conditions, no quantitative studies on cross-flow instability transition can be performed as these mechanisms are too weak and do not cause the boundary layer transition.

Two strategies can be followed in order to enhance the CFI: increasing the Reynolds number [94] or increasing the favourable pressure gradient. Increasing the Reynolds number allowed to visualize cross-flow stationary waves and the transition front shifted more upstream. Despite this, increasing the Reynolds number is not suggested: the boundary layer would become too thin further challenging accurate measurements. Moreover, at higher free-stream velocities (of the order of  $U_\infty = 60 \text{ m s}^{-1}$ ), quantitative

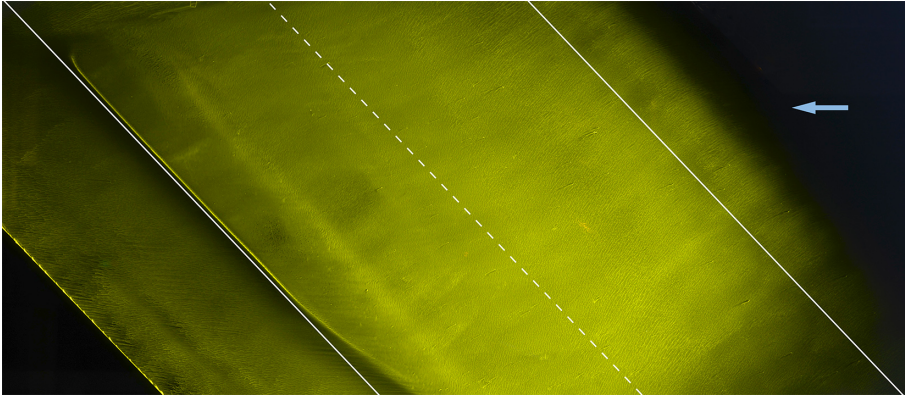


Figure 3.4: Fluorescent oil-flow visualization. The flow comes from right (indicated by the blue arrow).  $Re = 2.12 \cdot 10^6$  ( $U_\infty = 25 \text{ m s}^{-1}$ ) and  $\alpha = 0^\circ$ . The white dashed line is the wing mid section  $x/c = 0.50$ , the other two indicate station  $x/c = 0.25$  on the right and station  $x/c = 0.75$  on the left respectively.

hot-wire boundary-layer measurements would be cause vibrations of the probe holder. At higher velocities, flow-temperature drifts although limited by the active cooling of the tunnel, would also interfere with the measurements.

When placing the wing at an incidence of  $\alpha = 3^\circ$  and keeping the free stream velocity  $U_\infty = 25 \text{ m s}^{-1}$ , the scenario indeed changes drastically. The oil-flow visualization of this case is presented in figure 3.5 (with the same reference lines presented in figure 3.4). Here the cross-flow waves are evident. They appear at non-uniform streamwise locations along the span and they grow, in terms of intensity, towards the trailing edge. At the locations where the vortices first appeared, boundary-layer breakdown, evidenced by the turbulent wedges, occurs at first. The wave-fronts captured here are inclined of about  $5^\circ$  with respect to the horizontal direction  $X$ . The transition location is not well defined given the spanwise non-uniformity of the flow. Nevertheless, it can be estimated in a spanwise-averaged sense, to occur roughly at  $x/c \approx 65\%$ . This is again very downstream and close to the adverse pressure gradient region thus not excluding that TS waves are amplifying as well [75, 107]. In figure 3.5, a white dashed rectangle is also plotted. The detailed view of that region is presented in figure 3.7a where a reference line 10 mm long is also shown. When comparing this line to the wavefronts' spacing, it appears that they are of the same order. It can also be observed though that this wavelength is not uniformly repeated along the span for this flow.

To achieve a more uniform base flow, Radeztsky *et al.* [94] and Reibert *et al.* [97] installed an array of roughness elements at the wing leading edge. To overcome the lack of spanwise uniformity observed in figure 3.5, this approach was followed in this study. This consisted in applying small roughness elements in the wing leading edge region spaced as the observed dominant stationary mode. By forcing this mode, the boundary layer resulted destabilized by a much narrowed band of modes centred about the forced one. In section 2.4, a detail of the employed elements was shown. The DREs were spaced with  $\lambda_z = 9 \text{ mm}$  following the LST estimations presented later. Even the extremely small employed elements ( $d_r = 2.8 \text{ mm}$ ,  $h_r = 10 \text{ }\mu\text{m}$ ) were effective for the purpose leading to

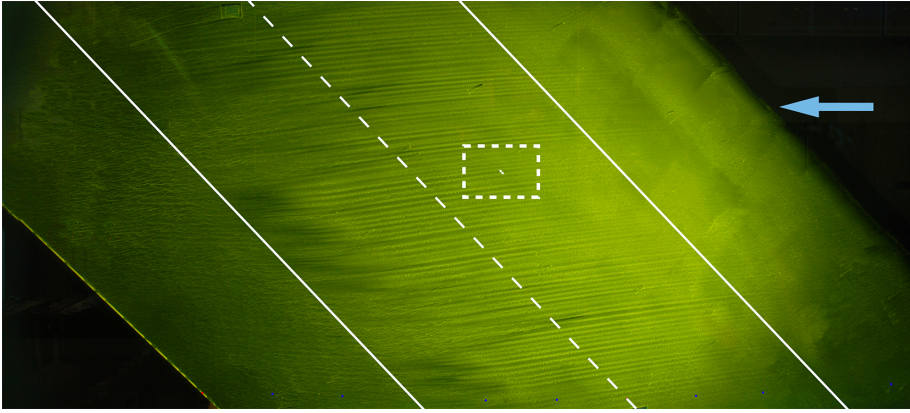


Figure 3.5: Same notation of figure 3.4.  $\alpha = 3^\circ$ .

the flow presented in figure 3.6 and in detail in figure 3.7b. It can be seen that the forcing led to a more uniform flow field with respect to both the waves onset and their spacing compared to the unforced boundary layer. Furthermore, given the larger initial amplitude of the cross-flow waves, the transition location is also anticipated to  $x/c \approx 45\%$ , so well within the accelerated flow region (compare figure 3.1).

It has to be noted that all the flow visualizations presented in figures 3.4, 3.5 and 3.6 are for the model without the streamlined liners mounted. All these pictures capture the flow evolution within the location of the pressure tap series  $AA'$  and  $BB'$ , thus meaning that about  $60\text{cm}$  of span over the total  $125\text{cm}$  are presented. They all show a good spanwise-uniformity, when looking at the main features as boundary layer separation and transition thus indicating that the model has a span large enough to have wall effects confined to the tip regions. The separation line of figure 3.4 tends to vanish at more bottom locations but this was caused by some tape installed on the model (just below the lower end of the photo), in order to protect the pressure taps from the leaking oil. The tape edges directly caused the boundary layer transition.

### 3.3.3. CROSS-FLOW INSTABILITY

Hot-wire boundary-layer measurements were also performed to quantitatively inspect the developing CFI. These measurements were done by using a fully automated three degrees-of-freedom traverse mounted downstream of the model in the wind tunnel. The traverse allowed very accurate probe displacements. A constant temperature hot-wire system was used. Measurements were acquired at a sampling rate of  $50\text{ kHz}$  for a period of 4 seconds. They were performed at several stations along the free-stream direction in planes aligned with the leading edge line  $z$  and the local wall-normal directions. These planes consist of 3200 points (50 measurements along the wall normal direction times 64 spanwise stations). The probe was aligned with the global  $Z$  axis, so to be exposed to the flow magnitude from the  $U$  and  $V$  velocity components. Wire calibration was performed in the wind tunnel by using a Pitot-static probe and flow temperature and pressure corrections were applied.



Figure 3.6: Same notation of figure 3.4.  $\alpha = 3^\circ$ . Cylindrical roughness elements ( $d_r = 2.8$  mm and  $k_r = 10$   $\mu$  m) installed at  $x/c = 0.025$  spaced 9 mm.

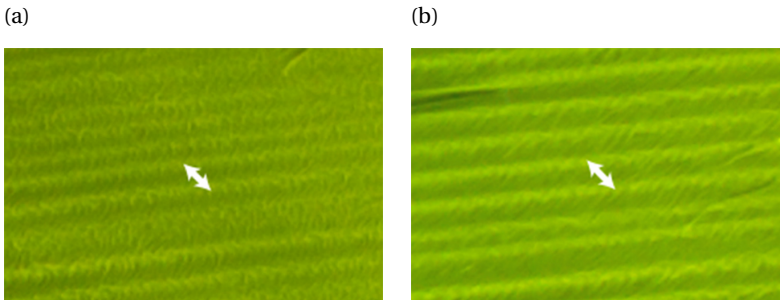


Figure 3.7: Details, corresponding to the white dashed box, of figure 3.5 (a) and of figure 3.6 (b). The white reference line is 10 mm long.

The time averaged velocity field, measured at  $x/c = 0.50$  for  $Re = 2.12 \cdot 10^6$  ( $U_\infty = 25$   $\text{m s}^{-1}$ ) and  $\alpha = 3^\circ$  under natural transition conditions and with the 9 mm mode forced by DREs, are shown in figure 3.8(a) and (b), respectively. This is a view as seen by the flow entering the page. Reflecting the scenario illustrated with the oil-flow, presented in figure 3.5, the hot-wire contour of figure 3.8(a) does not show a spanwise-uniform arrangement. As natural transition processes are occurring in this case, it is likely that several wavelengths will be present as it was already seen by Radeztsky *et al.* [94] and Reibert *et al.* [97]. A spanwise measurement on a wider domain will in this case help allowing spectral analysis of the CFI modal content as done by Radeztsky *et al.* [94] in their study. Going back to the velocity field, we can observe several very weak waves on the left part of the plot and an evident stationary vortex placed at  $z = 33$  mm. When analysing the contours of the forced case of figure 3.8(b), a much more uniform flow is captured. As expected, the wave spacing corresponds to the forced wavelength and the waves show a larger and more uniform amplitude with respect to the non-forced case.

It can be concluded that these hot-wire measurements agree with the flow visualiza-

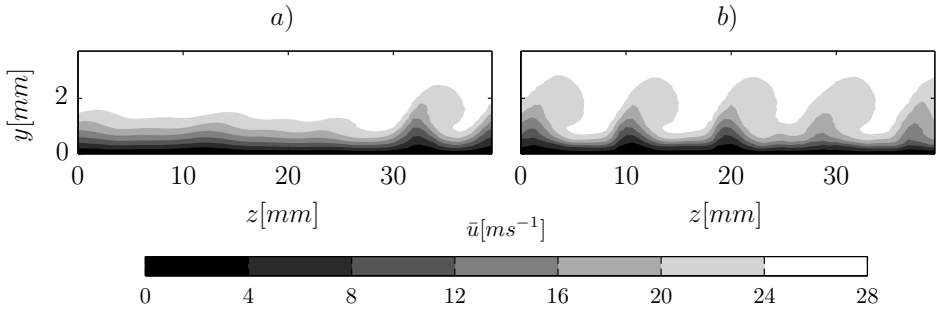


Figure 3.8: Contour of the time averaged free stream velocity component at  $x/c = 0.50$ , as seen by the flow entering the plane for  $Re = 2.12 \cdot 10^6$  ( $U_\infty = 25 \text{ m s}^{-1}$ ) and  $\alpha = 3^\circ$ . Natural transition (a) and 9 mm wavelength forcing (b).

tion of figure 3.5 and of figure 3.6.

### 3.3.4. EFFECTS OF FREE-STREAM TURBULENCE AND SURFACE ROUGHNESS ON CFI

Infrared termography visualization was performed to inspect the evolution of the transition front under a variety of parameters (angle of attack, free-stream turbulence and surface roughness). For this purpose, the free stream turbulence was increased by removing some anti-turbulence screens (discussed in section 2.3). To modify the surface roughness from the value of  $R_q = 0.20 \mu\text{m}$  (profilometer standard deviation) of the model, different plastic foils were mounted on the wing. The considered foils have values of  $R_q = 1.5 \mu\text{m}$ ,  $R_q = 2.5 \mu\text{m}$  and  $R_q = 10 \mu\text{m}$ .

The thermocamera used for this investigation is an *Optris PI 640* ( $640 \times 480 \text{ px}^2$ ,  $7.5 - 13 \mu\text{m}$  spectral range, 75 mK of sensitivity and  $\pm 0.1^\circ\text{C}$  of accuracy). The camera was placed at about 1 m from the model surface and imaged the latter through an opportune window. It featured a 41.5 mm lens and imaged almost the entire wing chord for the central span portion of the wing. Uniform active heating of the model was achieved with six 0.5 kW halogen lamps pointing to the model. The measurements started after the model reached the equilibrium temperature. The laminar-to-turbulent transition front was clearly detected given the different temperature (of approximately 4 degrees). The spanwise-averaged chordwise position of the transition front ( $x_{tr}$ ) is plotted in figure 3.9a for three different anti-turbulence screens configurations (see 2.3 for the respective turbulence levels) and in figure 3.9b for the four surface roughness conditions. The test were performed for different angles of attack and at the free stream velocity of  $40 \text{ m s}^{-1}$ .

It appears that, for  $\alpha > 1^\circ$  where CFI transition occurs for the baseline case (lower  $R_q$  and  $Tu$ ), increasing both free stream turbulence and surface roughness causes an upstream shift of the transition front. Besides, being the transition scenario dominated by stationary CFI mechanisms, the effect of surface roughness is dramatic: going from the model roughness of  $R_q = 0.20 \mu\text{m}$  to the roughest foil ( $R_q = 10 \mu\text{m}$ ), the transition front moves upstream of more than 20% of the chord.

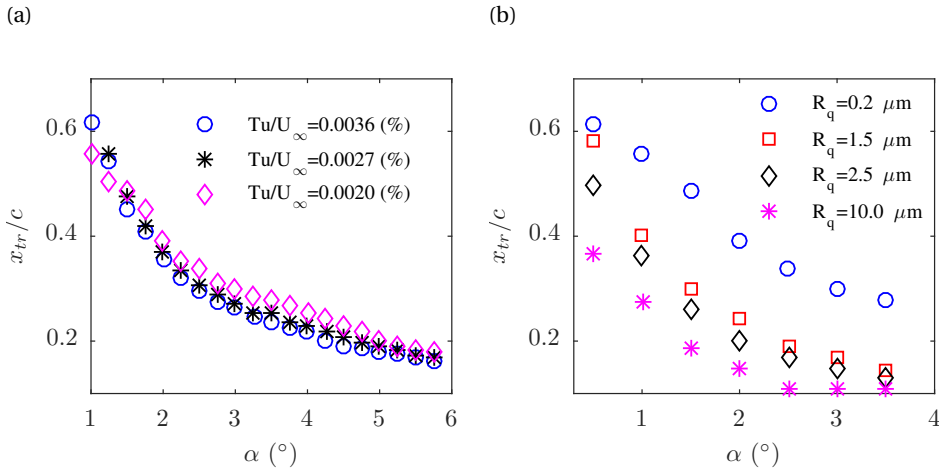


Figure 3.9: Spanwise-averaged chordwise position of the transition front against the angle of attack for  $U_\infty = 40 \text{ m s}^{-1}$ , (a) for three different free stream turbulence levels, from figure 2.3) and  $R_q = 0.20 \mu\text{m}$ ; (b) for four values of surface roughness with all the seven anti-turbulence screens installed.

### 3.4. STABILITY OF THE LAMINAR BOUNDARY LAYER

Linear stability theory analyses are performed for the boundary layer developing on the pressure side of the wind tunnel model set at 3 degrees of incidence and exposed at a free stream velocity of  $U_\infty = 25.6 \text{ m s}^{-1}$ . The solution of the laminar, steady, incompressible, 2.5-D flow equations discussed in section 2.5 is computed from the pressure distribution plotted in figure 3.3. The resulting  $u$  and  $w$  velocity distributions are shown in figure 3.10. These velocity fields together with their derivatives are used as input for the spatial-OS solver presented in section 2.6.

Following the definitions given in section 2.6, a comparison of envelope N-factors, between stationary and travelling modes of various frequencies is presented in figure 3.11a. Modes in the  $0 \text{ Hz} \leq f \leq 600 \text{ Hz}$  frequency band show strongest amplification close to the  $u$  velocity stagnation point. While the  $f=600 \text{ Hz}$  mode crosses branch-II at  $x/c=0.25$ , the lower frequency waves are amplified throughout the boundary layer with the 200 Hz mode being the most amplified mode. The fact that steady modes have lower growth than the travelling waves is a common outcome of LST analyses [77, 39]. Nevertheless, the eventual dominance of stationary modes over unsteady modes in practical cases is conditioned by the boundary-layer receptivity to surface roughness and free-stream turbulence, which is not accounted for in the LST eigenvalue problem. As such, while predicted by LST to be weaker, stationary vortices dominate the transition scenario in low turbulence flows [19, 27].

Lastly, it is important to note that higher-frequency modes are unstable only for shorter portions of the wing. For example, the  $f=1000 \text{ Hz}$  mode is only weakly amplified near the leading edge and by station  $x/c=0.113$  reaches  $N^{env} = 0$ . Modes with higher frequency are either less amplified or they never destabilise in the current conditions.

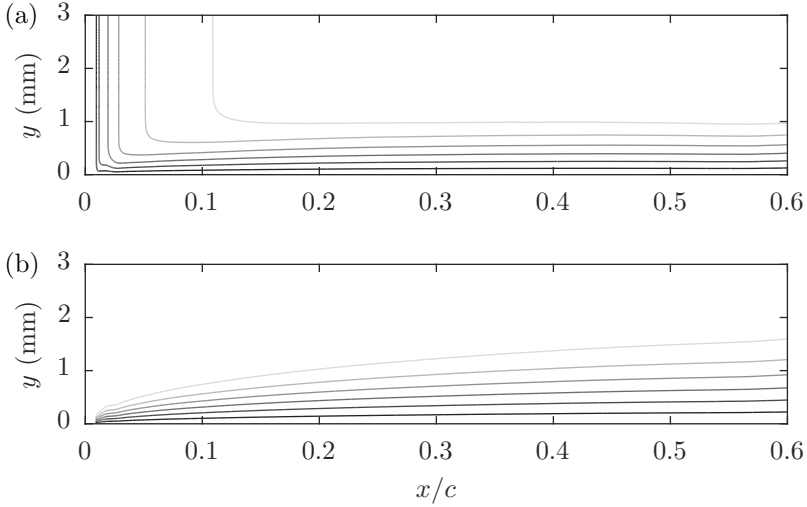


Figure 3.10: Boundary layer numerical solution of the laminar, steady, incompressible, 2.5-D flow ( $U_\infty = 25.6 \text{ m s}^{-1}$  and  $\alpha = 3^\circ$ ). (a) contour of  $u$  (7 levels, from 0 (black) to  $18 \text{ m s}^{-1}$  (white)) and (b) contour of  $w$  (7 levels, from 0 (black) to  $-18 \text{ m s}^{-1}$  (white)).

These preliminary results will serve as an initial handle towards choosing the forcing frequency of the AC-DBD plasma actuators used in the remainder. Specifically, the LST results suggest that unsteady forcing should be applied at frequencies that are higher than the shown unstable band.

A comparison between stationary modes with different wavelengths is shown in figure 3.11b. While in the most downstream regions the predicted instability is dominated by the  $\lambda_z=9 \text{ mm}$  mode (see also Serpieri & Kotsonis [114]), the smaller wavelengths modes are more amplified upstream as a consequence of the lower local Reynolds number. The DRE/UFD flow control strategy pivots on this phenomenon. Selective forcing of stationary modes with smaller wavelengths with respect to the eventually most amplified mode, delays the amplification of the latter and consequently postpones the flow breakdown (e.g. [100, 77, 129]). For the presently studied flow, a stationary mode with spanwise wavelengths in the range of  $\lambda_z=5\text{-}7 \text{ mm}$  should lead to this beneficial effects. The location of the  $u$  velocity stagnation point  $x_{st}$ , of the DREs forcing  $x_f$  and the critical location for the  $\lambda_z = 9 \text{ mm}$  ( $x_{cr}^{9mm}$ ) are also plotted.

It must be noted here that LST gives only indications of the pertinent modes evolution as it does not account for non-parallel and non-linear effects. Furthermore, it does not account for the disturbances initial amplitude (i.e. the receptivity problem). Finally, neither the boundary layer nor the OS equation solver account for the model curvature and flow non-parallel effects. The effects of these parameters have been thoroughly analysed by Haynes & Reed [39]. Nonetheless, the outcomes discussed here give valuable information on the stability of the studied boundary layer.

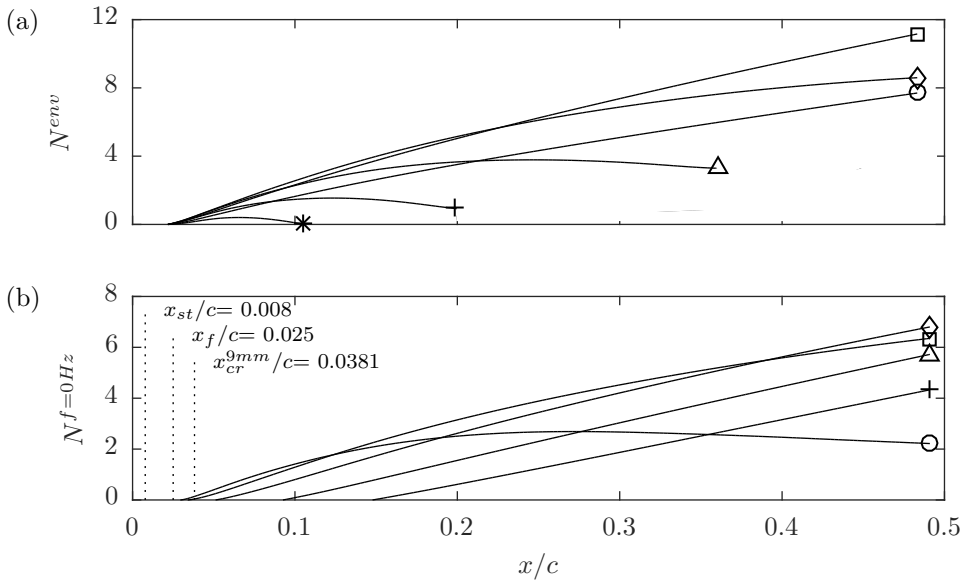


Figure 3.11: (a) Envelope N-factors for different frequencies ( $\circ$ : 0 Hz;  $\square$ : 200 Hz;  $\diamond$ : 400 Hz;  $\triangle$ : 600 Hz;  $+$ : 800 Hz;  $*$ : 1000 Hz). (b) N-factors of different stationary modes ( $\circ$ :  $\lambda_z=5$  mm;  $\square$ :  $\lambda_z=7$  mm;  $\diamond$ :  $\lambda_z=9$  mm;  $\triangle$ :  $\lambda_z=12$  mm;  $+$ :  $\lambda_z=15$  mm).  $x_{st}$  indicates the  $u$  velocity stagnation point,  $x_f$  is the forcing location and  $x_{cr}$  is the critical station for the given mode. See equations 2.13 for the formulation of the plotted quantities.

### 3.5. CONCLUSIONS

In this chapter, the steps necessary to design a swept wing model for cross-flow instability investigation are presented. First the choice criteria of an opportune airfoil have been illustrated. Then the steps for the design of the wall liners have been described. They can be resumed in the following points:

1. 2D inviscid simulation of the flow around the airfoil
2. Replication of the simulated flow field along the third dimension (normal to the 2D field)
3. Generation of the infinite swept wing flow by superposition of a free stream velocity in the orthogonal to the 2D field direction
4. Evaluation of the 3D streamlines around the swept wing in the wind tunnel reference system
5. Design of the streamlined wall-liners

The model design was validated by wall pressure measurements. These showed that the wall liners help to achieve a more spanwise-uniform flow but only for the most downstream stations. Whereas, for the  $\alpha = 3^\circ$  incidence at which most of the experiments

described in this booklet are performed, a good flow uniformity along the spanwise direction is respected also without the wall liners. Therefore, to facilitate the experiments, the latter were performed without wall liners.

3

Oil-flow visualization was also performed. It showed that the flow at  $Re = 2.12 \cdot 10^6$  and  $\alpha = 0^\circ$  is not sufficient to achieve CFI transition. In order to observe amplified cross-flow waves, the Reynolds number was kept constant but the angle of attack changed to  $\alpha = 3^\circ$  thus enforcing the favourable pressure gradient on the wing pressure side. At this incidence, in fact, the cross-flow waves were amplified much more leading to the boundary-layer transition. The oil-flow pictures as well as the hot-wire measurements showed the occurrence of CFI modes featuring several wavelengths. This is expected as, when natural transition occurs, the flow features a lower level of uniformity as already observed by Radeztsky *et al.* [94]. However, despite the increased strength of the stationary waves, the stationary CFI was shown to be still not capable to cause the flow breakdown before the airfoil decelerating region thus not excluding the amplification of Tollmien-Schlichting waves and the interaction of the modes of the two different types [131, 107]. As suggested by Radeztsky *et al.* [94], a boundary-layer forcing at the wavelength of the naturally dominant stationary mode, led to a more spanwise-uniform flow field. Following this approach, cross-flow stationary waves with  $\lambda_z = 9$  mm were forced with small roughness elements installed close to the leading edge. The CFVs' enhanced initial amplitude further promoted the flow breakdown.

The flow captured qualitatively with the oil-flow technique was measured quantitatively with hot-wire scans. The contours of the time-averaged streamwise velocity agree with the scenario illustrated by the oil-flow.

To evaluate the effect of free-stream turbulence intensity and surface roughness on the transition evolution, infrared thermography visualisation experiments were performed as well. These showed a clear upstream shift of the transition front when the two mentioned parameters were enhanced.

Finally, in order to have a preliminary picture of the boundary layer evolution and its stability characteristics, the boundary-layer equations described in section 2.5 have been numerically integrated. The computed velocity profiles have then been used as input for the spatial Orr-Sommerfeld solver. The resulting N-factors allowed to estimate the spacing of the most amplified cross-flow modes and to evaluate the development of stationary and travelling CFI modes.

# II

## FLOW DIAGNOSTICS



# 4

## PRIMARY CROSS-FLOW INSTABILITY

*In this chapter, the developing stationary CFI is experimentally investigated. Oil flow visualization showed the wall trace of the stationary vortices forced to a monochromatic arrangement by means of leading edge roughness elements. Boundary layer measurements by means of hot-wire anemometers and three-components three-dimensional particle image velocimetry (tomographic or tomo-PIV) were performed. Hot-wire scans covered a wider region in space allowing to trace the growth of the instability mode. The tomo-PIV investigation was instead confined to the boundary layer region where the primary stationary waves saturate and retrieved full volumetric three-components velocity measurements. Comparison between the two quantitative measurements is shown to give very good results for the time-averaged flow field whereas the statistical fluctuations measured by tomo-PIV suffered from higher measurement noise.*

---

**J. Serpieri** & M. Kotsonis, *Three-dimensional organisation of primary and secondary cross-flow instability*, *Journal of Fluid Mechanics*, **799**, 200–245 (2016)

**J. Serpieri** & M. Kotsonis, *Tomographic-PIV investigation of cross-flow instability of swept wing boundary layers*, *46<sup>th</sup> AIAA Fluid Dynamics Conference*, Washington DC, USA, (2016)

## 4.1. INTRODUCTION

Cross-flow stationary vortices dominate the boundary-layer transition evolution in low free-stream turbulence environments [6, 104]. They cause a strong modulation, along the spanwise direction, of the velocity field within the boundary layer and undergo secondary instability of convective type, for swept wing flows [40, 77, 129, 135].

The modulation of the velocity field causes a modulation of the wall shear stresses as well as of the convective heat flux. Consequently, these vortices have been studied with flow visualization experimental techniques built upon these two quantities (wall shear stresses and convective heat flux) such as naphthalene sublimation [18, 100, 134], oil flow [112, 113], hydrogen bubbles tracing [6] or infrared thermography [103]. Through visualization experiments the laminar versus turbulent regions of boundary layer are accessible. The width of the transition front is also a quantity of interest as it gives an indication of the stationary to travelling CFI ratio [27]. Thus, a preliminary picture of the transition evolution for the flow case investigated here is given from an oil flow visualization experiment.

Quantitative velocity measurements mainly relied on hot-wire scans (e.g. [97, 19, 51, 135]). The benefits and drawbacks of this technique have been described in section 2.1. Within the research presented in this chapter, the evolution of stationary CFVs is captured by detailed hot-wire scans. Moreover, the velocity field within a full, although rather limited, volume is captured by tomographic-PIV retrieving a complete picture of the flow evolution in transitional CFI boundary layers. The velocity-derivative tensorial field is also captured. This is crucial for secondary instability calculations [35]. Finally, the main contribution of having spatially correlated measurements will be evident in the next chapter where the investigation of the unsteady flow field is presented.

## 4.2. EXPERIMENTAL SETUP

### 4.2.1. FLOW CONDITIONS

The flow field investigated in this chapter is the boundary layer developing on the 66018M3J wing placed at the incidence of 3 degrees and exposed to a free stream flow of  $U_\infty = 25.6 \text{ m s}^{-1}$  (free stream Reynolds number of  $Re = 2.17 \cdot 10^6$ ). The critical stationary mode with  $\lambda_z = 9 \text{ mm}$  was forced with leading edge roughness elements as described in § 2.4.

### 4.2.2. FLOW VISUALISATION

Flow visualisation was performed by application of a fluorescent mineral oil on the model surface. The applied mixture consists of paraffin oil (*Shell Ondina*), petroleum and fluorescent mineral pigments in customised ratios according to the tested velocity regime and flow temperature. In this experiment, the mixture was carefully applied on the model surface in a homogeneous manner, taking care to omit the leading edge region in order not to influence the inception of cross-flow instability. Illumination was provided by an ultraviolet (UV) lamp and a digital camera equipped with UV filters was used for imaging.

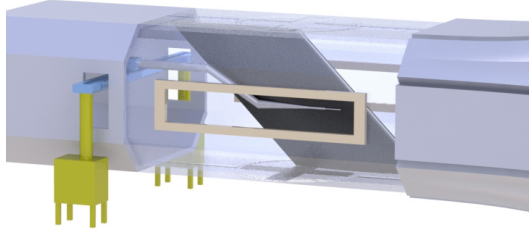


Figure 4.1: Schematic of the hot-wires setup. The flow comes from right. The automated traverse system, the hot wire sting and the wing are represented as installed in the LTT facility. The testing chamber is drawn semi-transparent for better visualisation.

### 4.2.3. HOT-WIRE ANEMOMETRY

Hot-wire measurements were performed with a single-wire boundary layer probe (*Dantec Dynamics P15*). A second single-wire probe (*Dantec Dynamics P11*) performed simultaneous free-stream measurements approximately 20cm away from the boundary-layer probe. Both the probes were operated by a *TSI IFA-300* constant temperature bridge with automatic overheat ratio adjustment.

The wind tunnel is temperature regulated via a heat exchanger, resulting to minimal temperature drifts over long running periods. Nevertheless, flow temperature and pressure were continuously monitored and used to correct the calibrated hot-wires signal. The CTA bridge signals were sampled at a frequency of  $f_s = 50$  kHz and filtered using an analog lowpass filter at a cutoff frequency of  $f_{co} = 20$  kHz before amplification. Time series of 4 seconds were recorded at every probe position to ensure statistical convergence.

A three degrees-of-freedom automated traverse system was installed in the wind tunnel diffuser as shown in figure 4.1. The traverse system is capable of step resolution of  $2.5 \mu\text{m}$  in all three directions. Hot-wires scans of the developing boundary layer were performed at several stations along the  $x$  direction. Special care was taken to account for the slight inclination of the developing stationary CF waves with respect to the free stream direction.

Each hot-wire scan consisted of a sequence of point measurements on the local  $y_t$ - $z$  plane located at constant chordwise stations. The boundary-layer scans in the local wall-normal direction ( $y_t$ ) consisted of 50 equally spaced points in order to fully resolve the development of the wall shear layer. The spacing of the measurement points was selected so as to cover the extent of the boundary layer from near the wall (0.1 times the local external velocity) to the local free stream. Due to the streamwise growth of the boundary layer, the achieved wall-normal resolution varied between  $40 \mu\text{m}$  and  $132 \mu\text{m}$ . In the spanwise direction ( $z$ ) 64 equally spaced boundary layer traverses were conducted for a total of 3200 measurement points per  $x$  station. The spanwise traverse was  $625 \mu\text{m}$  yielding a total resolved spanwise range of 40 mm. The measured range enabled the resolution of three full CF vortices forced at 9 mm wavelength at all the chord stations.

For the entirety of this study, the hot-wire probe was aligned in the global reference

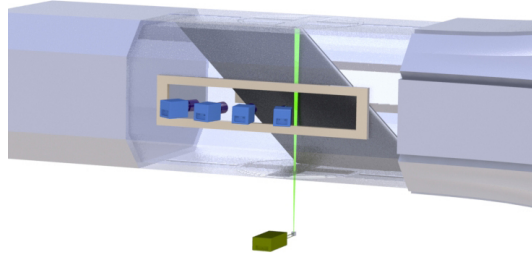


Figure 4.2: Schematic of the tomo-PIV setup. The flow comes from right. The four cameras (outside the tunnel looking through the optical window), the laser head (beneath the testing chamber), the laser light (entering vertically in the testing chamber) and the wing are represented as installed in the LTT facility. The testing chamber is drawn semi-transparent for better visualisation.

system. As such, it was mainly measuring the Euclidean sum of velocity components in the  $X$ - $Y$  plane:  $|V^{HWA}| = (U^2 + V^2)^{\frac{1}{2}}$ . The hot-wire probes were calibrated in situ every 24 hours. The maximum error in the sensor calibration is estimated to be lower than 4%.

#### 4.2.4. TOMOGRAPHIC PIV

Tomographic PIV [29] was selected to measure the instantaneous distribution of the velocity vector and the velocity gradient tensor in a three-dimensional domain of interest. The flow was seeded homogeneously by water-glycol droplets of average diameter of  $1\mu\text{m}$ . The droplets were produced with a *SAFEX* fog generator with seeding inlet downstream of the test section, which minimizes disturbances. Illumination was provided by a *Quantel Evergreen* Nd:YAG dual-cavity laser (200 mJ pulse energy). The laser light was introduced from a transparent port in the bottom wall of the test section. Light sheet optics were used to shape the beam into a sheet 50 mm wide and 4 mm thick along the wall-normal direction. The imaging system comprised of four *LaVision Imager LX* CCD cameras (16 Mpixels, 12 bits, pixel size  $7.4\mu\text{m}$ ). The cameras were equipped with 200 mm focal length Nikon Micro-Nikkor objectives. The numerical aperture was set to  $f_{\#} = 8$  to obtain focused particle images across the full depth of the measurement domain. A lens-tilt mechanism allowed to comply with the Scheimpflug condition with a plane of focus corresponding to the median adapters. The cameras were installed outside the wind tunnel test section with a tomographic aperture that subtended an arc of 60 degrees. The setup is presented in the schematic of figure 4.2.

The active area of the cameras sensors was reduced to  $1700 \times 1700 \text{ px}^2$ , due to illumination constraints. The cameras were placed at distance of approximately 1 m from the surface of the model and the imaged volume was  $50 \times 50 \times 4 \text{ mm}^3$ , centred at  $x/c = 0.45$ . The magnification factor for this experiment was 0.25. The time separation between laser pulses was set to  $22 \mu\text{s}$ , returning a particle image displacement of 20 pixels (0.6 mm) in the flow outside of the boundary layer. The large displacement ensures a relatively high dynamic range of the velocity measurement [1], which is suited to enable the measurement of the weak velocity components in planes orthogonal to the streamwise direction.

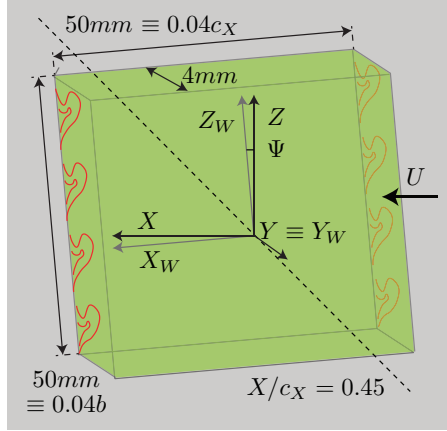


Figure 4.3: Schematic of the imaged tomo-PIV volume and of the reference system  $(X_W Y_W Z_W)$  aligned with the stationary CF vortices (indicated in red). The dashed line is parallel to the leading edge direction and shows the position of the volume, centred at  $x/c = 0.45$ . The flow comes from right. The grey background represents the model surface.

However, it compromises the measurement of the highly sheared regions close to the wall due to the distortion of the particle image pattern beyond 0.5 pixels/pixel [105], as it will be discussed in later sections. A dual layer target was used for the calibration of the tomographic imaging system. The obtained object-to-image space mapping function was corrected using the volume self-calibration procedure [137] available in the *LaVision* software *DaVis 8* thus reducing the calibration uncertainty to less than 0.1 px.

Image acquisition, preprocessing, volume reconstruction and frame correlation were performed with *LaVision Davis 8*. The raw images were preprocessed reducing the background intensity caused by laser light reflection from the wing surface. Volume reconstruction and correlation were performed in a dedicated coordinate system, aligned with the stationary cross-flow vortices  $(X_W Y_W Z_W)$ . This system is presented in figure 4.3 along with the dimensions of the volume. It must be noted that a mild natural inclination of the stationary vortices with respect to the  $X$  direction is expected. An estimation of this inclination angle ( $\Psi$ ) is presented in § 2.6 and § 4.3.1. Due to the small curvature of the wing at the station centred with the tomo-PIV volume (compare with the wing section presented in figure 2.2), the  $Y_W$  axis (normal to the chord plane) is practically aligned with the local wall-normal direction ( $y_t|_{0.45c_X} \equiv Y_W$ ). For the remainder of this study these two directions will be considered identical.

For the volume reconstruction, the *CSMART* algorithm was used. The spatial cross-correlation was performed in the Fourier domain and with final interrogation volume size of  $2.6 \times 0.67 \times 0.67 \text{ mm}^3$  in the  $X_W$ ,  $Z_W$  and  $Y_W$  directions respectively. The relative overlap of adjacent interrogation volumes was set to 75% for an accurate estimate of the velocity fields. The final vector field was interpolated on a grid with a uniform spacing of 0.15 mm in all three directions. This length, corresponding to the final vector spacing along  $Y_W$  and  $Z_W$ , implies interpolation only along  $X_W$ . After volume reconstruction and

correlation the final resolved domain narrowed to  $35 \times 35 \times 3\text{mm}^3$ .

The measurements comprise 500 sets of image pairs acquired at a rate of 0.5 Hz. The uncertainty associated with the instantaneous velocity measurements is estimated to be 0.3 voxels, following Lynch & Scarano [74], therefore the relative random error, considering the free stream displacement of 20 voxels, is approximately 1.5%. The uncertainty on the mean velocity will be dominated by the ensemble size. In fact, given the sampling rate for this measurement and the characteristic frequencies of the expected unsteady flow phenomena, the instantaneous fields are not correlated in time. The relative error of the time-average field ( $\varepsilon_{\bar{u}}$ ) is equal to the amplitude of the flow root mean square (r.m.s.) fluctuations (estimated to be below 10%) divided by the square root of the ensemble size:  $\varepsilon_{\bar{u}} < 0.1/\sqrt{500} \approx 0.45\%$ . The relative error of the r.m.s. fluctuation field ( $\varepsilon_{u'}$ ) is dominated by the r.m.s. bias due to random errors that will not average out, therefore an estimation of this error leads to:  $\varepsilon_{u'} = 1.5\%$ .

### 4.3. RESULTS AND DISCUSSION

The evolution of the primary stationary mode is described by means of flow visualisation, hot-wire boundary layer scans and tomo-PIV measurements. The results are presented in the following three subsections respectively.

#### 4.3.1. LAMINAR-TO-TURBULENT TRANSITION

A detail centred on the wing mid-chord station of the flow visualisation test is presented in figure 4.4. Stationary mode critical forcing at  $\lambda_z^F = 9\text{mm}$  has been applied. The flow direction is from right to left as indicated. The boundary-layer transition from laminar to turbulent is evident from the change in surface oil concentration. The characteristic transition front with a jagged pattern of turbulent wedges pertinent to this type of boundary layers is clearly visible [104]. Despite the spanwise uniform forcing via the discrete roughness elements, the transition front is highly modulated. As such, the location of transition can only be estimated based on a spanwise average simplification. It is estimated to occur at approximately  $x/c = 0.50$ . Notwithstanding the care in applying the oil film on the surface, this estimate has to be considered just as an indication of the transition location because the layer of oil can be the source of slight alterations in the transition process.

The presence of the PIV seeding particles in the flow did not appear to result in any changes in the transition pattern. A comparison between the tomo-PIV and the HWA velocity fields, presented later in § 4.3.4, further confirms this.

A second prominent feature revealed by the oil flow test are the streaks caused by the stationary CF modes. These are locked to the 9mm wavelength of the discrete roughness elements. Compared to cases of non-forced boundary layers, these streaks appear more uniform in both their streamwise onset and spanwise spacing [97, 51, 113]. This behaviour is indicative of the strong conditioning of CF vortices by initial amplitude effects, related further to receptivity processes near the leading edge.

Two reference systems are also shown in figure 4.4. These are the un-swept reference system ( $XYZ$ ) and the stationary cross-flow mode reference system ( $X_W Y_W Z_W$ ). In order to move from one system of coordinates to the other, a rotation of  $\Psi = 5^\circ$  about the coincident  $Y \equiv Y_W$  axes is required (as discussed in § 4.2.4). The magnitude of the

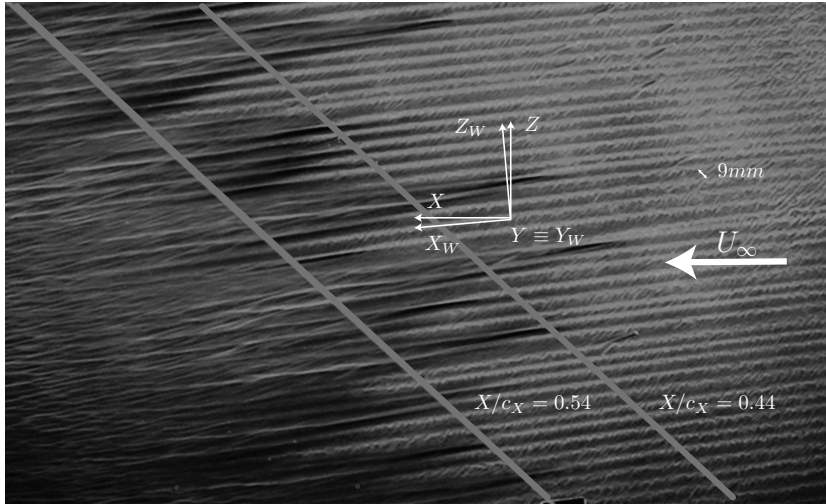


Figure 4.4: Fluorescent oil flow visualisation of the transition region. The flow comes from right. The two grey lines indicate two streamwise stations. The  $X_W Y_W Z_W$  system is rotated of  $\Psi = 5^\circ$  about the  $Y_W \equiv Y$  axis with respect to the  $XYZ$  system. A reference line of 9 mm length is plotted in the  $z$  direction.

angle  $\Psi$  is, within few degrees, in agreement with the predictions of linear stability theory (not shown). This angle is not constant along the chord and approximately inferred by this technique. Nevertheless, the value of  $5^\circ$  for the region centred at  $x/c = 0.45$  is an acceptable estimate and will be used for the coordinate system of the tomo-PIV experiment.

#### 4.3.2. STREAMWISE EVOLUTION

The hot-wire probe was aligned so as to measure mainly the Euclidean sum of the  $U$  and  $V$  velocity components (i.e. aligned with  $Z$ ). The automated traverse was programmed to shift the probe in the local  $y_t$ - $z$  plane at the selected  $x/c$  stations. As shown in figure 4.4, the primary cross-flow waves are inclined with a small angle with respect to the free stream direction. This was taken into account for the hot wire scans in order to correctly follow the evolution of the individual CF modes both in the streamwise and spanwise areas of interest.

The most upstream station where hot-wire scans are performed is at  $x/c = 0.15$  while the most downstream is located in the fully turbulent region at  $x/c = 0.55$ . Contours of time-averaged velocity (denoted with the bar symbol), non-dimensionalised with the time-averaged local external velocity ( $|\bar{V}_e^{HWA}|$ ), for six streamwise stations are presented in figure 4.5. Velocity contours are presented as seen in the direction of the flow (i.e. as seen from upstream). The origin of the  $z$  coordinate has been changed to align the stationary waves at all the reported streamwise stations. Additionally, it must be stressed that the measurements were performed from the boundary-layer outer edge to the wall-normal location where the local velocity attained approximately 10% of the external velocity. However, the position of the wall is linearly extrapolated from the measured velocity

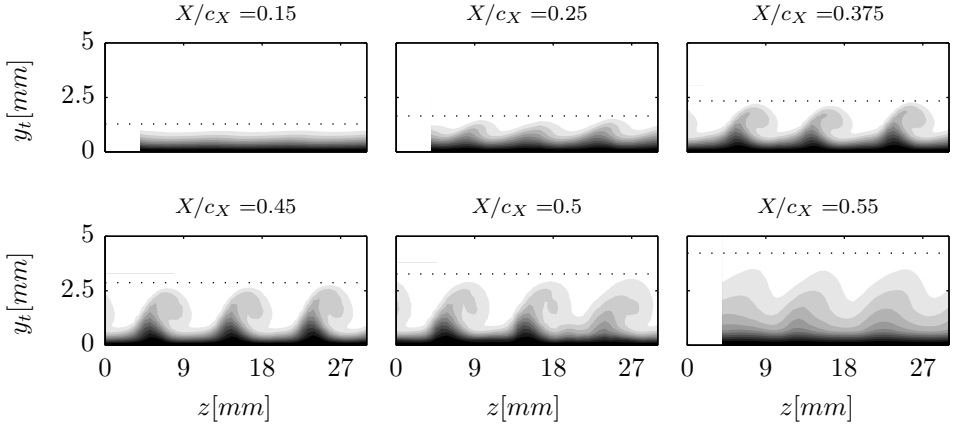


Figure 4.5: Contours of time-averaged velocity ( $|\bar{V}^{HWA}| = (\bar{U}^2 + \bar{V}^2)^{\frac{1}{2}}$ ) non-dimensionalised with the mean local external velocity ( $|\bar{V}_e^{HWA}|$ ) (10 levels from 0 to 1). The dotted lines show the boundary layer thickness averaged along  $z$  and based on the  $0.99|V_e^{HWA}|$  threshold ( $\delta_{99}^z$ ). The plots are stretched along the vertical direction for better visualisation and presented as seen from upstream.

profiles. This procedure has been performed for all the velocity profiles constituting the contours. It should be mentioned here that application of this strategy is common practice in studies on laminar boundary layers, whereas in intermittent or turbulent boundary layers, is expected to introduce an error in the estimation of the wall position, due to the wall non-linear velocity profiles. This is the case for the measured stations downstream of  $x/c = 0.50$  in this study. Despite this, small errors in the position of the model surface have a minimal effect for the performed analyses and conclusions of this investigation.

In the figure, the boundary-layer thickness averaged along  $z$  and based on the  $0.99|\bar{V}_e^{HWA}|$  threshold is also plotted with a black dotted line to infer the growth of the boundary layer and the relative size of the stationary vortices. This quantity will be henceforth defined as  $\delta_{99}^z$ . At  $x/c = 0.15$ , the primary vortices are barely visible and only a weak modulation of the outer edge of the boundary layer can be seen. For the remainder of this study, station  $x/c = 0.15$  will be considered as the first onset of the stationary instability. Already at  $x/c = 0.25$ , the development of strong spanwise modulation becomes clearly evident. The standing CF modes appear as a sequence of corotating vortices rigorously spaced at 9 mm from each other. The effect of the CF standing vortices is a strong modification of the base flow within the boundary layer. Low momentum flow is extracted from the region close to the wall and ejected to the outer edge and *vice versa*.

The stationary CF modes evolve in the streamwise direction both by increasing amplitude and changing topological features. From  $x/c = 0.25$  to  $x/c = 0.45$  the characteristic *lobe* structure is formed. The vortices tend to roll about their axis and eventually collapse further downstream at  $x/c = 0.50$ . Of interest is the furthest downstream measured station at  $x/c = 0.55$  where the flow has fully transitioned to turbulence. At this location strong spanwise modulation of the turbulent boundary layer is still evident indicating the

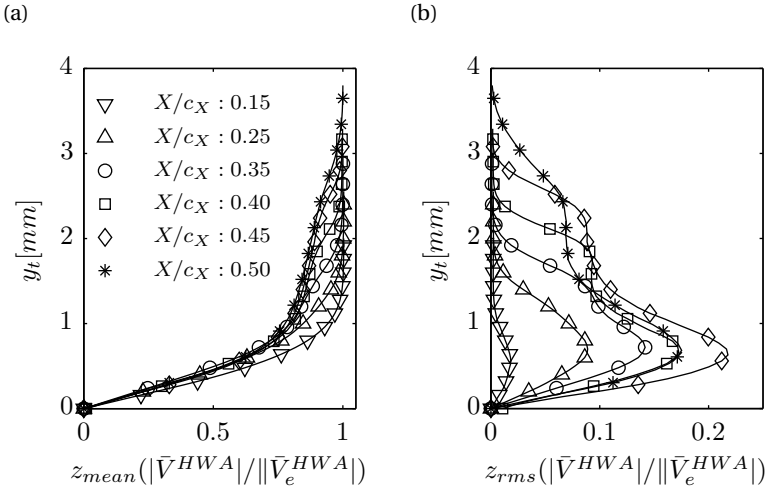


Figure 4.6: Spanwise (a) mean (base flow) and (b) standard deviation (mode shape) of the time averaged velocity profiles at several chord stations non-dimensionalised with the local external velocity. For clarity, only one over four measured values is reported with a marker symbol. The profiles presented pertain to three full stationary vortices.

persevering nature of the mean flow distortion due to CF vortices in the early turbulent boundary layer [34]. This is further supported by the streaky structures captured by the surface oil visualisation downstream of the transition front seen in figure 4.4.

Spanwise average of the mean velocity profiles and the respective standard deviation can be extracted and used to track the streamwise evolution of the standing CF mode. To be noted, the velocity fields pertaining to three full stationary waves have been used for this analysis at all the chord stations. Moreover, it should be noted that the forced stationary 9 mm mode, as well as other modes that might eventually non-linearly amplify are ensemble-averaged by this analysis. The presence of other modes can be due to non-linear development of higher harmonics of the fundamental mode. In order to carefully assess the occurrence and strength of these modes, extended spanwise measurements and spectral analysis are necessary. The limited spatial range of the spanwise HWA traverse did not allow this measurement. Despite this, inspection of figure 4.5 reveals the effectiveness of the roughness forcing in locking the stationary disturbances to a single fundamental mode (9 mm), even at the more downstream stations. This observation establishes that the following analysis of the primary instability mainly refers to the fundamental forced mode. This analysis is presented for several streamwise stations in figure 4.6. The results closely follow the ones reported by Reibert *et al.* [97], Radeztsky *et al.* [94], Haynes & Reed [39] and White & Saric [135].

The spanwise average velocity profiles of figure 4.6a reveal the evolution along the streamwise direction of the boundary layer through the stages of primary instability growth and saturation. Between the first two stations ( $0.15 \leq x/c \leq 0.25$ ) the growth of approximately self-similar laminar boundary layer occurred while the profiles from

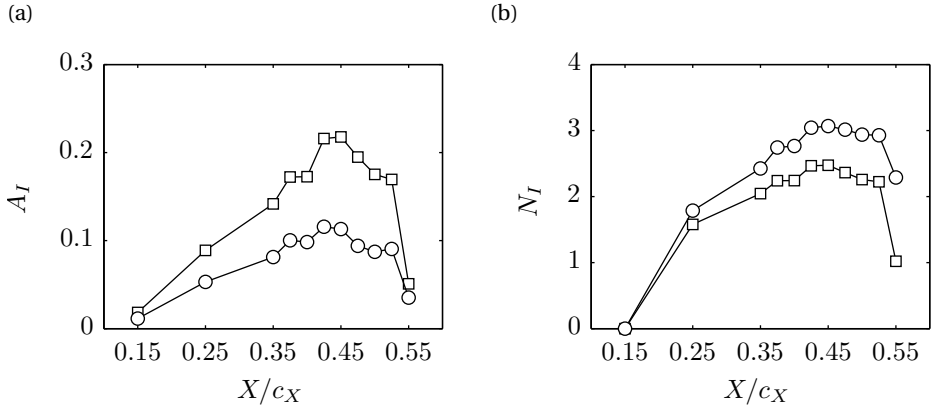


Figure 4.7: (a) Non-dimensional amplitudes and (b) N-factors based on the maximum metric ( $A_I^{max}$ ;  $\square$ ) and on the wall-normal integral metric ( $A_I^{int}$ ;  $\circ$ ) of the mode shape profiles of figure 4.6b, computed using equations 2.21, 2.22 and 2.23. The analysis refers to three full stationary vortices.

$x/c = 0.35$  show a different curvature with a point of inflection. The most downstream profile presented, at  $x/c = 0.50$ , reveals a less distorted boundary layer.

The mode shape profiles of figure 4.6b provide further insight into the evolution of the developing CF modes. Again for the first two stations a growth of the primary disturbance is observed, while between  $x/c = 0.25$  and  $x/c = 0.35$  a change occurs for these profiles as well. This relates not only with an increase in amplitude but also with changes in the shape of the mode, most notably the development of two local maxima. The second maximum of the curve at station  $x/c = 0.35$  is related to the increased size of the stationary vortices and the eventual rolling over of the characteristic *lobe* structure. This behaviour has been related to the onset of secondary instability modes [39, 135]. These features are further enhanced in the more downstream stations until  $x/c = 0.45$  where a peak value of  $0.21|\bar{V}_e^{HWA}|$  is attained by the mode shape profile. This is identified as a typical saturation value reported by Downs & White [27] based on experiments performed at similar conditions (see figure 19 of their article). Moving further in the developing transitional boundary layer ( $x/c = 0.50$ ) both maxima are reduced, indicating dampening of the primary mode due to turbulent diffusion.

The streamwise growth of the CF mode can be extracted from figure 4.6b using the metrics expressed in section 2.7. Results are presented in form of absolute amplitudes ( $A_I$ ) in figure 4.7a and in form of N-factors ( $N_I$ ) in figure 4.7b. For the experimental results of this study the onset of primary instability is assumed to be the first measured station,  $x_0 = 0.15 \cdot c$ . The growth of the primary CF mode is monotonic from the first observation station until approximately  $x/c = 0.45$ . Further downstream a notable reduction of both the local maxima and the integral of the mode shape profile is evident. This indicates primary-mode amplitude saturation. Saturation has been typically associated with the rise of non-linear interactions between the primary mode and secondary instability [77, 39, 135]. At the more downstream stations, the forced  $\lambda_z^F = 9$  mm stationary waves start decaying

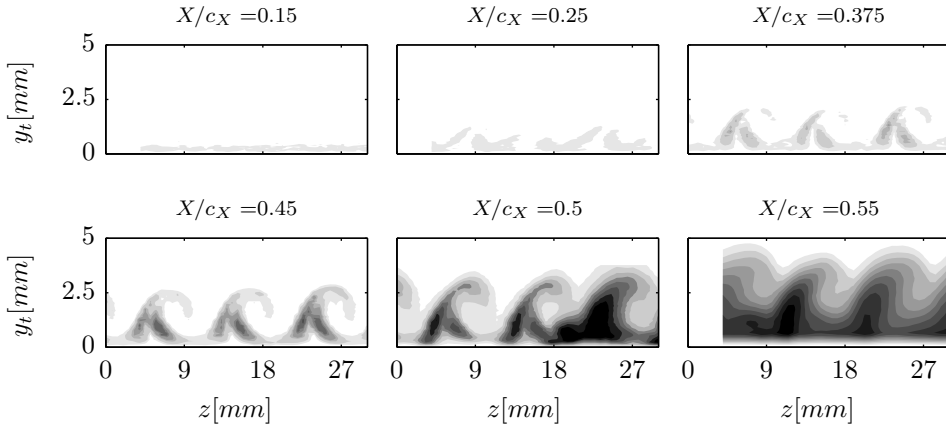


Figure 4.8: Contours of velocity standard deviation non-dimensionalised with the time-averaged local external velocity ( $|\tilde{V}_e^{HWA}|$ ) (10 levels from 0 to 0.1). The contours are stretched along the vertical direction for clarity and presented as seen from upstream.

rapidly, with a steep reduction at  $x/c = 0.55$  where a fully turbulent boundary layer has developed.

Additional to the mean flow distortion due to the primary CF mode, the developing boundary layer exhibits an intricate topology of velocity fluctuations. The standard deviation of the velocity fluctuations is computed and non-dimensionalised with the mean local external velocity. Contours of velocity fluctuations are shown in figure 4.8 for several streamwise stations. Fluctuations observed at  $x/c = 0.15$  are mainly associated with the existence of weak travelling CF modes [19]. The relatively low free stream turbulence of the wind tunnel facility and the use of discrete roughness elements dictate the dominance of stationary CF instabilities. Nonetheless, the appearance of travelling modes cannot be avoided in an experimental framework [19, 40, 27].

Further downstream, at stations  $x/c = 0.25$ ,  $x/c = 0.375$  and  $x/c = 0.45$  the spatial topology of velocity fluctuations is strongly influenced by the mean flow distortion due to the primary CF mode (compare with figure 4.5). The saturation of the primary CF mode downstream of station  $x/c = 0.45$  signifies the onset of rapid growth of secondary instability. Similar observations have been established in previous studies (e.g. [40, 77, 51, 39, 129, 135]). At wing mid-chord the flow is undergoing turbulent breakdown. The contours of the r.m.s. fields show the rightmost wave experiencing a much higher level of fluctuations. Furthermore, the fluctuations maximum at  $z = 20\text{mm}$  near the wall is indication of the apex of a turbulent wedge [135]. At the most downstream measured station ( $x/c = 0.55$ ) a fully turbulent boundary layer sets in and redistribution of the fluctuating energy and related dampening of the coherent structures are taking place.

In the region of stationary vortices saturation, the fluctuations are mainly observed in three distinct areas within the spatial domain occupied by a single CF wave (figure 4.9a). These areas are associated with unsteady instabilities of a distinct nature [40, 77, 129, 135]. One area of high fluctuation intensity can be identified as overlapping to the outer side of

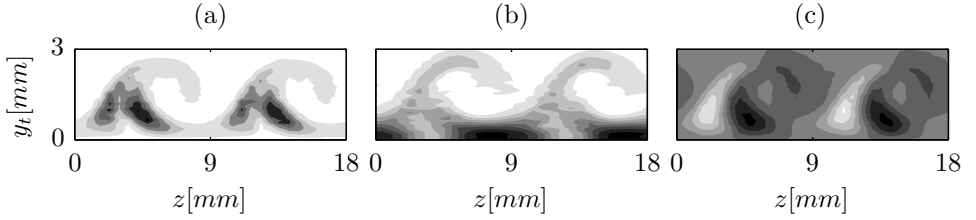


Figure 4.9: (a) Contours of velocity standard deviation (10 levels from 0 to 0.1), (b) gradient of time-averaged velocity in wall-normal direction (10 levels from -1.7 to 16.6) and (c) in spanwise direction (10 levels from -3.6 to 2.7). The velocity fields, sampled at  $x/c = 0.45$ , are non-dimensionalised with the time-averaged local external velocity ( $|\bar{V}_e^{HWA}|$ ), while the lengths with  $\lambda_z^E$ . The contours are stretched along the vertical direction for clarity and presented as seen from upstream.

the upwelling region of the CF vortex. This area is coincident with the local minimum of the spanwise gradient of the mean velocity ( $\partial|\bar{V}^{HWA}|/\partial z$ ) as presented in figure 4.9c. Malik *et al.* [77] classified these fluctuations as  $z$ -mode secondary instability. These are defined as *type-I* modes in this paper, following Wassermann & Kloker [129, 130]. A second area of pronounced fluctuating velocity is evident on the top of the CF vortices. Inspecting the velocity shears (figure 4.9b), this area overlaps with pronounced velocity wall-normal gradients ( $\partial|\bar{V}^{HWA}|/\partial y$ ). Respectively, this can be identified as the  $y$ -mode of the secondary instability [77], here defined as *type-II* mode [129]. A third area of strong fluctuations is located at the inner side of the upwelling low momentum air where the  $z$  velocity gradients show a local maxima. The disturbances captured in this region are related to the interaction between travelling and stationary primary CF vortices and are named *type-III* mode [45, 129, 8]. Finally, velocity fluctuations are also evident between the discrete CF vortices in the near-wall region. This area is characterised by the downwelling motion of high momentum flow due to the mean flow distortion induced by the primary CF mode. This results in the formation of a locally thin boundary layer with extremely high wall-normal shear as evident in figure 4.9b.

### 4.3.3. COMPARISON BETWEEN COMPUTED AND MEASURED BOUNDARY LAYERS

As already described in section 2.6, the LST analysis is based on a laminar boundary layer mean flow, computed numerically using the pressure distribution of figure 3.3. At this point a comparison between the computed velocity profiles and the HWA measurements can be performed. In figure 4.10, this is done for the three most upstream measured stations. The considered HWA profiles are the  $z$ -mean of the time-averaged measured planes in order to average the effect of the developing stationary vortices. The computed boundary layer has a prescribed sweep angle of  $45^\circ$  while the computed velocity components are transformed to match the ones seen by the hot-wire probe.

The velocity profiles appear similar for the first stations with a larger discrepancy at station  $x/c = 0.35$  where the measured velocity field is evidently distorted by the stationary CF vortices (see also figure 4.6a). Instead the satisfactory agreement at  $x/c = 0.15$  indicates that the curvature of the model, not modelled in the boundary layer solver, is not very

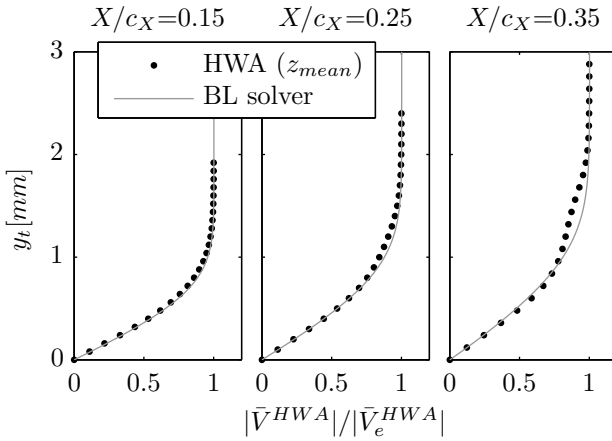


Figure 4.10: Comparison between the computed boundary layer based on experimental pressure distribution (BL solver) and the hot-wire measurements (averaged along  $z$ ), at the most upstream stations. For clarity, only one out of two measured values is reported with a marker symbol.

relevant at this station. This comparison further corroborates the estimations of the LST for the most upstream regions of the studied flow.

#### 4.3.4. SPATIAL ORGANISATION

The analysis of the primary boundary layer instability is further expanded to the results of the tomo-PIV experiment. As mentioned in section 4.2, the measured velocity field is aligned with the coordinate system of the primary stationary vortices ( $X_W Y_W Z_W \equiv X_W y_t Z_W$ ). The time-averaged flow field of the velocity component along the stationary vortices axes, non-dimensionalised with the time-averaged external velocity, is presented in figure 4.11. Three  $y_t$ - $Z_W$  planes, at the  $X_W$  locations corresponding to the most upstream end, to the most downstream end and to the centre of the measured domain, are shown with 10 contour levels. Additionally, two isosurfaces pertaining to levels of velocity of  $\bar{U}_W/\bar{U}_{We} = 0.9$  and  $\bar{U}_W/\bar{U}_{We} = 0.8$  are also plotted to facilitate the visualisation of the three-dimensional evolution of the vortical structures. The point at  $X_W = 0$  is at  $x/c = 0.45$  while the  $Z_W = 0$  is at  $Z = 0$  (wing mid-span). The position of the wall is linearly extrapolated from the measured velocity profiles. Almost five stationary waves are captured by this measurement. Their spacing is relatively constant, corresponding approximately to a wavelength along  $Z_W$  of 6.9 mm. A wavelength of 6.9 mm in the  $X_W Y_W Z_W$  coordinate system corresponds to 9 mm in the  $xyz$  domain, consistent with the spacing of the discrete roughness elements at the leading edge. A small discrepancy is observed regarding the position of the rightmost wave at approximately  $Z_W = 17$  mm. This could be attributed to non-uniformities of the discrete roughness elements or to occasional debris depositing on the model surface, slightly displacing this vortex.

The unprecedented application of tomo-PIV for the measurement of transitional swept-wing boundary layers necessitates the rigorous comparison of the measurements against established techniques such as HWA. This requires some care given the different

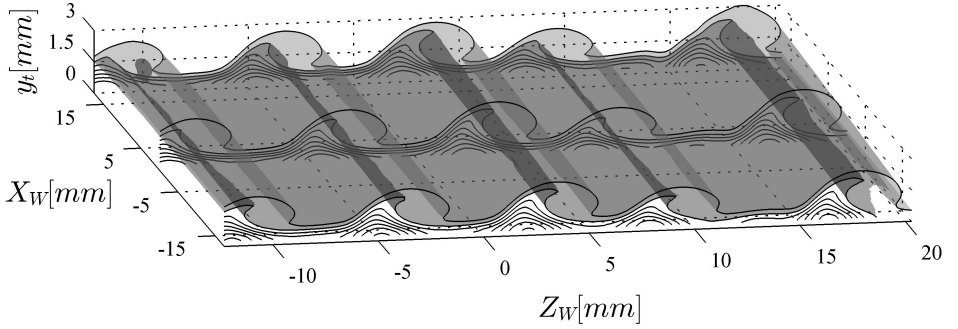


Figure 4.11: Time-averaged velocity magnitude along the stationary cross-flow axis measured with tomo-PIV. The local origin at  $X_W = Z_W = 0$  coincides with  $x/c = 0.45$  and  $Z = 0$ . The semi-transparent isosurfaces attain to values of  $\bar{U}_W/\bar{U}_{We} = 0.9$  and  $\bar{U}_W/\bar{U}_{We} = 0.8$ . The flow is presented as seen from upstream.

reference systems and velocity components measured by the two techniques. Towards this goal, a plane aligned with  $y_t$ - $z$  is extracted at  $x/c = 0.45$  from the volume presented in figure 4.11 thus coinciding with the hot-wire measured plane. The velocity components are then transformed such to match the signal measured by the hot-wire ( $|V^{HWA}| = (U^2 + V^2)^{\frac{1}{2}}$ ). The result of such comparison is presented in figure 4.12 for the time-averaged velocity. The values of the velocities are non-dimensionalised with the time-averaged local external velocity while the wall position is linearly extrapolated from the measured data. The agreement between the two measurement techniques is striking.

At the upper-left corner of the two contours three (+) symbols are plotted to show the spatial  $y_t$ - $z$  resolution of the two experiments<sup>1</sup>. In spite of the higher wall-normal resolution of the hot-wire measurements compared to tomo-PIV, the latter appears to be capturing the strong shears due to the modulated flow with the same accuracy. A further comparison of the two velocity fields is presented in terms of velocity profiles in figure 4.12c. The velocity distribution across the wall-normal direction, at the two spanwise stations denoted with the same markers on figure 4.12a and 4.12b and pertaining respectively to regions of reduced and strong wall-normal shears, is measured by the two techniques with good agreement, showing a maximum discrepancy of  $0.058|\bar{V}_e^{HWA}|$ .

It now becomes important to further establish a comparison between the two experiments in measuring the statistical quantities of the unsteady field. This comparison is presented in figure 4.13 where the r.m.s. of the velocity fluctuations, non-dimensionalised with the external velocity, is shown. A notable feature of the fluctuation field captured by tomo-PIV is the elevated level measured in the free stream. This effect is attributed to the inherent limits associated with PIV in general and tomo-PIV specifically. The background r.m.s. level has an average value of  $0.015\bar{V}_e^{HWA}$  that corresponds to the error estimated in section 4.2.4.

Despite the elevated fluctuation levels in the free stream, the tomo-PIV measurement captures the local maxima associated with *type-I*, *type-II* and *type-III* instabilities in both magnitude and location. Both inner and outer upwelling regions as well as the top

<sup>1</sup>To be noted that the contours are stretched along the  $y_t$  direction.

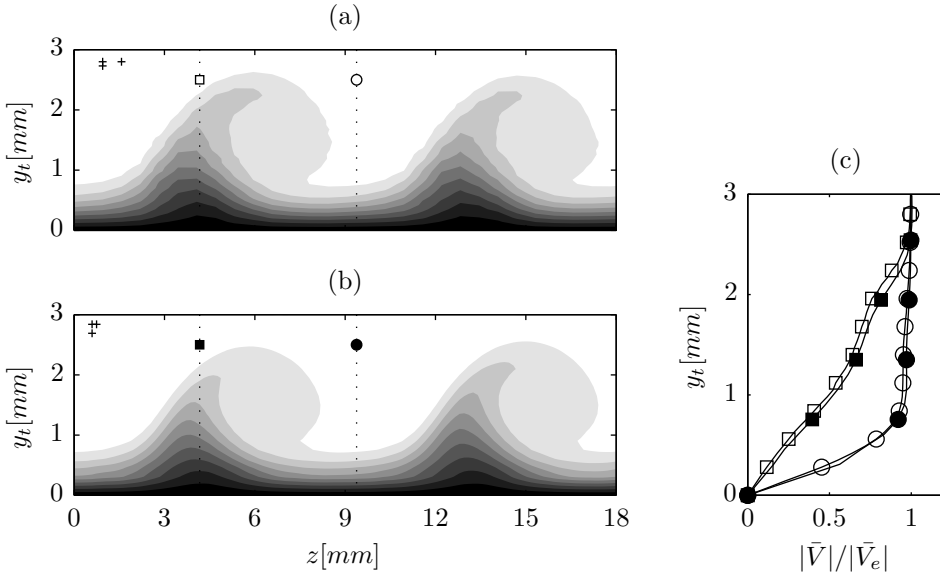


Figure 4.12: Contours of time-averaged velocity magnitude, non-dimensionalised with the mean local external velocity (10 levels from 0 to  $|\bar{V}_e^{HWA}|$ ) from (a) HWA and (b) tomo-PIV. The spatial resolution along  $z$  and  $y_t$  of the two measurements is presented with the (+) symbols at the upper-left corner of the contours. (c) Velocity profiles at the stations indicated with identical symbols on contours (a) and (b). For clarity only one out of four measured values is reported with a marker symbol.

region are in relative agreement to the hot-wire measurements. Unfortunately, the same cannot be said for the near-wall portion of the downwelling region (centred at  $z \approx 0, 9, 18$  mm in figure 4.13). At this region, the inherent downwelling action of the primary CF instability results in elevated shears near the wall, as showed in figure 4.9b. Such high shears are beyond the measurable threshold of 0.5 px/px reported by Scarano [105] for PIV measurements. It is believed that the pronounced errors are not deemed disruptive to the conclusions of this study because they appear in a region not associated with a particular instability mode. For the remainder of the analysis of the unsteady flow features, the near-wall region of the tomo-PIV fields ( $y_t < 0.95$  mm indicated with the dotted line on the contour) will not be taken into account. The r.m.s. maximum of the inner upwelling region, pertaining to the *type-III* mode, appears also partially affected by the described measurement error. This is again disregarded to be influencing the analysis of chapter 5 where POD of the tomo-PIV vector fields is presented. POD allows the identification of spatially coherent structures thus filtering out most of the measurement noise [96].

A slice at  $x/c = 0.45$  of the volume shown in figure 4.11 is presented in figure 4.14 for all the three velocity components. Additionally, the velocity components are presented in the primary CF vortices coordinate system ( $U_W V_W W_W$ ). The  $\bar{U}_W$  component dominates over the two in-plane components ( $\bar{V}_W$  and  $\bar{W}_W$ ) by two orders of magnitude. The relative magnitude of the three velocity components reveals the effectiveness of the in-plane components in modifying the mean boundary layer and thus the out-of-plane velocity.

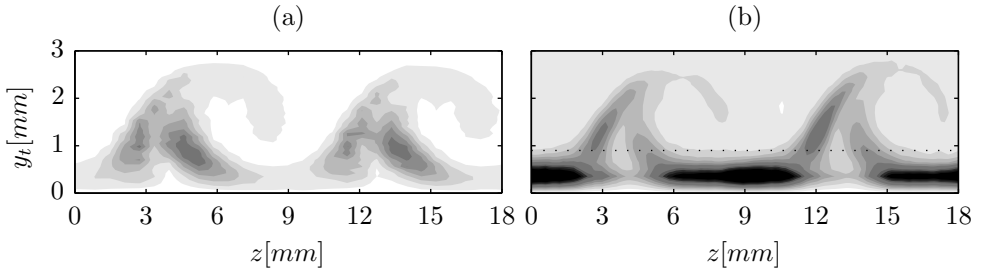


Figure 4.13: Contours of the velocity standard deviation, non-dimensionalised with the mean local external velocity (12 levels from 0 to  $0.12|\bar{V}_e^{HWA}|$ ) from (a) HWA and (b) tomo-PIV. The black dotted line at  $y_t = 0.95$  mm in the tomo-PIV contour indicates the region disregarded in the unsteady flow analysis of chapter 5.

The wall-normal velocity maxima at  $z = 5.0$  mm and  $14.0$  mm are responsible for the upwelling of the low momentum flow from the lower regions of the boundary layer. The minimum at  $z = 9$  mm is instead the effect of the downwelling motion with the consequent transport of higher momentum flow from the boundary layer outer edge towards the wing surface. At  $z = 2.8$  mm and  $z = 11.8$  mm a second local minimum of the wall-normal velocity is observed. This is located in a region where Malik *et al.* [76], Wassermann & Kloker [129] and Bonfigli & Kloker [8] reported a second stationary vortex, the effect of which was found to be not relevant in the transition scenario. The spanwise velocity ( $\bar{W}_W$ ) contour reveals the cross-flow velocity in the regions near the wall. The non-zero value of  $\bar{W}_W$  at the outer edge is instead dictated by the chosen coordinate system. As the stationary CF axis is not exactly aligned with the inviscid flow, what is plotted contains the projection of the streamwise velocity along the  $Z_W$  direction.

Summarising, although the primary waves are manifested as relatively weak spanwise perturbations of the  $V_W$  and  $W_W$  components, the change they induce in the axial velocity component is dramatically larger. Although this is a known feature of CF instability, the simultaneous characterisation of all three components of velocity was so far possible only in the realm of numerical simulations [129, 8]. Moreover, the full volumetric velocity derivatives tensorial field is also captured by the presented measurement. These fields are necessary to consider the usage of secondary LST theories to evaluate the boundary layer secondary stability [35].

A visualization of the three-dimensional streaklines around a single cross-flow vortex is presented in figure 4.15a, along the measured volume, and in figure 4.15b, projected in the  $Z_W - y_t$  plane. In the figures, it appears more evident what is the relative magnitude of the velocity components. The flow field is such that within the measured  $X_W$  domain, the particles of flow trapped in a stationary vortex, roughly travel a quarter of the vortex azimuthal extent. The pitch of the primary waves can hence be estimated to be such that a full revolution along the vortex axis is completed approximately in 144 mm (four times the 36 mm measured domain). The large disparity of magnitudes for the three velocity components, occurring in this flow, require a large dynamic range measurement to be accurately resolved. Though further increasing the time-separation between the light pulses, and hence the displacement of the particles, would lead to even larger (and

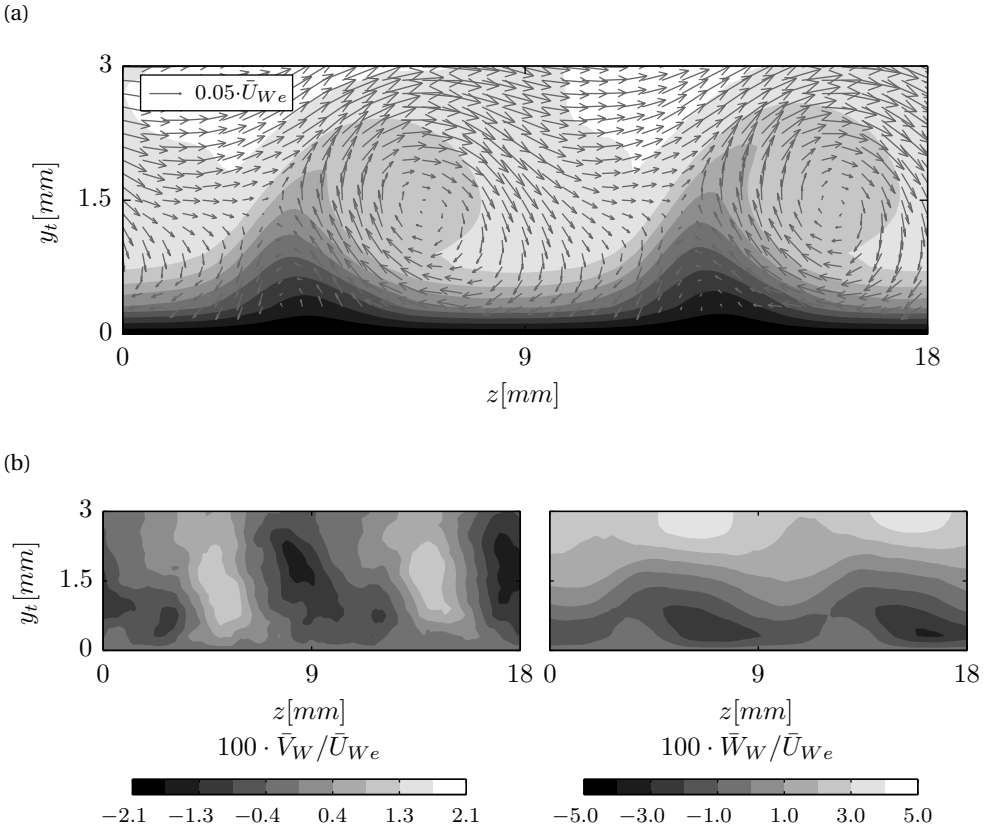


Figure 4.14: Non-dimensional time averaged velocity components sampled along a constant chordwise plane at  $x/c = 0.45$ . (a)  $\bar{U}_W / \bar{U}_{We}$  (10 levels, from 0 to 1) and vectors of  $(\bar{V}_W^2 + \bar{W}_W^2)^{1/2} / \bar{U}_{We}$  (reference vector at the upper-left corner). For clarity, only one every three vectors is plotted along  $z$ . (b)  $\bar{V}_W / \bar{U}_{We}$ ,  $\bar{W}_W / \bar{U}_{We}$ .

non-measurable) modulation of the velocity shears.

### 4.4. CONCLUSIONS

The developing stationary cross-flow instability was forced to a monochromatic arrangement by means of leading-edge surface roughness elements spaced, along the leading edge direction, at the wavelength of the most amplified mode (in agreement with many studies e.g. [97, 19, 135]).

The boundary layer was preliminarily inspected through a flow visualisation experiment making use of fluorescent oil. This visualisation showed the effectiveness of the leading edge forcing in locking the stationary modes wavelength and indicated the turbulent breakdown front. The latter showed the typical jagged pattern previously reported [104] with a spanwise averaged onset around the 50% of the chord.

The organisation of the stationary CF vortices was quantified by hot-wire measure-

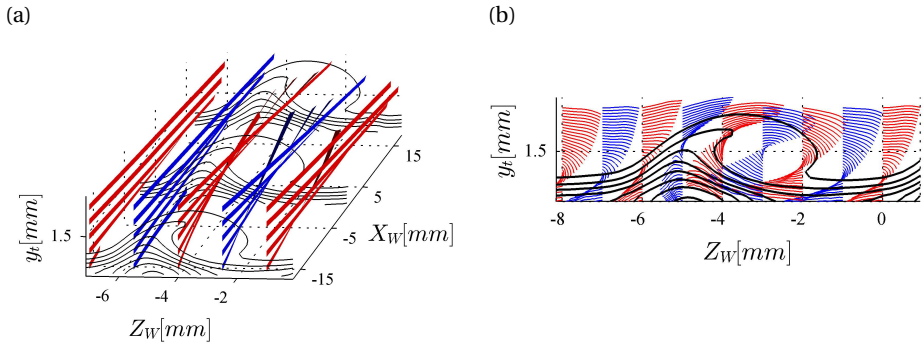


Figure 4.15: Three-dimensional streakribbons and streaklines along a single cross-flow vortex: (a) three-dimensional view; (b)  $Z_W - y_t$  plane. The fields are presented as seen from upstream.

ments at several constant-chord planes. The waves' streamwise evolution was evaluated in terms of amplitudes and N-factors of the mode shape profiles following the definitions by Haynes & Reed [39] and Downs & White [27]. The primary stationary mode grows downstream until reaching amplitude saturation after which it starts decaying (downstream of  $x/c = 0.45$ ). Finally, the hot-wire spanwise averaged profiles were compared to the boundary-layer solutions discussed in section 2.5. The measured and computed velocity distributions showed good agreement. More downstream, the mean flow deformation caused by the amplified vortices, not captured by the laminar solution, causes the measured profiles to deviate.

The primary stationary CF waves in near proximity of the saturation location have been measured for the first time with tomographic PIV. This flow diagnostic experimental technique allows the simultaneous measurement of volumetric, three-component velocity fields thus yielding a full picture of the flow field as, for instance, the pitch of the vortices. Compared to hot-wire scans, tomo-PIV time-averaged fields showed striking agreement whereas the statistical fluctuations suffered of higher noise from the 3D optical technique. Furthermore, the velocity-derivative tensorial field is also captured by the measurement allowing upcoming research where secondary stability theory tools were applied on this measured flow field [35].

In addition to these outcomes, the main advantage brought by this technique will be evident in the following chapter where the unsteady flow field is investigated. For that analysis, the region close to the wall, encompassing larger levels of measurement noise, was disregarded.

# 5

## SECONDARY CROSS-FLOW INSTABILITY

*This chapter is dedicated to the investigation of the unsteady secondary CFI modes. This is achieved by mean of hot-wire measurements and tomographic Particle Image Velocimetry. The hot-wire measurements revealed the spectral content of these modes. Furthermore, they allowed to analyse both the boundary layer regions influenced by and the chordwise evolution of the related flow structures. The flow topology of the structures was inspected by means of Proper Orthogonal Decomposition of the tomo-PIV flow fields. Taylor's hypothesis allowed to match the wavelength of the spatially resolved structures with the fluctuations frequencies measured with the hot-wire. The validity of the approach resides on previous literature but is experimentally confirmed by spatio-temporally resolved measurements making use of very high-speed PIV. Finally, a low-frequency meandering of the stationary vortices was observed in both the optical experiments.*

---

**J. Serpieri**, & M. Kotsonis, *Three-dimensional organisation of primary and secondary cross-flow instability*, *Journal of Fluid Mechanics*, **799**, 200–245 (2016)

**J. Serpieri** & M. Kotsonis, *Time-resolved PIV investigation of the secondary instability of cross-flow vortices*, 10<sup>th</sup> Symposium on Turbulence and Shear Flow Phenomena (TSFP 10), Chicago, USA, (2017)

## 5.1. INTRODUCTION

The strong shears caused by the primary CFVs, whether of steady or travelling type, can undergo secondary instability [129, 130]. Three different modes have been individuated: *type-I* and *type-II* are KH instabilities of the spanwise and wall-normal velocity shears [77, 135, 8] while the *type-III* is a linear/non-linear interaction between the primary steady and travelling modes [30, 8]. Also the nature, absolute versus convective, of these modes has been a topic of research [54, 51]. Differences between axisymmetric flows and flows over swept geometries were highlighted in the last decades in this regard [70, 71, 43]. Most of the reported studies are based on numerical simulations [40, 129] or secondary stability calculations [76, 77, 8]. Nonetheless, several experimental investigations were carried out dedicated to these secondary instability modes. From the early observations of Poll [93] and Kohama *et al.* [55] to the dedicated experiments of White & Saric [135], the statistical footprint of the unsteady modes on the boundary layer, their chordwise evolution and spectral content were experimentally assessed. Moreover, the effect of different primary CFI flow configurations on the evolution of secondary modes was investigated by White & Saric [135]. To investigate the topology of the related flow structures, Kawakami *et al.* [51] conditioned the frequency and phase of the secondary modes by means of unsteady wall suction. In a similar way, Chernoray *et al.* [13] performed phase reconstructed measurements of the (secondary) unsteady modes of the steady vortices downstream of an isolated roughness. Finally, Glauser *et al.* [34] measured the wall fluctuations caused by the secondary CFI modes with multiple hot-films. Through these simultaneous measurements, correlation-based analyses were presented.

In this chapter, the first spatially and spatio-temporally resolved measurements on the naturally developing secondary modes are presented. To achieve these results, tomographic-PIV and high speed planar PIV are deployed to investigate the transition region. Modal decomposition techniques based on spatial correlation (POD) are sought to capture the weak flow structures of interest. To bridge the spatially resolved flow structures and the frequency spectra retrieved by hot-wire scans, Taylor's advection hypothesis is appealed and confirmed by high speed PIV measurements.

## 5.2. EXPERIMENTAL SETUP

For the hot-wire and tomo-PIV setups the reader should refer to the experimental setup section of chapter 4. The flow conditions are the same discussed in § 4.2.1.

### 5.2.1. TIME-RESOLVED PIV

Particle image velocimetry was used to inspect the boundary layer velocity field. The inspected plane is aligned to the  $X - Z$  directions and is positioned at 1.5 mm from the model surface. The measurement region is centred with the station  $x/c = 0.545$ .

The PIV experimental setup is presented in figure 5.1a. As shown, the camera was looking from outside the wind tunnel through opportune optical windows. It was placed at approximately 1 m from the measured plane. The camera used in this experiment is a *Lavision Imager HS* featuring a sensor of  $2016 \times 2016$  px<sup>2</sup>, pixel size of  $11 \mu\text{m}$  and 12 bits of digital resolution. However in order to increase the acquisition frame rate, the camera's active sensor was reduced to  $348 \times 176$  px<sup>2</sup> for the current experiment. The

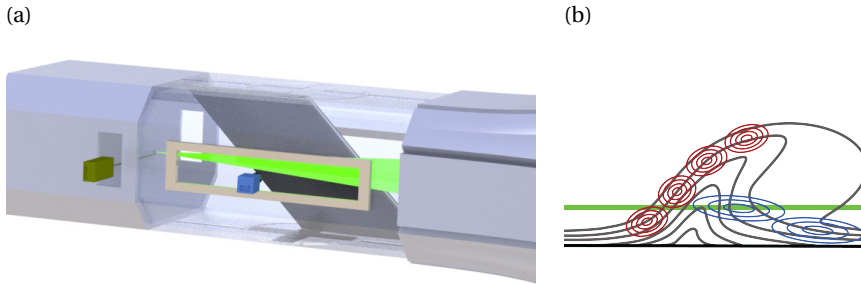


Figure 5.1: (a) Schematic of the PIV setup. The flow comes from right. The camera (blue) looks at the illuminated region (light green) from outside the testing chamber (drawn semi-transparent) through opportune optical windows. The laser head is shown (dark green) and illumination comes from downstream. (b) Schematic of the laser sheet (light green) w.r.t. the primary cross-flow vortex (grey) and *type-I* (red) and *type-III* (blue) secondary modes. Perspective from upstream. Schematics not to scale

camera was equipped with a *Nikon Nikkor 200 mm micro* lens operated at  $f_i=5.6$ . The resulting magnification factor of the PIV experiment is  $M=0.24$ . Illumination was provided from downstream as shown in the schematic. A Nd:YAG high speed *Continuum Mesa PIV* (18 mJ per pulse) was employed. The light beam was opportunely shaped into a sheet less than 1 mm thick. The light sheet was oriented such to be parallel to the model surface. The flow was seeded using *Safex* water glycol injected downstream of the testing chamber. The average particle diameter is  $1 \mu\text{m}$ . Cross-correlation was performed with final interrogation windows of  $24 \times 24 \text{px}^2$  with relative overlap set to 75%. As such, the final vector spacing was approximately 0.18 mm in both  $X$  and  $Z$ . The time interval between the two pulses was set to  $15 \mu\text{s}$  such to give an average displacement in the free stream of  $\approx 10 \text{px}$ . The system was operated at the very high-frequency of 20 kHz and a sequence of 65000 image pairs was acquired thus the resulting sampling time was 3.25 s.

### 5.3. RESULTS AND DISCUSSION

While the role of primary stationary cross-flow instability in low free-stream turbulence environments typically dominates the transition scenario, travelling CF waves are also destabilised. Their interaction with the stationary modes results in characteristic flow structures of primary relevance for the final breakdown of the transitional boundary layer. Furthermore in the high shear regions of the flow caused by the primary stationary instability, high-frequency secondary modes are also observed. This section presents measurements of the unsteady modes and their interaction with the primary stationary waves. Hot-wire measurements are subjected to spectral analysis and selective bandpass filtering in order to reveal the statistical properties of the various modes of the velocity fluctuations. Additionally, proper orthogonal decomposition analysis is applied on the instantaneous tomo-PIV fields in order to identify the development, topology and features of spatially coherent structures in the unsteady flow field.

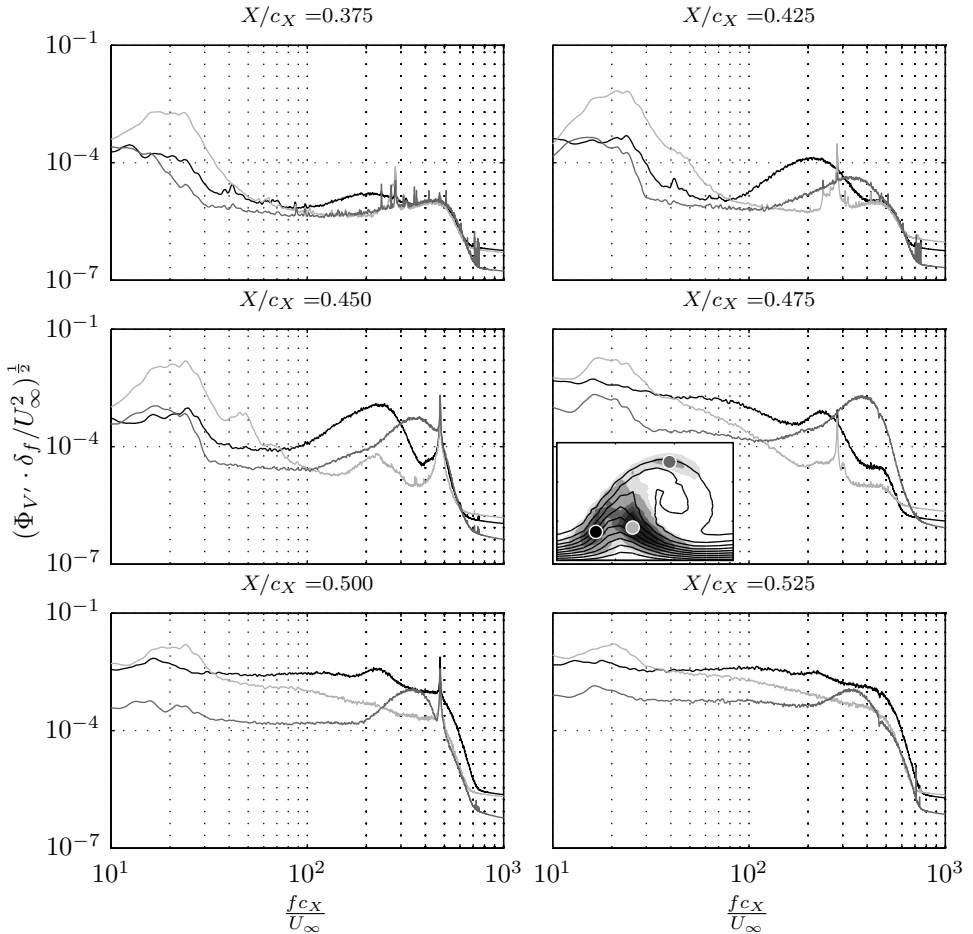


Figure 5.2: Non-dimensional spectra of the velocity fluctuations, for six chordwise stations, at the locations indicated by the (○) markers in the inset figure (coded with the corresponding colours). Inset: contour of the time-averaged velocity field (black lines, 10 levels from 0 to 1) and velocity fluctuations field (grey scale, 10 levels from 0 to 0.084) non-dimensionalised with the mean local external velocity  $|\bar{v}_e^{HWA}|$ , at  $X/c_X = 0.475$ .

### 5.3.1. SPECTRAL CHARACTERISTICS

As discussed in the previous section, the fluctuations field features three local maxima, corresponding to the location of the velocity gradients (see figure 4.9). At these locations, the time series of the velocity fluctuations were used to compute the power spectral density ( $\Phi_{V'}$ ) using the average periodogram method introduced by [133]. A single-point HWA measurement consists of  $2 \cdot 10^5$  instantaneous readings. The spectra were computed for segments of 5000 samples, with a relative overlap of 50%, averaged together. All the presented spectra feature a frequency resolution of  $\delta_f = 10$  Hz.

The non-dimensional spectra  $(\Phi_{V'} \cdot \delta_f / U_\infty^2)^{\frac{1}{2}}$  are plotted in figure 5.2 for several chordwise stations. The lines are coded with the same colours of the bullet markers of the contour, presented in the inset, where the velocity signals are sampled. The analysis of the three fluctuation regions shows respective dominance of significantly disparate spectral content and diverse streamwise evolution. At the first considered station,  $X/c_X = 0.375$  (first panel of figure 5.2), the inner upwelling region (marked by the light grey colour as in the inset) is characterised by pronounced spectral energy in a band of low Strouhal numbers between  $St = 15$  ( $f = 300$  Hz) and  $St = 25$  ( $f = 550$  Hz). At higher frequencies the spectral energy significantly drops to the level of background noise. Several narrow spikes appear above  $St = 250$  which can be attributed to electronic noise. Additionally, a low power frequency band from  $St = 150$  and  $St = 500$  is present which is traced to inherent characteristics of the hot-wire bridge and does not correspond to physical events [99]. The low frequencies dominating the inner upwelling region are consistent with observations of Deyhle & Bippes [19], Malik *et al.* [77] and White & Saric [135] and are attributed to primary travelling cross-flow instabilities which initially develop in the boundary layer independently of the primary standing modes. Later, when the stationary vortices reach a considerable amplitude, these travelling waves undergo the spanwise modulation imposed on the boundary layer by the steady modes [30, 40, 45, 8]. This is further confirmed by the predictions of LST which identified amplified modes at approximately  $St = 15$  ( $f = 300$  Hz) (section 3.4).

The fluctuations in the outer region of the upwelling flow (indicated with the black colour) are instead characterised by a pronounced band of Strouhal numbers between  $St = 124$  ( $f = 2.5$  kHz) and  $St = 348$  ( $f = 7$  kHz). Such high frequencies have been typically associated with secondary instability of the Kelvin-Helmholtz type [8] arising as a perturbation of the primary CFI flow (cf. Malik *et al.* [77], Janke & Balakumar [45], White & Saric [135]).

Moving downstream, the energy content of the associated frequency bands is drastically increased indicating growth of all unsteady modes. The spectra at  $X/c_X = 0.425$  show that both the low-frequency band associated with the inner side of the upwelling region of the CF vortex and the high-frequency hump occurring in the outer side, exhibit large amplitude growth. Moreover, the spectrum of fluctuations in the top region of the primary wave (marked in dark grey), coinciding with a maximum of the velocity gradient along  $y_t$  (see figure 4.9b), shows also a band of high energy centred at  $St = 373$  ( $f = 7.5$  kHz). This indicates destabilisation of the *type-II* mode as well [77, 135].

At  $X/c_X = 0.45$  the *type-III* mode (light grey line), sampled in the inner side of the upwelling region, further amplifies. Additionally, the two higher harmonics of this mode (at approximately  $St = 46$  ( $f = 925$  Hz) and  $St = 65$  ( $f = 1300$  Hz)) become evident at this station. At this station, the *type-I* high-frequency mode greatly enhanced its magnitude compared to the previous chord station. It features a larger growth than that experienced by the low-frequency travelling waves, suggesting a stronger growth rate for this secondary instability (cf. [40, 129, 135]). Sudden growth occurs as well to the higher-frequency *type-II* mode (dark grey line) sampled in the top region of the primary vortex, reaching a comparable amplitude to the *type-I* mode just discussed.

Further downstream, at  $X/c_X = 0.475$ , the low-frequency fluctuations in the vortex inner upwelling region and those in the top region are further enhanced, although the

magnitude of the background neighbouring frequencies is also increased. The *type-II* mode on the upper region of the primary vortex shows a steep increase, overcoming, at this location, the magnitude of the *type-I* instability. The last two stations where the spectral analysis is performed are located at  $X/c_X = 0.50$  and  $X/c_X = 0.525$ . The two high-frequency *type-I* and *type-II* modes appear to peak in energy but they also appear to be almost overtaken by the broadband fluctuations pertaining to a more turbulent boundary layer. The low-frequency mode instead does not show any appreciable change between  $X/c_X = 0.45$  and  $X/c_X = 0.525$ . This further suggests the independence of the *type-III* mode from the growth of secondary instability although the growth of all three modes appears to be related to the saturation of the stationary vortices, as will be better described later.

### 5.3.2. STREAMWISE EVOLUTION

The analysis of the spectra presented so far pertains to rigorous amplification of the three unsteady modes in the region between primary mode amplitude saturation ( $X/c_X \approx 0.45$ ) and turbulent onset ( $X/c_X \approx 0.50$ ). A way to track this evolution is presented by White & Saric [135] and Downs & White [27] and consists of computing the growth rates of the unsteady modes. To do this, the velocity fields are bandpass filtered, by means of zero phase shift fourth-order digital filtering, in the respective frequency bands. Root-mean-square contours of the bandpass filtered fields are presented in figure 5.3 for stations  $X/c_X = 0.45$ ,  $X/c_X = 0.475$  and  $X/c_X = 0.50$ . Additionally, the time-averaged velocity field respective to the station is superimposed. The contours on the first column on the left and indicated with band 1<sup>1</sup>, refer to the band  $17.4 \leq St \leq 27.3$  ( $350 \text{ Hz} \leq f \leq 550 \text{ Hz}$ ) pertaining to the *type-III* instability. Contours indicated with band 2 correspond to the range  $248.0 \leq St \leq 298$  ( $5 \text{ kHz} \leq f \leq 6 \text{ kHz}$ ) related to the *type-I* mode. Band 3 relates to the range  $348 \leq St \leq 397$  ( $7 \text{ kHz} \leq f \leq 8 \text{ kHz}$ ), pertaining to the *type-II* mode. The contours are non-dimensionalised with the free stream velocity ( $U_\infty$ ). Note that the band 1 contours attain larger values than the ones of bands 2 and 3.

It becomes evident that the three modes possess characteristic topological arrangement and streamwise development. The spatial locations, with respect to the primary vortices, pertaining to the three modes are revealed confirming previous observations by e.g. Högberg & Henningson [40], Malik *et al.* [77] and White & Saric [135]. Moving past the wing trailing edge, it can be seen how the high-frequency modes grow strongly passing from  $X/c_X = 0.45$  to  $X/c_X = 0.50$ . The low-frequency mode, although having a larger amplitude, does not show such a steep growth, as already commented.

Although the absolute magnitude of r.m.s. intensity reveals the overall growth of each mode, a more robust evaluation of the growth rates is sought. To this end, the disturbances amplitude expressed by equation 2.24 (as defined by White & Saric [135] and Downs & White [27]) is used.

The computed amplitudes ( $A_{II}$ ) are presented in figure 5.4a, while the N-factors ( $N_{II}$ ) of the unsteady modes are shown in figure 5.4b. The need to present both the curves resides in the observation that the choice of the initial normalising amplitudes for the different modes is not trivial and can lead to misleading conclusions. The low-frequency mode exhibits the strongest and earliest growth. Indeed within only 20% of the chord,

<sup>1</sup>Not to be confused with the *type-I* mode

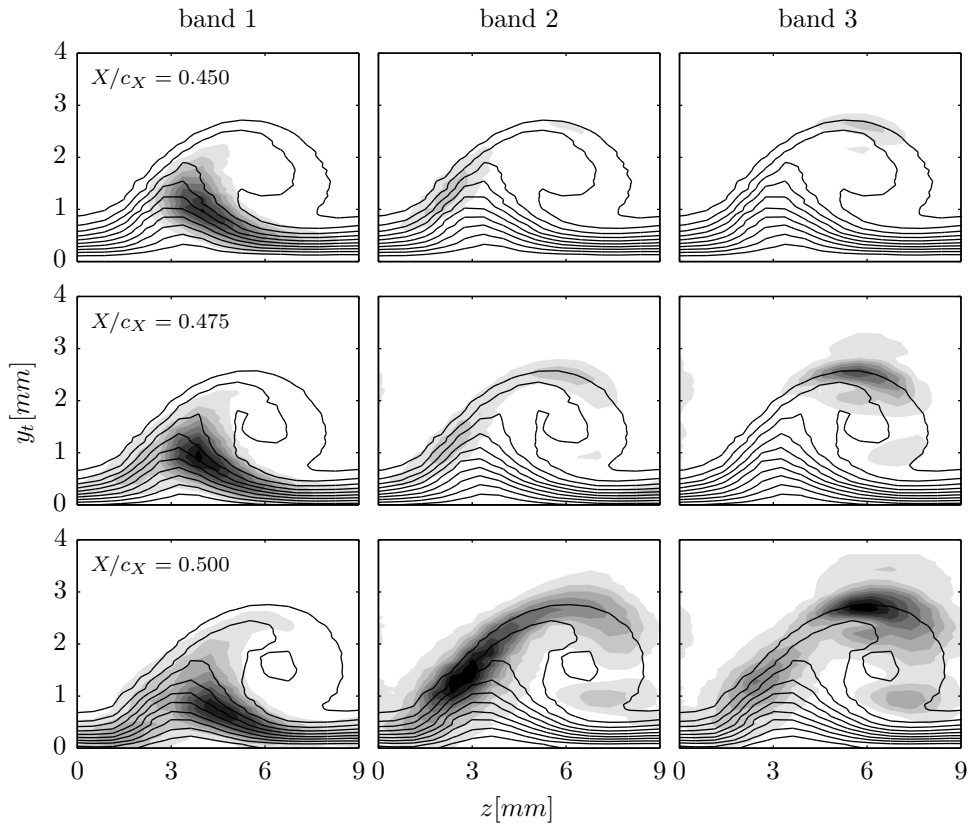


Figure 5.3: Bandpass filtered velocity fluctuation fields (grey scale) and time average velocity fields (black lines, 10 levels from 0 to  $U_\infty$ ). Frequency band 1:  $17.4 \leq St \leq 27.3$  ( $350 \text{ Hz} \leq f \leq 550 \text{ Hz}$ ) (10 levels from 0 to  $0.24 U_\infty$ ), band 2:  $248.0 \leq St \leq 298.3$  ( $5 \text{ kHz} \leq f \leq 6 \text{ kHz}$ ) (10 levels from 0 to  $0.6 U_\infty$ ) and band 3:  $348.0 \leq St \leq 397.8$  ( $7 \text{ kHz} \leq f \leq 8 \text{ kHz}$ ) (10 levels from 0 to  $0.6 U_\infty$ ).

spanning from  $X/c_X = 0.35$  to  $X/c_X = 0.55$ , the amplitude of fluctuations attributed to the low-frequency mode increases by approximately two orders of magnitude. Moreover, it can be seen that this mode grows monotonically in the considered range, with a steeper slope between  $X/c_X = 0.45$  and  $X/c_X = 0.475$ .

It is important to note here that since travelling cross-flow modes essentially *sweep* the measurement plane, their fluctuations intensity would be expected not to significantly vary in the  $z$  direction. It is evident from figure 5.3a that this is not the case as the low-frequency band is only dominant in the inner upwelling region of the standing CF vortex. As discussed, this is caused by the interaction with the stationary CF vortices. Moreover, since this mode is initially a primary instability mechanism [30, 40, 45, 8], its growth along the streamwise direction is expected to not show the explosive nature of the secondary modes. After the saturation of the steady modes however, the amplitude of this mode shows larger values. The two high-frequency modes instead show the previously reported

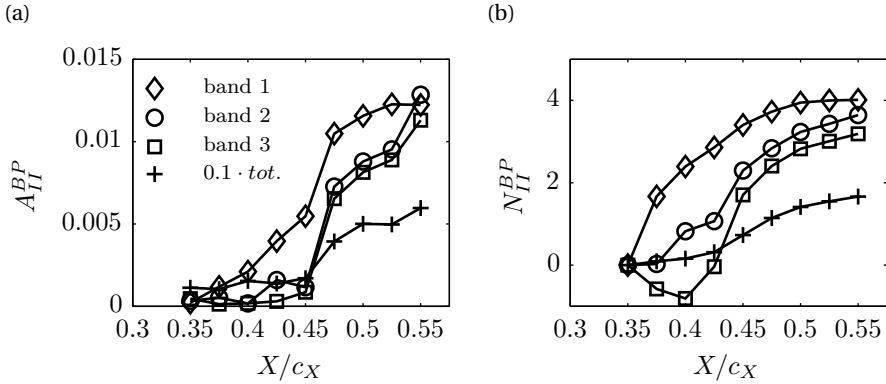


Figure 5.4: (a) Amplitudes and (b) N-factors of total and bandpass filtered velocity fluctuations, computed using equations 2.24 and 2.25. Same frequency bands as figure 5.3. This analysis refers to the flow field pertaining to three full stationary vortices.

[129, 135] sudden growth from  $X/c_X = 0.45$  and, within only the 10% of the wing chord, they amplify to 30 (*type-I*) and 20 (*type-II*) times their initial amplitude.

It can also be seen that the three inspected frequency bands drive the amplitude of the full-spectrum fluctuations, which also shows a sudden enhancement after station  $X/c_X = 0.45$ . At the last considered station  $X/c_X = 0.55$ , turbulent breakdown occurs as seen in figure 4.5 and further indicated by the steeper slope of all the curves. The three bands show comparable amplitudes, reaching together approximately 60% of the total fluctuations. At this station, the bands cannot be related any more to the instability modes.

### 5.3.3. SPATIAL ORGANISATION

The large disparity of length scales and time scales associated with the instability modes in a swept-wing boundary layer necessitate the deployment of robust and objective mode identification techniques. One such technique is proper orthogonal decomposition, originally introduced by Lumley [73] for identification of coherent turbulent structures. This is a powerful technique which capitalises on the spatial coherence of orthogonal modes in order to identify and prioritise them with respect to their energy content.

In this experiment, POD was applied on the full set of 500 instantaneous tomo-PIV flow fields using the snapshot technique introduced by Sirovich [119]. Furthermore, the investigated volume was cropped compared to the full tomo-PIV domain of figure 4.11. This was done for several reasons: firstly, POD inherently identifies spatially coherent unsteady modes within a given flow field. In the case of CF instability-dominated boundary layers, these would effectively be the primary travelling waves and secondary instability vortices. Additionally, these modes exhibit strong non-linear behaviour with respect to the standing CF mode (see section 5.3.2 and work of [76]) but not with the high-frequency instabilities developing on a neighbouring stationary CF vortex, as reported by Bonfigli & Kloker [8]. These observations bring specific considerations regarding the application of

POD to a flow field encompassing multiple standing CF vortices. The instability modes developing within each standing CF vortex will be directly associated with the strength and topology of their respective *carrier* CF wave. Although, the primary waves have been forced with identical roughness elements, total similarity cannot be guaranteed in an experimental framework. Any slight disparity between individual standing CF vortices and in their secondary destabilisation would consequently introduce discrepancies between *sets* of unsteady modes in terms of amplitude and spatial coherence which would degrade the ability of POD to identify them. Based on this, a domain encompassing a single standing CF vortex was selected for POD analysis. The full tomo-PIV domain is therefore cropped in the spanwise range of  $0 \text{ mm} \leq Z_W \leq 6 \text{ mm}$ . A second consideration is the apparent failure of tomo-PIV to capture the near-wall region as evident by the discrepancies in figure 4.13. As discussed, this is due to inherent limits of PIV in regions of high shears. Fortunately, the bandpass filtered fluctuation distributions presented in figure 5.3 indicate little modal content in the near-wall region, other than a fraction of the *type-III* mode. Following this, the considered domain for POD was further cropped to dismiss the near wall-region ( $y_t < 0.95 \text{ mm}$ ).

The relative turbulent kinetic energy (TKE) distribution of the first twenty POD modes is shown in figure 5.5. The first POD mode clearly dominates in the unsteady flow field with approximately 16% of the total fluctuation kinetic energy. The energy content of the following modes diminishes rapidly. At this point some notes are necessary regarding the interpretation of POD modes. In typical application cases such as bluff body aerodynamics [89] or turbulent breakdown of free jets [127], the inherent ability of POD to prioritise spatially coherent modes according to their energy content is rather straightforward. In contrast, in highly multiscale, non-linear problems such as transitional boundary layers, POD modal energy is weakly coupled to the importance of the respective mode in the transition process. In the present study, spatially coherent modes corresponding to the developing instabilities within the standing CF vortex are sought. It is already known from the existing hot-wire measurements (cf. section 5.3.2) and previous investigations [129] that these modes are rather weak compared to the free stream velocity, and hence prone to be overshadowed by other sources such as measurement noise. Finally, it must be stressed that the exact sorting of these modes is additionally dependent on the domain of the flow field considered for POD.

Considering the previous points, it becomes important to identify the modes relevant to the transition process based on features other than their energy content. One such feature is the expected spatial wavelength associated with the mode, which can be derived using the Taylor hypothesis from the previously described hot-wire measurements. A second feature stems from the fact that the sought instability modes are inherently convective [51, 129, 8]. As such, the POD procedure will generate a harmonically coupled pair of POD modes, shifted by  $\pi/2$ , for each physical convecting coherent structure [126]. Both these features have been used as selection criteria in this study in order to identify the POD modes corresponding to the relevant instability modes in the transitional boundary layer. Following this approach, four modes ( $\Phi_6$ ,  $\Phi_7$ ,  $\Phi_9$  and  $\Phi_{10}$ ) have been selected and are presented in sections 5.3.3 and 5.3.3. Before moving to the analysis of the secondary instability modes, the first POD mode ( $\Phi_1$ ) is inspected due to its considerably high energy content and particular spatial topology (§ 5.3.3).

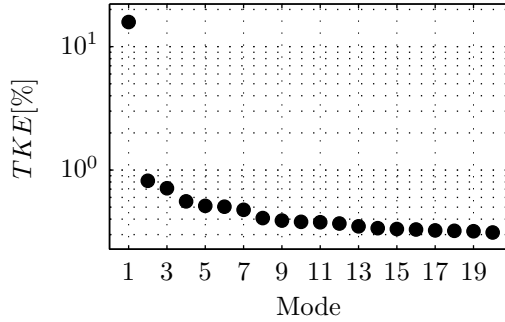


Figure 5.5: Relative turbulent kinetic energy distribution of the first 20 POD modes.

#### QUASI-STATIONARY CROSS-FLOW VORTICES

The first POD mode ( $\Phi_1$ ) is presented in figure 5.6, in terms of isosurfaces of  $U_W/\bar{U}_{We} = \pm 0.086$ , together with three cross-cut contours of the  $\bar{U}_W/\bar{U}_{We}$  velocity field pertaining to the standing CF vortex. The isosurfaces appear aligned with the spanwise ( $z$ ) shears of the mean velocity field (compare with figure 4.9c). In addition, no streamwise variation of the mode can be identified. The spatial topology of the mode suggests a slow velocity fluctuation which occurs mainly in the  $Z_W$  direction. Finally, the mode is not harmonically coupled to any of the remaining POD modes suggesting a global and not convective structure. In order to further aid understanding of this phenomenon, a flow field reconstruction based on the sum of the mean flow and mode  $\Phi_1$  is performed. This is presented in figure 5.7a where the locus of the isoline at  $\bar{U}_W/\bar{U}_{We} = 0.9$  is shown for the mean field (black line) against all instantaneous realisations of the reconstructed field (grey scatter symbols). The characteristic grid pattern stemming from the interpolation of the selected isoline on the discrete vector spacing of the tomo-PIV measurement is evident. Despite this, it can be clearly affirmed that POD mode  $\Phi_1$  pertains to a global shift of the stationary CF vortices mainly along the  $Z_W$  direction. The positions of the rightmost locus of the instantaneous isolines, (indicated with the  $\circ$  symbol in figure 5.7a) have been fed in a normal probability density function distribution (pdf) to inspect the displacements along  $Z_W$  ( $\Delta Z_W$ ) in terms of magnitude and occurrence. The result is shown in figure 5.7b. The sparsity of the pdf is again related to the discreteness of the measurements. The mean position of the isoline (plotted with a black solid line) pertains to the value of  $\mu = -0.015$  mm while the standard deviation (dotted lines) is  $\sigma = 0.12$  mm.

As previously mentioned, the origin of the first mode is not of immediate interpretation. The appearance of such global spanwise oscillation of the flow field would be caused by a small shift, along  $Z_W$ , of the PIV cameras and/or of the wing model (shaking of the laser light has no detrimental effect in tomo-PIV measurements). While the model and the cameras were mounted on stiff supports, the time series of the PIV images were inspected in order to identify equipment vibrations. Indeed, no such movement was detected within the accuracy of a single pixel (about 0.03 mm), thus excluding a relative motion of the cameras and the model.

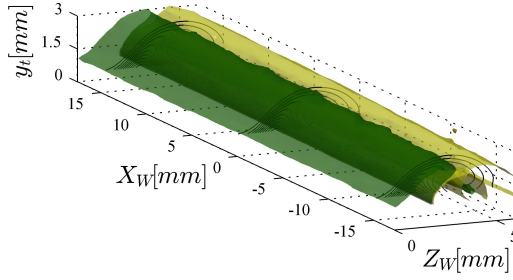


Figure 5.6: Isosurfaces of  $U_W/\bar{U}_{We} = \pm 0.086$  of POD mode  $\Phi_1$ . Three contours of  $\bar{U}_W/\bar{U}_{We}$  at  $X_W = -15, 0$  and  $15$  mm (10 levels from 0 to 1).

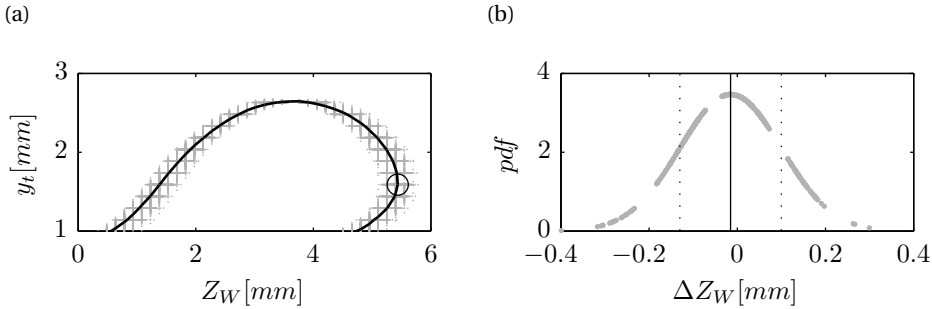


Figure 5.7: (a) Contour of the isoline at  $\bar{U}_W/\bar{U}_{We} = 0.9$  for the time-averaged field (black line) and the isolines of instantaneous realisations of the reconstructed field from POD mode  $\Phi_1$  (grey symbols). (b) Normal distribution of the realisations ( $\Delta Z_W$ ) of the  $U_W/\bar{U}_{We} = 0.9$  isoline at the location of the bullet symbol in figure 5.7a. The black line indicates the mean ( $\mu = -0.015$  mm) and the dotted lines indicate the standard deviation ( $\sigma = 0.12$  mm).

Based on the previous analysis, it becomes apparent that mode  $\Phi_1$  is physical and pertains to a low-frequency spanwise shift of the stationary structures. This further justifies the extremely high energy content of this mode, since it is essentially a mean flow distortion. The source of such movement can currently only be conjectured. A possible cause is a low-frequency modulation of the free stream flow due to unsteadiness inherent to the wind tunnel or other environmental factors. Such an effect would eventually modulate the local Reynolds number and consequently the stability characteristics of the boundary layer, including the wavenumber angle of the 9 mm CF mode. An alternative explanation would be a vortex self-induction oscillatory movement due to the presence of the wall. Fluctuations of the attachment line or stemming from the wind tunnel walls turbulent boundary layer could also cause similar structures. Independent of the source, the described motion is minuscule. One must keep in mind that the observed CF vortices shift of  $\sigma = \pm 0.12$  mm at  $X = 0.45 \cdot c_X$  (figure 5.7a) would be caused by a change of wavenumber angle of just  $\delta\Psi = \tan^{-1}(\sigma/X) = \pm 0.011^\circ$  (assuming the stationary CF vortices stem from the discrete roughness elements). Additionally, it is likely that such behaviour has not

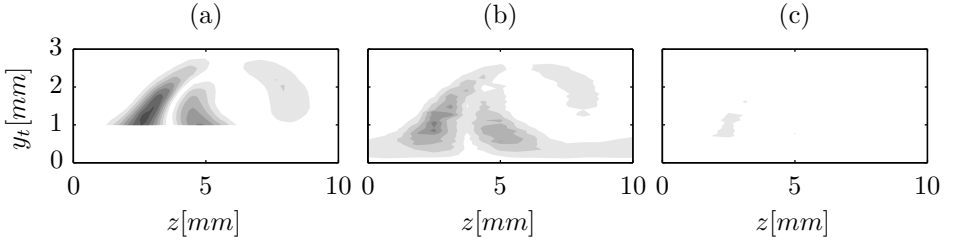


Figure 5.8: Non-dimensional fluctuations fields (a) from the reconstructed POD mode 1 and from the hot-wire measurements bands: (b)  $0.05 \leq St \leq 0.99$  ( $1 \text{ Hz} \leq f \leq 20 \text{ Hz}$ ) and (c)  $0.99 \leq St \leq 1.99$  ( $20 \text{ Hz} \leq f \leq 40 \text{ Hz}$ ); (10 levels between 0 and  $0.08 |\bar{V}_e^{HWA}|$ ). Cross-cut fields at  $X/c_X = 0.45$ .

been reported so far in the literature due to the lack of spatially correlated, low-frequency measurements. In the numerical simulations a perfect spanwise uniformity is usually prescribed, which although desired, cannot be fully respected in experimental frameworks. In order to better show the effect of this mode on the stationary waves, a flow field reconstruction based on the mean flow and on the first POD mode has been performed.

To assess whether the fluctuations pertaining to this mode are captured also by the hot-wire experiment the same procedure of bandpass filtering the measured time series done in § 5.3.2 is repeated, considering one single CF vortex and using second-order Butterworth filters. The signal is therefore filtered in bands of 20 Hz width, ranging from 1 Hz to 100 Hz ( $0.05 \leq St \leq 4.97$ ). Comparison between the several bands is made applying equation 2.24. Strong fluctuations are revealed only by the lower-frequency band, spanning between  $St=0.05$  and  $St=0.99$  ( $1 \text{ Hz} \leq f \leq 20 \text{ Hz}$ ). This band features almost 55% of the total full spectrum amplitude ( $A_{II}^{tot}$ ). For comparison referring to the definitions given in § 5.3.2, the band 1, pertaining to the *type-III* mode, encompasses at this station  $0.30 A_{II}^{tot}$ . The high-frequency band 2 (*type-I* mode) and band 3 (*type-II* mode) pertain to  $0.031 A_{II}^{tot}$  and  $0.035 A_{II}^{tot}$  respectively.<sup>2</sup>

The fluctuation field, reconstructed from the POD mode  $\Phi_1$ , is presented in figure 5.8 together with the r.m.s. fields of bands  $0.05 \leq St \leq 0.99$  ( $1 \text{ Hz} \leq f \leq 20 \text{ Hz}$ ) and  $0.99 \leq St \leq 1.99$  ( $20 \text{ Hz} \leq f \leq 40 \text{ Hz}$ ). The POD r.m.s. field features similar structures compared to the lowest-frequency field thus suggesting that the fluctuations pertaining to the POD mode 1 occur at frequencies contained in the  $0.05 \leq St \leq 0.99$  ( $1 \text{ Hz} \leq f \leq 20 \text{ Hz}$ ) band. The high energy level of this unsteady phenomenon was also captured by the POD energy distribution (figure 5.5).

Despite the theoretically interesting aspects regarding the origin of mode  $\Phi_1$ , the rather low-frequency oscillation of the stationary CF vortices is unlikely to be related to other unsteady transition modes or play any appreciable role in the transition process. Nevertheless, this low-frequency mode should be taken into account in experimental investigations as it features high energy levels especially when compared to the energies of the arising secondary instability modes.

<sup>2</sup>It has to be noted that because of leakage through the digital filters, the sum of all band amplitudes will be larger than the full-spectrum energy. As such, these results are to be considered as a qualitative relative comparison among the different bands.

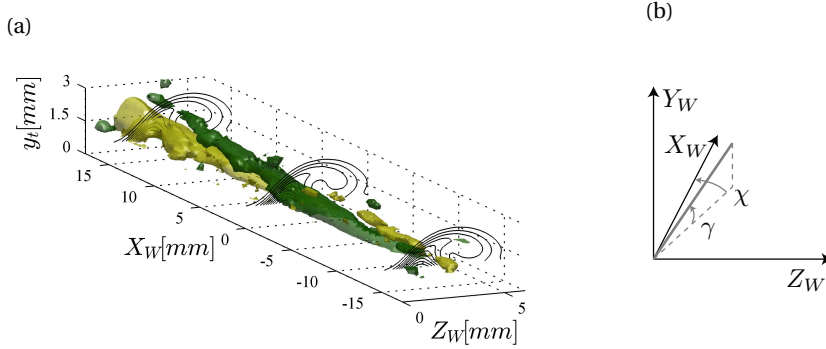


Figure 5.9: (a) Isosurfaces of  $U_W/\bar{U}_{We} = \pm 0.086$  for POD mode  $\Phi_7$ . Three contours of  $\bar{U}_W/\bar{U}_{We}$  at  $X_W = -15, 0$  and  $15$  mm (10 levels from 0 to 1). (b) Definition of elevation angle ( $\gamma$ ) and azimuthal angle ( $\chi$ ). The grey line represents the vortex axis and the angles are defined positive by the arrows.

#### TYPE-III INSTABILITY

POD modes  $\Phi_6$  and  $\Phi_7$  are the most energetic modes which are harmonically coupled and feature a wavelength relevant to the transition process. Respective isosurfaces to the ones presented for mode  $\Phi_1$  are presented in figure 5.9a for mode  $\Phi_7$  (mode  $\Phi_6$  is physically similar and phase shifted by  $\pi/2$ ). The isosurfaces reveal an elongated low-speed/high-speed pair forming in the inner upwelling region of the stationary CF vortex. The orientation of these structures with respect to the primary stationary waves can be quantified by defining an azimuthal angle ( $\chi$ ) and an elevation angle ( $\gamma$ ) as indicated in the schematic of figure 5.9b. The secondary structures axis is denoted by the grey line and the angles are considered positive in the direction shown by the arrows. For the structures pertaining to this mode, the respective angles are:  $\chi = -0.8^\circ$  and  $\gamma = 3.5^\circ$ . In the investigation of the swept flat plate with streamwise pressure gradient, Bonfigli & Kloker [8] describe similar structures whose spinning direction is the same as the one of the primary stationary vortices. They report a null azimuthal angle considering the vortices orientation at their centroid, whereas the estimation of the elevation is not clear (refer to figure 33 of Bonfigli & Kloker [8]).

The spatial phase shift of the mode pair can be better assessed by extracting a single plane from the presented volume. This is done at  $Z_W = 2.5$  mm, where the structure attain to higher values, and the resulting contours are plotted in figure 5.10a for mode  $\Phi_6$  and figure 5.10c for mode  $\Phi_7$ . Moreover, the measured velocity along a line at constant  $y_t$  is further extracted from these planes, at the location of the white dotted line of figures 5.10a and 5.10c, and plotted in figures 5.10b and 5.10d.

The phase shift of the two modes is  $\pi/2$ , establishing the convective nature of these structures. Furthermore, the extracted velocity at constant  $Z_W$  and  $y_t$  provides the wavelength of the structures which results to be  $\lambda_{X_W}^{6-7} \approx 25$  mm. Inspecting the isosurfaces of figure 5.9a, it can be commented that these structures are located in the inner side of the upwelling region of the stationary CF vortices, where the low-frequency fluctuations

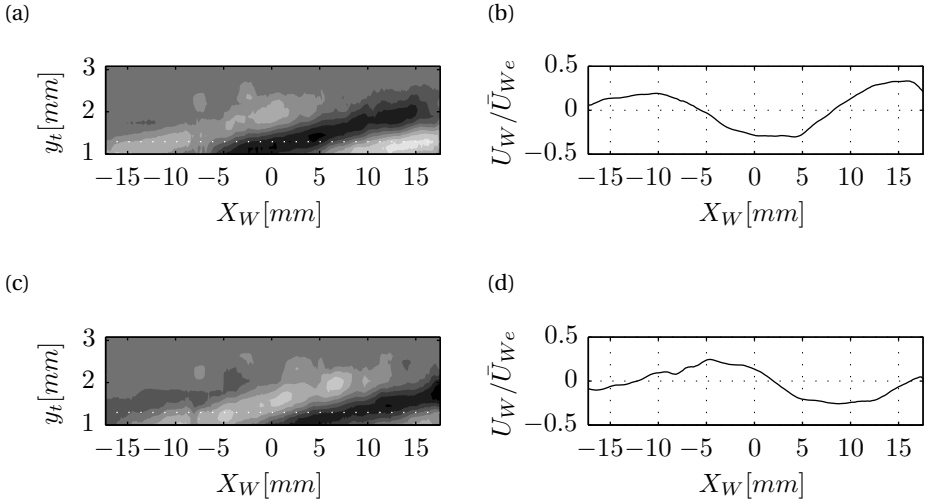


Figure 5.10: Contour of  $U_W/\bar{U}_{We}$  (10 levels between  $\pm 0.39$ ) in planes extracted at  $Z_W = 2.5$  mm from the volume of figure 5.9a pertaining to POD modes  $\Phi_6$  (a) and  $\Phi_7$  (c). (b) Velocity sampled along the dotted line of figure 5.10a and (d) of figure 5.10c.

field has a local maximum (compare with figure 5.3). The spectral analysis of the hot-wire signal at this location revealed notable energy in the frequency band of  $17.4 \leq St \leq 27.3$  ( $350 \text{ Hz} \leq f \leq 550 \text{ Hz}$ ) (figure 5.2). The measured mean out-of-plane velocity at this location is  $\bar{U}_W \approx 0.65\bar{U}_{We}$ . This can be directly associated with the phase velocity of the convective structure ( $u_c^{6-7}$ ) [13, 8]. Kawakami *et al.* [51] report a value of 0.47 times the local external velocity for the convecting velocity of these structures. Applying Taylor's hypothesis, which entails that convective velocity and structure wavelength do not change appreciably within the considered spatial domain, yields the temporal frequency that would be measured at a fixed point in the boundary layer intersected by this mode as  $St \approx 24.9$  ( $f \approx 500 \text{ Hz}$ ). The estimated frequency and the pertaining boundary layer region affirm that the structures captured by the harmonically coupled POD modes  $\Phi_6$  and  $\Phi_7$  are the effect on the primary stationary cross-flow waves of *type-III* instability. These conclusions agree with the description of this instability mode presented in previous studies [40, 51, 45, 130, 8]. It should be noted that the isosurfaces in figure 5.9a do not show appreciable growth within the presented domain, consistent with HWA measurements of figures 5.4a and 5.4b. A composite visualisation of this mode can be performed by reconstructing the two pertinent POD modes ( $\Phi_6$  and  $\Phi_7$ ) multiplied respectively with artificial sinusoidal signals, in phase quadrature, at the estimated frequency of  $St \approx 24.9$  ( $f \approx 500 \text{ Hz}$ ).

#### TYPE-I INSTABILITY

Following an approach similar to that for POD modes  $\Phi_6$  and  $\Phi_7$ ,  $\Phi_9$  and  $\Phi_{10}$  are identified as the second harmonically coupled pair of POD modes. Velocity isosurfaces of mode  $\Phi_9$  are presented in figure 5.11. The structures revealed here (isosurfaces at  $U_W/\bar{U}_{We} =$

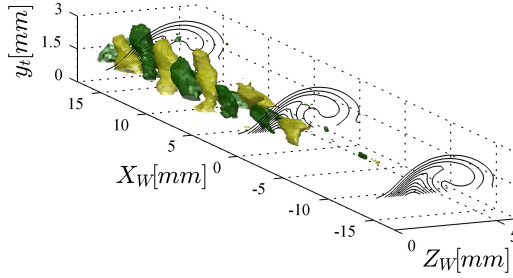


Figure 5.11: Isosurfaces of  $U_W/\bar{U}_{We} = \pm 0.086$  for POD mode  $\Phi_{10}$ . Three contours of  $\bar{U}_W/\bar{U}_{We}$  at  $X_W = -15, 0$  and  $15$  mm (10 levels from 0 to 1).

$\pm 0.086$ ) are significantly different to the ones pertaining to modes  $\Phi_6$  and  $\Phi_7$ , appearing as a more narrowly spaced sequence of high-speed/low-speed *fingers*. The axis of these structures is tilted at a notable angle with respect to the stationary CF axis and pointing towards the upper bound of the domain, leading to azimuthal and elevation angles of  $\chi = -18.2^\circ$  and  $\gamma = 21^\circ$ , respectively. Bonfigli & Kloker [8] report, for their flat plate flow, angles of  $\chi = -18.2^\circ$  and  $\gamma = 12^\circ$ ; Janke & Balakumar [45] and Wassermann & Kloker [129] report, for similar flow cases, the azimuthal inclination for this type of mode to be  $\chi = -29.9^\circ$  and  $\chi = -20^\circ$ , respectively. Despite the differences in the estimated orientation of these secondary vortices, it is clear from all the reported studies that they are inclined at a relevant angle with respect to the axis of the primary vortices. The orientation of these structures is a direct cause of their topology. In fact by spanning almost all the boundary layer thickness, they are advected with different velocities pertaining to the different wall-normal regions thus showing the reported helicoidal shape.

Additionally, the structures are located in the outer side of the upwelling region of the primary vortices and are, on average, further away from the wall than modes  $\Phi_6$  and  $\Phi_7$ . This is the location of the *type-I* secondary instability (e.g. [19, 40, 77, 129, 135]). The general topological features revealed by modes  $\Phi_9$  and  $\Phi_{10}$  are similar to those presented in cross-cut planes, by Malik *et al.* [77], Högberg & Henningson [40], Kawakami *et al.* [51] and Janke & Balakumar [45] and to those described, in their three-dimensional organisation, by Wassermann & Kloker [129, 130], Bonfigli & Kloker [8] and by Chernoray *et al.* [13].

The constant-plane velocity contours, extracted at  $Z_W = 2.0$  mm, and the velocity sampled along a line, at constant  $Z_W$  and  $y_t$ , are shown in figure 5.12 for POD modes  $\Phi_9$  and  $\Phi_{10}$ . The phase quadrature of the POD modes is again evident thus confirming the convecting nature of the reported structures. The inferred wavelength ( $\lambda_{X_W}^{9-10}$ ) is approximately 4.6 mm. The structures are on average located further from the wall than the primary travelling cross-flow and thus are subject to higher average convective velocity of  $u_c^{9-10} \approx 0.8\bar{U}_{We}$  (Malik *et al.* [77] reported  $0.84U_\infty$ ; Kawakami *et al.* [51] found 78% of the local external velocity). Considering the Taylor hypothesis, a temporal frequency of approximately  $St = 248.0$  ( $f = 5000$  Hz) is estimated. This frequency is within the dominant band measured with the hot-wire on the outer side of the upwelling region of the boundary layer (figure 5.3).

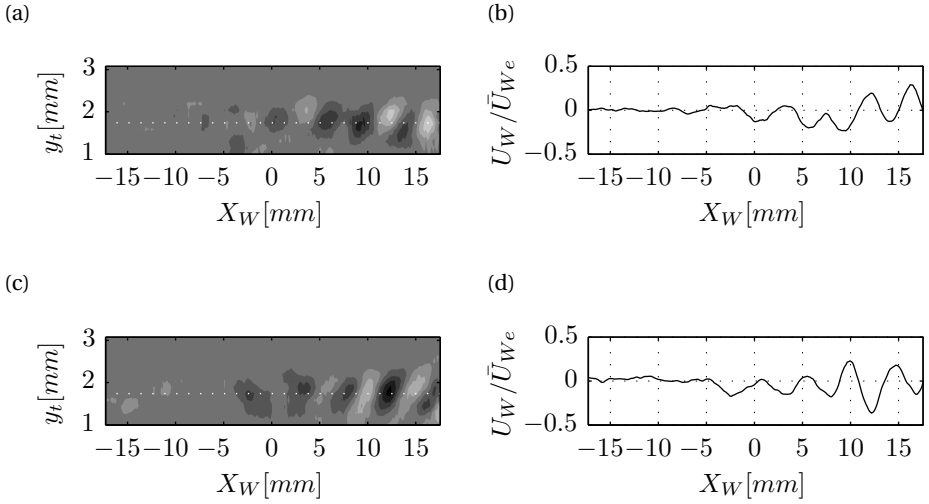


Figure 5.12: Contour of  $U_W / \bar{U}_{W_e}$  (10 levels between  $\pm 0.39$ ) in planes extracted at  $Z_W = 2$  mm from the volume of figure 5.11 pertaining to POD modes  $\Phi_9$  (a) and  $\Phi_{10}$  (c). (b) Velocity sampled along the dotted line of figure 5.12a and (d) of figure 5.12c.

Moreover, the strong spatial growth along  $X_W$  of these modes is evident as their initial appearance occurs at approximately  $X_W = 0$  which coincides to the wing  $X/c_X = 0.45$  station. This further justifies the position of these modes in the POD energy distribution (figure 5.5) and demonstrates the insufficiency of modal energy as a selection criterion for relevant modes related to secondary instability phenomena. Modal decompositions based instead on modes spatial amplification, such as for instance Dynamic Mode Decomposition (DMD), would be more effective for these investigations but unfortunately would require spatio-temporal correlated measurements. The  $X/c_X = 0.45$  station has been shown to be the location where primary stationary CF vortices saturate (figure 4.7). Additionally, this corresponds to the location where the sudden growth of the high-frequency secondary instability modes occurs (figure 5.4a). These considerations lead to the conclusion that what is captured by POD modes  $\Phi_9$  and  $\Phi_{10}$  is the footprint, in terms of  $U_W$  modulation, of the *type-I* secondary instability. Similar to what was done for the *type-III* mode, a time evolution visualisation of this instability mode is performed by reconstructing the two pertinent POD modes ( $\Phi_9$  and  $\Phi_{10}$ ) multiplied respectively with artificial sinusoidal signals at the estimated frequency of  $St = 248.0$  ( $f = 5000$  Hz).

#### SOME CONSIDERATIONS ON THE CURRENT EXPERIMENT

The spatial organisation of the low-frequency *type-III* mode and the *type-I* high-frequency secondary instability has been captured by POD of the tomo-PIV fields. The derived properties of the coupled POD modes related to *type-III* and *type-I* modes described in this section are summarised in table 5.2.

These results offer the first three-dimensional experimental measurement of these structures under natural flow conditions offering an important comparison with previous

POD modes	mode	$\lambda_{X_w}$ [mm]	$u_c$ [% $\bar{U}_{We}$ ]	$St$	$f$ [kHz]	$\chi$ [°]	$\gamma$ [°]
$\Phi_6 - \Phi_7$	<i>type-III</i>	25	65	24.9	0.5	-0.8	3.5
$\Phi_9 - \Phi_{10}$	<i>type-I</i>	4.6	80	248	5	-18.2	21

Table 5.1: Properties of POD modes related to secondary instability modes.

literature (e.g. [40, 77, 53, 129, 130, 8]) regarding the spatial organisation and the convecting nature of these modes, although the experiments performed by Kawakami *et al.* [51] and Chernoray *et al.* [13] forcing the unsteady modes gave already illuminating outcomes in this regard.

Few other POD modes showed similar structures to the ones presented in figures 5.11. This is expected given the broad spectral band of the *type-I* secondary instability seen in the previous section. Nonetheless, they did not feature a clear relative phase shift and therefore are not considered. No modes in the domain investigated by POD showed structures related to the *type-II* secondary vortices and hence no comparison with the hot-wire results presented in section 5.3.2 can be performed. It is likely that having a more extended domain in the downstream region would lead to the capturing of the *type-II* mode as well as its interaction with the other instability modes until the turbulent breakdown.

#### 5.3.4. TIME-RESOLVED ANALYSIS

Time-resolved PIV allows direct inspection of the spatio-temporal evolution of the unsteady flow structures. Additionally, the extended sampling time of the current experiment leads to converged statistic fields. In figure 5.13(a), the time-averaged ( $\bar{U}$ ) and standard deviation ( $U_{RMS}$ ) velocity fields are shown. The contour presents a cross-cut plane, at 1.5 mm from the model surface, of a stationary cross-flow vortex at the streamwise location corresponding to its turbulent breakdown [114]. In figure 5.1b, a schematic shows the measurement plane with respect to the analysed flow structures. The lower part ( $Z/\lambda_Z^f < 0.3$ ) of the velocity field is the high-speed region in-between neighbouring vortices. In the upper part of the field, a low-speed region occurs that corresponds to the upwelling flow, shifted upwards by the stationary vortex. The second velocity minimum in the contour shows instead the downwelling flow, associated with the falling lobe of the primary waves. The fluctuations are stronger in the high-shear regions as reported in literature (e.g. Malik *et al.* [77], Wassermann & Kloker [129], White & Saric [135]).

In order to facilitate inspection of the spectral content of the flow field, the full time series of the  $U$ -velocity fluctuations is sampled along the constant chord segment AB of figure 5.13(a) and Fourier-transformed. The modified periodogram method of Welch [133] was used. The spectra have a final resolution of 10 Hz. The results are presented in figure 5.13(b). High spectral energy density is observed at very low frequencies and throughout the extension of the stationary vortex. The analysis of the tomo-PIV investigations presented before in § 5.3.3 reported a low-frequency spanwise oscillation of the stationary vortices encompassing most of the turbulent kinetic energy.

The spectra of figure 5.13(b) indicate very high fluctuation energy between 0 and 10

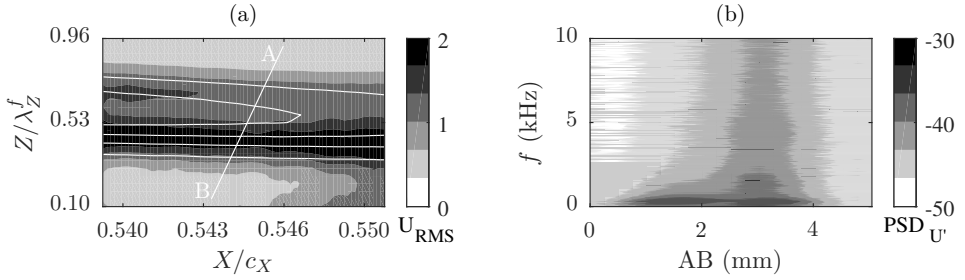


Figure 5.13: (a)  $U$ -velocity field: time averaged (solid lines: 6 levels from 18 to 28  $\text{m s}^{-1}$ ) and standard deviation (shaded: levels in  $\text{m s}^{-1}$ ). The flow comes from left. (b) Power spectral density ( $\delta_f=10$  Hz) of  $U'$ -velocity sampled along the constant-chord (at  $X/c_X=0.545$ ) segment AB (shaded: levels in dB/Hz).

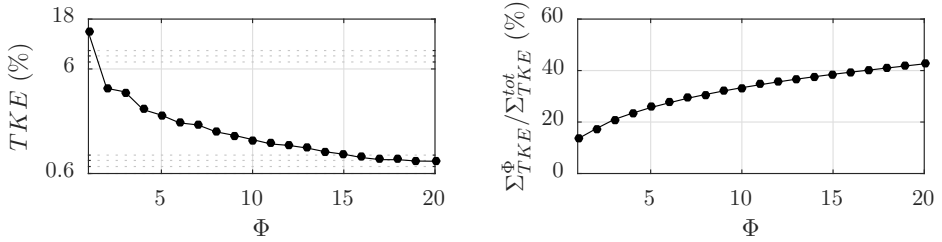


Figure 5.14: POD turbulent kinetic energy (TKE) distribution: values (left) and relative cumulative sum (right) for the first 20 modes.

Hz. It is likely that this energy pertains to the described meandering of the stationary waves and it will be further inspected in the remainder of this analysis. The frequency band  $10 \text{ Hz} \leq f \leq 400 \text{ Hz}$  also features relatively high energy levels. It can be conjectured that the *type-III* mode is the main driver of this particular range. Finally, a third area of significant spectral energy is centred at  $f = 4.5 \text{ kHz}$ , however fluctuations are spreading throughout the spectrum reaching, with still high energy, the highest resolved frequency (i.e. 10 kHz). This band is related to the secondary instability modes generated by the perturbation of the stationary velocity shears [8].

Following the analysis of the tomo-PIV fields, proper orthogonal decomposition of the instantaneous velocity fields is performed to highlight the coherent flow structures. The snapshot POD approach [119] is exploited. The turbulent kinetic energy (TKE) distribution of the first 20 modes is shown in figure 5.14 in both absolute values and relative (w.r.t the total sum) cumulative sum. The first POD mode appears at significant levels of energy. This mode replicates the POD mode 1 discussed in § 5.3.3 as it will be shown later. The remainder POD ensemble indicates the cascade of energy with the first 20 POD modes encompassing more than 40% of the total TKE.

Several POD modes appear paired as indicated by similar energy levels (e.g.  $\Phi_2$ - $\Phi_3$ ,  $\Phi_4$ - $\Phi_5$ ,  $\Phi_8$ - $\Phi_9$ ). Mode pairs in relative phase quadrature are indicative of advecting structures [126]. Serpieri & Kotsonis [114], reported two pairs of modes that were harmonically coupled, comparing the flow topology and estimating the mode frequency from the

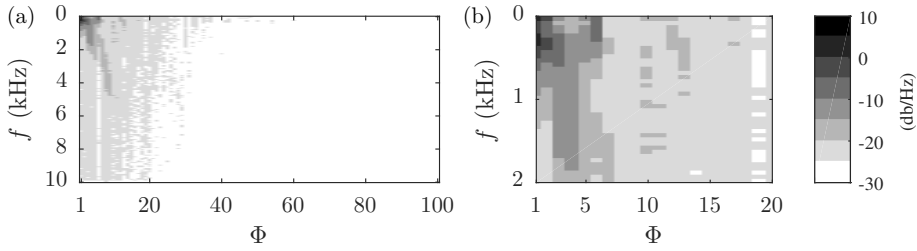


Figure 5.15: Power spectral density ( $\delta_f=50$  Hz) of the time coefficients of (a) the first 100 POD modes and (b) magnified view of the first 20 POD modes.

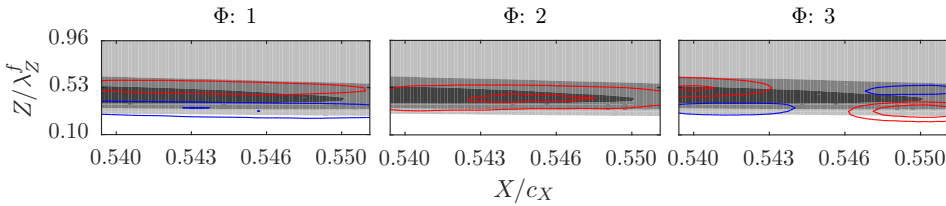


Figure 5.16:  $U$ -velocity field: time averaged (shaded: 5 levels from 18 to 28  $\text{m s}^{-1}$ ) and structures pertaining to different POD modes (shaded: 3 levels between  $-0.05$  and  $-0.005$  red lines and 3 levels between  $0.005$  and  $0.05$  blue lines).

extracted wavelengths, to *type-III* and *type-I* mechanisms. Capitalising on the very high sampling frequency of the current experiment, direct inspection of the modes spectra can be performed. The POD temporal coefficients, derived from the projection of the instantaneous flow-fields on the POD base, are analysed using once again Welch's method. The power spectral density for the first 100 POD modes is shown in the leftmost contour of figure 5.15. The spectra are estimated to a resolution of 50 Hz. It becomes evident that most of the spectral energy density corresponds to the first 20 POD modes (as from figure 5.14). The related fluctuations are mainly confined in the band between 0 Hz and 5 kHz (as shown in figure 5.13(b)). The rightmost contour of figure 5.15 offers a magnified view of this region. The first three modes feature the highest energy density. This is contained within the band 0-500 Hz. However the first five POD modes have also rather high energy levels up to 2.3 kHz. POD modes from 8 to 10 have most of their energy in the band  $3.4 \text{ kHz} \leq f \leq 5.2 \text{ kHz}$ .

The spectral analysis of the temporal POD coefficients (figure 5.15), reveals a close proximity of the pertinent spectral bands for the first three POD modes. These are highly energetic modes in a rather low-frequency band, suggesting their possible interaction. In a physical context, this suggests the existence of a low-frequency modulation described as a whole by POD modes 1 to 3. The flow structures related to the POD spatial eigenfunctions are presented in figure 5.16. POD mode 1 features the same type of structures as the respective POD mode 1 of the tomo-PIV POD. Two elongated lobes, aligned with the stationary vortex shears, define the footprint of the previously described global oscillation of the cross-flow vortices in the spanwise direction. The structure of pod mode 2 is

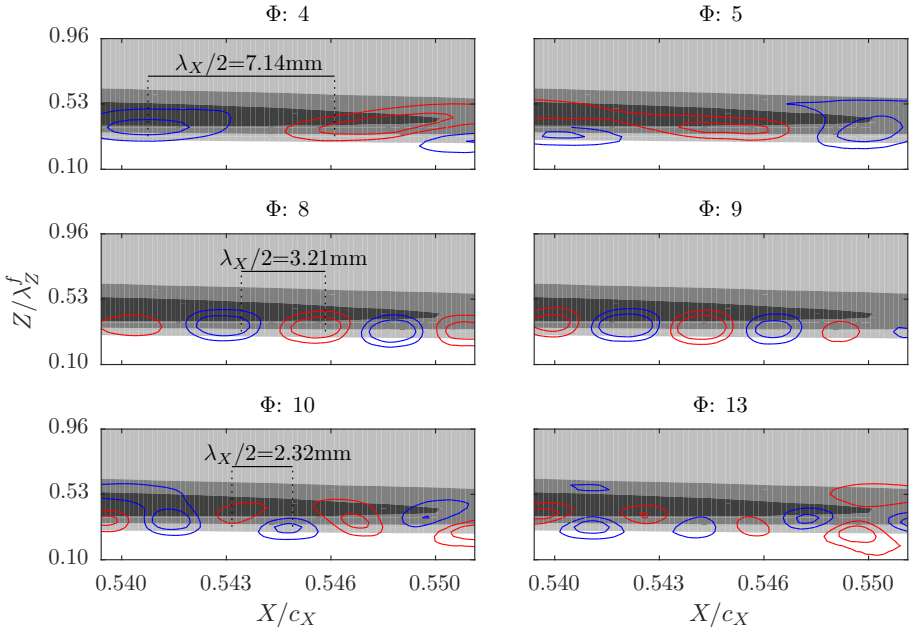


Figure 5.17:  $U$ -velocity field: time averaged (shaded: 5 levels from 18 to 28  $\text{m s}^{-1}$ ) and structures pertaining to different POD modes (shaded: 3 levels between  $-0.05$  and  $-0.005$  red lines and 3 levels between  $0.005$  and  $0.05$  blue lines).

presented in figure 5.16(b). It presents a single lobe aligned with the stationary waves but shifted of  $\pi/2$  with respect to the structures of  $\Phi_1$ . POD mode 3 has instead a quadrupole structure thus indicating a rotation of the stationary waves (see figure 5.16(c)). From these considerations and recalling that the time-coefficients spectra presented in figure 5.15 for  $\Phi_1$ ,  $\Phi_2$  and  $\Phi_3$  occupy the same low-frequency band, it is believed that these three POD modes describe the same flow feature.

As discussed in § 5.3.3, the roughness elements lock the wavelength of the stationary mode but also its onset and position. Therefore, more than a rigid translation of the stationary waves along the span, the POD modes 1, 2 and 3 refer to a small but highly energetic rotation of the vortices about the roughness element.

POD modes 4 and 5 show structures related to *type-III* modes. These are presented

POD modes	Instability mode	$\lambda_X$ (mm)	$f$ (kHz)	$u_X^c$ ( $\text{m s}^{-1}$ )
$\Phi_1 - \Phi_2 - \Phi_3$	<i>CFVs meandering</i>	-	0-0.5	-
$\Phi_4 - \Phi_5$	<i>type-III</i>	14.28	0.5	4.85
$\Phi_8 - \Phi_9$	<i>type-I</i>	6.42	4.00	25.6
$\Phi_{10} - \Phi_{13}$	<i>type-I</i>	4.64	4.85	22.1

Table 5.2: Properties of the analysed POD modes.

in figure 5.17. They show elongated structures extending from the outer upwelling side of the stationary waves to the inner downwelling region. The wavelength of this mode was evaluated from the tomo-PIV fields to be 25 mm along the stationary vortices axes. The structures of  $\Phi_4$  and  $\Phi_5$  have a wavelength of  $\lambda_X=14.28$  mm along the  $X$  direction. The frequency of the *type-III* mode is centred at 500 Hz (§ 5.3.1). However, the hot-wire measurements showed a rather broad band around this frequency. The spectrum presented in figure 5.15 shows a pronounced band centred at 340 Hz thus falling in the frequency band of the *type-III* mode. Comparing the frequency, the wavelength and the topology of the structures of POD modes  $\Phi_4$  and  $\Phi_5$ , it can be concluded that they are related to the *type-III* instability mode.

The POD mode 8 and 9 and 10 and 13, presented in figure 5.17, correspond to KH travelling waves caused by the destabilisation of the strong span-wise shears [8]. The wavelength of the structures related to this mode was evaluated from the tomo-PIV experiment to be 4.6 mm while the frequency to be centred at 5 kHz. The measured wavelengths are  $\lambda_X=6.42$  and 4.64 mm respectively for the two pairs presented in the  $X$  direction. The frequency of these POD modes pairs is 4 kHz for  $\Phi_{8-9}$  and 4.85 kHz for  $\Phi_{10-13}$ . The phase velocity is  $u_X^c=25.6$  m s<sup>-1</sup> for  $\Phi_{8-9}$  and  $u_X^c=22.1$  m s<sup>-1</sup> for  $\Phi_{10-13}$ . Note that despite the different characteristics of these two pairs of POD modes, the topology and their location with respect to the stationary vortex allow to associate them to the *type-I* mode. Furthermore also for this instability mode, the velocity spectrum shown in figure 5.15 reported a rather broad hump comprising the frequencies of  $\Phi_{8-9}$  and  $\Phi_{10-13}$ .

The analysed properties of the described POD modes are summarized in table 5.2. Both wavelengths and frequencies agree with the outcomes of the previous low-speed tomo-PIV measurements thus confirming that POD correctly extracts the main flow mechanisms. Moreover, retrieving the frequencies of the modes from the wavelength, applying Taylor's hypothesis, (approach followed in the tomo-PIV discussion) is proved to give physical outcomes.

## 5.4. CONCLUSIONS

In stationary CFI boundary layers, flow fluctuations of secondary-instability nature undergo sudden growth (e.g. [40, 77, 51, 129, 135]).

Hot-wire scans have been used to inspect fluctuations statistics and the spectra at several chord stations. The three modes discussed in the introduction, namely *type-I*, *type-II* and *type-III*, were individuated and their chordwise evolution was tracked by means of opportune metrics.

The primary stationary CF waves in near proximity to their saturation location has been measured for the first time with tomographic PIV. Comparison between hot-wire and tomo-PIV fields was presented in the previous chapter. The wall region of the measured volume suffered of higher measurement noise and was not considered for the analysis of the unsteady flow field.

Simultaneous volume measurements led to the analysis of the unsteady fluctuations field based on their spatial coherence. POD of the tomo-PIV flow fields led to the individuation of two pairs of modes in clear relative phase quadrature. Inspection of the spatial organisation of these two pairs of modes, in terms of wavelength and location with respect to the stationary CF vortices, was used to infer their correspondence to the

secondary instability modes. The higher energy pair of POD modes refers to *type-III* instability mode arising from the interaction between the travelling and the stationary CF waves [30, 40, 45, 8]. The lower energy pair is instead related to the high-frequency secondary *type-I* mode. The results are in good agreement with the dedicated literature (e.g. [40, 77, 51, 54, 129, 135, 8]). Applying a convection velocity, based on the Taylor hypothesis and justified by previous studies [77, 51, 129, 13, 8], these structures were indeed verified as modes *type-III* and *type-I*, respectively. The estimated frequencies correlated with the hot-wire measurements.

The most energetic mode identified by the POD analysis is of particular interest. It attains alone to a much higher level of energy compared to all subsequent POD modes (about four times larger than the first pair of advecting modes) and presents structures aligned with the spanwise velocity shears. The mode appears as a low-frequency spanwise oscillation of the stationary CF vortices. Comparison with the hot-wire measurements suggests spectral features in the band of  $0.05 \leq St \leq 0.99$  ( $1\text{Hz} \leq f \leq 20\text{Hz}$ ). The exact source of this mode cannot be established from the low sampling rate measurements. It appears that in an experimental framework the stationary CF vortices, despite being fixed by the roughness elements at the leading edge, undergo an oscillatory position shift. The high energy pertaining to this mode is hence ascribed to a mean flow distortion which should be accounted for in experimental investigations.

The use of tomo-PIV allowed detailed investigation of the steady and unsteady modes developing in a swept-wing boundary layer subject to cross-flow instability providing information that spatially uncorrelated measurements can not infer. This led to the description of the three-dimensional spatial organisation and evolution of the unsteady modes. The measurements presented in this study offer an experimental comparison with the results of previous numerical and theoretical studies (e.g. [76, 77, 40, 45, 129, 130, 8]). Despite this, the tomo-PIV investigation did not capture the last stages of the transition process and the turbulent breakdown due to limitations in domain size.

Finally, planar 2C-PIV at the very high-frequency of 20 kHz was employed retrieving a spatio-temporally resolved measurement of the secondary instability modes arising on and eventually breaking down the stationary cross-flow vortices. Spectral analysis of capture velocity fields showed very high energy in the frequency band comprised between 0 and 400 Hz. Moreover, higher energy levels were reported centred at 4.5 kHz. The fluctuations related to these two bands were inspected by means of proper orthogonal decomposition. The POD modes offered a clear representation of the developing low-frequency *type-III* and high-frequency *type-I* secondary mechanisms. This analysis offers a confirmation to Taylor-hypothesis-based advection of the structures measured through tomo-PIV.

The low-frequency oscillation of the stationary vortices reported from the tomo-PIV fields POD, is observed as well with wall-parallel planar PIV. The spectrum of this mode (captured by three POD modes) showed high energy in the lowest resolved band.

# III

## FLOW CONTROL



# 6

## PRIMARY CROSS-FLOW INSTABILITY

*In this chapter, selective forcing of cross-flow instability modes is achieved by means of spanwise-modulated plasma actuators, positioned near the leading edge. In the perspective of laminar flow control, the followed methodology holds on the discrete roughness elements/upstream flow deformation approach. The authority of the actuators in forcing monochromatic stationary cross-flow modes at different spanwise wavelengths is assessed by means of infrared thermography. Moreover, quantitative spatio-temporal measurements of the boundary layer velocity field are performed using time-resolved particle image velocimetry. The results reveal distinct steady and unsteady forcing contributions of the plasma actuator on the boundary layer. It is shown that the actuators introduce unsteady fluctuations in the boundary layer, amplifying at frequencies significantly lower than the actuation frequency. In line with the DRE/UFD strategy, forcing a sub-critical stationary mode, results in less amplified primary vortices and related fluctuations, compared to the critical forcing case.*

---

**J. Serpieri**, S. Yadala Venkata & M. Kotsonis, *Conditioning of cross-flow instability modes using dielectric barrier discharge plasma actuators*, *Journal of Fluid Mechanics*, **833**, 164–205 (2017)

## 6.1. INTRODUCTION

The present study investigates the possibility of conditioning the natural flow arrangement of a transitional swept-wing boundary layer by means of AC-DBD plasma actuators, as the first step towards the UFD approach. While similar in concept to the work of Schuele *et al.* [111] on the supersonic yawed cone and of Dörr & Kloker [24] on the swept-flat plate simulations, the present study is, to the authors knowledge, the first experimental demonstration of plasma flow control on a swept wing at flight-order-of magnitude ( $O(10^6)$ ) Reynolds numbers. The primary objective of this study is, thus, the elucidation of the effects of AC-DBD plasma actuators on the development of CFI transition in view of future efforts towards LFC using plasma actuators. Emphasis is given to the investigation of the actuators steady and unsteady effects on the boundary layer. To this goal, a dedicated experiment making use of high-speed PIV was carried out to characterise the actuator mechanical performance. The effect of actuation on the CFI evolution was investigated by means of infrared thermography and time-resolved PIV measurements. Additionally, a simplified model of the effects of steady forcing on the flow stability is proposed. This approach leverages upon numerical solutions of the laminar stationary boundary layer equations combined with experimentally extracted body force fields and linear stability theory.

## 6.2. EXPERIMENTAL SETUP

The plasma actuators were placed at  $x/c=0.025$ , close to the primary mode critical station (see the LST analysis of section 2.6). The plasma actuators were designed towards forcing a single monochromatic primary cross-flow mode. To force the desired mode, the employed actuators feature one straight electrode, which is exposed to the flow and is powered by the high-voltage supply. The grounded electrode is encapsulated below the dielectric barrier and is made of a series of stems spaced equally from each other and oriented along  $x$  (see figure 2.7a). The spacing between the stems defines the spanwise wavelength of the plasma forcing, and as such the spanwise wavelength of the forced CF modes. Three different modes were forced in this study, namely  $\lambda_z=9$  mm, which corresponds to critical mode [114], and  $\lambda_z=7$  mm and  $\lambda_z=12$  mm, corresponding to sub-critical and super-critical modes respectively.

A detail of the DBD plasma actuators used in this study is presented in figure 2.6b. The covered electrode stems are  $d=10$  mm long and  $w=3$  mm wide. They are projected towards the straight electrode overlapping with it by  $o=2$  mm, in order to ensure consistent plasma formation. Given the relative large length of these stems, the flow ionisation region corresponds only to the electrode overlapping area thus ensuring the desired spanwise modulation of the forced jet. It is important to note that the exposed electrode was placed downstream such to have the induced jet aligned with  $-x$  (see figure 2.7a).

*Kapton* polyimide film of  $50 \mu\text{m}$  thickness was used as dielectric barrier. A second layer of *Kapton* was placed between the actuator and the model surface to better protect the latter. As such, the total thickness of the actuator was measured to be  $125 \mu\text{m}$ . In order to avoid exposure of the incoming flow to a step of such high thickness, the *Kapton* sheet was wrapped around the wing leading edge. This ensured that the only surface perturbation seen by the flow was a two-dimensional backward facing step of  $125 \mu\text{m}$  at

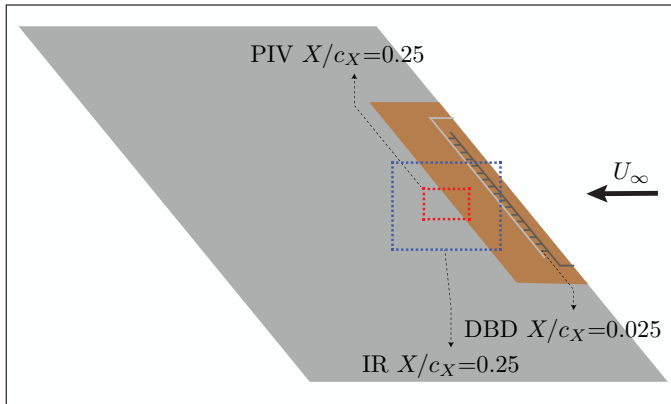


Figure 6.1: Schematic of the wind tunnel model with the actuators (*Krypton* sheet in orange, CE in dark grey, EE in light grey). Definition of the FOVs of the IR thermography (blue dashed rectangle) and of the PIV (red dashed rectangle) experiments.

approximately 10% of the model chord. Preliminary investigations, using PIV and infrared thermography, indicated no adverse effects on the transition location by the physical presence of the actuator on the wing.

The actuator was powered using a *Trek 20/20C HS* high-speed high-voltage amplifier. Depending on the case, the actuation signal was sinusoidal with amplitudes ( $E$ ) between 2 kV and 3 kV. The scope of this study is to prove the applicability of DBD plasma actuators as control devices to condition the spanwise wavelength of primary cross-flow instability modes. As such, the high voltage signal frequency (carrier frequency) was chosen considering the development of unsteady instability modes in the boundary layer. Preliminary linear stability theory analysis (presented in section 2.6) showed that the considered boundary layer is unstable to travelling primary instability modes comprised in the band 0-1 kHz. Therefore for the main tested cases, the actuators were operated at 2 kHz. To decouple the effects of unsteady forcing from the effects of forcing monochromatic CFI modes, a two-dimensional spanwise-uniform actuator was also considered.

### 6.2.1. INFRARED THERMOGRAPHY

The boundary-layer transition evolution was inspected by IR thermography. The model was irradiated by two 1kW halogen lamps placed approximately one meter from the model. The convective heat flux from the wing surface to the flow is a function of the local wall shear. As such, regions of high shear cool more rapidly than respective low-shear regions. Differences in wall temperature captured by the thermal camera can therefore be used for visualisation between laminar and turbulent regions (see also [103]). In addition, using highly sensitive, actively cooled thermal imagers, details in the shear distribution of laminar boundary layers, such as the characteristic streaky footprint of CFVs can be retrieved.

The setup for the IR thermography experiment is presented in the schematic of figure 6.2. The camera was mounted at about 1m distance from the model surface and

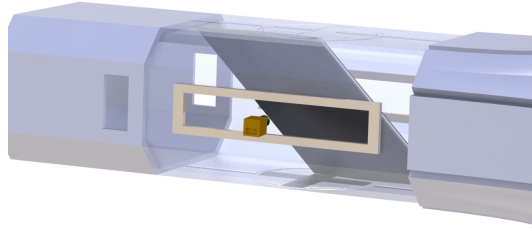


Figure 6.2: Schematic of the IR thermography setup. The flow comes from right. The IR camera (in brown) looks at the model surface (in black) from outside the testing chamber (drawn semi-transparent) through the opportune IR window.

placed outside the wind tunnel, looking through an opportune germanium window. The imaged field of view was  $480 \times 360 \text{ mm}^2$  and centred at  $X/c_X=0.25$ ,  $Z=0$  (see the schematic of figure 6.1, where the IR domain is shown with a dashed blue rectangle). The IR camera used for the current experiment was a *CEDIP Titanium 530L*, featuring a mercury-cadmium-telluride quantum sensor with  $320 \times 256 \text{ px}^2$ . The sensor is actively cooled by means of a Stirling cycle to the working temperature of 77 K resulting to a Noise Equivalent Temperature Difference (NETD) of less than 18 mK. The integration time and the operated frame rates were  $200 \mu\text{s}$  and 100 Hz respectively. The camera was equipped with a 25 mm focal length germanium lens operated at  $f_{\#}=2.0$ .

Being the scope of this experiment the visualization of the boundary-layer transition process, no quantitative thermography is required. As such the results are presented as raw output from the thermocamera and no calibration to transform them in temperature data is applied.

### 6.2.2. PARTICLE IMAGE VELOCIMETRY

Particle image velocimetry was performed towards quantification of the boundary layer velocity field. Planar high-speed PIV was chosen for this experiment. The inspected planes are along the  $X - Z$  directions and are placed at a distance of 1.5 mm from the model surface. The planes are centred with the station  $X/c_X=0.25$ - $Z=0$  of the model (see the schematic of figure 6.1, where the PIV domain is shown with a dashed red rectangle).

The PIV experimental setup is presented in figure 6.3. As shown, the camera was imaging the field of view (FOV) from outside the wind tunnel through available optical windows and was placed at approximately 1m distance from the measured plane. The camera used in this experiment is a *Lavision Imager HS* featuring a sensor of  $2016 \times 2016 \text{ px}^2$  and pixel size of  $11 \mu\text{m}$  and 12 bits of digital resolution. The active image sensor was reduced to  $1632 \times 496 \text{ px}^2$  for the current experiment. The imager was equipped with a *Nikon Nikkor 200 mm micro* lens operated at  $f_{\#}=5.6$ . The resulting magnification factor of the PIV experiment is  $M=0.24$ . Illumination was provided from downstream as shown in the schematic of figure 6.3. A Nd:YAG high speed *Continuum Mesa PIV* laser (18 mJ per pulse) was employed for particles illumination. The light beam was opportunely shaped into a sheet of approximately 1 mm thickness. The light sheet was oriented such to be parallel to the model surface for all the imaged domain as shown in figure 6.4. In the

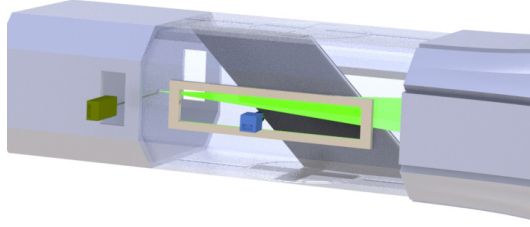


Figure 6.3: Schematic of the PIV setup. The flow comes from right. The camera (in blue) looks at the illuminated region (in bright green) from outside the testing chamber (drawn semi-transparent) through the opportune optical window. The laser head is also shown (in dark green) and illumination comes from downstream.

schematic the AC-DBD plasma actuator is also shown. The *Kapton* sheet is in light grey and the electrodes in dark grey. To note that this is the wing cross-section orthogonal to the leading edge direction.

The flow was seeded using *Safex* water glycol injected downstream of the testing chamber. The average particle diameter is  $1 \mu\text{m}$ . Synchronization of the system was guaranteed by using the *LaVision Davis 8.2* suite and a *LaVision High Speed Controller* unit. Image acquisition, pre-processing and correlation were performed with the same software. Cross-correlation was performed with final interrogation windows of  $24 \times 24 \text{ px}^2$  with relative overlap set to 75%. As such the final vector spacing was approximately 0.27 mm in both  $X$  and  $Z$ . The time interval between the two laser pulses was set to  $15 \mu\text{s}$  such to give an average particle displacement in the free stream of 15 px. The measurement frame rate (FR) was 3000 Hz and sequences of 6000 image pairs were acquired, for every tested flow case. The resulting measurement time was 2 s.

The correlation random error in planar PIV is estimated to be 0.1 px [95]. Therefore the random error, relative to the free stream velocity, is  $\varepsilon_{(U,V)} = 0.1/15 = 0.007$ . This is also the measurement error for the statistic velocity fluctuations fields (i.e.  $\{U'_t, V'_t\}_{RMS}$ ). Here  $U'_t$  and  $V'_t$  are the time velocity fluctuations (i.e. after subtracting the time-average). The uncertainty on the time-averaged velocity fields is retrieved from the flow fluctuations magnitude, estimated to be less than 10% of the free stream velocity, and from the measurement ensemble size ( $ES$ ):  $\varepsilon_{(\bar{U}, \bar{V})} = 0.1/\sqrt{ES}$ , where the overbar denotes time-averaging. The ensemble size to be considered here does not encompass all the 6000 captured fields. These are correlated in time with respect to the travelling instability modes, which account for most of the fluctuation energy at the measurement location [114]. The fluctuations related to this instability feature high energy content in the frequency band  $100 \text{ Hz} \leq f \leq 400 \text{ Hz}$  [114]. Therefore a conservative time sub-sampling of the measured fields is required in order to formally render them uncorrelated in time. This factor can be estimated as  $\text{FR}/\min(f_{(U'_t, V'_t)}) = 3000 \text{ Hz}/100 \text{ Hz} = 30$  and is used to estimate the uncorrelated ensemble size as a fraction of the total of the captured samples:  $ES_u = ES/30 = 200$ . Finally, the uncertainty on the time-averaged velocity fields can be evaluated as  $\varepsilon_{(\bar{U}, \bar{V})} = 0.1/\sqrt{ES_u} \approx 0.018$ .

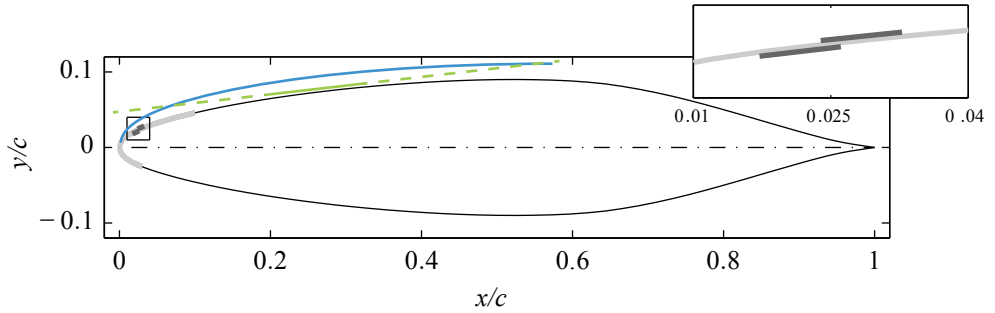


Figure 6.4: Wing section and schematic (not to scale) of the laser light (light green) and of the boundary layer (cyan). The AC-DBD plasma actuator is also shown: *Kapton* sheet in light grey; electrodes in dark grey. Inset: magnified view of the actuator. The wing section is orthogonal to the leading edge.

### 6.2.3. AC-DBD PLASMA ACTUATOR

In this section, the mechanical performance of the used actuators is quantified. The spanwise-uniform 2D actuator is chosen for this analysis, simplifying the flow field to a two-dimensional arrangement. The identified amplitude effects are expected to reasonably describe the performance of the spanwise-modulated actuators, considering that their electrode width ( $w$ ) remains constant. The characterisation is carried out in quiescent flow. Planar high-speed PIV was employed to measure the induced velocity and compute the actuator body-force and the related thrust (for details on the body force extraction methods see Kotsonis *et al.* [58]). Furthermore, spectral analysis of the unsteady flow-field is presented to infer the unsteady flow-field induced by the actuators.

#### EXPERIMENTAL SETUP

The camera, laser and synchronisation equipment used for this experiment are the same as described in 6.2.2. For this experiment, the camera's active sensor was reduced to  $960 \times 440$  px<sup>2</sup> to increase its maximum frame rate. The camera was equipped with a Nikon Nikkor 200mm macro lens operated at  $f_{\#}=8$ . The magnification factor was  $M=1.14$ . The air in the closed box was seeded with droplets of paraffin oil,  $1 \mu\text{m}$  in average diameter, generated by a *TSI Atomizer* nozzle. The coordinate system used in this experiment is represented by the symbols  $x_p, y_p, z_p$  (see figure 2.7a). The system is arranged such that the  $x_p$  axis is in the direction of the induced jet (i.e. orthogonal to the electrodes length), the  $y_p$  is perpendicular to the plane of the actuator and  $z_p$  is along the length of the electrodes. The plasma actuator was installed in a transparent acrylic-glass box enclosing a volume of  $0.25 \text{ m}^3$  (1 m long along  $x_p$ ). The plane inspected with PIV is aligned with  $x_p - y_p$ , given the uniformity of the induced flow field along  $z_p$ . The laser, camera and transparent box were installed on a pneumatically stabilised table (i.e. an optical table) to avoid vibrations on the setup which could be detrimental for such high magnification planar PIV experiment. Cross-correlation was carried out with final interrogation windows of  $24 \times 24$  px<sup>2</sup> with relative overlap set to 75%. As such, the final vector spacing was approximately  $0.053 \text{ mm}$  in both  $x_p$  and  $y_p$  directions. The system was operated at acquisition rate of  $10 \text{ kHz}$  in single-frame mode thus the pulse separation between the correlated frames was  $100 \mu\text{s}$ .

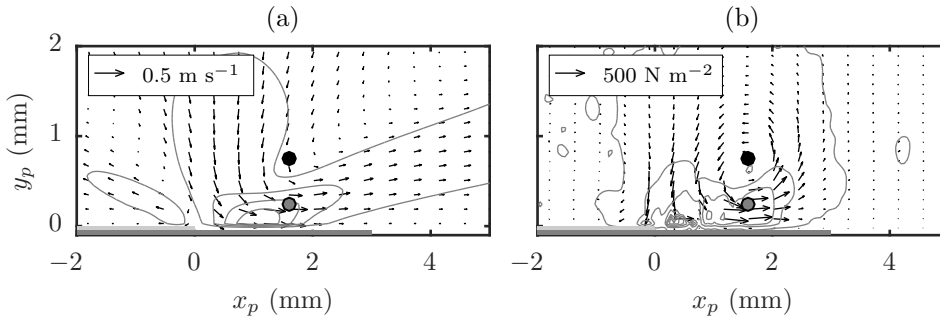


Figure 6.5: (a) Time-averaged velocity magnitude field (grey solid lines: 5 levels, from 0 to  $0.6 \text{ m s}^{-1}$ ). (b) Body force magnitude field (grey solid lines: 5 levels, from 50 to  $1000 \text{ N m}^{-2}$ ). Vectors:  $x_p - y_p$  components of the respective contour variables (reference vector in the upper left corner). AC-DBD actuator operated at  $f_f=2 \text{ kHz}$  -  $E=3 \text{ kV}$ . The two horizontal grey lines below  $y_p=0$  represent (to scale) the electrodes of the actuator. The markers at  $x_p=1.6 \text{ mm} - y_p=0.25$  (grey) and  $0.75 \text{ mm}$  (black) refer to figure 6.6.

Sequences of 25000 images were acquired for each test case for a total measurement time of 2.5 s. The measurement started prior to plasma actuation thus capturing the initial flow acceleration phase.

### PERFORMANCE

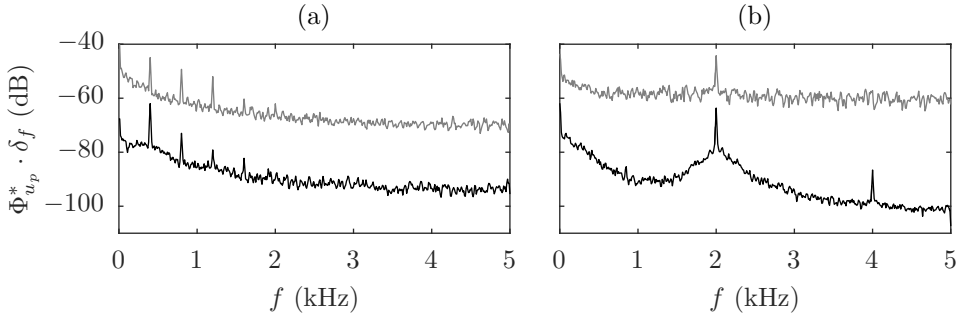
In quiescent flow environments, when the actuator is supplied with the voltage signal, the strong electric field established between the electrodes ionises and accelerates the air molecules. The incompressible Navier-Stokes momentum equation is used to retrieve the induced body force. In this very initial regime, advection, diffusion and pressure terms are negligible with respect to the unsteady acceleration and body force terms. Following [58], under the specified assumptions, the momentum equation reduces to  $\vec{F} = \rho \partial \vec{U} / \partial t$ , where  $\vec{F}$  is the body force and  $\vec{U}$  the velocity. Lowpass filtering of the measured velocity signal was applied in order to eliminate high frequency oscillations associated with the AC voltage frequency. In addition to the body forces, the time-averaged velocity field is computed, after the induced jet has fully developed, from the measured time series and presented in figure 6.5 for the cases of  $f_f=0.4 \text{ kHz} - E=3 \text{ kV}$  and  $f_f=2 \text{ kHz} - E=3 \text{ kV}$ .

The induced jet originates in the vicinity of the inner edge of the exposed electrode and is mainly aligned with the  $x_p$  direction. The wall-normal velocity component, at the electrodes interface, supplies the mass for the wall-parallel jet [58]. A secondary wall-parallel jet, oriented opposite to the main velocity, is observed on top of the exposed electrode. This secondary jet is not observed with the usual copper electrode actuators and can be caused by the extremely low thickness of the employed actuators building up a competing electrical field. A confined region of negative  $x_p - y_p$  body force is also observed. The body force field is overall rather weak, for the tested conditions, and predominant along the  $x_p$  direction [56].

Spatial integration of the body-force field retrieves the exerted specific (i.e. per actuator unit length) thrust. This is eventually used to compute the momentum coefficient, according to equation 2.26, which is used to compare the actuators forcing authority for the different forcing conditions, where the local (at the actuator position) boundary layer

Voltage $E$ (kV)	Frequency $f_f$ (kHz)	$T_{x_p}$ (mN/m <sub>act</sub> )	$C_\mu$
3	0.4	0.0118	0.013
2	2	0.351	0.037
3	2	0.432	0.046

Table 6.1: AC-DBD actuator induced thrust and momentum coefficient.

Figure 6.6: Non-dimensional normalised power spectra of the actuators induced velocity  $u_p$  ( $\Phi_{u_p}^* \cdot \delta_f / U_\infty^2$ , see equation 2.20,  $\delta_f=10$  Hz) at the position of the markers ( $x_p=1.6$  mm -  $y_p=0.25$  (grey) and  $0.75$  mm (black)) in figure 6.5 (grey curve displaced by +10 dB for visualization). (a)  $f_f=0.4$  kHz -  $E=3$  kV, (b)  $f_f=2$  kHz -  $E=3$  kV.

edge velocity  $u_e=14$  m s<sup>-1</sup> and momentum thickness  $\vartheta_u=7.81 \cdot 10^{-2}$  mm are extracted from the boundary layer numerical solution for the investigated case.

The thrust generated by the plasma actuator along  $x_p$  and the respective momentum coefficient for the different test cases considered in this study are presented in table 6.1. When the actuator is operated at  $f_f=2$  kHz -  $E=3$  kV, the horizontal component of the thrust generated is  $T_{x_p}=0.432$  mN/m<sub>act</sub> and the momentum coefficient is  $C_\mu=0.046$ . This is the combination of supplied voltage and frequency that leads to the strongest induced jet. When the frequency is reduced to 400 Hz, the performance of the actuator is reduced. Similarly, decreasing the voltage amplitude to 2 kV at the same operated frequency of 2 kHz, lowers  $C_\mu$ .

For all the investigated configurations of table 6.1, the generated thrust is comparatively less than what reported by Chernyshev *et al.* [14] and Dörr & Kloker [22] in their respective studies. However, in the current study, the AC-DBD plasma jets are used in a respective fashion to isolated roughness elements for DRE/UFD flow control. In such a configuration, the actuators are used to induce a weak localised perturbation of the incoming flow thus requiring only moderate forcing amplitudes. The specific thrust applied by the actuators used by Dörr & Kloker [24] for the same purpose, is comparable to the values reported here.

Capitalising on the high sampling rate of the employed PIV method, access to the unsteady and spectral features of the plasma-induced flow-field is gained. Spectral analysis of the velocity fluctuations, at two points at  $x_p=1.6$  mm -  $y_p=0.25, 0.75$  mm (markers in figure 6.5(a)), was carried out for the two different frequencies at which the actuators were operated (0.4 and 2 kHz). The results are shown in figure 6.6. The spectra

Wavelength: $\lambda_f$ (mm)	Forcing typology	Frequency: $f_f$ (kHz)	Voltage: $E$ (kV)
-	unforced	-	-
0	2D	2	3
9	3D critical	2	3
7	3D sub-cr.	2	3
12	3D super-cr.	2	3
9	3D cr. lower frequency	0.4	3
9	3D cr. lower amplitude	2	2

Table 6.2: Tested flow cases.

are normalised according to equation 2.20 and non-dimensionalised with  $U_\infty^2$  thus they directly show the relative kinetic energy per frequency band. They reveal strong unsteady fluctuations at the respective carrier frequency as well as higher harmonic. Moreover, low frequency fluctuations close to the wall are observed. These can be attributed to a range of factors including plasma-induced thermal disturbances, measurement noise and unstable plasma formations. The exact origin of these fluctuations is beyond the scope of this study, however should be taken into account in the future for a complete characterisation of the plasma effect. Moreover, it is currently unclear to what extent these low frequency fluctuations would be present also on the wing mounted configuration under external flow condition. Such study will require a dedicated effort that goes beyond the scope of this study.

### 6.3. TEST CASES

Six forced flow cases are analysed in this study in addition to the unforced flow case. The first case corresponds to two-dimensional uniform forcing, enabled by a spanwise-invariant actuator. This is followed by three spanwise-modulated forcing cases at critical ( $\lambda_f=9$  mm), sub-critical ( $\lambda_f=7$  mm) and supercritical ( $\lambda_f=12$  mm) wavelengths. Notwithstanding the forced mode, the actuators were installed at identical locations ( $x_f/c=0.025$ ). The actuators were supplied with a sinusoidal signal at  $f_f=2$  kHz and with voltage amplitude of  $E=3$  kV (i.e. voltage peak-to-peak of 6 kV). The choice for the forcing frequency was based on the considerations in section 6.2.3. More specifically, the frequency was chosen to be 2 kHz such to lie considerably above the LST-predicted unstable CFI band of  $0 < f < 1000$  Hz. In addition to the aforementioned cases a low frequency and low amplitude case were considered. For the low-frequency case, the voltage amplitude is kept to  $E=3$  kV but the frequency is reduced to 400 Hz thus in the range of the amplified primary CFI (§ 2.6). For the low-amplitude case, a signal of reduced voltage ( $E=2$  kV) and same frequency (2 kHz) was inspected in order to elucidate the amplitude effects. The two additional cases were considered only for the critical wavelength actuator ( $\lambda_f=9$  mm). The parameters of the tested cases are summarised in table 6.2.

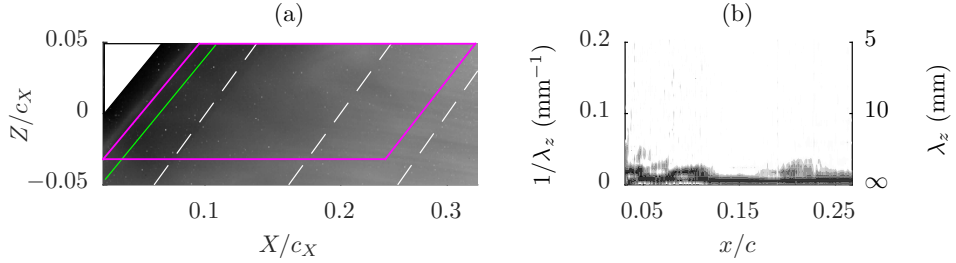


Figure 6.7: Natural transition flow case. (a) IR thermography fields. The flow comes from left. The solid (green) line divides the figure in two regions where different contrast levels are used. The dashed white lines are constant chord lines at  $x/c=0.1, 0.2$  and  $0.3$ . The region enclosed with the solid (magenta) lines refers to figure 6.7b. (b) Wavenumber power spectral density of the IR pixels intensity along the chord. The analysis is performed in the region within the solid (magenta) lines of figure 6.7a.

## 6.4. RESULTS AND DISCUSSION

In the following sections, the discussion of the results of the IR visualization and high-speed PIV experiments is presented. The last section presents a simplified model to estimate the effect of plasma actuators forcing on the boundary layer stability.

### 6.4.1. INFRARED FLOW VISUALISATION

In this section, flow visualisation results using IR thermography are presented. The IR fields will be used to inspect the effectiveness of the developed actuators in controlling and conditioning the stationary CFI modes. For all discussed results, geometrical mapping of the captured images was applied to account for the curvature of the model and the perspective effects from the camera.

The IR flow visualisation for the natural transition flow (i.e. with no boundary layer forcing) is presented in figure 6.7a. To enhance the signal-to-noise ratio of the measurements, time-averaging of the captured thermography fields was performed over the sampled period (300 samples). The flow shows strong homogeneity in both the spanwise and chordwise directions. For the considered model (i.e. geometry and surface roughness), angle of attack, Reynolds number and free stream turbulence level no strong CFI modes are amplified in the inspected range and the boundary layer remains laminar until the most downstream station inspected. To further analyse the spatial and spectral arrangement of the boundary layer from the IR image, the individual pixel intensities within the solid (magenta) lines depicted in figure 6.7a were sampled and analysed in the wavenumber spectral domain. This procedure was performed along constant chord lines. The power spectral density ( $\Phi$ ) was computed using Welch's algorithm [133]. The wavenumber resolution of the spectra is  $0.006 \text{ mm}^{-1}$ . The results are presented in figure 6.7b. No stationary modes appear above the measurement noise level for the unforced flow case.

The IR fields for the four actuators operated at  $f_f=2 \text{ kHz}$  -  $E=3 \text{ kV}$  ( $C_\mu=0.046$ ) are shown in figure 6.8. The plasma regions initiated by the actuators are clearly visible in the images close to the leading edge as localised regions of increased thermal radiation. This is mainly attributed to a weak heating effect of the model surface directly beneath

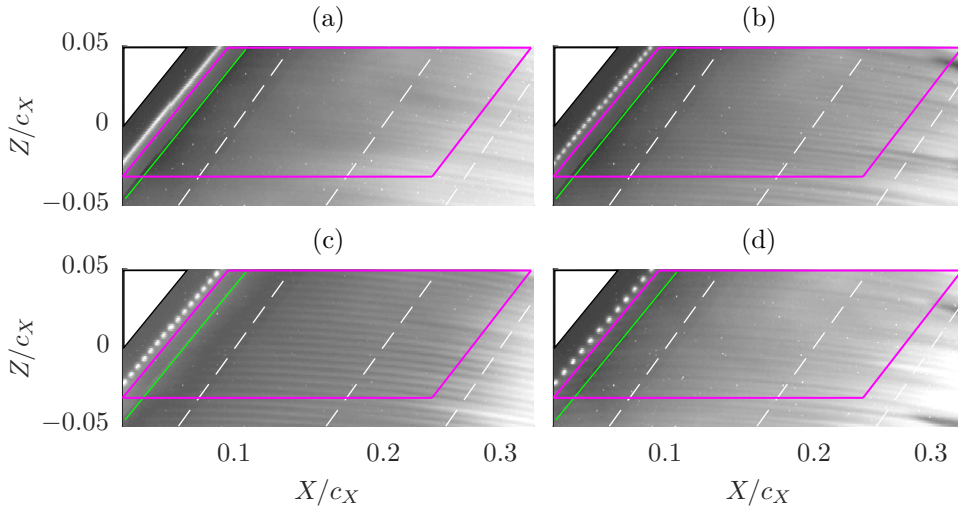


Figure 6.8: IR thermography fields. Actuators operated at  $f_f=2$  kHz -  $E=3$  kV ( $C_\mu=0.046$ ): (a) Spanwise-uniform forcing; (b) sub-critical forcing ( $\lambda_f=7$  mm); (c) critical forcing ( $\lambda_f=9$  mm); (d) super-critical forcing ( $\lambda_f=12$  mm). The regions enclosed with the solid (magenta) lines refer to figure 6.9.

the plasma formation as reported by [56]. In the case of spanwise-uniform forcing (figure 6.8a), the plasma manifests as a bright continuous line in the  $z$  direction. When the spanwise-modulated forcing is applied (figures 6.8b,c and d), the localised plasma regions spaced at the respective forced wavelength appear as a sequence of bright spots. Due to the high IR intensity of the plasma formation, intensity equalisation (de-saturation) has been applied to facilitate observation of IR intensity distribution downstream of the actuators (the solid (green) line in the fields divide the images in two regions with different contrast settings).

For the two-dimensional forcing, the flow does not exhibit significant alteration of the stationary vortices, compared to the unforced case. Eventually, moving more downstream, stationary waves do take place however their intensity and spacing appear uneven along lines parallel to the leading edge. No clear transition fronts, within the imaged FOV are evident in this flow case. When spanwise-modulated forcing is applied, the thermal footprint of primary instability modes becomes more visible in the IR fields. The resulting streaks appear locked to the spacing and the position of the plasma regions. Their relative intensity is also more uniform along constant-chord lines, further suggesting conditioning of both wavelength and amplitude of the stationary cross-flow vortices by the plasma actuator. Overall, for the spanwise modulated forcing, a more uniform flow topology is established with evident monochromatic structures present in the more upstream portion of the wing. Additionally, in figures 6.8b and d the appearance of turbulent wedges at the most downstream portions of the FOV suggest advancement of the transition front due to actuation.

The IR pixels intensity spectra for the flow cases of figure 6.8 are presented in figure 6.9. When spanwise-uniform forcing is applied, no dominating stationary modes are

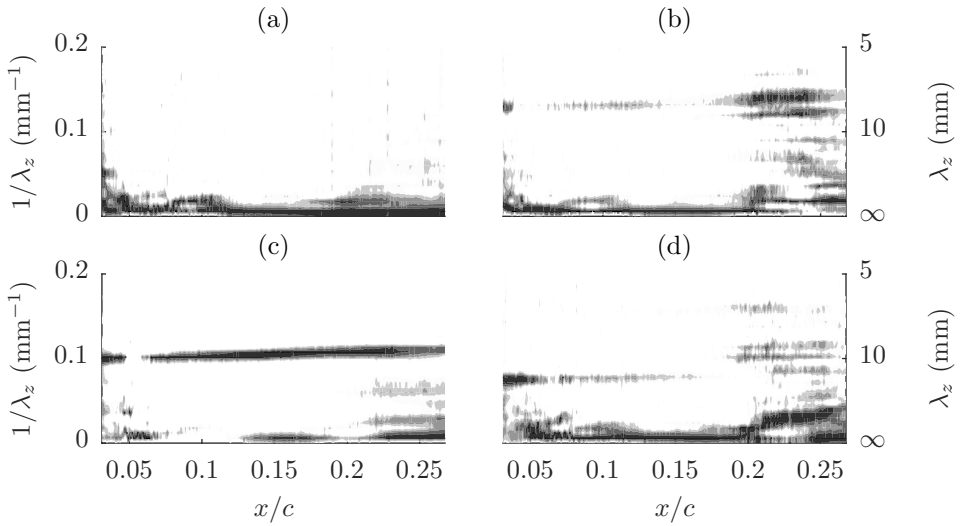


Figure 6.9: Wavenumber power spectral density of the IR pixels intensity along the chord. Same cases as figure 6.8.

present in the upstream portion of the FOV similar to the unforced flow case of figure 6.7. In the most downstream region, the spectrum shows weak energy levels corresponding to the development of some coherent streaks as shown in figure 6.8a. When spanwise modulated forcing is applied, the wavenumber spectra reveal the presence of harmonic peaks closely aligned to the forced wavelength. Comparing the spectra of figures 6.9b-d to the respective IR images in figures 6.8b-d it becomes apparent that the selective forcing at the plasma wavelength effectively conditions the formation of the stationary cross-flow vortices at approximately the same wavelength. This is especially evident for the  $\lambda_f=7$  mm and 9 mm actuators fields. Moreover, it is shown that the critical mode ( $\lambda_z=9$  mm) is the most receptive to leading edge forcing, showing the highest spectral energy levels throughout the inspected domain. When the sub-critical  $\lambda_z=7$  mm waves are forced (figures 6.9b), the most downstream portion of the domain shows a much broader spectrum with longer wavelengths modes being amplified. Finally, when the  $\lambda_z=12$  mm mode is forced (figures 6.9d), stationary waves at the forced wavelength are amplified. From  $x=0.19c$ , a super-harmonic mode with double wavenumber (wavelength of  $\approx 6.1$  mm) is also captured. Amplification of superharmonic modes is a commonly observed feature in CFI boundary layers [97] related to non-linear interaction between primary modes [39]. Energy at wavelengths of 10 mm and 9 mm is also captured downstream of  $x=0.19c$ .

The wavenumber spectra equivalent to those presented in figure 6.9 are presented in figure 6.10 for the spanwise modulated actuator of  $\lambda_f=9$  mm operated at the lower (400 Hz) frequency and at the lower voltage (2 kV). When the actuator is operated at  $E=3$  kV -  $f_f=400$  Hz ( $C_\mu=0.013$ ) (figure 6.10a), spectral energy at the forced wavelength (9 mm) is weakly observed only in the range  $0.18 \leq x/c \leq 0.22$  however this mode does not dominate the boundary layer and longer wavelength modes are strongly amplified. The

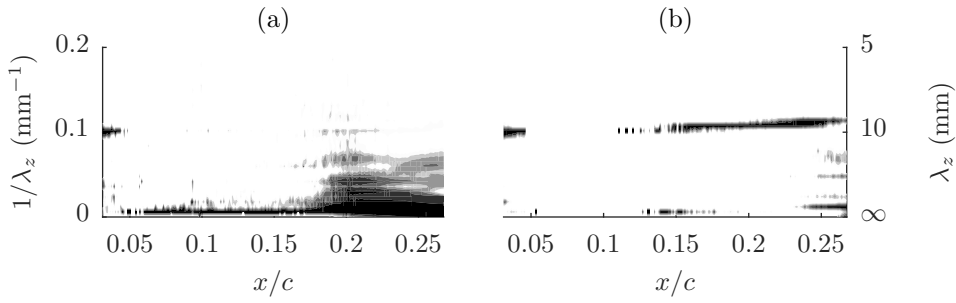


Figure 6.10: Wavenumber power spectral density of the IR pixels intensity along the chord.  $\lambda_f=9$  mm actuator operated at: (a)  $f_f=0.4$  kHz -  $E=3$  kV ( $C_\mu=0.013$ ); (b)  $f_f=2$  kHz -  $E=2$  kV ( $C_\mu=0.037$ ).

apparent weakness of the spectral coherence in this case, is attributed to the frequency of the applied forcing, which falls in the band of the primary travelling modes as predicted by LST (section 3.4a). In these conditions, the eventual presence of strongly amplified unsteady vortices dominate over the stationary CFI. Furthermore, at these operational parameters, the momentum coefficient of the actuator (table 6.1) attains the lowest values among the tested cases. For the  $E=2$  kV -  $f_f=2$  Hz ( $C_\mu=0.037$ ) case (figure 6.10b), the spectrum replicates similar features of the  $E=3$  kV -  $f_f=2$  Hz ( $C_\mu=0.046$ ) case (see figure 6.9(c)) albeit with lower energy levels. This indicates the possibility of adjusting the forcing amplitude of the actuators by tuning the supplied voltage, corroborating the observations of Schuele *et al.* [111] (further analysed in the remainder).

#### 6.4.2. VELOCITY FIELD

In this section, the results of the high-speed PIV investigations are presented. The effect of the plasma forcing on the primary instability is quantified by means of the velocity field statistics. The spatio-temporal evolution of the unsteady flow field is further elucidated through spectral and proper orthogonal decomposition analyses.

##### TIME-AVERAGED FLOW TOPOLOGY

The time-averaged  $U$  velocity fields for the different test cases are presented in figure 6.11. Figure 6.11a shows the unforced flow. The actuator is mounted on the wing but is not supplied with voltage. The boundary layer, within the imaged domain, is still laminar and slightly modified by natural CFI mechanisms as seen in figure 6.7. The appearance of stationary vortices is observed in the presented velocity field as a weak velocity modulation along the span.

When two dimensional forcing is applied (figure 6.11b), the flow drastically rearranges. The overall magnitude of velocity is reduced, showing a thickening of the boundary layer. Moreover, the velocity local minima are now more distinguishable, suggesting the enhancement of the stationary primary vortices. When spanwise modulated forcing is applied (figure 6.11c,d and e), separate and more uniform stationary vortices become clearly visible. The spanwise spacing, along a line parallel to the leading edge (segment AB in the contours) can be compared to the actuated wavelength. The velocity spanwise fluctuations ( $\overline{U}'_z$ ) are presented in the inset of figure 6.11, further reconciling with the

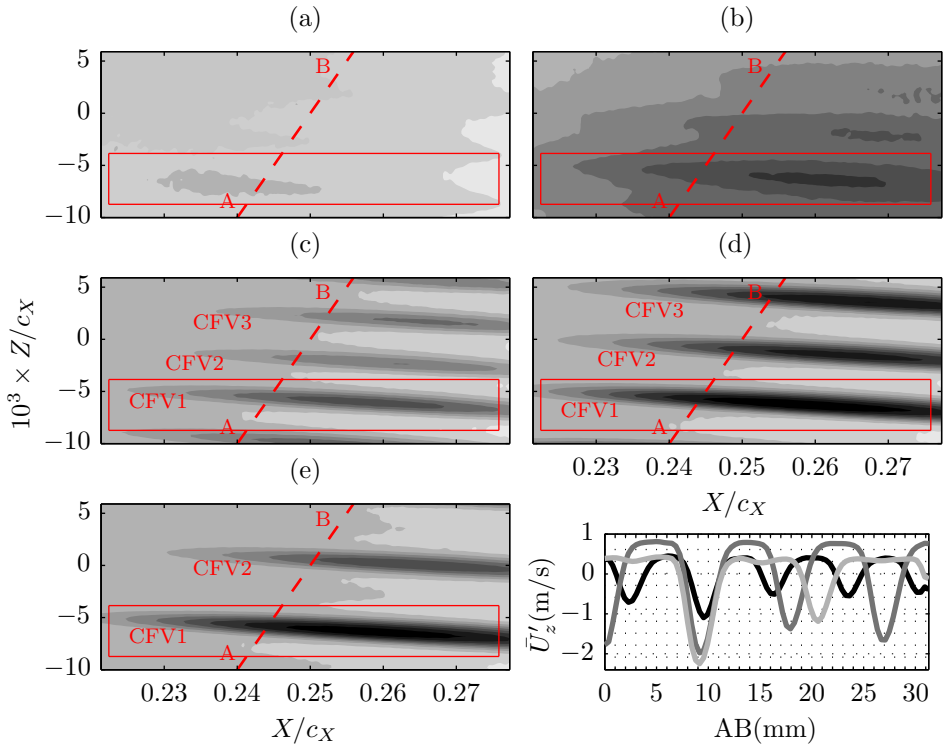


Figure 6.11: Time-averaged  $U$  velocity fields (10 levels, from 0.84 (black) to  $1 U_\infty$  (white)). The flow comes from left. (a) actuator non operated; (b) spanwise-uniform forcing; (c) sub-critical forcing ( $\lambda_f=7$  mm); (d) critical forcing ( $\lambda_f=9$  mm); (e) super-critical forcing ( $\lambda_f=12$  mm). Actuator operated at  $f_f=2$  kHz -  $E=3$  kV ( $C_\mu=0.046$ ). The (red) lines and labels refer to analyses presented in the remainder. Inset: spanwise-fluctuation of the  $\bar{U}'_z$  velocity signal sampled along the line AB in fields: (c) black, (d) dark grey, (e) light grey line.

outcomes of the flow visualisation experiment of § 6.4.1. When the super-critical mode ( $\lambda_f=12$  mm) is forced, the superharmonic mode seen before in figure 6.17e becomes evident, downstream of  $x/c = 0.25$ , in the regions in between the stronger CFVs. The lower side of the presented flow fields always shows lower velocities in comparison to the upper region. This effect is attributed to a possible small inclination of the laser sheet (i.e. rotation about the  $X$  axis), such that the lower illuminated region is slightly closer to the wall.

Inspecting the fields pertaining to the three different forced wavelengths shows that, when critical forcing is applied, the vortices appear more developed than the sub-critical and super-critical forcing cases. In fact it can be seen that the velocity minima corresponding to the low-momentum region attain the lowest values for the  $\lambda_f=9$  mm vortices. In addition, the spatial evolution of the stationary waves can be quantified by computing their amplitude as defined by equation 6.1 ([135] and [114]),

$$A^{CFV}(x) = \left\{ \left( \bar{U}'_z(x) / U_\infty \right) \Big|_{y_t=y_t^{PIV}} \right\}_z \quad (6.1)$$

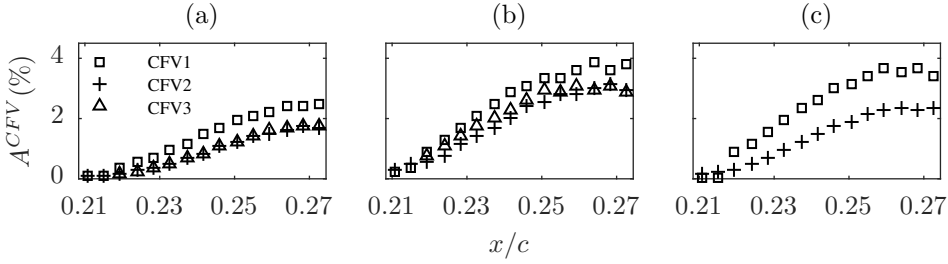


Figure 6.12: Spatial evolution of the individual vortices of figure 6.11c, d and e computed from equation 6.1. (a) sub-critical forcing ( $\lambda_f=7$  mm); (b) critical forcing ( $\lambda_f=9$  mm); (c) super-critical forcing ( $\lambda_f=12$  mm).

As evident in figure 6.11, ensembles of two to three individual vortices are available through the PIV measurements. Due to the fixed FOV, the number of fully resolved vortices is dependent on the forcing wavelength. For the calculation of the amplitudes, the individual vortices are tracked in their spatial evolution. The estimated amplitudes for the individual vortices in the spanwise-modulated forcing cases (figure 6.11c-e) are shown in figure 6.12a-c respectively.

Within the imaged field, the stationary vortices show similar growths despite the different amplitudes. Forcing the critical mode at  $\lambda_f=9$  mm leads to more developed waves compared to the other two modes, especially with respect to the sub-critical mode, in both initial amplitude and spatial amplification. These results, which match with the stronger energy shown for this mode in the IR spectra (figure 6.9), confirm that forcing sub-critical modes leads to less amplified stationary vortices (see e.g. Reibert *et al.* [97], Malik *et al.* [77] and Wassermann & Kloker [129]). All the fields show monotonic growth of the stationary vortices. However, the amplitudes appear to saturate at the most downstream portion of the fields. This is expected from boundary layers dominated by stationary CFVs undergoing laminar-to-turbulent transition [39, 114]. However, it has to be clarified here that performing this analysis on planes at constant distance from the model wall has some limitations. In fact, moving downstream, the stationary waves grow and so does the boundary layer (see the schematic of figure 6.4). Hence, moving downstream at a constant wall-normal position, the measurement plane intersects the stationary vortices in a lower region where the velocity modulation effect is milder. This results, when using the metrics of equation 6.1, in lower amplitudes. Therefore the growth rates of the stationary CF vortices should be retrieved from full three-dimensional fields [97, 39, 135, 129, 114]. Despite these observations, the effect is rather mild within small chordwise domains, such as the one considered here.

An additional consideration in the analysis of figure 6.12, relates to the fact that the mean flow distortion of the considered fields caused by the primary CFVs is not even. In fact, more developed vortices modify the mean flow more significantly. A way to inspect this effect is proposed here by comparing the measured spanwise-mean velocity magnitude ( $z_{mean}\{\bar{V}^{tot}\}_{y_t=y_t^{PIV}}$ ) from the velocity fields of figure 6.11 (sampled along the AB segment) and the undisturbed boundary layer numerical solution (described in section 2.5). The outcomes of this comparison are presented in figure 6.13. Evidently, the

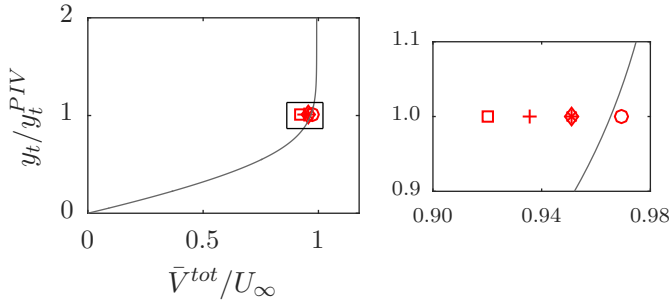


Figure 6.13: Comparison between the measured spanwise-mean velocity magnitude ( $z_{mean}\{\bar{V}^{tot}\}_{y_t=y_t^{PIV}}$ ) from the velocity fields of figure 6.11 (symbols) and the boundary layer numerical solution (solid line) at  $x/c=0.25$ . (○) actuator non operated; (□) spanwise-uniform forcing; (\*) sub-critical forcing ( $\lambda_f=7$  mm); (+) critical forcing ( $\lambda_f=9$  mm); (◇) super-critical forcing ( $\lambda_f=12$  mm). Inset: magnified view.

boundary layer corresponding to the spanwise-uniform and spanwise-modulated critically forced ( $\lambda_f=9$  mm) flows underwent significant mean flow distortion. The unforced flow case as well as the super-critical ( $\lambda_f=12$  mm) and sub-critical ( $\lambda_f=7$  mm) forcing cases are distorted more mildly. The measured unforced boundary layer agrees relatively well with the numerical prediction. The slight discrepancy is attributed to modelling assumptions in the boundary-layer approximation as well as measurement uncertainties in the PIV fields.

The time-averaged velocity field for the additional forcing case of the critical mode actuator operated at the lower frequency (400 Hz) and same voltage amplitude (3 kV,  $C_\mu=0.013$ ) is presented in figure 6.14a. The velocity field shows a spanwise modulation with amplified stationary vortices at different wavelengths. When the actuator is operated at  $f_f=2$  kHz -  $E=2$  kV ( $C_\mu=0.037$ ) (figure 6.14b), the boundary layer features weaker stationary vortices when compared to the  $f_f=2$  kHz -  $E=3$  kV case (figure 6.11(d)). This further confirms the dependency of forced cross-flow vortex strength to the momentum coefficient of the actuator.

A comparison of the present study to the passive control investigation of [114], is shown in figure 6.15. In this previous work, the critical cross-flow instability mode was conditioned with leading edge micron-sized roughness elements (diameter:  $d_r=2.8$  mm, height:  $k_r=10$   $\mu$ m) installed at the same chordwise position as the plasma actuators in the present study ( $x/c=0.025$ ). The velocity profile was acquired with hot-wire scans. Note that the velocity measured in that experiment, coincides mainly with  $\sqrt{\bar{U}^2 + \bar{V}^2}$ , however, given the strong predominance of the  $U$  component [114], this comparison can still be valid. The comparison demonstrates that, when the actuator is operated at  $f_f=2$  kHz -  $E=3$  kV ( $C_\mu=0.046$ ), the spanwise-averaged value of the mean velocity attains the lowest value among all cases. For the lower frequency case, the lower velocity value compared to the laminar solution is explained by the more advanced transitional status of the forced boundary layer. When the actuator was operated at 400 Hz, the boundary layer showed multiple stationary modes (figure 6.10a) and enhanced fluctuations (see the discussion of figure 6.18a). Moving to the other flow cases, the comparison with the passive roughness elements used by Serpieri & Kotsonis [114] is more instructive given

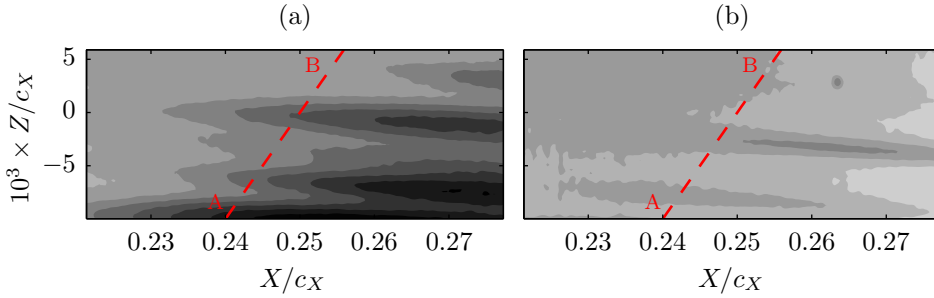


Figure 6.14: Time-averaged  $U$  velocity fields (10 levels, from 0.84 (black) to  $1 U_\infty$  (white)). (a)  $f_f=0.4$  kHz -  $E=3$  kV ( $C_\mu=0.013$ ); (b)  $f_f=2$  kHz -  $E=2$  kV ( $C_\mu=0.037$ ).

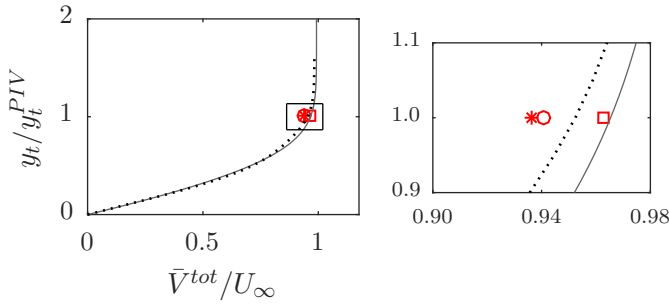


Figure 6.15: Comparison between the measured spanwise-mean velocity magnitude ( $z_{mean}\{\bar{V}^{tot}\}_{y_t=y_t^{PIV}}$ ) from the velocity fields of figure 6.14 (symbols), the boundary layer numerical solution (solid line) at  $x/c=0.25$ . Critical forcing ( $\lambda_f=9$  mm): (○)  $f_f=0.4$  kHz -  $E=3$  kV ( $C_\mu=0.013$ ); (□)  $f_f=2$  kHz -  $E=2$  kV ( $C_\mu=0.037$ ); (\*)  $f_f=2$  kHz -  $E=3$  kV ( $C_\mu=0.046$ ). Dotted line:  $d_r=2.8$  mm -  $k_r=10$   $\mu$ m passive roughness [114]. Inset: magnified view.

the CFI monochromatic state of the compared boundary layers. The hot-wire profile shows already at this chordwise station a small deviation from the laminar profile, caused by the mean-flow distortion [114]. Moreover, the profile crosses the station of the current PIV measurements ( $y_t=1.5$  mm) between the velocity values of the tested voltages thus showing that the  $d_r=2.8$  mm -  $k_r=10$   $\mu$ m passive roughness has a milder effect on the boundary layer than the  $f_f=2$  kHz -  $E=3$  kV ( $C_\mu=0.046$ ) active roughness but stronger compared to the  $f_f=2$  kHz -  $E=2$  kV ( $C_\mu=0.037$ ) case.

#### FLOW FLUCTUATIONS

As demonstrated in section 6.2.3, the employed plasma actuators produce an inherently fluctuating forcing effect, at a frequency aligned to the oscillation of the AC high voltage signal. The effect of this unsteady forcing on the boundary layer is investigated in this section. Dörr & Kloker, in their studies [22, 23] (Reynolds number based on plate length and free-stream velocity orthogonal to the leading edge  $Re = 460000$ ), showed very little direct effect of unsteady forcing on the unsteady instability modes. The actuators in the aforementioned studies were modelled with stationary or periodic high frequency body force inputs in their numerical setup. However, in the case of unsteady force, the actuators

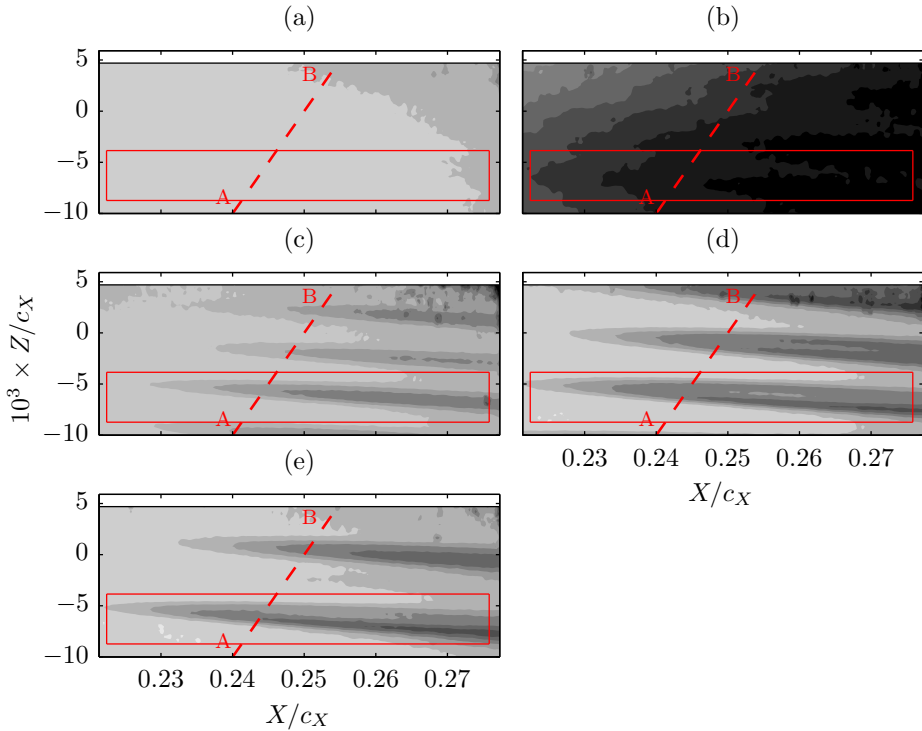


Figure 6.16: Standard deviation of  $U$  velocity fields (10 levels, from 0 (white) to  $0.0784 U_\infty$  (black)). (a) actuator non operated; (b) spanwise-uniform forcing; (c) sub-critical forcing ( $\lambda_f=7$  mm); (d) critical forcing ( $\lambda_f=9$  mm); (e) super-critical forcing ( $\lambda_f=12$  mm). Upper region masked for higher measurement noise.

were operated at a frequency more than four times higher than the frequency of the pertinent *type-I* secondary instability mode. The present study is conducted at a higher Reynolds number (chord Reynolds number  $Re = 1.08 \times 10^6$ ), at which the respective mode peaks at a frequency of 5.5 kHz [114]. In the current experimental framework, achieving frequencies four times larger than the *type-I* mode frequency was technically unfeasible (§ 6.2.3). This restriction was already envisioned by Dörr & Kloker as a possible limitation for UFD-LFC with AC-DBD actuators for high Reynolds numbers flows. Based on the above considerations, it was chosen to operate the actuators of the present study at a frequency of 2000 Hz. Such frequency is beyond the primary travelling modes band ( $0 < f < 1000$  Hz), yet below the frequency range corresponding to secondary instabilities ( $f > 4000$  Hz) [114].

#### STATISTICAL ANALYSIS

The statistic fluctuation fields, for the test cases presented in figure 6.11, are presented in figure 6.16. The overall level of velocity fluctuations for the unforced flow (figure 6.16a) is very low. In contrast, spanwise-uniform forcing dramatically enhances the unsteady field (figure 6.16b). This flow case was chosen to investigate the effects that the

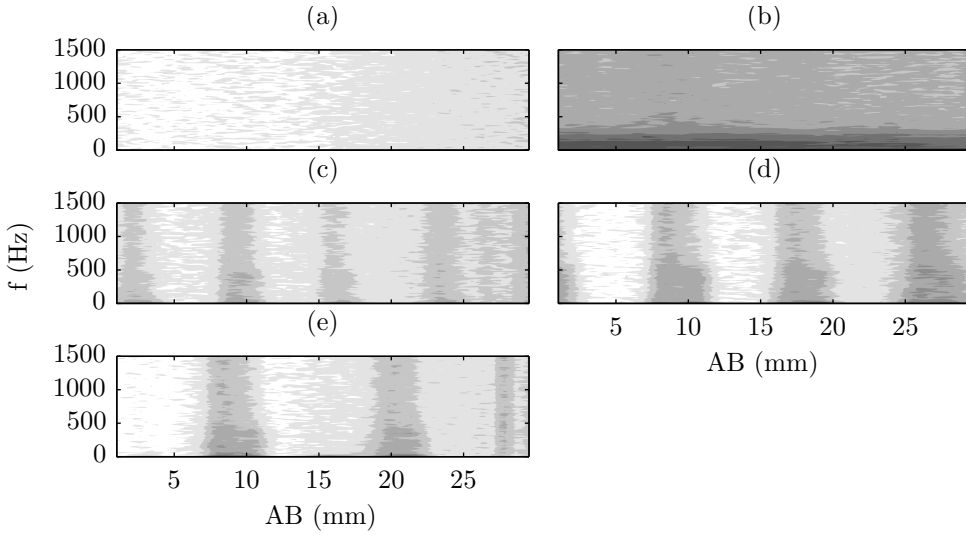


Figure 6.17: Non-dimensional normalised power spectra ( $\Phi_{U'_t}^* \cdot \delta_f / U_\infty^2$ , see equation 2.20,  $\delta_f=10$  Hz) of the  $U'_t$  velocity signal sampled along the AB line at  $x/c=0.25$  of figures 6.11 and 6.16 (10 levels, from -60 (white) to -30 dB (black)). (a) actuator non operated; (b) spanwise-uniform forcing; (c) sub-critical forcing ( $\lambda_f=7$  mm); (d) critical forcing ( $\lambda_f=9$  mm); (e) super-critical forcing ( $\lambda_f=12$  mm)

employed unsteady forcing has on the boundary layer. The higher level of fluctuations in conjunction to the thickening of the boundary layer discussed before (figure 6.11) suggest that this flow is in a more advanced transitional state compared to the unforced case.

When spanwise-modulated forcing is applied (6.16c, d and e for sub-critical, critical and super-critical wavelengths, respectively), the flow fluctuations appear enhanced only in the regions of the conditioned stationary vortices. This is expected in boundary layers dominated by stationary cross-flow vortices as the latter introduce strong velocity shears [51, 77, 135, 8]. The lower level of fluctuations for the sub-critical mode suggests a more stable flow in line with the DRE/UFD control strategies (this aspect will be addressed later in § 6.4.2).

#### SPECTRAL CHARACTERISTICS

Time series of the  $U'_t$  velocity signal sampled along the AB segment at  $x/c=0.25$  of figures 6.11 and 6.16 are analysed in the Fourier domain. The power spectra are computed using Welch's method [133] with a final frequency resolution of  $\delta_f=10$  Hz. The spectra are normalised according to equation 2.20 and non-dimensionalised with  $U_\infty^2$ . The results are presented in figure 6.17 for the five flow cases of figures 6.11 and 6.16. While the unforced flow shows very low spectral energy in all the resolved band ( $0 \text{ Hz} \leq f \leq 1500 \text{ Hz}$ ), the spanwise-uniform actuation results in very pronounced fluctuations in the band  $0 \text{ Hz} \leq f \leq 350 \text{ Hz}$ . This is somewhat unexpected as the operated AC voltage is fixed at the frequency of  $f_f=2000$  Hz which is well beyond the corresponding band of travelling modes at these flow conditions (cfr. § 2.6). While at this point the analysis is inconclusive, it is

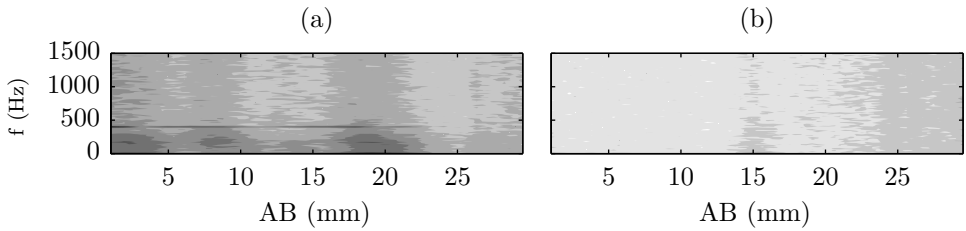


Figure 6.18: Same notation as figure 6.17 for the fields of figure 6.14 (10 levels, from -60 (white) to -30 dB (black)). (a)  $f_f=0.4$  kHz -  $E=3$  kV ( $C_\mu=0.013$ ); (b)  $f_f=2$  kHz -  $E=2$  kV ( $C_\mu=0.037$ ).

likely that either low frequency fluctuations directly introduced by the actuator (recall the results of section 6.2.3) or non-linear interactions between the plasma-induced jets and the boundary-layer modes take place in the unsteady velocity field, thus enhancing the fluctuations energy in the travelling CF waves band. Moreover, the spanwise-uniformity of the unsteady forcing is also present in the spectra. This is a direct consequence of the absence of amplified steady vortices in this flow field as seen in the statistics fields (figure 6.11b).

Analysis of the spanwise-modulated actuated flows shows that the fluctuations are modulated along the span directly corresponding to the position of the conditioned cross flow vortices. They attain considerable energy throughout the resolved spectrum, albeit stronger at the lower frequencies. Among the different spanwise-modulated actuators, the 9 mm and 12 mm wavelength actuators are responsible for the strongest fluctuations. The Nyquist frequency of the implemented PIV measurements is lower than the secondary instability band [114] and hence the secondary instability mechanisms cannot be directly inspected in the frequency domain. This analysis is presented in the remainder, capitalising on the measurements spatial resolution.

The velocity spectra of the velocity fields of figure 6.14 are shown in figure 6.18. Forcing the flow at  $f_f=0.4$  kHz -  $E=3$  kV ( $C_\mu=0.013$ ), enhances the low-frequency modes considerably, as expected. A narrow band of strong fluctuations at the forced frequency is clearly distinguishable thus suggesting the receptivity of the particular flow to this range of frequencies. The fluctuations are less modulated along the span than the energy comprised in the band  $0 \text{ Hz} \leq f \leq 350 \text{ Hz}$  which occur at the locations of local velocity shears in the time-averaged fields. These two bands appear rather distinguished suggesting a different origin. While the 400 Hz fluctuations are directly introduced by the actuator, the lower-frequency, wider-band fluctuations resemble those reported in figure 6.17b-e. The origin of these fluctuation will be discussed in following sections.

For the case of  $f_f=2$  kHz -  $E=2$  kV ( $C_\mu=0.037$ ), the actuation introduces rather weak velocity fluctuations. The spectrum is similar to the unforced field of figure 6.17(a) as for this voltage the actuator has a reduced strength.

#### SPATIAL ORGANISATION

The results discussed hitherto confirm the initial estimations towards the applicability of AC-DBD plasma actuators for control of cross-flow instabilities based on the UFD approach. More specifically, the capability of conditioning the amplified stationary mode

with spanwise-modulated actuators is experimentally demonstrated for the swept wing case, analogous to the work of [111] in the supersonic cone case. However, the effects of forcing on the unsteady field result to strong amplification of travelling modes, which potentially can have detrimental effects for future LFC purposes.

Towards gaining insight on the low-frequency fluctuations enhanced by the unsteady actuation (§ 6.4.2), description of the spatial organisation of the fluctuating velocity fields is sought. The unsteady flow field pertaining to a single stationary wave is analysed. Unsteady fluctuations are stronger when the stationary vortex is more amplified due to elevated shears. As such, the flow field encompassing the most amplified stationary vortex (CFV1, enclosed by the (red) rectangle in figures 6.11 and 6.16) is henceforth considered. Two forcing cases pertaining to the critical mode forcing ( $\lambda_f = 9$  mm) and the spanwise uniform forcing are selected for comparison in the following analysis. The choice of these cases is dictated by their inherently different forcing spectrum. While the  $\lambda_f = 9$  mm forces the most critical stationary mode, the uniform forcing case is spanwise invariant and, as such, does not favour a certain wavelength.

Irrespective of the chosen forcing case, the velocity fluctuations occurring at this stage of the boundary-layer development are still rather weak and therefore challenging to identify considering the experiment dynamic range. Technically, the latter could be increased by augmenting the PIV laser pulses separation, however such approach would compromise the effective resolution of the velocity shears [105]. As such, statistical decomposition based on spatial coherence is employed. More specifically, proper orthogonal decomposition following the snapshot formulation [119] is used, similar to previous analyses on tomo-PIV data by Serpieri & Kotsonis [114].

As mentioned, Serpieri & Kotsonis [114] investigated the same flow case as the one considered in the present study, albeit using DREs for conditioning the cross-flow vortices. They reported that a significant portion of kinetic energy, captured by the first POD mode, was related to a low frequency oscillation of the stationary vortices. Further analyses on less energetic POD modes allowed the identification of flow structures related to the *type-I* and *type-III* instabilities. The *type-I* mode, corresponding to a secondary instability mode of the strong spanwise shears [40, 51, 77, 129] was shown to be of Kelvin-Helmholtz nature [8]. Serpieri & Kotsonis [114] reported the *type-I* mode to have a wavelength of about 4.6 mm along the stationary vortices axes and occur in a range of frequencies centred at 5 kHz. The *type-III* mode is instead caused by the interaction of primary stationary and travelling waves [30, 40, 51, 77]. Serpieri & Kotsonis [114] found these vortices to have a wavelength of 25 mm and a frequency of  $\approx 500$  Hz.

The high sampling frequency of the current experiment allows direct investigation of the temporal evolution of the low frequency fluctuations (i.e. the *type-III* mode for the flow cases where stationary vortices have amplified). The secondary instability modes are instead occurring at higher frequencies, which lie beyond the measured band. Analysis of the temporal coefficients of the POD modes can infer the nature of the related structures. The spectra of the first 30 POD modes temporal coefficients is shown in figure 6.19 for the cases of spanwise-uniform forcing and critical forcing at  $\lambda_f=9$  mm. The spectra frequency resolution is  $\delta_f=10$  Hz. When the spanwise uniform actuator is employed, high energy levels are observed in the presented POD modes-frequency plane. In particular almost 50% of the total turbulent kinetic energy pertains to the first ten POD modes (not

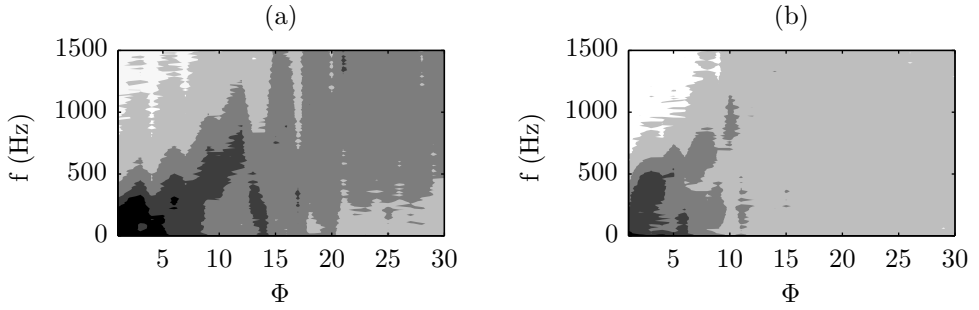


Figure 6.19: Power spectra ( $\delta_f=10$  Hz) of the first 30 POD modes' time coefficients (5 levels, from -20 (white) to 10 dB) (black). The DBD plasma actuator is operated at  $f_f=2$  kHz -  $E=3$  kV ( $C_\mu=0.046$ ). (a) spanwise-uniform forcing; (b) critical forcing ( $\lambda_f=9$  mm).

shown). These first ten modes feature most of their energy in the  $0 \text{ Hz} \leq f \leq 500 \text{ Hz}$  band, further corroborating the outcomes of figure 6.17(b). For the spanwise-uniform forced flow, the absence of strong stationary vortices, and related shears, leads to a different instability evolution without the growth of secondary high frequency instability modes. A continuous energy cascade towards higher frequency eddies and higher POD modes is therefore characterising the flow.

In the presence of strong stationary waves (figure 6.19b), the spectral energy is less spread through the POD modes. POD Mode 1 shows very high energy at the lowest frequencies and is related to the POD mode 1 observed by Serpieri & Kotsonis [114]. High energy concentrations occur in the first ten POD modes, featuring strong fluctuations within the band  $0 \text{ Hz} \leq f \leq 500 \text{ Hz}$  and reaching the relative cumulative TKE level of 23% (not shown). This is the frequency band where the primary travelling waves are expected as predicted by LST (§ 2.6), as well as experimentally observed by [114]. Proceeding towards higher index modes, the associated energy shifts towards higher frequencies beyond the resolved band. In fact, inspection of the POD eigenmodes, suggests that these POD modes pertain to *type-I* secondary instability mechanisms along the stationary vortex shears (as will be shown in § 6.4.2). These modes feature frequencies in the range of 4-9 kHz for the same flow case, as reported in [114]. Due to the limited PIV sampling rate in the present study, frequencies higher than 1500 Hz are not resolved. This limits the following analysis to the low frequency/high energy fluctuations.

A reduced-order reconstruction of the instantaneous velocity field based on the first 10 POD modes, which were shown to be resolved in time by the performed measurement, is presented in figure 6.20, for the same flow fields of figure 6.19. Three subsequent instantaneous flow fields, separated from each other by  $\Delta_t=1/3000 \text{ Hz}=3.3 \cdot 10^{-4} \text{ s}$ , are plotted by means of  $U'_t$  velocity contours. When spanwise-uniform forcing is supplied, strong velocity fluctuations take place compared to the unforced flow field shown in figure 6.16a. These fluctuations are captured in the reconstructed field of figure 6.20a. They appear as a sequence of broad structures, spanning the entire vertical extent of the field and advected mainly along  $X$  with a smaller oscillating component along the  $Z$  direction. The reconstructed time series for the case of critical spanwise modulated forcing ( $\lambda_f=9$

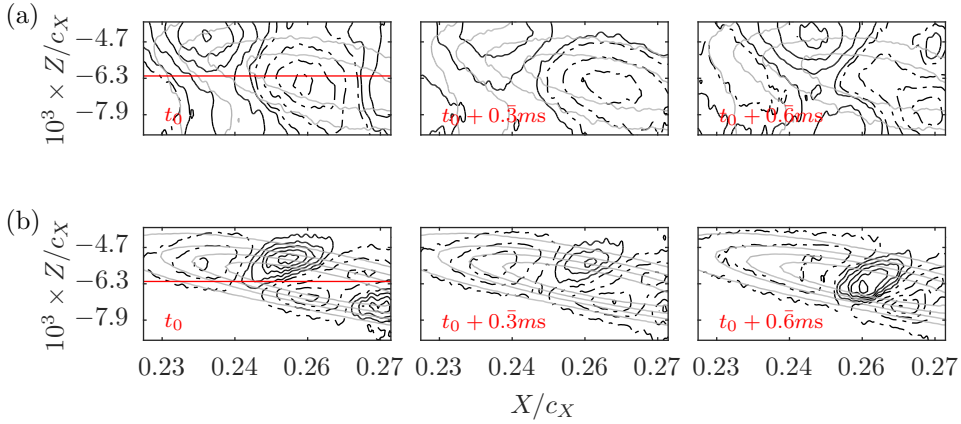


Figure 6.20: Reconstructed time sequence of the  $U'_t$  velocity fields (mean subtracted) from the first 10 POD modes (black lines: solid (positive) and dashed-dotted (negative), 5 levels, from  $\pm 0.058$  to  $\pm 0.004 U_\infty$ ) and time-averaged velocity field (solid grey lines: 5 levels, from  $0.84$  to  $1 U_\infty$ ). The flow fields presented here are shown with the (red) rectangle in figures 6.11 and 6.16 (b and d). (a) spanwise-uniform forcing; (b) critical forcing ( $\lambda_f=9$  mm). The solid (red) lines in the leftmost contour refer to figure 6.21.

mm) is presented in figure 6.20b. In this case, the flow structures appear significantly smaller and localised in space compared to the spanwise-uniformly forced flow. The structures are advected downstream, moving from the downwelling flow region towards the upwelling region of the stationary waves similarly to what reported in previous studies for the *type-III* modes [40, 51, 77, 129, 8, 114].

The presented time sequence encompasses a total period of  $\approx 1$  ms hence it is not representative of the whole fluctuations evolution. To better represent the latter, a spectral analysis is sought. The instantaneous velocity signal for the entire measurement time (2 s) is sampled along a line parallel to  $X$  and centred in the domain of figure 6.20 (along the (red) solid line in the leftmost contours). The signals are therefore function of  $X$  and time:  $g = g(X, t)$ . The  $g$  signals are divided in segments of 600 time samples with 50% overlap between neighbouring segments, weighted with a two-dimensional Hanning function and decomposed in their spatio-temporal Fourier modes. The resulting frequency-wavenumber spectra are then averaged together [133]. The spectra have a frequency resolution of  $\delta_f=10$  Hz and a spatial resolution of  $\lambda_X^{min}=2.16$  mm (two times the size of the interrogation windows [110]).

The spectra are shown in figure 6.21 for the two considered cases. The relation between the wavenumber and the frequency, directly corresponding to the structures phase velocity (referred to as  $U_c = f\lambda_X$ ), can be retrieved from the presented plots. A least-squares linear fit (dashed (red) lines in figure 6.21) through the energy maxima per wavelength was applied on the spectra giving the values of  $U_c = 17.60$  m s $^{-1}$  ( $0.69 U_\infty$ ) for the spanwise-uniform actuator and  $U_c = 27.50$  m s $^{-1}$  ( $1.08 U_\infty$ ) for the critical mode flow. The different values of advection velocity correlate with the lower values of the local velocity seen in the time-averaged fields (figure 6.11b and d). The phase velocity

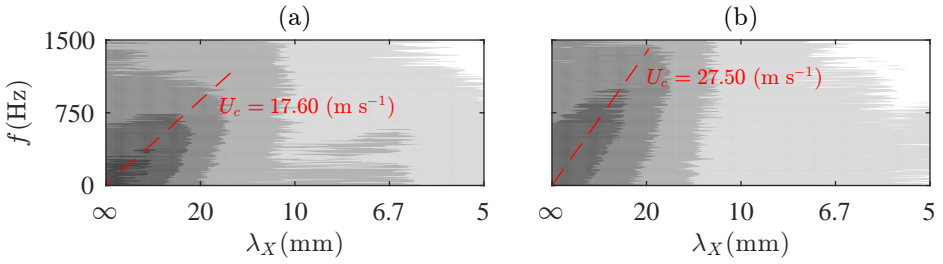


Figure 6.21: Wavenumber-frequency power spectra for  $g = g(X, t)$  of the full time series presented in figure 6.20 (6 levels, from -15 (white) to 35 dB (black)). (a) spanwise-uniform forcing; (b) critical forcing ( $\lambda_f = 9 \text{ mm}$ ). The velocity signal were extracted along the (red) solid lines shown in the leftmost contours of figure 6.20. The (red) dashed lines indicate the phase velocities ( $U_c$ ).

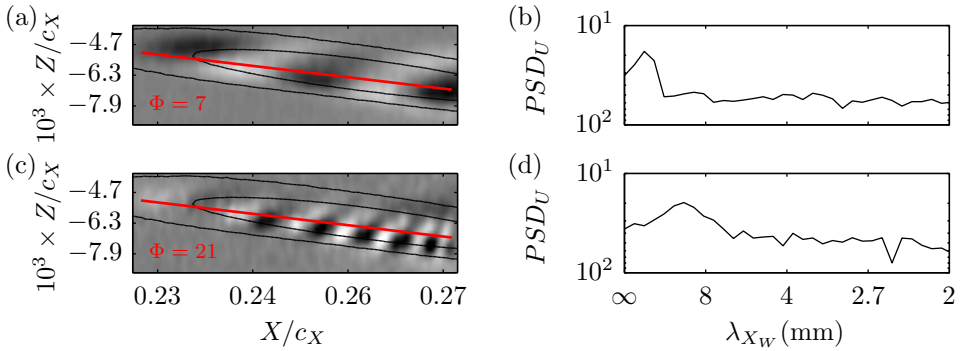


Figure 6.22: (a and c)  $U$  velocity fields of normalised POD modes (mode index indicated in the lower left corner) (shaded: 11 levels comprised between  $\pm 0.05$ ) and time-averaged velocity field (solid black lines: 3 levels, from 0.84 to  $1 U_\infty$ ). The flow fields presented here are shown with the (red) rectangle in figures 6.11(d) and 6.16(d) (critical forcing ( $\lambda_f = 9 \text{ mm}$ )). (b and d) Wavenumber power spectral density of the velocity signal sampled along the (red) line of (a) and (c) respectively, inclined along the stationary vortex.

component in the  $Z$  direction could be estimated in a similar fashion (sampling the velocity time series along the  $Z$  direction). However, given the small magnitude of this velocity component, the results are not deemed reliable.

Summarising, while the instantaneous fields for the critical stationary mode case are dominated by *type-III* structures, strong velocity fluctuations mainly advecting along the free-stream direction are amplified by the unsteady 2D forcing. These observations indicate that, for the current flow cases, the unsteady flow field is strongly modified by the used plasma actuators. In section 6.4.3 a further effort in understanding this phenomenon is presented. Despite this undesired effects, the actuators showed authority in conditioning the developing CFI to the forced modes. Therefore a comparative analysis of the unsteady fields pertaining to the different forced modes can be sought.

### UFD FLOW CONTROL USING PLASMA ACTUATORS

In this section, the unsteady fields of the spanwise modulated forcing cases are further examined within the perspective of UFD flow control. To this goal, the unsteady fields pertaining to the three forced wavelengths cases (same forcing amplitude) are reconstructed from selected POD modes. The POD modes were first analysed in their wavenumber spectral content along lines parallel to the CFVs axes (inclined  $-2.12^\circ$  at the measurement location w.r.t.  $X$ ). Note that, given this small angle, approximately the same wavelength limits described in the previous section are resolved. In figure 6.22, two POD modes with longer and shorter wavelength structures, respectively, are shown together with the wavenumber velocity spectra along the stationary vortices to illustrate the followed procedure.

Serpieri & Kotsonis [114] report, for the same flow field, wavelengths of  $\lambda_{X_W} = 25$  mm for *type-III* modes and of  $\lambda_{X_W} = 4.6$  mm for *type-I* modes. Following their results, the wavelength  $\lambda_{X_W} = 20$  mm was used here as a dividing threshold to reconstruct the  $U$  fluctuations in two bands. Similarly, White & Saric [135] and Serpieri & Kotsonis [114] used time filters to separate the different frequency bands from hot-wire measurements. The results are presented in figure 6.23. It can be seen that, for both the longer and shorter wavelengths bands, the sub-critical control mode ( $\lambda_f = 7$  mm) demonstrates lower fluctuations level. The other stationary modes show enhanced disturbances. This is especially evident for the shorter wavelength disturbances, which are related to secondary mechanisms (note that these modes are not resolved in time, given the high frequency as shown in figure 6.19). These are located on the outer upwelling flow side of the stationary waves [77, 129], as shown in figure 6.23c. This analysis further corroborates the known beneficial aspects of the UFD flow control approach on the evolution of secondary instability mechanisms.

#### 6.4.3. EFFECTS OF PLASMA FORCING ON FLOW STABILITY: A SIMPLIFIED MODEL

As shown in section 6.4.2, the plasma-actuator operation leads to strongly enhanced unsteady disturbances in the boundary layer. Two mechanisms are considered as drivers of this effect. The first pertains to the actuator's unsteady nature. It is well known from previous plasma characterisation studies [56], as also shown in section 6.2.3, that the plasma actuators feature a strong periodic forcing component, associated with the AC frequency of the high voltage input signal. Additionally, Pereira *et al.* [90], provided an analytical model, demonstrating the strong receptivity of laminar boundary layers to high-frequency forcing. Nonetheless, low frequency fluctuations were also observed in the boundary layer (figure 6.6). Considering these events in the context of the swept wing transition scenario, the introduced disturbances can interact with and condition the primary and secondary cross-flow instabilities. This type of interaction will be hereafter referred to as *unsteady effect*. The second considered mechanism relates to the effects of actuation on the time invariant flow. The actuator time-averaged forcing might modify the receptivity/stability characteristics of the local boundary layer, thus possibly indirectly affecting the amplification of unsteady modes (P. C. Dörr and M. J. Kloker, private communication). This mechanism is named henceforth as *steady effect*. In this section an effort is made towards verifying whether the forcing, its magnitude and direction, change

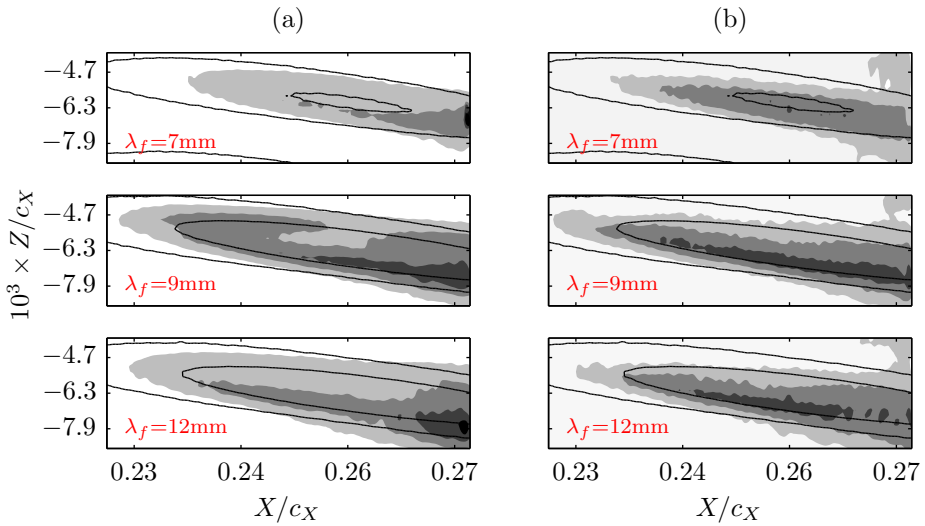


Figure 6.23: Standard deviation of the reconstructed  $U$  field from POD: (a) modes with  $\lambda_{X_W} > 20$  mm; (b) modes with  $\lambda_{X_W} \leq 20$  mm (shaded: 5 levels, from 0 (white) to  $0.04 U_\infty$  (black)) and time-averaged velocity field (solid black lines: 3 levels, from 0.84 to  $1 U_\infty$ ). The flow fields presented here are shown with the (red) rectangle in figures 6.11 and 6.16 (c, d and e).

the boundary-layer stability. No conclusions about eventual effects on the receptivity can be retrieved from the proposed approach.

Recently, Dörr *et al.* [26] showed effective UFD control also in the presence of (different shape, frequency and relative position w.r.t. the actuator) free stream eigenmodes impinging on the forced boundary layer. Nevertheless also in that study, no conclusions were made on the forcing effect on the local boundary layer receptivity.

#### MODEL AND FLOW CASES

To investigate the effects of both forcing direction and magnitude, five cases are presently considered. Additional to the unforced baseline case, two cases consider the use of the body force field ( $C_\mu=0.046$ ) of figure 6.5 oriented along and against the boundary layer flow in  $x$  respectively, thus respecting the semi-infinite (spanwise invariant) swept wing assumption. Finally, two cases consider a five-fold body force ( $C_\mu=0.230$ ) oriented again along and against the flow in  $x$ . An overview of the modelled cases, and respective notation, is given in table 6.3.

#### RESULTS

The boundary layer solutions for the unforced,  $5F_x$  and  $-5F_x$  cases, at three different chordwise stations close to the actuator, are shown in figure 6.24. The one-fold body force results (cases  $1F_x$  and  $-1F_x$ ) are not shown for ease of visualization. The velocity profiles in the proximity of the actuator are inspected in the inviscid streamline system (figure 2.7a) as the CFI modes directly descend from the amplitude of the cross-flow component ( $-w_{ISL}$ ).

Actuator	Forcing direction	$C_\mu$	Case
none	-	-	unforced
2D	x	0.046	$1F_x$
2D	-x	0.046	$-1F_x$
2D	x	0.230	$5F_x$
2D	-x	0.230	$-5F_x$

Table 6.3: Modelled flow cases. Body force distribution of figure 6.5b.

Considering that, at the actuators location, the inviscid streamline angle is  $-59.73^\circ$  from  $x$ , forcing along  $x$  has an enhancing effect on both the streamwise and cross-flow velocity components. The opposite holds when the induced jet is along  $-x$ , i.e. the actuator opposes both components as shown in figure 6.24. However, already at  $x/c=0.1$ , the forced flow profiles tend to collapse on the unforced flow curve, with differences of less than 2% (figure 6.24b). Considering the weak induced velocity, the body force magnitude and spatial extent (note that the five-fold amplification affects only the body force magnitude and not its shape) measured in section 6.2.3, it is expected that the actuation effects do not extend for long portions of the chord.

The flow stability of the considered five cases is analysed with LST. The analysis presented here is limited to the stationary modes and to the unsteady modes with  $f=200$  Hz as this frequency features high energy at the measurement location (figure 6.17(b)). The related  $N$ -factor curves are presented in figure 6.25. The integral effect of the forcing direction can be inspected from these plots. For all the modes, the forcing along  $x$  has destabilising effects. Alternatively, forcing along  $-x$ , stabilises both stationary and travelling modes. The  $N$ -factors for the  $1F_x$  ( $-1F_x$ ) case lie in between the  $5F_x$  ( $-5F_x$ ) case and the unforced flow and are not shown. These results are in agreement with the outcomes of Dörr & Kloker [22, 24] and are direct consequence of the mean-flow modifications shown in figure 6.24.

The  $N$ -factor curves (figure 6.25) show how a rather weak and confined perturbation of the mean-flow influences the flow stability characteristics, considering the integral nature of the  $N$ -factors. Moreover, they show that increasing  $\lambda_z$ , thus driving  $\beta_r$  and  $\Psi$  ( $\Psi = \tan^{-1}(\beta_r/\alpha_r)$ ) closer to zero, the CFI modes become less amplified and the forcing effect reduces. Eventually, very close to the actuator, the effect of the forcing direction inverts for waves with smaller  $\Psi$  i.e. waves travelling mainly along  $x$  (not shown). However, these waves are highly stable for most of the considered flow (given the strong favourable pressure gradient) and are far from the most amplified mode thus usually they are not observed in three dimensional boundary layers [130]. The analysis presented in § 6.4.2 identified waves mainly advected along the local flow direction (roughly coinciding with  $X$  at the measurement location). From these considerations, it is concluded here that the observed enhanced low-frequency fluctuations at the measurement location must be caused by the actuator *unsteady effect* attributed to a combination of low frequency fluctuations directly introduced by the actuator or to non-linear interactions between the plasma jets and local boundary layer modes. A further detailed receptivity measurement/analysis of this effect is deemed necessary to fully elucidate this effect (see also the comments of Dörr *et al.* [26] on this point).

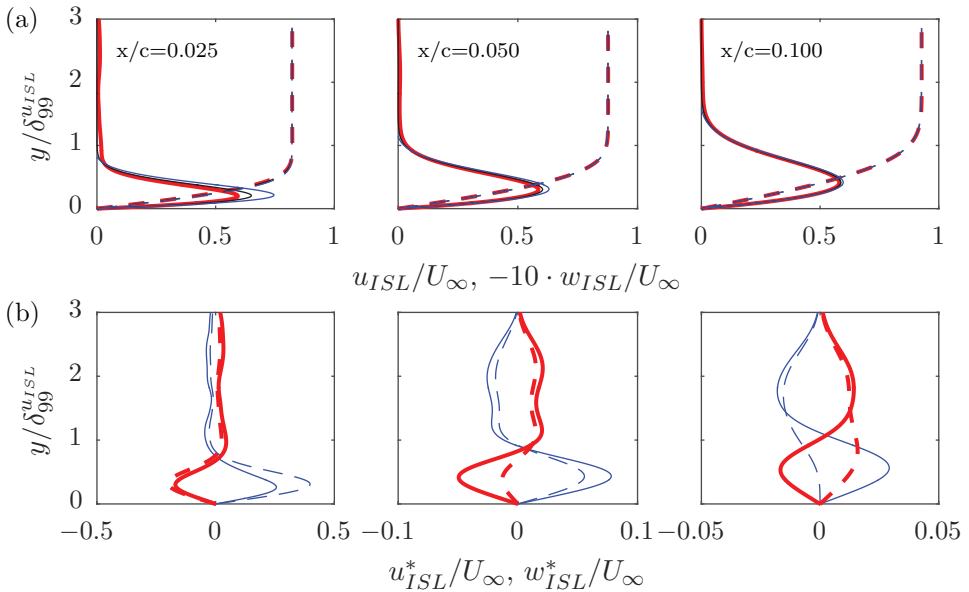


Figure 6.24: (a) Velocity profiles along ( $u_{ISL}$ : dashed line) and orthogonal ( $w_{ISL}$ : solid line) to the inviscid streamline at three different stations (upper left corner): unforced (black line);  $5F_x$  (thin (blue) line);  $-5F_x$  (thick (red) line). (b) Velocity difference profiles ( $u_{ISL}^*$ : dashed line;  $w_{ISL}^*$ : solid line) between the forced ( $5F_x$ : thin (blue) line;  $-5F_x$ : thick (red) line) and unforced case at same stations of (a). The wall normal axis is non-dimensionalised with the boundary layer thickness based on  $0.99 \cdot u_{ISL}$  from the local unforced profile.

Summarizing, it becomes evident that the  $-x$  forcing actuator has the beneficial effect of reducing the cross-flow velocity component (figure 6.24) thus stabilising the boundary layer with respect to stationary and travelling CFI modes (figure 6.25). As shown by Dörr & Kloker [24], the forcing direction is more effective for boundary layer stabilisation when against the mean cross-flow (i.e. along  $z_{ISL}$ ). However, the direction along which the actuators have the highest UFD authority is against the local flow (i.e. along  $-x_{ISL}$ ) as it maximises the flow blockage. Therefore, a compromise between the actuator's UFD authority and CF counteraction can lead to the decision of aligning the actuator-induced jets with  $-x$ , thus orienting the forcing components along  $z_{ISL}$  and  $-x_{ISL}$  (as shown in figure 2.7a). Furthermore, the combined effect of two and three-dimensional forcing, the former along  $z_{ISL}$  and the latter along  $-x_{ISL}$ , could sum together to some extent the two beneficial approaches (UFD and CF counteraction) for further stabilization effects, in an analogous manner to the 'formative suction' control studied by Messing & Kloker [81].

## 6.5. CONCLUSIONS

An experimental investigation on the effect of AC-DBD plasma actuators on cross-flow instability modes is performed. The flow control philosophy holds on the DRE/UFD sub-critical forcing approach, where stationary modes at smaller wavelength than the naturally dominating mode are forced with leading edge devices [100, 77, 129]. Plasma

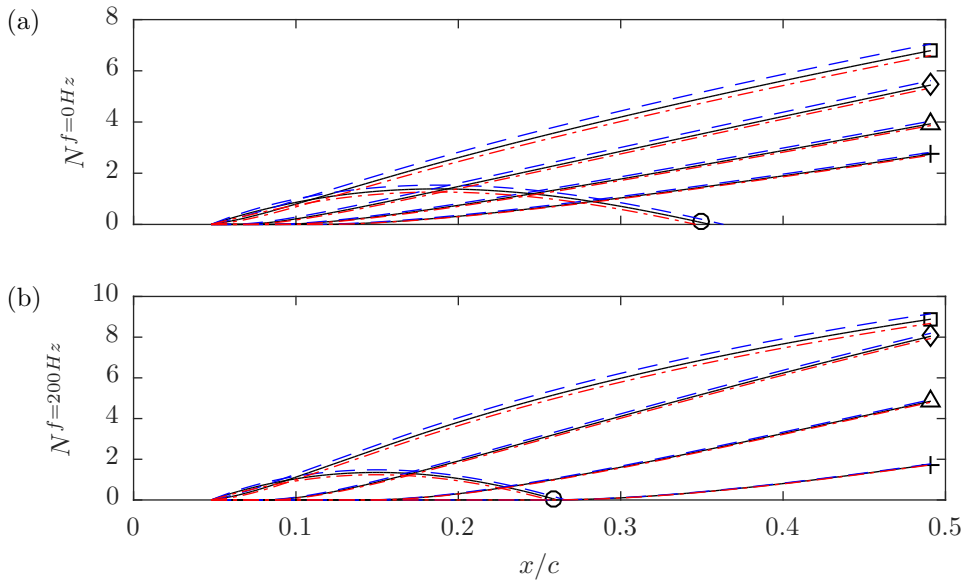


Figure 6.25: N-factors of different modes for  $f=0$  Hz (a) and  $f=200$  Hz (b) ( $\circ$ :  $\lambda_z=4.5$  mm;  $\square$ :  $\lambda_z=9$  mm;  $\diamond$ :  $\lambda_z=13.5$  mm;  $\triangle$ :  $\lambda_z=18$  mm;  $+$ :  $\lambda_z=22.5$  mm): unforced (black solid line);  $5F_x$  (dashed blue line);  $-5F_x$  (dashed-dotted red line).

actuators could potentially provide a viable alternative to passive roughness elements due to several inherent features. Firstly, their operation is easily adjustable through remote manipulation of the electric driving signal, allowing real-time adaptations of forcing amplitude and frequency [17]. Additionally, through strategic fabrication and integration on the wing, varying spanwise wavelengths can be forced by activating or deactivating selected number of actuators. Indeed, based on novel fabrication techniques, customised and low-thickness actuators can be designed specifically for cross-flow instability control. The combination of these features makes these actuators ideal for active flow control throughout the entire flight envelope (i.e. for different Reynolds numbers and wing incidences). Finally, a control strategy that holds on tuning the natural flow stability, as the UFD concept, requires only moderate input energy, assuring significant net improvement in efficiency of the control device [24].

Despite these advantages, the use of AC-DBD plasma actuators for controlling CFI poses significant technical and theoretical challenges. Apart from reliability considerations, which pertain more to industrial applications, their inherent unsteady forcing effect becomes highly important for flight Reynolds number flows. At these regimes, primary and secondary cross-flow instabilities appear at frequencies which are of the same order as the frequencies typically used for the plasma AC high voltage ( $O(\text{kHz})$ ). This allows for the actuator to trigger the primary travelling CF waves or secondary cross-flow instabilities and potentially promote transition, restricting any benefits from the steady UFD effect. This possibility was already highlighted by Dörr & Kloker [24] in their numerical

simulations using plasma actuators as UFD devices. However, this effect has received limited attention up to now as the published numerical studies of Dörr & Kloker [22, 24], Dörr *et al.* [26] and Shahriari [118] consider steady (or very high frequency unsteady) body force models for the used plasma actuators. In their experimental study, Schuele *et al.* [111], which employed plasma actuators on a supersonic yawed cone experiment, did not infer the unsteady flow field. This aspect is considered crucial, as CFI-dominated boundary layers are highly receptive to fluctuations [19]. Therefore, the main object of the current study was the analysis of the steady as well as unsteady mechanisms pertaining to the use of AC-DBD plasma actuators as UFD devices.

6

Novel actuators were therefore developed, characterised and used on a  $2.17 \cdot 10^6$  Reynolds number swept-wing flow. Four geometries were tested allowing to force the critical mode, a shorter wavelength mode and a longer wavelength mode (i.e. a sub-critical and a super-critical mode, respectively). To isolate the wavelength effect and to better analyse the consequences of using AC-DBD plasma actuators on the unsteady flow field, a spanwise-uniform actuator was tested as well. All the actuators were operated at an AC frequency ten times higher than the most unstable travelling CFI mode. A case where the actuators were operated in the unstable CFI band was also tested for comparison. Finally, a reduced voltage test allowed to inspect the effect on the boundary layer of lowering the forcing amplitude and to compare the actuators with passive roughness element from a previous experiment [114].

Infrared thermography visualisation measurements highlighted the authority of spanwise-modulated plasma actuators in conditioning stationary CFI modes at the selected wavelengths. Quantitative boundary-layer measurements were carried out using high-speed PIV. These measurements corroborated the outcomes of the flow visualisation, further indicating a reduced growth for the sub-critically forced CFI, compared to the growth of the critical modes. Consequently, also the unsteady flow field (i.e. primary and secondary instability modes) showed reduced amplitudes for the sub-critical flow case in line with the DRE/UFD studies [100, 129, 72]. However, spectral analysis of the unsteady velocity field showed strong enhancement of fluctuations in the actuated flow cases, irrespective of the forced wavelength. The developing flow structures were further investigated and characterised through proper orthogonal decomposition and reduced-order-model reconstruction analyses.

The origin of these fluctuations was traced back to two possible, concurrent mechanisms. The first mechanism relies on the direct introduction of disturbances by the unsteady body force component of the employed actuators (referred to as *unsteady effect*). In the investigated conditions, LST predictions indicated no amplified primary travelling waves near the forcing frequency of 2000 Hz. However, in the forced cases, enhanced velocity fluctuations within a band significantly lower than the forcing frequency were detected, suggesting triggering of these instabilities through direct introduction of low frequency fluctuations (also observed in the actuator characterization experiments) or non-linear interactions between the actuator pulsed jets and the boundary layer modes. The second mechanism is a *steady effect*: the steady forcing component locally modifies the mean boundary layer, and by consequence its stability and receptivity characteristics to different modes (Dörr and Kloker, private communication). As such, the boundary layer could amplify unsteady modes, originating from the *unsteady effect* of the actuators

or from receptivity to free stream disturbances [26].

This hypothesis was inspected through a simplified model, making use of numerical solutions of the forced boundary layer and linear stability theory. The outcomes of this investigation, as well as the *unsteady effect* require further dedicated efforts. However, through the presented model, it was possible to show that the *steady effect*, at least within the coverage of linear stability, has negligible consequences on the time-invariant flow stability. No conclusions on the effects on the boundary layer receptivity can be made at this point. Furthermore, through the actuator characterization experiment, low frequency fluctuations were observed thus suggesting the *unsteady effect* as the cause of the enhanced low frequency fluctuations. As a consequence of these findings, UFD plasma actuators for effective LFC need to be designed, built and operated such to minimize the introduction of low frequency disturbances.

Additional to UFD configurations, plasma actuators can also be used to directly change the base flow to a more stable state. Forcing against the local cross-flow (along  $z_{ISL}$ , see figure 2.7a), leads to the optimum boundary-layer stabilisation of CFI as it minimizes the cross-flow velocity component [22]. When the plasma forcing is against the local flow velocity (along  $-x_{ISL}$ ), the strongest effects in inducing the monochromatic forced mode are obtained. This choice is optimal for plasma-based UFD, as it maximizes the local flow blockage.

However, in the perspective of base-flow manipulation [22], forcing close to the leading edge, where the inviscid streamline is almost aligned with  $z$ , can be a good option. In this case, the forcing direction that stabilizes the boundary layer is close to the  $-x$  direction, thus, spanwise-uniform actuators can be used for this purpose.



# 7

## SECONDARY CROSS-FLOW INSTABILITY

*In this chapter, the boundary layer fluctuations were phase- and frequency-conditioned using concurrent forcing by means of a dielectric barrier discharge plasma actuator mounted upstream of the measurement domain. The actuator effect, when positioned sufficiently upstream the secondary modes onset, was tuned such to successfully condition the high frequency type-I and the low frequency type-III modes without modifying the transition evolution. Two primary stationary cross-flow vortices of different amplitude were measured, revealing the effect of base flow variations on the growth of travelling instabilities. The response of these two stationary waves to the naturally occurring and forced fluctuations was captured at different chordwise positions. Additionally, the deterministic conditioning of the instability phase to the phase of the actuation allowed phase-averaged reconstruction of the spatio-temporal evolution of the unsteady structures providing valuable insight on their topology. Finally, the effect of locating the actuator at a more downstream position, closer to the secondary instability branch-I, resulted in laminar-to turbulent breakdown for the high frequency actuation while the low frequency forcing showed milder effects on the transition evolution.*

---

**J. Serpieri** & M. Kotsonis, *Conditioning of unsteady cross-flow instability modes using dielectric barrier discharge plasma actuators*, [Experimental Thermal and Fluid Science](#), **93**, 305-318 (2018)

## 7.1. INTRODUCTION

To achieve spatio-temporally resolved information on the travelling primary and secondary instability modes arising on saturating CFVs, Kawakami *et al.* [51] and Chernoray *et al.* [13] conditioned the unsteady flow field by external predetermined forcing. They used periodic suction/blowing at the wall close to the primary vortices saturation location. A similar approach is followed in the current study. In contrast to the localised point-forcing of Kawakami *et al.* [51] and Chernoray *et al.* [13], spanwise-invariant forcing is sought by means of a straight plasma actuator aligned with the leading edge direction. Plasma actuators present several attributes rendering them ideal for localized, deterministic actuation of transitional flows [59, 139, 83]. Most pertinent to this study is their ability to work on electrical rather than mechanical time scales, thus able to introduce a wide band of frequencies in the flow. Such band easily encompasses the relevant frequency range, governing swept boundary layer instabilities such as the *type-III*, *type-I* and *type-II* modes described in the previous section. Given the novel plasma actuator fabrication technique, a dedicated experiment was carried out with the aim of evaluating the actuator performance.

The actuator was mounted on the wing surface close to the primary cross-flow vortices saturation location. It was operated at different voltages and at different forcing frequencies. The deterministic forcing slightly enhanced the amplitude of the secondary instability modes without affecting the primary stationary mode, allowing to narrow their spectral content and to condition their phase. As a consequence, a phase-averaged reconstruction of the hot-wire measurements, based on the actuator signal, is performed. The projection of the secondary vortices on constant-chord planes and their temporal evolution is captured and compared to the previous effort of Kawakami *et al.* [51] and Chernoray *et al.* [13] and to the tomo-PIV experiments by [114]. The evolution of the secondary modes at different chord stations and for different actuator positions is investigated.

The results of the simulations by Wassermann & Kloker [129] and Choudhari *et al.* [15] and of the stability computations by Groot *et al.* [35] showed how the secondary instability evolution depends on the strength of the carrying stationary vortex. To experimentally compare those results, two different stationary vortices, whose initial amplitude is tweaked by DREs of different height, are measured under natural and forced condition.

## 7.2. EXPERIMENTAL SETUP

### 7.2.1. HOT-WIRE ANEMOMETRY

Hot-wire measurements were performed with a single-wire boundary layer probe (*Dantec Dynamics P15*). A second probe (*Dantec Dynamics P11*) performed simultaneous measurements of the outer inviscid flow. This second probe was mounted about 10 cm away from the boundary layer probe along the  $Y$  axis at the same  $X - Z$  position. This second sensor allowed investigations of the free-stream turbulence levels as well as eventual electro-magnetic interference (EMI) from the plasma actuator. Both probes were operated by a *TSI IFA-300* Constant Temperature Anemometer (CTA). Wire calibration was performed in the wind tunnel itself, far from the model and close to a Pitot-static probe. Flow temperature and atmospheric pressure corrections were applied. The hot-wire

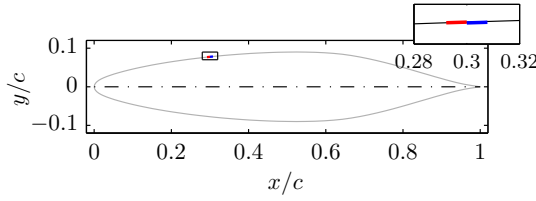


Figure 7.1: Schematic (to scale) of the airfoil (orthogonal to the wing leading edge) used in the present work with the AC-DBD actuator installed at  $x/c = 0.30$ . Inset: detailed view of the actuator. Red line: exposed electrode; blue line: covered electrode.

was operated at a sampling frequency of  $f_s = 40$  kHz and lowpass filtered with a cutoff frequency of  $f_{co} = 15$  kHz before bridge amplification. Time series of 4 seconds were recorded at every probe position to ensure statistical convergence. A three degrees of freedom automated traverse was installed in the wind tunnel diffuser. The traverse has a resolution of  $2.5 \mu\text{m}$  in all three directions.

The hot-wire scans were performed in  $y_t - z$  planes at different chordwise locations corresponding to the primary instability saturation (cf. [114]). Every measured plane consisted of 420 points: 28 scans in the local wall-normal direction  $y_t$  times 15 stations in the  $z$  direction spaced  $0.625$  mm from each other. The range of the  $y_t$  scans was chosen to span from the location where the local mean velocity was 10% of the local outer velocity until the inviscid flow-field. The wires were aligned with the vertical direction such to mainly measure the Euclidean sum of velocity components along the axes  $X$  and  $Y$ :  $|V^{HWA}| = (U^2 + V^2)^{\frac{1}{2}}$ .

### 7.2.2. AC-DBD PLASMA ACTUATOR

The AC-DBD plasma actuator configuration is described in this section. Moreover, given the novel fabrication technique, a dedicated experiment was performed to characterize the actuator mechanical performance.

#### CONFIGURATION

Details on the plasma actuators used in this study are described in section 2.4 The plasma actuator was placed at two different chordwise positions ( $x/c = 0.30, 0.375$ ) to investigate the effect of the forcing location on transition. The electrodes were aligned with the leading edge-parallel direction ( $z$ ) and such to induce an air flow along  $x$ . The schematic in figure 7.2 is a representation of the experiment including the wall-mounted actuator. In figure 7.1, the exact position ( $x/c = 0.30$ ) and relative dimensions of the AC-DBD actuator w.r.t. the wing section are shown.

Depending on the case, the actuation signal was sinusoidal with amplitudes ( $E$ ) of 1.2 kV and 1.5 kV. The high voltage signal frequency (carrier frequency) was chosen such to excite the desired unsteady modes. During the hot-wire measurements, the high-voltage monitor output of the amplifier was concurrently recorded in order to allow the phase-reconstruction procedure. A schematic of the time series of the actuator voltage and of the hot-wire measurements is shown in figure 7.3. Cases with the actuator operating at two frequencies  $f_{DBD} = 0.4$  kHz and  $f_{DBD} = 4$  kHz, proper of the *type-III*

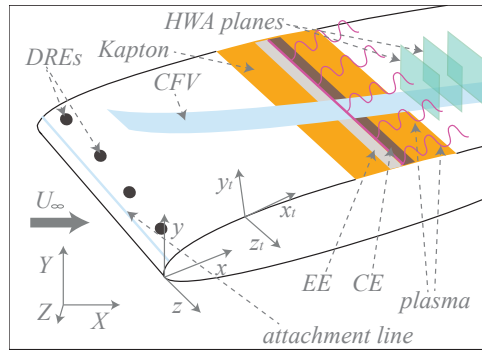


Figure 7.2: Schematic (not to scale) of the model with leading edge DREs and plasma actuator (EE: exposed electrode; CE: covered electrode and Kapton dielectric film). Definition of the reference systems  $xyz$ ,  $XYZ$  and  $x_t y_t z_t$ . Illustration of the HWA measurement planes, of the stationary CFV and of the downstream advecting plasma waveforms.

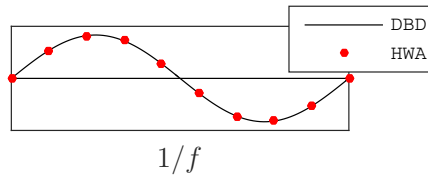


Figure 7.3: Schematic of the time signal of the AC-DBD actuator voltage and of the hot-wire measurements.

and *type-I* instability modes, respectively (cf. [114]), were performed. The hot-wire measurements were performed at acquisition frequency of  $f_s = 40$  kHz, leading to phase averaged reconstruction of the low frequency mode ( $f_{DBD} = 0.4$  kHz) within 100 discrete phases. Each phase average was constructed using 1600 instantaneous measurements. Respectively, the high frequency mode ( $f_{DBD} = 4$  kHz) was resolved within 10 discrete phases, using 16000 instantaneous samples per phase.

### PERFORMANCE

A dedicated experiment was performed to assess the performance of the used actuator. High speed particle image velocimetry was used to measure the velocity field induced by the actuator in quiescent air. To do so, the setup was enclosed in a box of  $1 \times 0.5 \times 0.5$  m<sup>3</sup>. The box was made out of transparent acrylic glass thus allowing optical access. The camera used in this experiment is a *LaVision Imager HS* featuring a sensor of  $2016 \times 2016$  px<sup>2</sup>, pixel size of  $11 \mu\text{m}$  and 12 bits of digital resolution. In order to facilitate higher sampling rates, the camera's active sensor was reduced to  $960 \times 440$  px<sup>2</sup>. The camera was equipped with a Nikon Nikkor 200mm macro lens and the optical magnification resulted to  $M = 1.14$ . Paraffin oil particles (*Shell Ondina*),  $1 \mu\text{m}$  in average diameter, were generated by a *TSI Atomizer* nozzle. A Nd:YAG high speed *Continuum Mesa PIV* laser (18mJ per pulse) was employed as light source. A 1mm thick light sheet was shaped by means of an opportune set of lenses and aligned with the induced jet, orthogonal to the actuator electrodes. Image acquisition and correlation were performed with *LaVision DAVIS 8.3*.

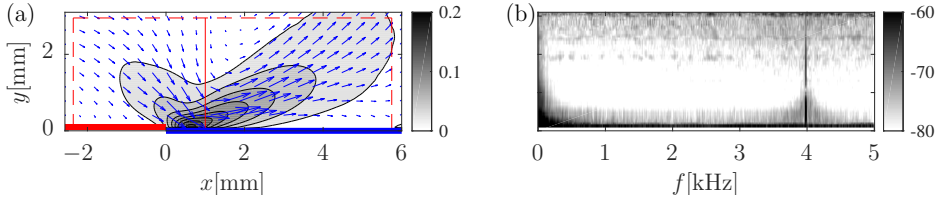


Figure 7.4: (a) Time-averaged velocity field (one every five vectors shown); shaded: wall-parallel component ( $\text{m s}^{-1}$ ). Red dashed lines: boundaries of the control volume for the evaluation of the exerted thrust. Horizontal thick lines: red EE, blue: CE. (b) Wall-parallel velocity power spectral density ( $\text{dB Hz}^{-1}$ ). Velocity sampled along the vertical red solid line of (a). Actuator operated at  $f_{DBD} = 4$  kHz -  $E = 1.2$  kV.

The final vector spacing was approximately  $0.053$  mm in both directions. The system was operated at the acquisition rate of  $10$  kHz in single-frame mode thus the pulse separation between consequent frames was  $100$   $\mu\text{s}$ . Sequences of  $25000$  images were acquired for each test case for a total measurement time of  $2.5$  s. The high sampling rate and long measurement time ensure to capture both the instantaneous flow evolution as well as the converged statistical fields.

Following Kotsonis [56], the time-averaged velocity field induced by the actuator is used to retrieve the thrust exerted by the actuator. The time averaged wall-parallel field is presented in figure 7.4(a). The maximum velocity in this direction is  $0.19$   $\text{m s}^{-1}$ . When the actuator was mounted on the wing surface (see figures 7.1 and 7.2), the induced jet resulted aligned with  $x$ . The momentum flux, through the boundaries of a control volume large enough to encompass the total body force (see the red dashed lines in figure 7.4(a)), is computed. For the  $f_{DBD} = 4$  kHz -  $E = 1.2$  kV case, the actuator thrust, normalised by unit length, in the wall-parallel direction resulted in  $T = 2.30$   $\mu\text{N m}^{-1}$ . From this quantity the momentum coefficient exerted by the actuator follows from equation 2.26. At  $x/c = 0.30$  ( $u_e = 18.36$   $\text{m s}^{-1}$  and  $\vartheta_u = 2.31 \times 10^{-4}$  m), the momentum coefficient attains the value of  $C_\mu = 4.82 \times 10^{-5}$  while at  $x/c = 0.375$  ( $u_e = 19.14$   $\text{m s}^{-1}$  and  $\vartheta_u = 2.53 \times 10^{-4}$  m) it is  $C_\mu = 4.06 \times 10^{-5}$  under the assumption that the oncoming flow does not modify the actuator performance [91, 21] and neglecting the mean-flow distortion caused by the developing CF instability. It must be noted that, for fixed voltage and frequency inputs (thus for fixed values of thrust), the relative effect of the forcing at the more downstream position is milder due to the increased momentum-loss of the local boundary layer and to increased external velocity. The values of velocity, thrust and momentum coefficient are relatively low compared to standard applications of AC-DBD plasma actuators [86, 17]. A comparative example is provided by the work of Dörr & Kloker [23], where plasma actuators were used to attenuate non-linear CFVs. Scaling the dimensional force from the study of Dörr & Kloker [23] to the conditions of the present experiment (i.e.  $x/c = 0.30$ ,  $u_e = 18.36$   $\text{m s}^{-1}$  and  $\vartheta_u = 2.31 \times 10^{-4}$  m), an equivalent  $C_\mu = 4.8 \cdot 10^{-2}$  is estimated, which is three orders of magnitude larger than the actuator of this study, further confirming the weak nature of the presently used actuators. This is in line with the scope of this experiment which is to condition the unsteady modes without modifying their development or affecting the base-flow. Towards this goal, rather weak jets are required as will be shown in the results section.

Instability mode	$f_{DBD}$ [kHz]	$E$ [kV]	HWA planes: $x/c$			
natural flow	-	-	0.40	0.425	0.45	0.475
<i>type-III</i>	0.4	1.5	0.40	0.425	0.45	0.475
<i>type-I</i>	4.0	1.2	-	-	0.45	-

Table 7.1: Test cases

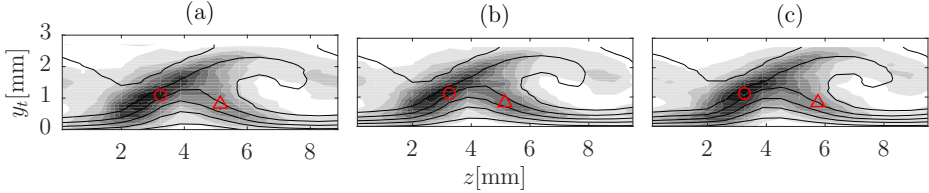


Figure 7.5: Time averaged velocity fields (solid lines: 7 levels, from 0 to  $|\bar{V}_e^{HWA}|$ ) and velocity fluctuation fields (shaded: 10 levels, from 0 to  $0.1 |\bar{V}_e^{HWA}|$ ) at  $x/c = 0.45$ . AC-DBD actuator installed at  $x/c = 0.30$ : (a) non-operative; (b)  $f_{DBD} = 0.4$  kHz -  $E = 1.5$  kV; (c)  $f_{DBD} = 4$  kHz -  $E = 1.2$  kV. The red markers indicate locations of spectral analysis presented in figure 7.6.

When the actuator was supplied with the  $f_{DBD} = 0.4$  kHz -  $E = 1.5$  kV voltage, the induced jet resulted even weaker thus not allowing to extract the exerted thrust with acceptable accuracy despite the slightly augmented voltage amplitude to compensate the frequency response of the actuator [86, 17]. A consequence of the reduced carrier frequency is that the actuator lifetime can be significantly longer (several tens of hours of operation), compared to high-frequency forcing. Vice-versa operation at high frequencies causes dielectric failure after a few hours of operation. The limited lifetime of the considered actuator at high frequency necessitated a restricted testing matrix for high frequency forcing in this study as it will be shown in section 7.3.

Capitalizing on the very high frame rate of the PIV experiment, spectral information of the induced velocity field is also accessible. The power spectral density, computed following Welch's method [133], with final frequency resolution  $\delta_f = 10$  Hz, of the wall-parallel velocity signal sampled along the solid line of figure 7.4(a) is shown in figure 7.4(b). It appears that most of the spectral energy occurs at the carrying voltage frequency as reported in previous studies on standard actuators [17] thus confirming the capability of the considered actuator in forcing the chosen narrow-band fluctuations. However, increased spectral energy at relatively low frequencies ( $0 < f < 0.2$  kHz) is also evident in figure 7.4(b). At this point it cannot be concluded whether this low frequency component is an artefact of quiescent conditions testing (i.e. recirculation in the box, drafts etc.) or an inherent plasma oscillation. Nevertheless, as will be shown in the results section, at these low frequencies no effect significant to the transition evolution can be detected in the wind tunnel measurements.

Finally, a note must be made regarding the use of HWA in close proximity to plasma actuators. Hot-wires are electrically balanced devices, relying on minute variations of voltage signals, thus sensitive to electromagnetic noise. Previous studies have shown pronounced levels of electromagnetic interference affecting the hot-wire when in the

vicinity of operating plasma actuators [61, 56]. Typically EMI would appear as a narrow peak in the measured signal at the plasma carrier frequency. In the present study, the effect of EMI was identified by utilizing the second hot-wire probe positioned in the inviscid flow and measuring concurrently to the boundary layer probe. As will be shown in the results section, EMI effects were detected by the inviscid hot-wire, albeit several orders of magnitude less energetic than the physical velocity fluctuations pertaining to boundary layer instabilities, detected by the boundary layer probe (see figure 7.6). As such, the effect of EMI on the statistical and phase-reconstructed flow fields was confirmed to be negligible. The relatively low levels of EMI can be attributed to the large distance between the plasma actuator and the hot-wires (minimum distance was approximately 120 mm) and the relatively low amplitude of high voltage.

### 7.3. TEST CASES

The plasma actuator was operated at two different voltages in order to reconstruct the spatio-temporal characteristics of the two developing instability modes of *type-I* (in the 4000 Hz band) and *type-III* (in the 400 Hz band) [114]. These fluctuations were weakly amplified by the actuation and their respective phase was locked to the actuator signal as it will be shown in section 7.4.4.

Measurements were performed at four different chordwise stations ( $x/c=0.40, 0.425, 0.45, 0.475$ ) for both the unforced and the low-frequency forcing cases. Given the reduced lifetime of the dielectric *Kapton* sheet when the actuator was operated at the higher frequency and the long measurement time necessitated by HWA measurements (about 40 minutes were needed per each measured plane), only the plane at  $x/c = 0.45$  was measured for the 4 kHz case. The three test cases are summarized in table 7.1.

## 7.4. RESULTS AND DISCUSSION

The effect of periodic forcing on the statistical flow fields is inspected in the following section. The spectral content is analysed by means of single-point spectra and band-pass filtered fields followed by the investigation of the spatio-temporal evolution of the unsteady modes. Finally the effect of the amplitude of the 'carrying' stationary vortex and of the actuator position is presented.

### 7.4.1. STATISTICAL ANALYSIS

As described in the experimental setup, the hot-wire probe was aligned such to measure mainly the Euclidean sum of the  $U$  and  $V$  velocity components. Time averaged (denoted with the overbar symbol) velocity fields non-dimensionalised with the local external velocity ( $|\bar{V}_e^{HWA}|$ ) and pertaining to the three investigated cases are presented in figure 7.5. For all cases, the characteristic structure pertaining to the fully developed cross-flow vortex is evident at the chordwise location of  $x/c = 0.45$ . Previous extended investigations by the authors [114] showed that, at this station, the primary stationary vortices are undergoing amplitude saturation. Based on the same study and previous work [19, 77, 129, 135], amplitude saturation of the primary CF mode is usually accompanied by rapid growth of secondary high frequency instabilities. The stationary CF vortices have very weak in-plane velocity components compared to the component along the vortices axes

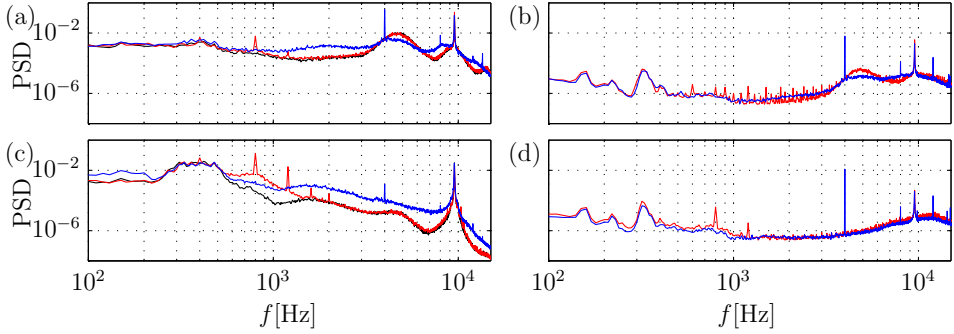


Figure 7.6: Normalised power spectral densities of the velocity fluctuations (see equation 2.20) at  $x/c = 0.45$ . Velocity sampled at the location of local maximum of fluctuations in (a) the outer upwelling air region (denoted by  $\circ$  in figure 7.5) and (c) the inner upwelling air region (denoted by  $\triangle$  in figure 7.5). Velocity sampled in the outer inviscid flow (b) simultaneously to (a) and (c) simultaneously to (d). Black lines: unforced flow; red solid lines:  $f_{DBD} = 0.4$  kHz; blue solid lines:  $f_{DBD} = 4$  kHz.

[129, 114]. Nonetheless, the displacement of high momentum fluid in low momentum regions (and vice-versa), consequent of these vortices, has a dramatic impact in the organization of the boundary layer. The contours presented in figure 7.5 clearly show this effect. Furthermore, it can be concluded that the unsteady plasma forcing at both the lower and higher frequency does not produce any considerable effect on the morphology of the stationary vortices.

Inspection of the velocity fluctuation fields, provided in figure 7.5, for the three flow cases show pronounced fluctuations levels. These are mainly occurring in two regions of the boundary layer corresponding to the inner and the outer upwelling flow regions of the primary vortex. Malik *et al.* [77] showed that these regions correspond to the locations of large positive and negative values of the spanwise velocity gradient respectively. Previous research (e.g. [40, 77, 51, 129, 135]) showed that the outer side of the cross-flow vortices is occupied by high frequency fluctuations, defined as *type-I* mode, of Kelvin-Helmholtz nature (cf. Bonfigli & Kloker [8]). The inner region of the primary vortices is instead interested by low frequency fluctuations, defined as *type-III* mode which arise from the interaction between the stationary and the travelling cross-flow waves, with the latter featuring the reported lower frequencies and growth rates [30, 40, 77, 51, 129, 8].

Upstream plasma forcing at  $x/c = 0.3$  results in mild changes in the distribution of dominant fluctuations within the stationary CFV flow-field. By operating the actuator at the frequency of  $f_{DBD} = 0.4$  kHz, the *type-III* mode is enhanced. This is confirmed by the contour of figure 7.5(b), where the fluctuations in the inner 'leg' of the stationary vortex are slightly increased. When instead the unsteady forcing is applied at  $f_{DBD} = 4$  kHz, the *type-I* fluctuations are stimulated. The contour of figure 7.5(c) indicates a slight increase of fluctuations associated with the left leg of the vortex.

The apparent invariance of the statistical flow-fields to actuation confirms the initial premise of utilization of the AC-DBD actuator as a forcing agent with minimal effect on the base flow. This was achieved using rather weak high voltage amplitudes as well as placing the actuator in the fully developed primary instability field but considerably upstream of

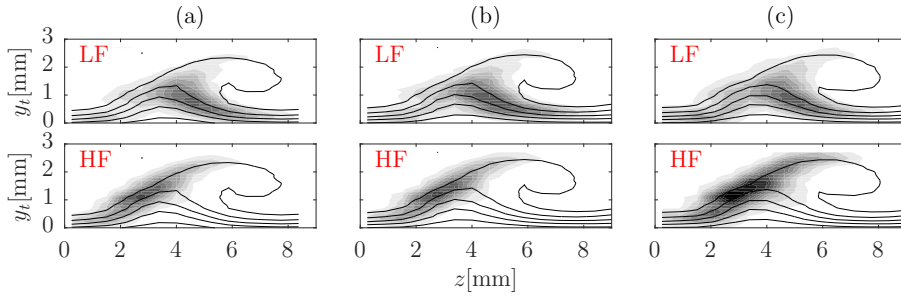


Figure 7.7: Contours of the band-pass filtered (top: LF; bottom: HF) fluctuations (shaded, 10 levels from 0 to  $0.05 |\bar{V}_e^{HWA}|$ ) at  $x/c = 0.45$ . AC-DBD actuator installed at  $x/c = 0.30$ : (a) non-operative; (b)  $f_{DBD} = 0.4$  kHz -  $E = 1.5$  kV; (c)  $f_{DBD} = 4$  kHz -  $E = 1.2$  kV. Black line contours denote time averaged velocity.

the secondary modes onset (i.e. marginal stability branch-I). Further discussion on the effect of the actuator position is provided in section 7.4.6.

### 7.4.2. SPECTRAL ANALYSIS

It is instructive to inspect the effect of the unsteady forcing of *type-III* and *type-I* instability modes in the spectral domain. To this goal, the hot-wire velocity signal was sampled at locations of fluctuations maxima described in the previous section and corresponding to the marker positions in the flow-field of figure 7.5. Averaged periodogram PSD were computed [133]. The spectra feature a frequency resolution of  $\delta_f = 10$  Hz. The spectra feature a frequency resolution of  $\delta_f = 10$  Hz. The presented spectra are normalised based on Parseval's theorem as shown in equation 2.20.

The spectra of the fluctuations maximum in the outer upwelling air region are presented in figure 7.6(a) for the three investigated flows. The spectra show that at the higher frequencies, when the 4 kHz forcing is applied, the broadband energy between 3 and 7.5 kHz (related to the *type-I* mode) attains to lower levels compared to the unforced and low-frequency forcing cases. The spectra of these two last cases are practically overlapping on each other throughout the resolved band. Nevertheless, the energy at 4 kHz is considerably increased thus showing the possibility of conditioning the frequency of the secondary modes through external monochromatic forcing. Furthermore, the spectrum of the high-frequency forcing shows enhanced energy levels throughout the band suggesting a contamination of fluctuations, due to actuation. The low-frequency forcing shows discrete peaks stemming beyond the unforced case spectrum at the forcing frequency and at the first two harmonics (400, 800 and 1200 Hz).

The spectra sampled at the location of maximum fluctuation in the inner CFV leg are shown in figure 7.6(c). As for the previously discussed spectra, the 4 kHz forcing has stronger effects on the full spectrum fluctuations. The 400 Hz forcing shows higher peaks at the forcing frequency and at the first five harmonics (until 2 kHz). All spectra feature a broadband hump centred at  $f = 0.4$  kHz. This hump is related to the *type-III* mode [114]. Moreover, the fluctuations comprised in the band  $500 \text{ Hz} \leq f \leq 2 \text{ kHz}$  are significantly increased, even beyond the high-frequency forcing spectrum, by the 400 Hz forcing.

The spectra of the second hot-wire placed outside the boundary layer (about 10cm

forcing	$A_I$	$A_{II}^{tot}$	$A_{II}^{LF}$	$A_{II}^{HF}$	$A_{II}^{PR}$
none	0.119	0.0302	0.0058	0.0048	-
0.4 [kHz] - 1.5 [kV]	0.1181	0.0329	0.0069	0.0050	0.0042
4.0 [kHz] - 1.2 [kV]	0.1175	0.0352	0.0074	0.0091	0.0064

Table 7.2: Stationary ( $A_I$ ) and unsteady full spectrum ( $A_{II}^{tot}$ ), band-pass filtered ( $A_{II}^{LF}$ : low-frequency band,  $A_{II}^{HF}$ : high-frequency band) and phase-reconstructed ( $A_{II}^{PR}$ ) disturbances amplitudes from equations 2.22 and 2.24 evaluated at  $x/c = 0.45$ .

7

from the boundary layer probe) at the same  $X - Z$  position are plotted in figures 7.6(b) and (d). They show different discrete spikes that are to be related to electro-magnetic interference (EMI). Despite the undesired occurrence of these spikes their overall energy is several orders of magnitude lower than the pertinent frequencies in the boundary layer, suggesting negligible influence of EMI on the measurements. The high-frequency hump of the second wire signal is instead an artefact of the CTA hardware [99].

Analysing the spectral contents at higher frequencies, it appears that, when unsteady low and high frequency forcing is applied, the broadband energy between 0.5 and 7 kHz attains to higher levels. Part of this band, in the range  $2 \text{ kHz} \leq f \leq 7 \text{ kHz}$ , is typically associated with the occurrence of the *type-I* instability. It appears that both the low and high frequency forcing lead to amplified fluctuations within this band.

The spectra at the inner upwelling air region (figure 7.6(c), show higher energies for all the frequencies when the forcing is active. The hump at 400 Hz show mild deviations from the unforced case for the high and low frequency forcing. When  $f_{DBD} = 4 \text{ kHz}$ , a broadband of high energy fluctuations roughly centred at 1.5 kHz appears. The origin of this band is currently unknown. Additionally, when the actuator is operated at 400 Hz, higher harmonics take place. The EMI, plotted in figure 7.6(d), show similar spikes at the frequency and harmonics of the high frequency forcing.

To further evaluate the effect of the applied forcing on the boundary layer, the velocity fluctuations were band-pass filtered in the relevant frequency bands by means of a fourth order Butterworth digital filter [114]. The two inspected bands covered frequencies between 350 Hz and 550 Hz (low frequency (LF) band) and between 3.5 kHz and 4.5 kHz (high frequency (HF) band) respectively. The analysis was performed for the three flow cases investigated so far and is presented in figure 7.7. It is evident that the unsteady modes are strictly confined in the described zones of the boundary layer. Forcing at the high frequency has major effects, given that the spectral hump of the *type-I* mode is much wider than the respective low frequency band under low frequency actuation. The analysis of the spectra and band-pass filtered fields allows to conclude that the chosen operating voltages for the two forced frequencies (summarized in table 7.1) are enough to enhance the desired instability modes, without strongly affecting the overall evolution of the boundary layer, or the transition process.

To quantify the field amplitudes of the primary and secondary instability mechanisms, the metrics described in equations 2.22 and 2.24 are used, where  $z^m = \lambda_f = 9 \text{ mm}$ .

The quantity  $A_{II}$  is evaluated for the total spectrum ( $A_{II}^{tot}$ , with  $f_1 = 0 \text{ Hz}$  and  $f_2 = f_s/2$ ) and for the low ( $A_{II}^{LF}$ , with  $f_1 = 350 \text{ Hz}$  and  $f_2 = 550 \text{ Hz}$ ) and high ( $A_{II}^{HF}$ , with  $f_1 = 3.5 \text{ kHz}$  and  $f_2 = 4.5 \text{ kHz}$ ) frequency bands. Therefore the fluctuation fields shown in figure 7.5

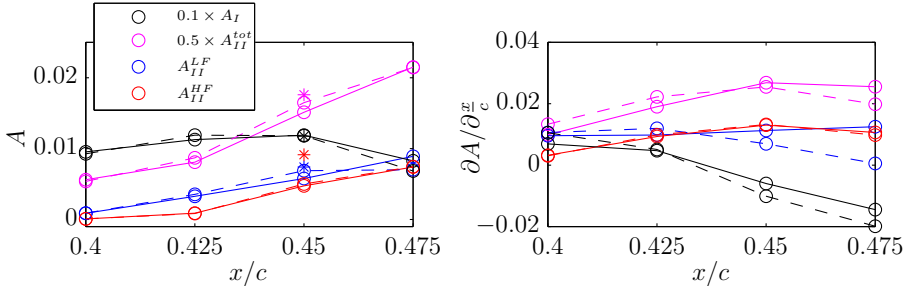


Figure 7.8: Chordwise evolution of stationary modes and fluctuations amplitudes (see equations 2.22 and 2.24) and related chordwise gradients. Solid lines: unforced flow; dashed lines: actuator operated at  $f_{DBD} = 0.4$  kHz -  $E = 1.5$  kV; symbol \*: actuator operated at  $f_{DBD} = 4$  kHz -  $E = 1.51.2$  kV.

and 7.7 are the considered integrands of equation 2.24. Finally,  $A_{II}^{PR}$  is the fluctuations amplitude of the phase-reconstructed (PR) mode with  $f_1 = f_{DBD} - \delta_f$  and  $f_2 = f_{DBD} + \delta_f$  (note that this is true under the assumption that, through phase averaging, only the fluctuations pertaining to the monochromatic reconstructed mode are considered). The results are summarized in table 7.2. The unforced stationary vortex, at the measurement location, reached the amplitude of  $A_I = 0.119$ . Comparing this value with the one reported at the same chordwise station and flow conditions by Serpieri & Kotsonis [114] (c.f. figure 11a) where no actuators were mounted on the wing ( $A_I = 0.113$ ), shows that the steps caused by the layer of dielectric have no effect on the developing stationary cross-flow instability.

When the actuator is operated, the amplitude of the CFV is slightly decreased by the enhanced fluctuations. Moreover, forcing at both the considered frequencies causes an increase of the fluctuations amplitude in both the forced band and in the full spectrum amplitude with the higher frequency forcing showing the largest effects (as seen in figure 7.7).

### 7.4.3. SPATIAL EVOLUTION

In this section, the effect of the forcing on the chordwise development of the stationary and unsteady fields is investigated. For this purpose, the same cross-flow vortex analysed so far is traced along the  $x$  direction (consider that the CFVs are roughly aligned with the local flow). Measurements were therefore performed at three more chordwise positions:  $x/c = 0.40, 0.425, 0.475$ . The hot-wire scans have the same spanwise resolution (0.625 mm) as for station  $x/c = 0.45$ . However, the wall-normal scans are slightly adjusted to compensate the different wall-normal extent of the boundary layer while still encompassing 28 points per wall-normal profile. For this analysis both the unforced boundary layer as well as the  $f_{DBD} = 0.4$  kHz -  $E = 1.5$  kV case were considered.

In figure 7.8, the fluctuation amplitudes are plotted versus the measured locations together with their chordwise gradient. It appears that, for the most upstream station ( $x/c = 0.40$ ), both the steady modes and the fluctuation amplitudes are not strongly affected by the actuation. However, the amplitude gradients (representative of local growth rates) of both stationary and unsteady fields are initially larger for the forced cases.

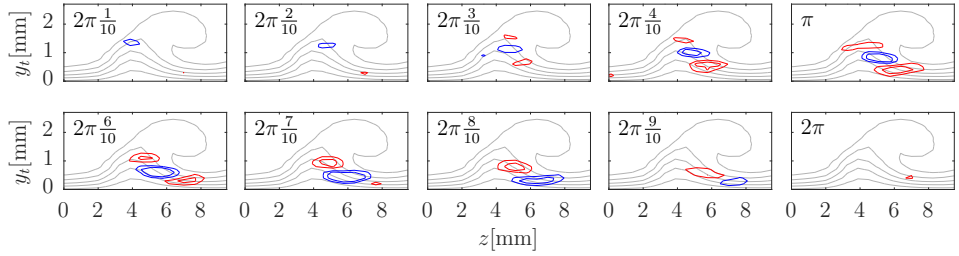


Figure 7.9: Phase reconstructed velocity fluctuation fields at  $x/c = 0.45$ : ten equally spaced (see the upper left corner label) phases (5 levels, red lines between  $-0.03 |\tilde{V}_e^{HWA}|$  and  $-0.003 |\tilde{V}_e^{HWA}|$ ; blue lines between  $0.003 |\tilde{V}_e^{HWA}|$  and  $0.03 |\tilde{V}_e^{HWA}|$ ) superimposed on contours of time-averaged velocity (grey lines: 6 levels, from 0 to  $|\tilde{V}_e^{HWA}|$ ). AC-DBD actuator installed at  $x/c = 0.30$  and operated at  $f_{DBD} = 0.4$  kHz -  $E = 1.5$  kV.

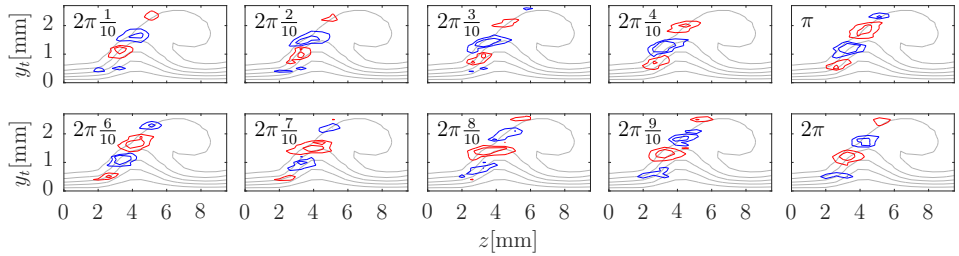


Figure 7.10: Same caption as figure 7.9 (5 levels, red lines between  $-0.04 |\tilde{V}_e^{HWA}|$  and  $-0.004 |\tilde{V}_e^{HWA}|$ ; blue lines between  $0.004 |\tilde{V}_e^{HWA}|$  and  $0.04 |\tilde{V}_e^{HWA}|$ ) superimposed on contours of time-averaged velocity (grey lines: 6 levels, from 0 to  $|\tilde{V}_e^{HWA}|$ ). AC-DBD actuator installed at  $x/c = 0.30$  and operated at  $f_{DBD} = 4$  kHz -  $E = 1.2$  kV.

Therefore, at  $x/c = 0.45$ , larger amplitudes in all the three considered bands are observed, as discussed before. Similar effects occur when the actuator is operated at the higher frequency. The stationary mode amplitude at  $x/c = 0.45$  is almost the same for all the three cases, however the higher fluctuations for the forced field lead to the reduced  $A_I$  amplitude at the most downstream station. This indicates a more advanced transitional state with enhanced diffusion of the steady structures.

#### 7.4.4. SPATIO-TEMPORAL ORGANISATION

It becomes evident from the spectral analysis (figure 7.6) and band-pass filtered fluctuation fields (figure 7.7), that actuation at the selected frequencies results in the forcing of the respective instability modes. Due to the deterministic conditioning of both forcing signal and acquisition sequence, it can be expected that the triggered modes will be phase conditioned. This allows the reconstruction of the coherent spatial structures pertaining to these modes (the details were discussed in section 7.2.2), thus enabling phase-resolved measurements using a point measurement technique (HWA) [51, 13].

Phase averaged velocity fluctuation fields (mean flow subtracted) in the  $y_t - Z$  plane are presented in figure 7.9 for the low frequency forcing and in figure 7.10 for the high frequency forcing (10 equally spaced phases for both the forced modes). For both the

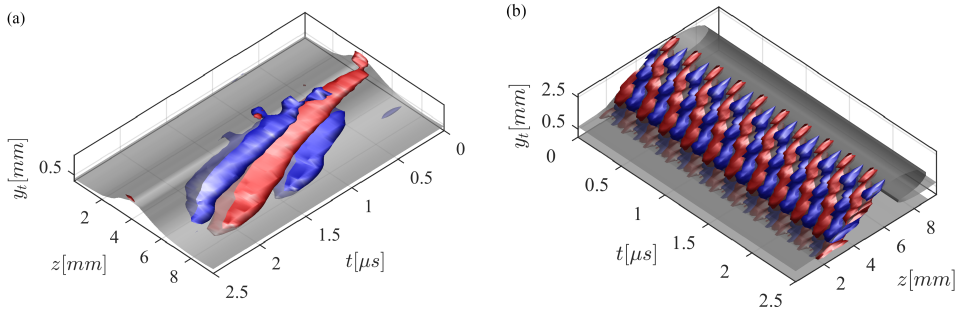


Figure 7.11: 'Pseudo-spatial' representation of the phase-reconstructed fields (red and blue isosurfaces at  $\pm 0.02 |\bar{V}_e^{HWA}|$ ) (a) of figure 7.9 ( $f_{DBD} = 0.4$  kHz (one period), view from upstream and larger  $z$ ) and isosurface of the time-averaged velocity (grey isosurface at  $0.6 |\bar{V}_e^{HWA}|$ ); and (b) of figure 7.10 ( $f_{DBD} = 4$  kHz (ten periods), view from upstream and smaller  $z$ ) and isosurface of the time-averaged velocity (grey isosurface at  $0.9 |\bar{V}_e^{HWA}|$ ).

modes it appears that, increasing phase (i.e. increasing time), the fluctuations maxima tend to move towards the wall. More specifically, the structures pertaining to  $f_{DBD} = 0.4$  kHz move towards the right side of the stationary vortex (increasing  $z$  and decreasing  $y_t$ ), while the structures pertaining to  $f_{DBD} = 4$  kHz displace towards the outer side on the left of the primary vortices (decreasing  $z$  and  $y_t$ ).

In order to better facilitate the topological description of the phase-resolved fluctuating structures, use of a 'pseudo-spatial' representation is made. This is achieved by representing time (i.e. subsequent phases) as the third dimension, whereas individual slices in the  $y_t - z$  plane are the measured phase averages. This approach is followed in figures 7.11a and 7.11b for the low and the high forcing frequencies, respectively. The plotted structures are captured at a fixed streamwise position, hence, to represent their 'pseudo-spatial' evolution, they are presented along the decreasing time direction (cf. Kawakami *et al.* [51]). This procedure can be mathematically expressed by the equation of a downstream propagating wave at a fixed spatial station:  $A(x_0, t) = \sin(\alpha_x x_0 - \omega t)$ , where  $\alpha_x$  is the wavenumber and  $\omega$  the angular frequency.

Such representation is to be considered only for facilitating visualization and not as a quantitative description of the spatial evolution of the mode. In the latter case, several limitations occur. The spatial amplification of the instability modes cannot be assessed by single-plane measurements. To properly capture the spatial evolution, full volumetric scans are required [13]. Alternatively, the true spatial evolution could be retrieved from the advection speed of the travelling waves. Serpieri & Kotsonis [114] estimated the convecting velocity by matching it with the local time-averaged boundary layer velocity. This approach is corroborated by the consideration that these structures are generated by inviscid instability mechanisms and hence are passively advected by the local flow (cf. Malik *et al.* [77], Bonfigli & Kloker [8]). This would allow to extrapolate the spatial shape and evolution of the unsteady structures. Despite these considerations, the authors believe that the rigorousness of this approach, applied to the current experiment,

would suffer for several reasons. The estimation of the local boundary layer velocity from the time-averaged fields is considered as a blunt approximation. In fact, the hot-wire measurements were performed in planes aligned with  $y_t - z$  hence not orthogonal to the primary CF vortices (direction of advection). Furthermore, the hot-wire measured the velocity magnitude of the  $U$  and  $V$  velocity components and not the velocity component along the stationary waves. Only the latter gives a correct estimation of the actual advecting velocity [114]. Due to these considerations, the 'pseudo-spatial' (i.e. decreasing time) representation was chosen.

Despite these limitations, figures 7.11a and 7.11b are considered an illustrative visualization. For a direct comparison between the two modes, the presented time-evolution refers to the full period of the lower forced frequency ( $T = 1/\min(f_{DBD}) = 2.5 \mu\text{s}$ ). Hence the structures pertaining to  $f_{DBD} = 4 \text{ kHz}$  have been replicated over ten periods. The low frequency structures appear as a sequence of positive and negative velocity regions in the inner upwelling air region of the stationary CF wave. In the 'pseudo-spatial' representation they appear oriented with a shallow angle pointing towards the inner part of the stationary waves and slightly slanted towards the upper region of the boundary layer.

The high frequency fluctuations pertaining to the *type-I* mode have a drastically different shape, compared to *type-III* structures. In figure 7.11b they appear as a more narrow sequence of high and low velocity structures riding on the outer side of the stationary vortices. The 'pseudo-spatial' plot shows that these waves appear significantly inclined with respect to the stationary vortices. It has to be stressed again that the third axis of figure 7.11b is in the direction of decreasing time. Hence the plotted structures, not accounting for the effective advecting velocity, do not accurately describe the three-dimensional shape of the instabilities but only give an indication of it. It can be commented that the structures span along the wall-normal direction through almost the entire boundary layer extent. As such, the local flow velocity, by which they are advected downstream, varies considerably thus leading to a more pronounced helicoidal shape w.r.t. the plotted figure [129, 13, 8, 114]. The 'pseudo-spatial' representation of the two modes closely resembles the structures presented by [114] from the Proper Orthogonal Decomposition analysis of the instantaneous tomo-PIV fields (compare figure 5.9a and 5.11 with figures 7.11a and 7.11b). The convincing qualitative agreement offers a validation of the Taylor hypothesis based estimation of the structures frequencies followed by Serpieri & Kotsonis [114].

In both phase-reconstructed fields of figures 7.9 - 7.11a and 7.10 - 7.11b, the amplitude of the high and low velocity fluctuations appears not constant throughout the reconstructed period. To better visualize this effect, the integral over the measured plane of the square power of the fields presented in figures 7.9 and 7.10 is computed per each phase. The expression of this amplitude, referred to as  $A_{\Phi}^{PR}$ , is presented in equation 7.1,

$$A_{\Phi}^{PR}(x, \Phi) = \frac{1}{y_t^m} \frac{1}{z^m} \int_0^{y_t^m} \int_0^{z^m} \left( \frac{|V_{PR}^{HWA}(x, \Phi)|}{|\bar{V}_e^{HWA}(x)|} \right)^2 dz dy_t \quad (7.1)$$

where  $|V_{PR}^{HWA}|$  is the phase-reconstructed velocity field at each phase. The evolution along the period of the reconstructed fluctuations is presented in figure 7.12 for both the low and high frequency fields. Both these amplitudes show an oscillation within the respective period. This effect can be attributed to the characteristics of the chosen actuator. AC-DBD plasma actuators are known to yield both a DC and an AC body force

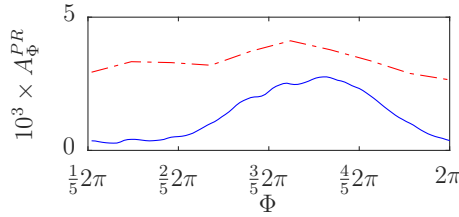


Figure 7.12: Amplitude of the reconstructed velocity fluctuation fields (evaluated according to equation 7.1) along one period. Solid blue line: fields of figure 7.9; dotted-dashed red line: fields of figure 7.10.

caused by the different momentum of the species accelerated within the actuation cycle [86, 17, 57]. Therefore, the modulation of the fluctuations energy along the period can be considered as an effect of the actuator.

#### 7.4.5. EFFECT OF STATIONARY CFVs AMPLITUDE

The effect of the 'carrying' primary stationary CFV on the unsteady field is investigated in this section. For this purpose, the experimental setup is partially modified. While the flow conditions and measurement approach are the same as described in section 7.2, the leading edge forcing of the stationary CFV is slightly modified. The micrometric roughness element triggering the stationary vortex was applied with higher force on the model surface, thus slightly reducing the effective protuberance height (see the difference between the two CFVs in figure 4.12) and therefore the initial amplitude of the stationary wave. While measuring the element height (using a mechanic profilometer) could not help to retrieve an accurate estimate (measured uncertainty about  $\pm 1 \mu\text{m}$ ), the measured velocity field can be used, by means of equation 2.22, to extract the effect, at the scan location, on the developing stationary wave. The stationary amplitude for the weaker CFV considered in this section at  $x/c = 0.45$  is  $A_I = 0.1078$ . This value is about ten percent less than the modal amplitude of the stronger vortex at the same position analysed in the previous sections (cf. table 7.2).

Measurements were carried out for the same actuator operating conditions and at the same chordwise positions reported in table 7.1. The chordwise evolution of the stationary and fluctuation amplitudes and their chordwise gradients are shown in figure 7.13. Despite the reduced amplitude at the most upstream station ( $x/c = 0.40$ ), the stationary mode attains to comparable saturation amplitudes to what is reported in table 7.2. Furthermore, also for this flow-case, saturation takes place in the proximity of  $x/c = 0.45$  (within the chordwise resolution of the current experiment). Stronger differences between the higher amplitude CFV (figure 7.8) and the reduced amplitude CFV (figure 7.13) relate to the fluctuations fields. The unforced weaker CFV features a full-spectrum amplitude of  $A_{II}^{tot} = 0.0175$  compared to  $A_{II}^{tot} = 0.03024$  for the stronger vortex at  $x/c = 0.45$ . In a similar way, the band-pass filtered fields are significantly reduced.

The phase reconstruction procedure, described in section 7.4.4, is performed, at  $x/c = 0.45$ , for the unsteady field of the weaker CFV. The results are plotted in figures 7.14 for the reconstructed low-frequency mode. The presented fields attain lower values compared to the respective modes along the stronger CFV presented in section 7.4.4.

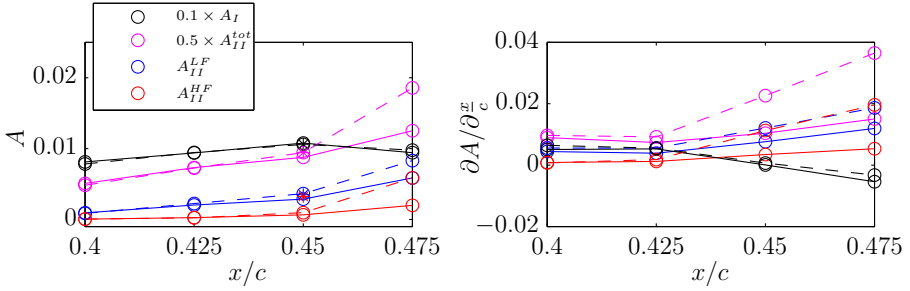


Figure 7.13: Same caption of figure 7.8. Reduced amplitude CFV.

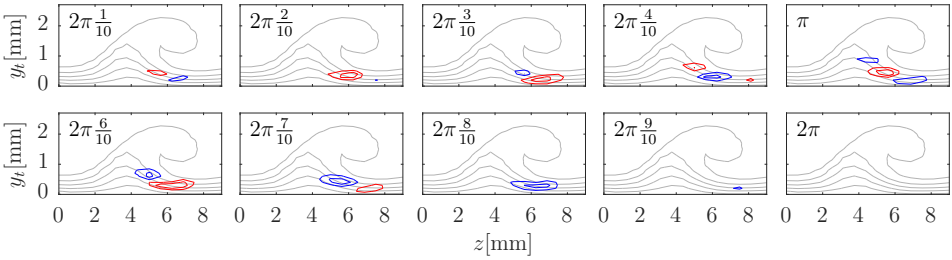


Figure 7.14: Same caption as figure 7.9. Reduced amplitude CFV.

The reconstructed fields for the high-frequency forcing yield very weak results and are not shown. The lower frequency correlated band amplitude is  $A_{II}^{PR} = 0.0025$  while the high-frequency mode yields  $A_{II}^{PR} = 0.0029$  thus about half compared to the values of the stronger wave (see table 7.2).

Malik *et al.* [77] analysing the terms of the secondary modes energy equation (namely the Reynolds-Orr equation), showed that the amplification of the *type-I* mode scales with the intensity of the stationary field velocity gradient along the spanwise direction while the *type-II* mode amplification is a function of the wall-normal shears. Because of this relationship, they introduced the alternative nomenclature of *mode-z* and *mode-y* for the two modes. [35] followed a similar approach (linear secondary stability theory) but making use of the experimental flow-field measured with tomographic PIV by Serpieri & Kotsonis [114] as base-flow. The experimental flow-field encompassed both the stronger and the weaker CFVs investigated in this study. One of the results shown by [35] is that the secondary *type-I* and *type-II* instability modes of the weaker wave are marginally stable while those of the stronger vortex are both unstable (and for a broad band of wavenumbers/frequencies). The energy terms analysis revealed that, for both the modes, the Reynolds stresses related to the spanwise shears were reduced (transferring less energy to the *type-I* mode and changing sign, thus becoming a disruptive term, for the *type-II* modes) for the weaker CFV flow-field. The Reynolds stresses related to the wall-normal shears transferred less energy from the *type-I* mode and did not change their effect on the *type-II* mode, when comparing the weaker to the stronger vortex base-flow. From the current measurements, Reynolds stresses are obviously not accessible. Despite

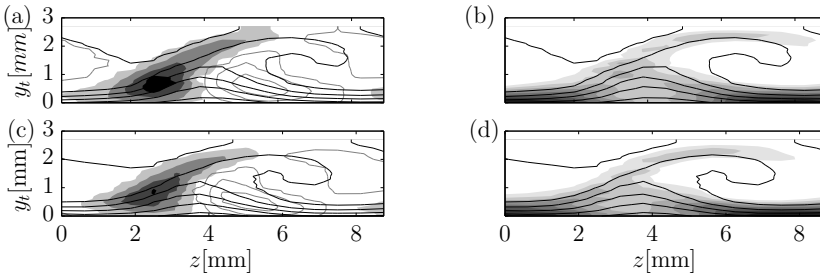


Figure 7.15: (a and c) non-dimensional spanwise velocity gradient ( $(\partial|\bar{v}^{HWA}|/\partial z)/(|\bar{v}_e^{HWA}|/\lambda_z)$ ) (10 levels, shaded: between  $-37.4$  and  $-3.74$ ; grey solid lines: between  $3.74$  and  $37.4$ ); (b and d) non-dimensional wall-normal velocity gradient ( $\partial|\bar{v}^{HWA}|/\partial y_t/(|\bar{v}_e^{HWA}|/\lambda_z)$ ) (10 levels, shaded from  $20.79$  to  $207.9$ ). (a and b) stronger CFV; (c and d) reduced amplitude CFV. Black line contours denote time averaged velocity.

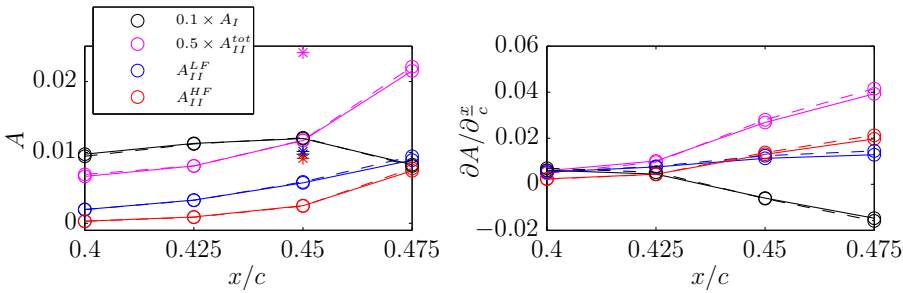


Figure 7.16: Same caption as figure 7.8. Actuator installed at  $x/c = 0.375$ , larger amplitude stationary vortex.

this, the spanwise and wall-normal velocity gradients for the two stationary vortices can be compared. This is done in figure 7.15, confirming the strong reduction of the spanwise shears (in the outer upwelling air region pertaining to *type-I* mode) and the weak modification of the wall-normal gradient (on the top region of the stationary wave) for the weaker vortex thus partially confirming the analysis of [35]. Furthermore, the POD analysis performed by [114] on the stronger CFV and leading to the individuation of the flow structures of both *type-I* and *type-III* modes did not yield the same clear results on the weaker CFV considered in this section.

The results presented in this section show the strong dependence of the unsteady field on the underlying stationary flow. This effect was investigated in numerical simulations by [129] and recently by [15] and [35] and here experimentally reconciled.

#### 7.4.6. EFFECT OF ACTUATOR LOCATION

The actuator was installed at a more downstream position ( $x/c = 0.375$ ) to investigate the effect that this has on the flow development. The larger amplitude stationary vortex is considered for this analysis. In figure 7.16, the spatial evolution of the stationary and unsteady modes is plotted for the unforced and for the low frequency forcing case. The evolution of the stationary mode is comparable to the one observed in figure 7.8 (these measurements encompass the same stationary vortex) showing that the actuator, when

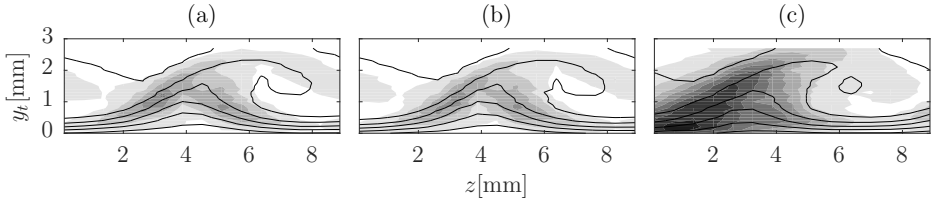


Figure 7.17: Time averaged velocity fields (solid lines: 7 levels, from 0 to  $|\bar{V}_e^{HWA}|$ ) and velocity fluctuation fields (shaded: 10 levels, from 0 to  $0.16 |\bar{V}_e^{HWA}|$ ) at  $x/c = 0.45$ , larger amplitude stationary vortex. AC-DBD actuator installed at  $x/c = 0.375$ : (a) non-operative; (b)  $f_{DBD} = 0.4$  kHz -  $E = 1.5$  kV; (c)  $f_{DBD} = 4$  kHz -  $E = 1.2$  kV.

not operated has negligible effect on the boundary layer. Also for this case, the CFV appears practically unaffected by the 400Hz actuation. The unsteady modes present instead some differences compared to the case of the actuator at  $x/c = 0.30$  especially at station  $x/c = 0.45$ . Overall, the low frequency forcing does not strongly change the flow, similarly to the upstream forcing location results. In contrast, the higher frequency forcing considerably enhances the full-spectrum fluctuations as well as the high and low frequency bands with the latter overtaking the former.

In order to gauge this effect, the boundary layer status is inferred by inspection of the statistical velocity fields for the three flow cases (unforced, low and high frequency actuation), shown in figure 7.16. While the low frequency actuation does not show evident effects on the flow field, the high frequency forcing triggers the breakdown of the stationary vortex with a broad area of high energy fluctuations spreading from the upwelling flow region (pertinent of the *type-I* mode) and merging with the inner vortex leg (where mode *type-III* develops) thus explaining the reported increased amplitude of both the high and low frequency fluctuations. A further consequence of the onset of flow breakdown by the high frequency actuation is that the amplitude of the phase reconstructed fluctuations drops to  $A_{II}^{PR} = 0.0016$  which is four times smaller than the same quantity measured with the actuator placed at  $x/c = 0.30$  (see table 7.2). Therefore the phase-reconstruction procedure for this flow field yields less clear results. These observations show that high frequency forcing at the downstream position ( $x/c = 0.375$ ) anticipates the flow breakdown with the related enhancement and spreading, in both space and frequency band of the unsteady field. This lies in contrast to the flow development when forcing is applied at  $x/c = 0.30$ .

A possible route to the more advanced transition process when downstream forcing is applied, can be sought by considering the stability and growth characteristics of secondary cross-flow instabilities. To this end, hot-wire measurements from the experiment by Serpieri & Kotsonis [114] are used. In figure 7.18, the chordwise evolution of the high and low frequency bands are measured according to equation 2.24. The velocity fields pertaining to three stationary vortices were measured and averaged ( $z^m = 3 \times \lambda_z = 27$  mm). The amplitudes are plotted in logarithmic scale to facilitate comparison of more upstream portions of the plot where the chordwise amplitudes of the high frequency mode evolve slowly. Figure 7.18 shows that the high frequency fluctuations, pertinent to the *type-I* mode forced in this study (denoted by the HF notation), undergo abrupt growth from  $x/c = 0.40$  while showing a rather flat amplitude evolution at the more upstream

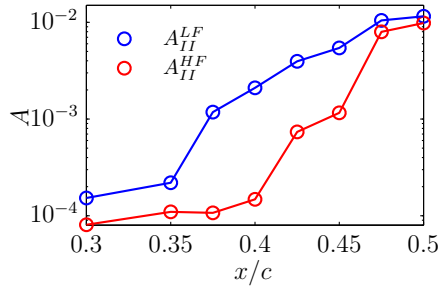


Figure 7.18: Chordwise evolution of fluctuation amplitudes (see equations 2.24) (logarithmic scale). Data from the experiment by [114]. HF and LF bands are the same of figure 7.7. Unforced flow without AC-DBD plasma actuator mounted.

stations. Considering the sensitivity associated with HWA, amplitudes of  $A < 10^{-4}$  can be considered as basically undetected, similar to the observations of White & Saric [135]. This further suggests that the boundary layer is only mildly unstable or even stable to secondary instabilities up to  $x/c = 0.375 - 0.40$ , for the conditions of this experiment. The implication of this observation, reconciles the behaviour of the presently studied flow under forcing at two different streamwise positions. Based on figure 7.18, an actuator which is forcing at  $x/c = 0.30$  would introduce secondary instabilities that need to travel a longer 'stable' region than an actuator placed at  $x/c = 0.375$ . Consequently, the instabilities forced by the upstream actuator would reach the branch-I onset position ( $x/c \approx 0.40$ ) at a relatively lower amplitude than the instabilities forced by the downstream actuator. Naturally, the aforementioned considerations pertain to forcing of equal initial amplitude. In absolute terms, this is the case for the present study as both voltage and frequency are kept constant for the two actuator positions. However, in momentum coefficient terms, the downstream actuator effect is even weaker (section 7.2.2), as, moving downstream, the local boundary layer becomes thicker and the external velocity higher. This further confirms that the observed flow-field changes under downstream forcing are related to the reduced stability of the flow to secondary instabilities at this position, compared to upstream forcing. The outcomes of this section suggest that a careful characterization of the unforced transitional boundary layer is needed for studies based on forcing of secondary modes as, even weak actuated disturbance, can cause flow breakdown if occurring close to the natural critical location [40, 7].

## 7.5. CONCLUSIONS

In this study, unsteady periodic forcing of the *type-I* and *type-III* modes was performed by means of an AC-DBD plasma actuator flush mounted to the model surface. The actuator was installed upstream of the measurement domain and consisted of a very thin strip of silver-printed electrodes, summing up to a two-dimensional roughness of  $125 \mu\text{m}$ . The actuator was operated at two different frequencies of  $f_{DBD} = 0.4 \text{ kHz}$  and  $f_{DBD} = 4 \text{ kHz}$  respective of the two analysed modes. The voltage amplitude was varied with the frequency and set such to minimize the effects on the transition pattern. Nonetheless,

when forcing was applied upstream of *type-I* mode branch-I, it demonstrated the capability of weekly enhancing and narrowing the spectral distribution of the forced modes. Finally, through the deterministic nature of the applied forcing, the phase of the triggered modes was successfully conditioned. The actuator signal was acquired simultaneously with the hot-wire and used to reconstruct, by means of phase averaging, the measured signals. This procedure allowed the inspection of the spatio-temporal evolution of both the low (*type-III*) and high (*type-I*) frequency modes. The presented results are in good agreement with results of previous attempts to force the secondary instability modes, by means of localized periodic blowing/suction, by Kawakami *et al.* [51] and Chernoray *et al.* [13]. The results further show that AC-DBD plasma actuators are suitable for this type of investigations. While avoiding three-dimensional artefacts, given their spanwise uniformity, the inherent body force production mechanisms of these actuators cause a modulation of the reconstructed modes, which needs to be taken into account. They can be operated at different frequencies (an order of magnitude apart in the current study) and their authority is easily adjusted by tuning the amplitude of the supplied voltage. Finally, the possibility of directing the forced jets along a specific direction becomes crucial in applications considering complex flows.

The outcomes of the phase-reconstruction analysis agree with the previous efforts in understanding the mechanisms leading to the breakdown of swept-wing boundary layers, providing an experimental companion to the numerical investigations of Högberg & Henningson [40] and Wassermann & Kloker [129], and the theoretical work of Malik *et al.* [77], Fischer & Dallmann [30] and Bonfigli & Kloker [8]. Finally the current results offer a validation of the recent tomographic PIV experiment performed by the same authors of this study [114].

Two cross-flow vortices of different amplitude (about ten percent difference in the mode shape amplitude defined in equation 2.22) were measured showing the influence on the development of secondary modes: the weaker wave is shown to be more stable to the unsteady disturbances especially under high-frequency forcing. This results are in line with the simulations of Wassermann & Kloker [129] and Choudhari *et al.* [15] and the stability computations of Groot *et al.* [35]. At these conditions, the high-frequency phase-correlated fluctuations become significantly weaker thus not allowing a clear representation of their topology and evolution. Finally, the effect of the actuator position was investigated. Placing the actuator more downstream and operating it at the higher frequency triggered the laminar-to-turbulent breakdown of the boundary layer. This effect was shown to be caused by the boundary-layer stability characteristics to secondary mechanisms.

# IV

## EPILOGUE



# 8

## CONCLUSIONS AND OUTLOOK

*The two main streams of this research are the investigation of naturally developing primary and secondary CFI modes in a swept-wing boundary layer and the attempt to artificially condition their evolution. The approach of the research is mainly experimental making use of state-of-art equipment. Numerical/theoretical tools have been developed and used along with the wind tunnel tests. The outcomes of a simplified model developed within this research and incorporating the effects of plasma actuators' forcing on the stability of the boundary layer, were experimentally verified. This led to successful anticipation and postponement of the transition front in an experimental campaign at high ( $O(10^6)$ ) Reynolds numbers that will be the object of forthcoming research efforts.*

---

S. Yadala Venkata, M. Hehner, **J. Serpieri**, N. Benard, P. Dörr, M. Kloker & M. Kotsonis, *Experimental control of swept wing transition by base-flow modification by plasma actuators*, Journal of Fluid Mechanics (under review)

## 8.1. FLOW DIAGNOSTICS

The research presented in this booklet investigates the primary and secondary cross-flow instability mechanisms and the possibility to actively condition the natural development. Nonetheless, the booklet opens with the description of the wind tunnel model design. The design procedure capitalizes on the spanwise flow invariance hypothesis and made use of the commercial *Ansys Fluent* suite. The mentioned hypothesis is also appealed to evaluate the developing boundary layer. This was done by a marching finite differences/spectral code solving the steady, laminar, incompressible boundary layer equations. The resulting velocity distribution was given in input to a linear stability theory solver retrieving spatial chordwise growth rates for modes with a given frequency and spanwise wavenumber. The stability solutions were used to compute N-factors to compare the different modes and evaluate their evolution. These results were then compared to preliminary wind tunnel tests and guided the design of the experimental campaigns.

8

The aim of the diagnostics effort was to experimentally measure the cross-flow vortices and the secondary instability modes they develop. While a big part of the wind tunnel time was dedicated to traditional experimental techniques such as oil flow/IR thermography visualizations or hot-wire anemometry, tomographic-PIV measurements were also achieved. Such a measurement allowed the investigation of the primary and secondary instability from wind tunnel campaigns with unprecedented detail. From literature, the only information on the spatio-temporal characteristics of the unsteady modes is available from numerical simulations (e.g. [40, 129, 130]), theoretical investigations (e.g. [77, 54]) or phase locked measurements ([51, 13, 7]). The deployment of tomo-PIV resulted crucial as it retrieved spatially correlated measurements of the unsteady flow structures naturally developing in CFI boundary layers. Spatio-temporally resolved measurements, by means of high-speed PIV, are also presented but limited to small planar fields. Proper orthogonal decomposition of the flow field time sequence yielded the flow structures related to the secondary *type-I* and *type-III* modes. The resolved flow structures were matched, given their convective nature [40, 129], to the fixed-point velocity fluctuations measured with the hot-wire by applying Taylor's advection hypothesis. Finally, the planar high-speed PIV measurements confirmed the approach directly resolving the frequency spectra of the POD modes related to the secondary CFI modes.

The stationary vortices were also found to undergo a small but yet non-negligible displacement around the roughness elements at the leading edge. While this phenomenon is considered irrelevant for the transition evolution, it should be considered in experimental campaigns as it contributes to a relevant share of kinetic energy.

Furthermore, volumetric data of the full velocity vectorial and velocity-derivative tensorial fields allowed to analyse the secondary instability modes under the perspective of secondary stability theory (Groot *et al.* [35]) similar to the efforts of Malik *et al.* [77], Koch *et al.* [54] and Bonfigli & Kloker [8] but from experimental base flows (not in this booklet). The advantage of this approach is its independence from modelling assumptions (e.g. initial modal amplitudes). Nevertheless, extended experimental campaigns based on high-resolution tomo-PIV are extremely time-consuming with the equipment available today at *Aerodynamics*. The studied flow requires a combination of extended measurement domain and spatial resolution which resulted to be very challenging to achieve. Smaller models with better optical access are heartily recommended for future campaigns.

## 8.2. FLOW CONTROL

The effort dedicated to condition the primary and secondary CFI modes goes in the perspective of laminar flow control. Also in this case, most of the more recent research comes from numerical simulations (e.g. [81, 31, 22, 23, 24, 118]). Therefore, innovative research work was done in this field leading to successful outcomes. Nonetheless, also unpredicted limitations of the considered configurations are reported.

The experiments levered on a powerful flow control device: alternating current dielectric barrier discharge plasma actuators. The power of this technology does not reside in its strength (in terms of velocity of the induced jet) but in the possibility of being operated at different frequencies/amplitudes. These actuators also offer the possibility of being designed and built with complex shapes without complicating their operation/installation and, in future industrial applications, their maintenance as they do not need complicated pneumatic/mechanic hardware. Finally, the possibility of exerting directional flow forcing peculiar of these actuators is very important for applications such as the control of boundary-layer instability. The employed actuators fulfilled the tasks of conditioning the wavelength of the stationary cross-flow vortices as well as the phase and frequency of the unsteady/secondary cross-flow instability modes. Nevertheless, further research needs to be done on the actuators and on their effect on the unsteady boundary-layer velocity field especially when operated in the frequency band of the secondary CFI.

The flow control strategy that builds upon the beneficial flow deformation caused by shorter wavelength CFI modes named upstream flow deformation has been attempted in this research. Nonetheless, considering all the parameters influencing the boundary layer transition process (pressure distribution and Reynolds number (boundary layer stability); free-stream turbulence intensity and spectrum and surface roughness (boundary layer receptivity)), this strategy is deemed successful in limited flow cases. The cross-flow direct counteraction as performed by Messing & Kloker [81] by means of suction and Dörr & Kloker [22] using plasma actuators is considered as a more robust strategy as it aims at reducing the main cause of boundary-layer transition notwithstanding the more elaborated considerations behind the UFD approach. This strategy can benefit from the proposed simplified model where the actuator body force is considered in the laminar-boundary-layer solution used as input for stability calculations. In this case, the proposed forcing is close to the attachment line where the streamline is closely aligned with the leading edge. Thus, a spanwise-uniform forcing as the one considered in the simplified model results in directly influencing the cross-flow velocity component. An experimental validation of this concept is sought and presented in the next section as outlook of this research. It showed effective control of the transition position with high-frequency spanwise-uniform plasma forcing leading to transition anticipation or postponement depending on the forcing configuration.

Finally, spanwise-uniform plasma actuators were used close to the stationary CFVs saturation to introduce small-amplitude monochromatic fluctuations fostering the natural development of the *type-III* and *type-I* secondary modes. They allowed to condition the spectrum and the phase of the flow structures pertaining to these modes allowing a phase-averaged reconstruction similar to what done by Kawakami *et al.* [51] and Cheronoray *et al.* [13]. This procedure yielded flow structures qualitatively similar to the ones captured by POD of the tomo-PIV fields. The effect of forcing on two cross-flow vortices

of different amplitudes was also presented in this research. Through this experiment, the evolution of secondary-instability modes of different-strength CFVs was also analysed. The results agree with the recent numerical studies of Wassermann & Kloker [129], Choudhari *et al.* [15] and the upcoming secondary stability calculations of Groot *et al.* [35] on the tomo-PIV velocity field (and velocity gradient tensor) presented in this booklet. Finally, the effect of the forcing position on the boundary layer was also inspected. Installing the actuator more downstream resulted in milder consequences for the evolution of *type-III* structures. Dramatic effects leading to flow breakdown were observed for the *type-I* mode fluctuations. The difference of reaction to forcing at the two frequencies was explained comparing the different growth rates pertinent to these modes. This study opened the route for further experimental campaigns aiming at externally conditioning the evolution of the secondary instability modes. The developed plasma actuators resulted in valid tools for the purpose.

### 8.3. OUTLOOK: A PROOF-OF-CONCEPT EXPERIMENT

The simplified model developed and described in section 6.4.3 allowed to investigate the effect of spanwise-uniform steady forcing on swept wing transition. It showed the potential of enhancing or reducing the CFI modes growth rates and N factors with plasma actuators.

An experimental validation of the model concept is sought and presented in this section. Nonetheless, for this purpose, a different flow configuration and plasma actuator setup is chosen. A complete description of this investigation can be found in [138]. A new actuator was designed and built for this purpose with the requirement of being operated at frequencies in the order of  $O(10 \text{ kHz})$  (see section 2.4.4), thus beyond the secondary CFI band. The higher actuation frequency is demanded in order to avoid the amplification of low-frequency fluctuations by the actuators as discussed in chapter 6.

As the inviscid streamline, at the attachment line, is aligned with the leading edge, the actuator was designed such to force, close to the leading edge, along  $\pm x$  in a spanwise-uniform configuration. This forcing, as shown in section 6.4.3, directly influences the cross-flow velocity component and the stability of the boundary layer notwithstanding the state of the CFI.

#### EXPERIMENTAL SETUP

The wind tunnel facility and model are the same discussed in section 2. The baseline case Reynolds number and the angle of attack are also unchanged. Besides the baseline flow, also different Reynolds number flows were tested. As flow diagnostics, infrared thermography is adopted. The portion of wing investigated spans from the leading edge to the transition front and the setup is the same as the one described in section 3.3.4. The camera recorded at  $f_s = 5 \text{ Hz}$  for 20 s thus acquiring 100 snapshots later averaged together to increase the measurement quality.

The boundary layer was forced to a monochromatic CFI arrangement by means of DREs (diameter  $d_r = 2 \text{ mm}$  and height  $k_r = 60 \mu\text{m}$ ) spaced 8 mm along the leading edge direction and installed at  $x/c = 0.017$ . This mode is close to the most amplified mode as predicted in section 3.4.

With these elements installed, when exposed to a free stream flow of  $U_\infty = 25 \text{ m s}^{-1}$

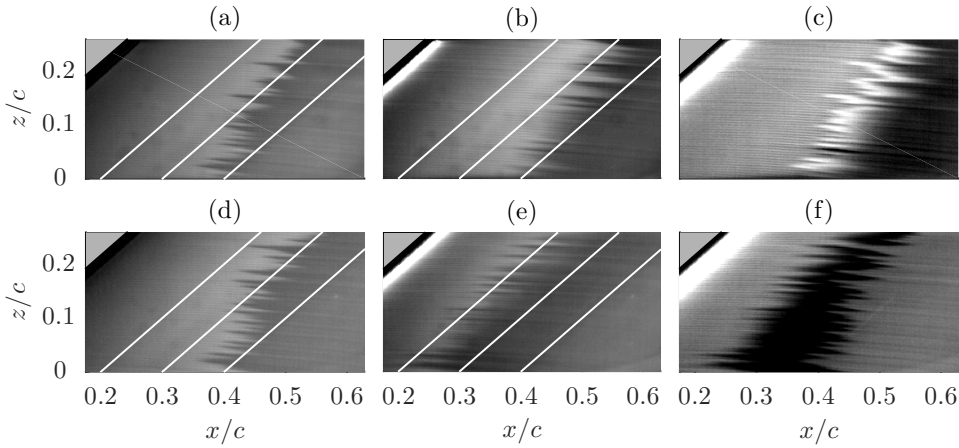


Figure 8.1: IR thermography mean fields ( $Re = 2.1 \cdot 10^6$ ,  $U_\infty = 25 \text{ ms}^{-1}$ ) mapped on the  $x-z$  plane. Constant chord stations are depicted with white solid lines. The flow comes from left. (a and d) Unforced case, (b and e)  $C_\mu = -0.71$  and  $C_\mu = 0.71$ , (c and f) Subtraction of forced from unforced cases ( $c=b-a$ ;  $f=e-d$ ).

( $Re = 2.1 \cdot 10^6$ ), transition occurred at  $x/c \approx 0.30$ . The choice of such a strong passive forcing was dictated by two considerations. The first is that anticipating the flow breakdown, the chordwise extent of flow field to be measured also reduces thus allowing higher resolution measurements. The second is that the envisioned base-flow manipulation should work independently from the state of the CFI. Therefore, a proof-of-concept experiment should be performed in the strongest CFI flow configuration (critical mode/high amplitude forcing) thus being in principle valid under less extreme conditions.

A 10 kHz and 4.5 kV voltage amplitude sinusoidal signal was fed to the actuators presented in section 2.4.4. Through PIV mechanical characterization experiments (not shown), the actuators thrust was measured to be  $T_x = 5.90 \text{ mN m}^{-1}$  and, considering equation 2.26 and the local boundary-layer parameters, the momentum coefficient resulted  $C_\mu = 0.71$ . The actuators were mounted at  $x/c = 0.035$  such to force along the  $\pm x$  directions (the sign of the momentum coefficient correspond to the sign of the forced  $x$  direction).

## RESULTS

In figure 8.1, the infrared thermography visualization of the unforced flow (a and d), of the forced flow (b and e for the forcing along  $-x$  and  $x$ , respectively) and of the difference between the former fields (c and f) are shown. It appears that forcing along  $x$  promotes the CFI modes anticipating transition. Whereas, forcing along  $-x$  yields a postponement of the transition front of  $x/c \approx 4.5\%$ .

This shows that leading edge spanwise-uniform quasi-stationary base-flow manipulation can successfully delay the laminar-to-turbulent transition and opens the route for future research on the topic. These results are, to the authors' knowledge, the first experimental evidence of transition anticipation/postponement in swept wing boundary layers by means of plasma actuators' active flow control. The experiment was performed with critical mode forcing. Further experiments for different Reynolds numbers but

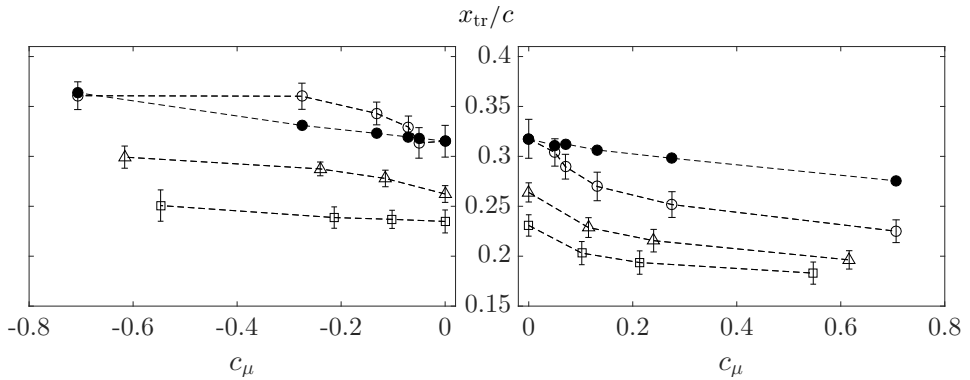


Figure 8.2: Transition locations ( $x_{tr}/c$ ) versus actuator forcing (momentum coefficient  $C_\mu$ ). Positive values: forcing along  $x$ ; negative values: along  $-x$ .  $\circ$ :  $U_\infty = 25 \text{ m s}^{-1}$  ( $Re = 2.1 \cdot 10^6$ ),  $\triangle$ :  $U_\infty = 27.5 \text{ m s}^{-1}$  ( $Re = 2.3 \cdot 10^6$ ),  $\square$ :  $U_\infty = 30 \text{ m s}^{-1}$  ( $Re = 2.5 \cdot 10^6$ ),  $\bullet$ : predicted transition location for  $U_\infty = 25 \text{ m s}^{-1}$  ( $Re = 2.1 \cdot 10^6$ ).

same 8 mm DREs forcing were conducted. The free stream velocity was thus increased to  $U_\infty = 27.5 \text{ m s}^{-1}$  ( $Re = 2.3 \cdot 10^6$ ), and  $U_\infty = 30 \text{ m s}^{-1}$  ( $Re = 2.5 \cdot 10^6$ ). The 8 mm mode features a larger wavelength compared to the critical modes at these conditions. Furthermore, different forcing amplitudes were tested. The actuator voltage amplitude was varied between 2.5 and 4.5 kV. This translates in different momentum coefficients, computed considering the local flow properties in agreement with equation 2.26, for the different Reynolds number flows. Namely, increasing the Reynolds number, the performance of the actuator weakens. The location and width of the transition fronts extracted considering the spanwise- mean and standard deviation from the thermography experiment, are presented in figure 8.2 for the different free stream and forcing conditions.

The results show transition delay and anticipation for the  $-x$  and  $+x$  forcing, respectively, for all the tested conditions: the stronger the forcing, the larger the shift of the transition front. Furthermore, the transition front width does not appear modified by the periodic forcing. This suggest that no boundary-layer fluctuations are amplified by the actuator [27] meaning that the very high frequency forcing is "seen" as constant by the flow. Finally, the model-predicted transition locations, i.e. extracting the forced transition locations from the un-forced critical N-factor, are also shown in figure 8.2. This shows that, while the model predicts correctly the trend, it underestimates the transition shift for both forcing directions. This result is explained by the many simplifications, discussed in section 6.4.3, from which the model is derived.

### RECOMMENDATIONS

Future research effort should be put towards optimizing the actuators setup. Curved actuators, aligned with the inviscid streamline can be considered and tested. Nonetheless, for such configurations, the actuators roughness needs to be minimal as the flow, flowing over the electrodes, would be subject to a cumulative roughness-disturbance. The forcing should be tested also for a broader range of transition-relevant parameters (pressure gradient and Reynolds number (boundary-layer stability) and free-stream turbulence and surface roughness (boundary-layer receptivity) to be proven robust.

# 9

## NOMENCLATURE

### MATHEMATICAL ENTITIES

$\bar{a}$	$a$ – Time-average
$\{a\}$	$a$ – Standard deviation w.r.t. the subscript quantity
$a'$	$a$ – Fluctuations (e.g. $a - \bar{a}$ , for temporal fluctuations)
$\vec{a}$	$a$ – Vector
$ \vec{a} $	$a$ – Vector magnitude
$\mathbf{a}$	$a$ – Matrix

### LATIN SYMBOLS

$A$	Amplitude
$b$	Wing span in the $Z$ direction
$c$	Wing chord in the $x$ direction
$c_f$	Skin friction coefficient
$C$	Cross-correlation
$C_\mu$	Actuator momentum coefficient
$C_p$	Pressure coefficient
$d$	Roughness elements diameter
$D$	Lens diameter
$E$	Voltage amplitude
$f$	Frequency, focal length
$f_\sharp$	Lens numerical aperture
$F$	Actuator body force
$h$	Convective heat flux coefficient
$I$	Intensity
$k$	Roughness elements height
$M$	Mach number, optical magnification

$N$	$N$ -factors
$q, Q$	Navier-Stokes primitive variables
$R$	Resistance, autocovariance matrix
$Re$	Reynolds number
$R_q$	Surface roughness (standard deviation)
$S$	POD snapshot matrix
$St$	Strouhal number
$t$	Time
$T$	Actuator thrust in the wall-parallel direction, temperature, period
$Tu$	Turbulence intensity (from single hot-wire measurements)
$u, v, w$	Velocity components along the $x, y, z$ directions
$u_c$	Convection velocity
$U, V, W$	Velocity components along the $X, Y, Z$ directions
$U_c$	Convection velocity along $X$
$U_W, V_W, W_W$	Velocity components along the $X_W, Y_W, Z_W$ directions
$x, y, z$	Wing coordinates
$x_t, y_t, z_t$	Wing surface coordinates
$X, Y, Z$	Wind-tunnel coordinates
$X_W, Y_W, Z_W$	Cross-flow wave coordinates

## GREEK SYMBOLS

$\alpha$	Angle of attack, wavenumber along $x$
$\alpha_0$	Hot-wires overheat ratio
$\beta$	Wavenumber along $z$
$\gamma$	Elevation angle, generic variable
$\delta$	Increment (of the subscript quantity)
$\delta_z$	Optical depth of focus
$\delta_{99}$	Boundary layer thickness based on the 99% threshold
$\epsilon$	Relative error
$\vartheta$	Boundary layer momentum-loss thickness
$\lambda$	Wavelength, POD eigenvalues
$\Lambda$	Sweep angle
$\mu$	Mean, viscosity
$\nu$	Kinematic viscosity
$\rho$	Air density
$\sigma$	Standard deviation
$\tau$	Skin friction
$\Phi$	Phase, power spectral density, POD spatial modes
$\chi$	Azimuthal angle, spatial coordinates vector
$\psi$	Stream function
$\Psi$	Wavenumber vector angle, stream function eigenfunction
$\omega$	Angular frequency

## SUB/SUPER-SCRIPTS

<i>BP</i>	Related to a frequency band
<i>co</i>	Cutoff
<i>cr</i>	Critical
<i>DBD</i>	Related to the actuator
<i>e</i>	At the boundary layer edge
<i>env</i>	Envelop of the maxima
<i>f</i>	Forced
<i>i</i>	Imaginary part
<i>HWA</i>	Related to a single hot-wire probe
<i>ISL</i>	Related to the inviscid stream line
<i>m</i>	At the maximum extent
<i>r</i>	Real part
<i>s</i>	Sampling
<i>st</i>	Related to the stagnation point
<i>t</i>	Transposed
<i>tot</i>	Related to the total frequency spectrum
<i>tr</i>	At the transition location
<i>w</i>	Related to the hot-wire
<i>W</i>	Related to stationary cross-flow wave
0	Related to a reference value
<i>I</i>	Related to primary modes
<i>II</i>	Related to secondary modes
$\Phi$	Related to phases
$\infty$	Free-stream quantity

## ABBREVIATIONS

AC-DBD	Alternating Current Dielectric Barrier Discharge
ASU	Arizona State University
BL	Boundary Layer
CE	Covered Electrode
CF	Cross-Flow
CFI	Cross-Flow Instability
CFV	Cross-Flow Vortex
CTA	Constant Temperature Anemometer
DLR	Deutsches Zentrum für Luft- und Raumfahrt
DMD	Dynamic Mode Decomposition
DNS	Direct Numerical Simulation
DRE	Distributed Roughness Element
EE	Exposed Electrode
EMI	Electro-Magnetic Interference
ES	Ensemble Size
FR	Frame Rate

HF	High Frequency
HWA	Hot-Wire Anemometry
IAG	Institut für Aerodynamic und Gasdynamic
IR	Infrared
KH	Kelvin-Helmholtz
LES	Large Eddy Simulations
LF	Low Frequency
(S)LST	(Secondary) Linear Stability Theory
LTT	Low Turbulence Tunnel
MART	Multiplicative Algebraic Reconstruction Technique
PET	Polyethylene Terephthalate
(N)PSE	(Non-) Linear Parabolised Stability Equations
OS	Orr-Sommerfeld
PIV	Particle Image Velocimetry
POD	Proper Orthogonal Decomposition
PR	Phase Reconstructed
PSD	Power Spectral Density
RMS, r.m.s.	Root Mean Square
TAMU	Texas A&M University
TKE	Turbulent Kinetic Energy
TS	Tollmien-Schlichting
UFD	Upstream Flow Deformation
UV	Ultraviolet
w.r.t.	with respect to

## REFERENCES

- [1] ADRIAN, R. J. & WESTERWEEL, J. 2011 *Particle image velocimetry*. Cambridge University Press.
- [2] ARNAL, D. & CASALIS, G. 2000 Laminar-turbulent transition prediction in three-dimensional flows. *Progress in Aerospace Sciences* **36** (2), 173 – 191.
- [3] ARNAL, D., GASPARIAN, G. & SALINAS, H. 1998 Recent advances in theoretical methods for laminar-turbulent transition prediction. *AIAA Paper* 1998-0223 .
- [4] BARLETT, M. S. 1950 Periodogram analysis and continuous spectra. *Biometrika* **37** (1-2), 1–16.
- [5] BENARD, N. & MOREAU, E. 2014 Electrical and mechanical characteristics of surface ac dielectric barrier discharge plasma actuators applied to airflow control. *Experiments in Fluids* **55** (11), 1–43.
- [6] BIPPES, H. 1999 Basic experiments on transition in three-dimensional boundary layers dominated by crossflow instability. *Progress in Aerospace Sciences* **35** (4), 363 – 412.
- [7] VAN BOKHORST, E. & ATKIN, C. J. 2017 Wall forcing of the secondary crossflow instability. *AIAA Paper* 2017-3458 .
- [8] BONFIGLI, G. & KLOKER, M. 2007 Secondary instability of crossflow vortices: validation of the stability theory by direct numerical simulation. *J. Fluid Mech.* **583**, 229–272.
- [9] BRIDGES, T.J. & MORRIS, P.J. 1984 Differential eigenvalue problems in which the parameter appears nonlinearly. *Journal of Computational Physics* **55** (3), 437–460.
- [10] BRYNJELL-RAHKOLA, M., SHAHRIARI, N., SCHLATTER, P., HANIFI, A. & HENNINGSON, D. S. 2017 Stability and sensitivity of a cross-flow-dominated falkner–skan–cooke boundary layer with discrete surface roughness. *J. Fluid Mech.* **826**, 830–850.
- [11] BUSHNELL, D. M. 2003 Aircraft drag reduction a review. *Proceedings of the Institution of Mechanical Engineers, Part G: Journal of Aerospace Engineering* **217** (1), 1–18.
- [12] BUTTERWORTH, S. 1930 On the theory of filter amplifiers. *Experimental Wireless and the Wireless Engineer* **7**, 536–541.

- [13] CHERNORAY, V. G., DOVGAL, A. V., KOZLOV, V. V. & LÖFDAHL, L. 2005 Experiments on secondary instability of streamwise vortices in a swept-wing boundary layer. *J. Fluid Mech.* **534**, 295–325.
- [14] CHERNYSHEV, S., KURYACHII, A., MANUILOVICH, S., RUSYANOV, D. & SKVORTSOV, V. 2013 Attenuation of cross-flow-type instability in compressible boundary layer by means of plasma actuators. *AIAA Paper* 2013-321 .
- [15] CHOUDHARI, M. M., LI, F. & PAREDES, P. 2016 Influence of stationary crossflow modulation on secondary instability. *AIAA Paper* 2016-3788 .
- [16] COOKE, J. C. 1950 The boundary layer of a class of infinite yawed cylinders. *Math. Proc. Camb. Phil. Soc.* **46** (4), 645–648.
- [17] CORKE, T. C., ENLOE, C. L. & WILKINSON, S. P. 2010 Dielectric barrier discharge plasma actuators for flow control. *Annu. Rev. Fluid Mech.* **42**, 505–529.
- [18] DAGENHART, J. R., SARIC, W. S., MOUSSEUX, M. C. & STACK, J. P. 1989 Crossflow vortex instability and transition on a 45-degree swept wing. *AIAA Paper* **89** (1982).
- [19] DEYHLE, H. & BIPPES, H. 1996 Disturbance growth in an unstable three-dimensional boundary layer and its dependence on environmental conditions. *J. Fluid Mech.* **316**, 73–113.
- [20] DISCETTI, S. & IANIRO, A. 2017 *Experimental aerodynamics*. CRC Press, Boca Raton.
- [21] DÖRR, P. C. & KLOKER, M. J. 2015 Numerical investigation of plasma-actuator force-term estimations from flow experiments. *Journal of Physics D: Applied Physics* **48** (39), 395203.
- [22] DÖRR, P. C. & KLOKER, M. J. 2015 Stabilisation of a three-dimensional boundary layer by base-flow manipulation using plasma actuators. *Journal of Physics D: Applied Physics* **48**, 285205.
- [23] DÖRR, P. C. & KLOKER, M. J. 2016 Transition control in a three-dimensional boundary layer by direct attenuation of nonlinear crossflow vortices using plasma actuators. *International Journal of Heat and Fluid Flow* pp. 449–465.
- [24] DÖRR, P. C. & KLOKER, M. J. 2017 Crossflow transition control by upstream flow deformation using plasma actuators. *Journal of Applied Physics* **121** (6), 063303.
- [25] DÖRR, PHILIPP C. & KLOKER, MARKUS J. 2018 Numerical investigations on tollmien-schlichting wave attenuation using plasma-actuator vortex generators. *AIAA Journal* pp. 1–5.
- [26] DÖRR, P. C., KLOKER, M. J. & HANIFI, A. 2017 Effect of upstream flow deformation using plasma actuators on crossflow transition induced by unsteady vortical free-stream disturbances. *AIAA Paper* 2017-3114 .
- [27] DOWNS, R. S. III & WHITE, E. B. 2013 Free-stream turbulence and the development of cross-flow disturbances. *J. Fluid Mech.* **735**, 347–380.

- [28] DUCHMANN, A., GRUNDMANN, S. & TROPEA, C. 2013 Delay of natural transition with dielectric barrier discharges. *Experiments in Fluids* **54** (3), 1461.
- [29] ELSINGA, G. E., SCARANO, F., WIENEKE, B. & VAN OUDHEUSDEN, B. W. 2006 Tomographic particle image velocimetry. *Experiments in Fluids* **41** (6), 933–947.
- [30] FISCHER, T. M. & DALLMANN, U. 1991 Primary and secondary stability analysis of a three-dimensional boundary-layer flow. *Physics of Fluids A: Fluid Dynamics (1989-1993)* **3** (10), 2378–2391.
- [31] FRIEDERICH, T. & KLOKER, M. J. 2012 Control of the secondary cross-flow instability using localized suction. *J. Fluid Mech.* **706**, 470–495.
- [32] GAPONENKO, V. R., IVANOV, A. V., KACHANOV, Y. S. & CROUCH, J. D. 2002 Swept-wing boundary-layer receptivity to surface non-uniformities. *J. Fluid Mech.* **461**, 93–126.
- [33] GASTER, M. 1962 A note on the relation between temporally-increasing and spatially-increasing disturbances in hydrodynamic stability. *J. Fluid Mech.* **14** (2), 222–224.
- [34] GLAUSER, M. N., SARIC, W. S., CHAPMAN, K. L. & REIBERT, M. S. 2014 Swept-wing boundary-layer transition and turbulent flow physics from multipoint measurements. *AIAA Journal* **52** (2), 338–347.
- [35] GROOT, K. J., SERPIERI, J., PINNA, F. & KOTSONIS, M. t.b.k. Secondary crossflow instability through biglobal analysis of measured base flows. *J. Fluid Mech.* (**under review**).
- [36] GRUNDMANN, S. & TROPEA, C. 2008 Active cancellation of artificially introduced tollmien–schlichting waves using plasma actuators. *Experiments in Fluids* **44** (5), 795–806.
- [37] HALL, P. & MALIK, M. R. 1986 On the instability of a three-dimensional attachment-line boundary layer: weakly nonlinear theory and a numerical approach. *J. Fluid Mech.* **163**, 257–282.
- [38] HALL, P. & SEDDOUGUI, S. 1989 On the onset of three-dimensionality and time-dependence in görtler vortices. *J. Fluid Mech.* **204**, 405–420.
- [39] HAYNES, T. S. & REED, H. L. 2000 Simulation of swept-wing vortices using nonlinear parabolized stability equations. *J. Fluid Mech.* **405**, 325–349.
- [40] HÖGBERG, M. & HENNINGSON, D. 1998 Secondary instability of cross-flow vortices in falkner-skan-cooke boundary layers. *J. Fluid Mech.* **368**, 339–357.
- [41] HOSSEINI, S. M., TEMPELMANN, D., HANIFI, A. & HENNINGSON, D. S. 2013 Stabilization of a swept-wing boundary layer by distributed roughness elements. *J. Fluid Mech.* **718**.

- [42] HUAI, X., JOSLIN, R. D. & PIOMELLI, U. 1999 Large-eddy simulation of boundary-layer transition on a swept wedge. *J. Fluid Mech.* **381**, 357–380.
- [43] IMAYAMA, S., ALFREDSSON, P. H. & LINGWOOD, R. J. 2014 On the laminar-turbulent transition of the rotating-disk flow: the role of absolute instability. *J. Fluid Mech.* **745**, 132–163.
- [44] IMAYAMA, S., ALFREDSSON, P. H. & LINGWOOD, R. J. 2016 Experimental study of rotating-disk boundary-layer flow with surface roughness. *J. Fluid Mech.* **786**, 5–28.
- [45] JANKE, E. & BALAKUMAR, P. 2000 On the secondary instability of three-dimensional boundary layers. *Theoretical and Computational Fluid Dynamics* **14** (3), 167–194.
- [46] JOSLIN, R. D. 1998 Aircraft laminar flow control. *Annu. Rev. Fluid Mech.* **30** (1), 1–29.
- [47] JOSLIN, R. D. & STRETT, C. L. 1994 The role of stationary crossflow vortices in boundary layer transition on swept wings. *Physics of Fluids* **6** (10), 3442–3453, arXiv: <http://dx.doi.org/10.1063/1.868401>.
- [48] JUKES, T. N. & CHOI, K.-S. 2012 Dielectric-barrier-discharge vortex generators: characterisation and optimisation for flow separation control. *Experiments in fluids* **52** (2), 329–345.
- [49] JUKES, T. N. & CHOI, K.-S. 2013 On the formation of streamwise vortices by plasma vortex generators. *J. Fluid Mech.* **733**, 370–393.
- [50] KACHANOV, Y. S. 2000 Three-dimensional receptivity of boundary layers. *European Journal of Mechanics - B/Fluids* **19** (5), 723 – 744.
- [51] KAWAKAMI, M., KOHAMA, Y. & OKUTSU, M. 1998 Stability characteristics of stationary crossflow vortices in 3-d boundary layer. *AIAA Paper* 1998-811 .
- [52] KLEBANOFF, P. S., TIDSTROM, K. D. & SARGENT, L. M. 1962 The three-dimensional nature of boundary-layer instability. *J. Fluid Mech.* **12** (1), 1–34.
- [53] KOCH, W. 2002 On the spatio-temporal stability of primary and secondary crossflow vortices in a three-dimensional boundary layer. *J. Fluid Mech.* **456**, 85–111.
- [54] KOCH, W., BERTELOTTI, F. P., STOLTE, A. & HEIN, S. 2000 Nonlinear equilibrium solutions in a three-dimensional boundary layer and their secondary instability. *J. Fluid Mech.* **406**, 131–174.
- [55] KOHAMA, Y., SARIC, W. S. & HOOS, J. A. 1991 A high frequency secondary instability of crossflow vortices that leads to transition. *Proc. R. Aeronaut. Soc. Conf. on Boundary-Layer Transition and Control*, Cambridge, UK .
- [56] KOTSONIS, M. 2015 Diagnostics for characterisation of plasma actuators. *Measurement Science and Technology* **26** (9), 092001.

- [57] KOTSONIS, M. & GHAEMI, S. 2011 Forcing mechanisms of dielectric barrier discharge plasma actuators at carrier frequency of 625 Hz. *Journal of Applied Physics* **110** (11), 113301.
- [58] KOTSONIS, M., GHAEMI, S., VELDHUIS, L. & SCARANO, F. 2011 Measurement of the body force field of plasma actuators. *Journal of Physics D: Applied Physics* **44** (4), 045204.
- [59] KOTSONIS, M., GIEPMAN, R., HULSHOFF, S. & VELDHUIS, L. 2013 Numerical study of the control of Tollmien–Schlichting waves using plasma actuators. *AIAA Journal* **51** (10), 2353–2364.
- [60] KOTSONIS, M., SHUKLA, R. K. & PRÖBSTING, S. 2015 Control of natural Tollmien–Schlichting waves using dielectric barrier discharge plasma actuators. *International Journal of Flow Control* **7** (1-2), 37–54.
- [61] KOTSONIS, M. & VELDHUIS, L. 2010 Experimental study on dielectric barrier discharge actuators operating in pulse mode. *Journal of Applied Physics* **108** (11).
- [62] KURZ, H. B. E. & KLOKER, M. J. 2014 Receptivity of a swept-wing boundary layer to micron-sized discrete roughness elements. *J. Fluid Mech.* **755**, 62–82.
- [63] KURZ, H. B. E. & KLOKER, M. J. 2016 Mechanisms of flow tripping by discrete roughness elements in a swept-wing boundary layer. *J. Fluid Mech.* **796**, 158–194.
- [64] LI, F., CHOUDHARI, M., CHANG, C. L., STRETT, C. & CARPENTER, M. 2011 Computational modeling of roughness-based laminar flow control on a subsonic swept wing. *AIAA Journal* **49** (3), 520–529.
- [65] LI, F., CHOUDHARI, M., PAREDES, P. & DUAN, L. 2016 High-frequency instabilities of stationary crossflow vortices in a hypersonic boundary layer. *Phys. Rev. Fluids* **1**, 053603.
- [66] LI, F., CHOUDHARI, M. M. & DUAN, L. 2015 Direct numerical simulation of transition due to traveling crossflow vortices. *AIAA Paper* 2015-2771 .
- [67] LI, F., CHOUDHARI, M. M. & DUAN, L. 2016 Stationary crossflow breakdown due to mixed mode spectra of secondary instabilities. *AIAA Paper* 2016-3789 .
- [68] LI, F., CHOUDHARI, M. M., DUAN, L. & CHANG, C. 2014 Nonlinear development and secondary instability of traveling crossflow vortices. *AIAA Paper* 2014-1132 .
- [69] LI, F. & MALIK, M. R. 1995 Fundamental and subharmonic secondary instabilities of Görtler vortices. *J. Fluid Mech.* **297**, 77–100.
- [70] LINGWOOD, R. J. 1995 Absolute instability of the boundary layer on a rotating disk. *J. Fluid Mech.* **299**, 17–33.
- [71] LINGWOOD, R. J. 1997 On the impulse response for swept boundary-layer flows. *J. Fluid Mech.* **344**, 317–334.

- [72] LOHSE, J., BARTH, H. P. & NITSCHKE, W. 2016 Active control of crossflow-induced transition by means of in-line pneumatic actuator orifices. *Experiments in Fluids* **57** (8), 1–10.
- [73] LUMLEY, J. L. 1967 The structure of inhomogeneous turbulent flows. *Atmospheric turbulence and radio wave propagation* pp. 166–178.
- [74] LYNCH, K. P. & SCARANO, F. 2014 Experimental determination of tomographic piv accuracy by a 12-camera system. *Measurement Science and Technology* **25** (8), 084003.
- [75] MACK, L. M. 1984 Boundary-layer linear stability theory. *AGARD Report 709*.
- [76] MALIK, M. R., LI, F. & CHANG, C.-L. 1994 Crossflow disturbances in three-dimensional boundary layers: nonlinear development, wave interaction and secondary instability. *J. Fluid Mech.* **268**, 1–36.
- [77] MALIK, M. R., LI, F., CHOUDHARI, M. & CHANG, C.-L. 1999 Secondary instability of crossflow vortices and swept-wing boundary-layer transition. *J. Fluid Mech.* **399**, 85–115.
- [78] MARXEN, O., LANG, M. & RIST, U. 2013 Vortex formation and vortex breakup in a laminar separation bubble. *J. Fluid Mech.* **728**, 58–90.
- [79] MARXEN, O., LANG, M., RIST, U., LEVIN, O. & HENNINGSON, D. S. 2009 Mechanisms for spatial steady three-dimensional disturbance growth in a non-parallel and separating boundary layer. *J. Fluid Mech.* **634**, 165–189.
- [80] MENEGHELLO, G., SCHMID, P. J. & HUERRE, P. 2015 Receptivity and sensitivity of the leading-edge boundary layer of a swept wing. *J. Fluid Mech.* **775**.
- [81] MESSING, R. & KLOKER, M. J. 2010 Investigation of suction for laminar flow control of three-dimensional boundary layers. *J. Fluid Mech.* **658**, 117–147.
- [82] MICHELIS, T. & KOTSONIS, M. 2015 Flow control on a transport truck side mirror using plasma actuators. *Journal of Fluids Engineering* **137** (11), 111103–111103–6.
- [83] MICHELIS, T., YARUSEVYCH, S. & KOTSONIS, M. 2017 Response of a laminar separation bubble to impulsive forcing. *J. Fluid Mech.* **820**, 633–666.
- [84] MICHELIS, T., YARUSEVYCH, S. & KOTSONIS, M. 2018 On the origin of spanwise vortex deformations in laminar separation bubbles. *J. Fluid Mech.* **841**, 81–108.
- [85] MISTRY, V. I., PAGE, G. J. & MCGUIRK, J. J. 2015 Simulation of receptivity and induced transition from discrete roughness elements. *Flow, Turbulence and Combustion* **95** (2), 301–334.
- [86] MOREAU, E. 2007 Airflow control by non-thermal plasma actuators. *Journal of Physics D: Applied Physics* **40** (3), 605.

- [87] MORKOVIN, M. V., RESHOTKO, E. & HERBERT, T. 1994 Transition in open flow systems—a reassessment. *Bull. Am. Phys. Soc* **39** (9), 1882.
- [88] MOYES, A. J., PAREDES, P., KOCIAN, T. S. & REED, H. L. 2017 Secondary instability analysis of crossflow on a hypersonic yawed straight circular cone. *J. Fluid Mech.* **812**, 370–397.
- [89] NATI, G., KOTSONIS, M., GHAEMI, S. & SCARANO, F. 2013 Control of vortex shedding from a blunt trailing edge using plasma actuators. *Experimental Thermal and Fluid Science* **46**, 199–210.
- [90] PEREIRA, R., KOTSONIS, M., DE OLIVEIRA, G. & RAGNI, D. 2015 Analysis of local frequency response of flow to actuation: Application to the dielectric barrier discharge plasma actuator. *Journal of Applied Physics* **118** (15).
- [91] PEREIRA, R., RAGNI, D. & KOTSONIS, M. 2014 Effect of external flow velocity on momentum transfer of dielectric barrier discharge plasma actuators. *Journal of Applied Physics* **116** (10).
- [92] PLOGMANN, B., WÜRZ, W. & KRÄMER, E. 2014 On the disturbance evolution downstream of a cylindrical roughness element. *J. Fluid Mech.* **758**, 238–286.
- [93] POLL, D. I. A. 1985 Some observations of the transition process on the windward face of a long yawed cylinder. *J. Fluid Mech.* **150**, 329–356.
- [94] RADEZTSKY, R. H., REIBERT, M. S. & SARIC, W. S. 1999 Effect of isolated micron-sized roughness on transition in swept-wing flows. *AIAA Journal* **37** (11), 1370–1377.
- [95] RAFFEL, M., WILLERT, C. E., WERELEY, S. T. & KOMPENHANS, J. 2007 *Particle Image Velocimetry*. Springer.
- [96] RAIOLA, M., DISCETTI, S. & IANIRO, A. 2015 On piv random error minimization with optimal pod-based low-order reconstruction. *Experiments in Fluids* **56** (4), 1–15.
- [97] REIBERT, M. S., SARIC, W. S., CARRILLO, R. B. JR. & CHAPMAN, K. 1996 Experiments in nonlinear saturation of stationary crossflow vortices in a swept-wing boundary layer. *AIAA Paper* 1996-0184 .
- [98] RIZZETTA, D. P. & VISBAL, M. R. 2017 Plasma-based control of excrescence-generated transition on a swept wing. *AIAA Journal* **55** (5), 1610–1621.
- [99] SADDOUGH, S. G. & VEERAVALLI, S. V. 1996 Hot-wire anemometry behaviour at very high frequencies. *Measurement Science and Technology* **7** (10), 1297–1300.
- [100] SARIC, W., CARRILLO R., JR. & REIBERT, M. 1998 Leading-edge roughness as a transition control mechanism. *AIAA Paper* 1998-781 .
- [101] SARIC, W. & REED, H. 2002 Supersonic laminar flow control on swept wings using distributed roughness. *AIAA Paper* 2002-147 .

- [102] SARIC, W., REED, H. & BANKS, D. 2004 Flight testing of laminar flow control in high-speed boundary layers. NATO-RTO-MP-AVT-111.
- [103] SARIC, W. S., CARPENTER, A. L. & REED, H. L. 2011 Passive control of transition in three-dimensional boundary layers, with emphasis on discrete roughness elements. *Philosophical Transactions of the Royal Society of London A: Mathematical, Physical and Engineering Sciences* **369** (1940), 1352–1364.
- [104] SARIC, W. S., REED, H. L. & WHITE, E. B. 2003 Stability and transition of three-dimensional boundary layers. *Annu. Rev. Fluid Mech.* **35** (1), 413–440.
- [105] SCARANO, F. 2002 Iterative image deformation methods in piv. *Measurement Science and Technology* **13** (1), R1.
- [106] SCARANO, F. 2013 Tomographic piv: principles and practice. *Measurement Science and Technology* **24** (1), 012001.
- [107] SCHLICHTING, H. & GERSTEN, K. 2000 *Boundary layer theory*. Cambridge University Press.
- [108] SCHRADER, L. U., BRANDT, L. & HENNINGSON, D. S. 2009 Receptivity mechanisms in three-dimensional boundary-layer flows. *J. Fluid Mech.* **618**, 209–241.
- [109] SCHRADER, L. U., BRANDT, L. & ZAKI, T. A. 2011 Receptivity, instability and breakdown of görtler flow. *J. Fluid Mech.* **682**, 362–396.
- [110] SCHRIJER, F. F. J. & SCARANO, F. 2008 Effect of predictor–corrector filtering on the stability and spatial resolution of iterative piv interrogation. *Experiments in Fluids* **45** (5), 927–941.
- [111] SCHUELE, C. Y., CORKE, T. C. & MATLIS, E. 2013 Control of stationary cross-flow modes in a mach 3.5 boundary layer using patterned passive and active roughness. *J. Fluid Mech.* **718**, 5–38.
- [112] SERPIERI, J. & KOTSONIS, M. 2015 Design of a swept wing wind tunnel model for study of cross-flow instability. *AIAA Paper* 2015-2576 .
- [113] SERPIERI, J. & KOTSONIS, M. 2015 Flow visualization of the boundary layer transition pattern on a swept wing. *10<sup>th</sup> Pacific Symposium on Flow Visualization and Image Processing*, Naples, Italy .
- [114] SERPIERI, J. & KOTSONIS, M. 2016 Three-dimensional organisation of primary and secondary crossflow instability. *J. Fluid Mech.* **799**, 200–245.
- [115] SERPIERI, J. & KOTSONIS, M. 2018 Conditioning of unsteady cross-flow instability modes using dielectric barrier discharge plasma actuators. *Experimental Thermal and Fluid Science* **93**, 305 – 318.
- [116] SERPIERI, J., YADALA VENKATA, S. & KOTSONIS, M. 2017 Conditioning of cross-flow instability modes using dielectric barrier discharge plasma actuators. *J. Fluid Mech.* **833**, 164–205.

- [117] SETTLES, G. 2009 Schlieren photograph of the thermal convection plume from an ordinary candle in still air.
- [118] SHAHRIARI, N. 2016 *On stability and receptivity of boundary-layer flows*. PhD Thesis, KTH Royal Institute of Technology, Stockholm, Sweden.
- [119] SIROVICH, L. 1987 Turbulence and the dynamics of coherent structures. part i: Coherent structures. *Quarterly of Applied Mathematics* **45** (3), 561–571.
- [120] SQUIRE, L. C. 1961 The motion of a thin oil sheet under the steady boundary layer on a body. *J. Fluid Mech.* **11** (2), 161–179.
- [121] TEMPELMANN, D., SCHRADER, L.-U., HANIFI, A., BRANDT, L. & HENNINGSON, D. S. 2012 Swept wing boundary-layer receptivity to localized surface roughness. *J. Fluid Mech.* **711**, 516–544.
- [122] THEOFILIS, V. 1998 On linear and nonlinear instability of the incompressible swept attachment-line boundary layer. *J. Fluid Mech.* **355**, 193–227.
- [123] TROPEA, C., YARIN, A. L. & FOSS, J. F. 2007 *Springer handbook of experimental fluid mechanics*. Springer Science+ Business Media, Berlin.
- [124] TUCKER, A. A., SARIC, W. S. & REED, H. L. 2014 Laminar flow control flight experiment design and execution. *AIAA Paper* 2014-909 .
- [125] VAN INGEN, J. L. 1956 A suggested semi-empirical method for the calculation of the boundary layer transition region. In *VTH-74*. Delft University of Technology, Delft, the Netherlands.
- [126] VAN OUDHEUSDEN, B. W., SCARANO, F., VAN HINSBERG, N. P. & WATT, D. W. 2005 Phase-resolved characterization of vortex shedding in the near wake of a square-section cylinder at incidence. *Experiments in Fluids* **39** (1), 86–98.
- [127] VIOLATO, D. & SCARANO, F. 2013 Three-dimensional vortex analysis and aeroacoustic source characterization of jet core breakdown. *Physics of Fluids (1994-present)* **25** (1), 015112.
- [128] WANG, J.-J., CHOI, K.-S., FENG, L.-H., JUKES, T. N. & WHALLEY, R. D. 2013 Recent developments in dbd plasma flow control. *Progress in Aerospace Sciences* **62** (Supplement C), 52 – 78.
- [129] WASSERMANN, P. & KLOKER, M. 2002 Mechanisms and passive control of crossflow-vortex-induced transition in a three-dimensional boundary layer. *J. Fluid Mech.* **456**, 49–84.
- [130] WASSERMANN, P. & KLOKER, M. 2003 Transition mechanisms induced by travelling crossflow vortices in a three-dimensional boundary layer. *J. Fluid Mech.* **483**, 67–89.
- [131] WASSERMANN, P. & KLOKER, M. 2005 Transition mechanisms in a three-dimensional boundary-layer flow with pressure-gradient changeover. *J. Fluid Mech.* **530**, 265–293.

- [132] WEIDEMAN, J. A. & REDDY, S. C. 2000 A matlab differentiation matrix suite. *ACM Trans. Math. Softw.* **26** (4), 465–519.
- [133] WELCH, P. D. 1967 The use of fast fourier transform for the estimation of power spectra: A method based on time averaging over short, modified periodograms. *Audio and Electroacoustics, IEEE Transactions on* **15** (2), 70–73.
- [134] WHITE, E. & SARIC, W. 2000 Application of variable leading-edge roughness for transition control on swept wings. *AIAA Paper* 2000-283 .
- [135] WHITE, E. B. & SARIC, W. S. 2005 Secondary instability of crossflow vortices. *J. Fluid Mech.* **525**, 275–308.
- [136] WHITE, F. M. & CORFIELD, I. 2006 *Viscous fluid flow*, , vol. 3. McGraw-Hill Higher Education Boston.
- [137] WIENEKE, B. 2008 Volume self-calibration for 3d particle image velocimetry. *Experiments in Fluids* **45** (4), 549–556.
- [138] YADALA VENKATA, S., HEHNER, M. T., SERPIERI, J., BENARD, N., DÖRR, P. C., KLOKER, M. J. & KOTSONIS, M. 2018 Experimental control of swept wing transition through base-flow modification by plasma actuators. *J. Fluid Mech.* .
- [139] YARUSEVYCH, S. & KOTSONIS, M. 2017 Steady and transient response of a laminar separation bubble to controlled disturbances. *J. Fluid Mech.* **813**, 955–990.
- [140] YE, Q., SCHRIJER, F. F. J. & SCARANO, F. 2016 Boundary layer transition mechanisms behind a micro-ramp. *J. Fluid Mech.* **793**, 132–161.

# SCIENTIFIC CONTRIBUTIONS

## IN THIS BOOKLET

### PEER-REVIEWED JOURNAL ARTICLES

- P. Rizzo, **J. Serpieri** & M. Kotsonis, *Effect of surface roughness and free stream turbulence on cross-flow instability transition*, (in preparation)
- S. Yadala Venkata, M. Hehner, **J. Serpieri**, N. Benard, P. Dörr, M. Kloker & M. Kotsonis, *Experimental control of swept wing transition by base-flow modification by plasma actuators*, *Journal of Fluid Mechanics* (under review)
- **J. Serpieri** & M. Kotsonis, *Conditioning of unsteady cross-flow instability modes using dielectric barrier discharge plasma actuators*, *Experimental Thermal and Fluid Science*, **93**, 305-318 (2018)
- **J. Serpieri**, S. Yadala Venkata & M. Kotsonis, *Conditioning of cross-flow instability modes using dielectric barrier discharge plasma actuators*, *Journal of Fluid Mechanics*, **833**, 164-205 (2017)
- **J. Serpieri** & M. Kotsonis, *Three-dimensional organisation of primary and secondary cross-flow instability*, *Journal of Fluid Mechanics*, **799**, 200-245 (2016)

### CONFERENCE PROCEEDINGS

- **J. Serpieri** & M. Kotsonis, *Time-resolved PIV investigation of the secondary instability of cross-flow vortices*, *10<sup>th</sup> Symposium on Turbulence and Shear Flow Phenomena (TSFP 10)*, Chicago, USA, (2017)
- **J. Serpieri**, S. Yadala Venkata & M. Kotsonis, *Towards laminar flow control on swept wings with AC-DBD plasma actuators as active roughness*, *55<sup>th</sup> AIAA Aerospace Sciences Meeting*, Grapevine, USA, (2017)
- **J. Serpieri** & M. Kotsonis, *Tomographic-PIV investigation of crossflow instability of swept wing boundary layers*, *46<sup>th</sup> AIAA Fluid Dynamics Conference*, Washington DC, USA, (2016)
- **J. Serpieri** & M. Kotsonis, *Spatio-temporal characteristics of secondary instabilities in swept wing boundary layers*, *46<sup>th</sup> AIAA Fluid Dynamics Conference*, Washington DC, USA, (2016)
- **J. Serpieri** & M. Kotsonis, *Flow visualization of swept wing boundary layer transition*, *10<sup>th</sup> Pacific Symposium on Flow Visualization and Image Processing (PSFVIP)*, Naples, Italy, (2015)
- **J. Serpieri** & M. Kotsonis, *Design of a swept wing wind tunnel model for study of cross-flow instability*, *33<sup>rd</sup> AIAA Applied Aerodynamics Conference*, Dallas, USA, (2015)

## NOT IN THIS BOOKLET

### PEER-REVIEWED JOURNAL ARTICLES

- **J. Serpieri**, F. Munaro & M. Kotsonis, *Swept wing boundary layer transition after isolated surface roughness*, (in preparation)
- S. Discetti, G. Bellani, R. Örlu, **J. Serpieri**, C. Sanmiguel Vila, M. Raiola, X. Zheng, L. Mascotelli, A. Talamelli & A. Ianiro, *Dynamic estimation of very large scale motions in pipe flow at high Reynolds numbers*, (in preparation)
- K. Groot, **J. Serpieri**, F. Pinna & M. Kotsonis, *Secondary crossflow instability through global analysis of measured base flows*, *Journal of Fluid Mechanics*, (under review)
- S. Pröbsting, **J. Serpieri** & F. Scarano, *Experimental investigation of aerofoil tonal noise generation*, *Journal of Fluid Mechanics*, **747**, 656-687 (2014)

### CONFERENCE PROCEEDINGS

- K. Groot, **J. Serpieri**, M. Kotsonis & F. Pinna, *Analysis of crossflow vortices using BiGlobal theory on PIV base flows*, *55<sup>th</sup> AIAA Aerospace Sciences Meeting, Grapevine, USA*, (2017)
- **J. Serpieri**, M. Gupta, S. Pröbsting & F. Scarano, *Effect of serrated trailing edge on boundary layer instability noise*, *21<sup>st</sup> AIAA/CEAS Aeroacoustics Conference, Dallas, USA*, (2015)
- S. Pröbsting, **J. Serpieri**, & F. Scarano, *High-speed PIV analysis of trailing edge aeroacoustics*, *10<sup>th</sup> International Symposium on Particle Image Velocimetry, Delft, the Netherlands*, (2013)
- S. Pröbsting, **J. Serpieri**, & F. Scarano, *Investigation of tonal noise generation on an airfoil with time-resolved PIV*, *19<sup>th</sup> AIAA/CEAS Aeroacoustics Conference, Berlin, Germany*, (2013)

### ORAL PRESENTATIONS

- S. Yadala Venkata, **J. Serpieri**, N. Benard, M. Kotsonis & E. Moreau, *Thin-electrode DBD plasma actuators for crossflow instability control*, *14<sup>th</sup> International Conference on Fluid Control, Measurements and Visualization (FLUCOME), Notre Dame, USA*, (2017)
- S. Yadala Venkata, M. Hehner, **J. Serpieri**, N. Benard, P. Dörr, M. Kloker & M. Kotsonis, *Control of crossflow instability using AC-DBD plasma actuators*, *14<sup>th</sup> International Conference on Fluid Control, Measurements and Visualization (FLUCOME), Notre Dame, USA*, (2017)
- S. Discetti, C. Sanmiguel Vila, M. Raiola, **J. Serpieri**, R. Örlu, X. Zheng, L. Mascotelli, G. Bellani, A. Talamelli, & A. Ianiro, *Very-large scale motions measurements in pipe flows at high Reynolds numbers*, *16<sup>th</sup> European Turbulence Conference (ETC), Stockholm, Sweden*, (2017)

### SEMINARS

- **J. Serpieri**, *On aerofoil tonal noise*, Instituto de Modelización y Simulación Numérica en Fluidodinámica, Nanociencia y Matemática Industrial "Gregorio Millán Barbany", Madrid, Spain, (2013)

# BIOGRAPHICAL NOTE

Curiosity towards everything characterized Jacopo's attitude to life since childhood. Emblematic episodes referring to this attitude are often told by those who met that cute annoying kid posing dozens of questions...

Today, Jacopo's main interests are Politics, Economics, Philosophy and History. He forgot how and why he ended up, back then, studying Aerospace Engineering and Fluid Dynamics in particular. Probably, the *Star Wars* saga coupled to the *Lego* gifts he received as kid somehow conditioned his later choices. Despite how it went, in 2013, he achieved his Master of Science *cum laude* from the University of Naples "Federico II" and later decided to challenge this "side interest" for almost other five years (considering the MSc thesis, the PhD and the ongoing research he is currently carrying out) at TU Delft *Aerodynamics*. This thesis summarizes the scientific aftermaths of Jacopo's PhD research. The scientific part is only a small portion of the treasure of knowledge and experiences this experience brought him.

He is also passionate about Arts (he contributed to opening and running an art gallery/laboratory in one of the socially most complicated neighbourhoods of his home town). Despite these interests, in any artistic expression, he is a shining example of incapacity. He showed, though, through the years, some soft skills. He became rather skilled in coordinating projects and advising colleagues, friends and students offering a peculiar mix of criticism and enthusiasm mitigated by his developed empathy. Furthermore, he is more than a decent cook especially when inspired by the colours, tastes and poetry of his homeland: Napoli and the Costiera.

Overall, Jacopo is a very social and outgoing person who loves being surrounded by his many friends. He is an aware citizen who takes seriously any social matter he faces, often offering himself as mediator or spokesman. Jacopo prefers considering his conscience rather than his own interest.

...  
*ma per seguir virtute e canoscenza*

Dante Alighieri, **Inferno XXVI**

